UNIVERSITY OF IOANNINA
COLLEGE OF SCIENCES AND TECHNOLOGIES
DEPARTMENT OF MATERIALS SCIENCE
ENGINEERING

SOTIRIOS A. GRAMMATIKOS
MATERIALS SCIENCE ENGINEER

Structural integrity assessment of aerostructures using innovative Non-Destructive Evaluation Techniques

Thesis for the degree of Doctor of Philosophy

Ioannina, 2013
Greece

ΠΑΝΕΠΙΣΤΗΜΙΟ ΙΩΑΝΝΙΝΩΝ
ΣΧΟΛΗ ΕΠΙΣΤΗΜΩΝ & ΤΕΧΝΟΛΟΓΙΩΝ
ΤΜΗΜΑ ΜΗΧΑΝΙΚΩΝ ΕΠΙΣΤΗΜΗΣ ΥΛΙΚΩΝ

ΣΩΤΗΡΙΟΣ Α. ΓΡΑΜΜΑΤΙΚΟΣ
ΜΗΧΑΝΙΚΟΣ ΕΠΙΣΤΗΜΗΣ ΥΛΙΚΩΝ

Αποτίμηση δομικής ακεραιότητας αεροπορικών δομών με χρήση καινοτόμων Μη-Καταστροφικών Τεχνικών

ΔΙΔΑΚΤΟΡΙΚΗ ΔΙΑΤΡΙΒΗ

ΙΩΑΝΝΙΝΑ 2013
Ελλάδα

Ημερομηνία αίτησης της/του κ. Γραμματικού Σωτήριου: 16/12/2008

Ημερομηνία ορισμού Τριμελούς Συμβουλευτικής Επιτροπής: 27/01/2009

Μέλη Τριμελούς Συμβουλευτικής Επιτροπής:

<u>Επιβλέπων</u>

Αλκιβιάδης Παϊπέτης, Αναπληρωτής Καθηγητής ΤΜΕΥ (επιβλέπων Καθηγητής)

<u>Μέλη</u>

Θεόδωρος Ματίκας, Καθηγητής ΤΜΕΥ
Νεκταρία-Μαριάνθη Μπάρκουλα, Επίκουρη Καθηγήτρια ΤΜΕΥ

Ημερομηνία ορισμού θέματος: 27/01/2009

ΑΠΟΤΙΜΗΣΗ ΔΟΜΙΚΗΣ ΑΚΕΡΑΙΟΤΗΤΑΣ ΑΕΡΟΠΟΡΙΚΩΝ ΔΟΜΩΝ ΜΕ ΧΡΗΣΗ ΚΑΙΝΟΤΟΜΩΝ ΜΗ-ΚΑΤΑΣΤΡΟΦΙΚΩΝ ΤΕΧΝΙΚΩΝ

<u>ΔΙΟΡΙΣΜΟΣ ΕΠΤΑΜΕΛΟΥΣ ΕΞΕΤΑΣΤΙΚΗΣ ΕΠΙΤΡΟΠΗΣ</u> : 20/12/2012

ΠΑΪΠΕΤΗΣ	ΑΛΚΙΒΙΑΔΗΣ
ΜΑΤΙΚΑΣ	ΘΕΟΔΩΡΟΣ
ΜΠΑΡΚΟΥΛΑ	ΝΕΚΤΑΡΙΑ-ΜΑΡΙΑΝΘΗ
ΜΠΕΛΤΣΙΟΣ	ΚΩΝΣΤΑΝΤΙΝΟΣ
ΚΑΛΠΑΚΙΔΗΣ	ΒΑΣΙΛΕΙΟΣ
ΛΕΚΑΤΟΥ	ΑΓΓΕΛΙΚΗ
ΔΑΣΣΙΟΣ	ΚΩΝΣΤΑΝΤΙΝΟΣ

<u>Έγκριση Διδακτορικής Διατριβής με βαθμό</u> **«ΑΡΙΣΤΑ»** στις: 07/02/2013

Πρόεδρος του Τμήματος Μηχανικών Επιστήμης Υλικών της Σχολής Επιστημών & Τεχνολογιών

Η Γραμματέας του Τμήματος

Ξανθή Τουτουνζόγλου

Application date: 16/12/2008

Designation date of the three member advising committee: 27/01/2009

Advising committee:

Supervisor

Alkiviadis Paipetis, Associate Professor MSE

Members

Theodore Matikas, Professor MSE
Nektaria-Marianthi Barkoula, Assistant Professor MSE

Designation date of thesis subject: 27/01/2009

STRUCTURAL INTEGRITY ASSESSMENT OF AEROSTRUCTURES USING INNOVATIVE NON-DESTRUCTIVE EVALUATION TECHNIQUES

Designation date of the seven member examining committee: 20/12/2012

ALKIVIADIS	PAIPETIS
THEODORE	MATIKAS
NEKTARIA-MARIANTHI	BARKOULA
KONSTANTINOS	BELTSIOS
VASILEIOS	KALPAKIDES
AGGELIKI	LEKATOU
KONSTANTINOS	DASSIOS

Doctor of philosophy certificate awarded with **«HONOURS»** on: 07/02/2013

Head of the Materials Science Engineering Department of the College of Sciences and Technologies:

Department Secretariat

Xanthi Toutountzoglou

To Orsa

Abstract

Advanced fibrous composite materials have been widely used by the aircraft industry over the last years due to their excellent specific properties. Aircraft industries are focusing on stretching the properties of advanced composite materials to their limits. The increased aging of the aircraft fleet has brought the need of novel repair methodologies that will assure and secure safe flights. It is therefore obvious, that efficient and effective non-destructive techniques are of primary importance in aerospace structures in order to provide full scale structural integrity assessment.

Within the scope of this work, innovative Non-Destructive Evaluation (NDE) techniques have been examined in this study. Quality assessment of materials and structures has been achieved via various modes of electrical, thermal and acoustic methods in both off-line (inspection on demand) and on-line conditions (structural health monitoring). More specifically, electrical techniques were employed in monitoring and mapping protocols, both in resistance and potential modes. Thermography was employed in Pulse, Pulse Phase and Lock-in mode. Finally, Acoustic Emission and ultrasonic scanning (B & C-scan) were employed as benchmarking methods. An innovative NDE approach developed within the context of this study involved the combination of electrical and thermal NDE approaches to a novel technique, i.e. the current injection thermography.

All techniques either individually or in conjunction were employed to interrogate a variety of specimen configurations, representing model configurations, structural details, or structures exploiting various forms of excitation as well as self sensing material principles. More specifically, at an initial level, the employed techniques were exploited for the characterization of damage in off-line conditions as this is typically the practice in aircraft maintenance. At a system level integration the investigated NDE techniques were applied in real time for structural health monitoring. The evaluation of the performance of the proposed NDE techniques in small scale structures preceded the highlight study of a real composite repaired helicopter wing (SW–4 /PZL-Swidnik /AgustaWestland).

Περίληψη

Προηγμένα σύνθετα υλικά χρησιμοποιούνται κατά κόρον στην αεροναυπηγική τεχνολογία τα τελευταία χρόνια λόγω των εξαιρετικών μηχανικών τους ιδιοτήτων. Η αεροναυπηγική βιομηχανία επενδύει στην έρευνα προηγμένων συνθέτων υλικών με σκοπό την περαιτέρω αύξηση των ειδικών μηχανικών τους ιδιοτήτων. Παράλληλα, η ολοένα αυξανόμενη ηλικία του αεροναυπηγικού στόλου έχει ανάγκη από νέες τεχνολογίες επισκευής οι οποίες θα διασφαλίσουν αξιόπιστες κατασκευές στα αεροσκάφη και εν συνεχεία ασφαλείς πτήσεις. Όπως είναι προφανές, καινοτόμοι Μη-Καταστροφικοί Έλεγχοι (ΜΚΕ) κρίνονται ως υψίστης σημασίας σε αεροδιαστημικές κατασκευές, σκοπεύοντας στην αποδοτική και ολοκληρωμένη εκτίμηση της δομικής τους ακεραιότητας. Αντικείμενο της διατριβής είναι η αξιολόγηση εσωτερικής βλάβης σε σύνθετα υλικά πολυμερικής μήτρας και ινώδους ενίσχυσης αλλά και σε επισκευές με χρήση επικολλώμενων επιθεμάτων ινωδών συνθέτων υλικών πολυμερικής μήτρας, κάνοντας χρήση πληθώρας καινοτόμων ΜΚΕ. Πιο αναλυτικά, έλαβε χώρα ποιοτική αξιολόγηση κατασκευών και υλικών μέσω ηλεκτρικών, θερμογραφικών αλλά και ακουστικών μεθόδων ΜΚΕ. Οι ηλεκτρικές τεχνικές χρησιμοποιήθηκαν για καταγραφή αλλά και χαρτογράφηση βλάβης μέσω μέτρησης της ηλεκτρικής αντιστάσεως όπως και του ηλεκτρικού δυναμικού. Η μέθοδοι Θερμογραφίας που μελετήθηκαν ήταν η Θερμογραφίας παλμού, φάσης παλμού όπως και η Θερμογραφία lock-in. Η τεχνική ακουστικής εκπομπής αλλά και η μέθοδος υπερήχων (B /C-scan) χρησιμοποιήθηκαν ως επαληθευτικές /συνδυαστικές τεχνικές σε όλα τα στάδια της διατριβής. Στο πλαίσιο της διατριβής, αναπτύχθηκε μια καινοτόμος προσέγγιση ΜΚΕ η οποία συνδυάζει τις τεχνικές Θερμογραφίας και ηλεκτρικών ιδιοτήτων όπου χρησιμοποιείται συνεχές ηλεκτρικό ρεύμα ως εξωτερική πηγή θερμικής διέγερσης.

Οι εξεταζόμενες μεθοδολογίες της διατριβής μη-καταστροφικού ελέγχου μελετήθηκαν ξεχωριστά αλλά και σε συνδυασμό για την ανίχνευση και παρακολούθηση βλάβης σε ποικιλία υλικών και κατασκευών χρησιμοποιώντας διάφορους τύπους εξωτερικής διέγερσης αλλά και αυτό-διάγνωσης. Συγκεκριμένα, η δομική αξιολόγηση των εξεταζόμενων υλικών μελετήθηκε σε δύο επίπεδα: σε εκτός (κατά απαίτηση) λειτουργίας και εν-λειτουργία (σε πραγματικό χρόνο) συνθήκες. Σε πρώτη φάση η έλαβε χώρα η ανίχνευση βλάβης σε κατάσταση εκτός λειτουργίας, όπως είθισται σε περιπτώσεις συντήρησης αεροσκαφών. Στη συνέχεια, οι ΜΚΕ τεχνικές εφαρμόσθηκαν σε πραγματικό χρόνο για την παρακολούθηση της δημιουργίας και εξέλιξης βλάβης σε εν-λειτουργία συνθήκες. Η αποτίμηση της αποδοτικότητας των ΜΚΕ σε κατασκευαστικές λεπτομέρειες, προηγήθηκε του αποκορυφώματος της διατριβής, το οποίο ήταν η χρήση η παρακολούθηση και αποτίμηση βλάβης σε μια πραγματική κατασκευή ενός φτερού ελικοπτέρου (SW–4 /PZL-Swidnik /AgustaWestland).

Acknowledgements

This PhD thesis would have never been realized without the vital contribution of a number of external factors. First and foremost, I feel obliged to my supervisor, Alkiviadis Paipetis, Associate Professor of the Materials Science Engineering (MSE) Department. I owe him a dept of sincere gratitude for everything that he has done during my whole scientific carrier since my undergraduate, my master and now my PhD work. Aside from that he is the friendliest person I have ever met, he is a distinguished scientist and has the gift of providing a solution to everything anytime needed in his pocket. Without his continuous encouragement, guidance and endless support, this thesis would not have been completed. Except for our scientific collaboration, a friendship was born escorting our collaboration for the past 5 years. He has played an imperative role in the success of my doctoral work and I would be more than glad to continue working in his team.

I wish to thank Theodore Matikas, Professor of MSE for his being a member of the advisory committee. I am grateful for his potent guidance and helpfulness for the conduction of my study. In addition, I would like to acknowledge his providing me access to all the equipment and laboratories of which is a director.

I wish to thank Nektaria-Marianthi Barkoula, Assistance Professor, of MSE for her being a member of my advisory committee. I am thankful to her for her help and support in as many ways as possible during my studies.

Furthermore, I would like to thank all the other members of the committee: Konstantinos Beltsios, Professor of MSE, Vasileios Kalpakides, Professor of MSE, Aggeliki Lekatou, Associate Professor of MSE and Kontsantinos Dassios, Lecturer of MSE.

Concurrently working in both "Mechanics of Composites & Smart Materials" and "Mechanics, Smart Structures & NDE" laboratories, I have been assisted in many ways by many colleagues. First and foremost, I am more than thankful to Evangelos Kordatos, an efficient PhD researcher and "master" in the field of thermography. I am convinced that his contribution was no less than crucial for the completion of my PhD. I would like to thank Dimitra Soulioti for her assistance in mechanical testing, Dimitris Exarchos for the help in thermographic testing and Michalis Dovas for his contribution to the ultrasonic testing. To continue, many thanks to all of the rest of my colleagues from both laboratories: Giannis Spyridon, Tasos Balaskas and Dimitris Bekas. Lastly, I am grateful to Dimitris Aggelis, Professor of the Vrije Universiteit Brussel (VUB) for initiating me in ultrasonics and acoustic emission techniques.

At that point, I have to express my thankfulness to my friend and "fellow traveler", Giorgos Gkikas. Studying together for those 9 years has been an honor for me, as he is an eminent researcher and, in parallel, a perfect character. I would like to thank him for his full support and for our great collaboration.

The next person I wish to acknowledge is a "special" person in my life, Orsa Boura. However, it would be a shame of me if I restricted my gratitude to her in just a paragraph. Briefly to praise her brilliant character and smart personality, along with her sea breeze - attitude and mentality.

Last but not least, I wish to thank my family members, my parents Athanasios and Vagia as well as my brother Evangelos. They have been helping me and supporting me in many ways, especially during these 9 years of my studies. They kept providing me all the psychological and financial support in order to achieve the maximum in my life.

Τέλος, ένα πολύ μεγάλο ευχαριστώ στην οικογένεια μου, στους γονείς μου Αθανάσιο και Βάγια και στον αδερφό μου Ευάγγελο, που με την αδιάλειπτη συμπαράσταση, υποστήριξη και κατανόηση τους σε ηθικό αλλά και υλικό επίπεδο μου δίνουν δύναμη και πυγμή ώστε να ανταπεξέρχομαι και να αποδίδω τα μέγιστα σε ότι πραγματεύομαι.

The PhD thesis was funded by the European project IAPETUS FP7:

Call ID: **"FP7-AAT-2008-RTD-1"**

Grant Agreement Number: **ACP7-GA-2008-234333**

Project acronym: **IAPETUS**

Project full title**: INNOVATIVE REPAIR OF AEROSPACE STRUCTURES WITH CURING OPTIMIZATION AND LIFE CYCLE MONITORING ABILITIES**

Ioannina, January 29th 2013
Sotirios A. Grammatikos

Ιωάννινα, 29 Ιανουαρίου 2013
Σωτήριος Α. Γραμματικός

Table of Contents

CHAPTER 1

Introduction

1.1 Introduction - overview

Composite materials in the aircraft industry are of major importance as they may have positive impact on a variety of critical functions. Enhanced specific properties are achieved by the use of such materials, like specific high strength and stiffness which allow reduction of the final weight with retained or improved mechanical properties [1]. As Hull mentions in his key monograph " Introduction to composite materials" [1], "the chief engineer of aircraft for the U.S. navy once mentioned that he likes composite materials because they do not "rot" (meaning corrode) and never "get tired" (meaning fatigue)".

Carbon Fibre Reinforced Polymers (CFRPs) as well as Glass Fibre Reinforced Polymers (GFRPs) are extensively used in aerospace, naval and civil structures. Concerning airborne structures, recent examples are the Airbus A380, Boeing 787 Dreamliner and the upcoming Airbus 350 XWB. These aircrafts employ more than 20%, 50% and 53% of composite materials in the airframe, respectively. As is reported, composite materials are used in wings, fuselage sections, doors as well as tail surfaces. It is well understood that the repair and the structural integrity evaluation are two highly important factors to be considered. With respect to the repair, bonded CFRPs have been widely investigated as repair elements in aluminum or either composite surfaces. Among others, sealing between the mother structure and the repair and the considerably decreased local stress concentrations are distinct benefits of the bonded repair methodology. However, before these bonded patches qualify as repair elements in aircraft, an effective Non-Destructive Evaluation (NDE) is critical in all stages of the lifetime of the repaired component. Quality assessment of an aircraft structure is essential during the manufacturing process, the assembling as well as its service life (maintenance-inspection and repair-operation). Aircraft industries are seeking effective, inexpensive and fast quality assessment of materials and structures. An ideal NDE technique should provide confidence for the required level of safety for aircrafts [2]. Defects invisible to the naked eye, initiation and propagation of any service induced damage should be efficiently identified and monitored.

The overall aim of the current thesis is the development and use of novel NDE techniques for the evaluation and monitoring of induced damage in composite materials as well as in composite repaired aircraft materials and structures. A variety of NDE techniques were employed for the accomplishment of the targets of this study. More specifically, IR Thermography (Pulsed Thermography-PT, Pulsed Phase Thermography-PPT, Lock-in Thermography-LT, Current Injection Phase Thermography-CIPT), Electrical Resistance

Change Monitoring (ERCM), Electrical Potential Change Monitoring (EPCM), Electrical Potential Mapping (EPM), Ultrasonics (C-scan imaging) and Acoustic Emission (AE) techniques were both individually and concurrently performed for the identification and monitoring of damage evolution in different composite laminate configurations and composite repaired materials and structures.

The employed NDE techniques were categorized into two basic scenarios; the Off-line and the On-line. The Off-line represents the Non-Destructive assessment of materials and structures in the manufacturing, after assembling and during maintenance (on-demand) processes. The On-line concept refers to the Non-Destructive assessment of materials and structures in real time or else during operation. This is also reported as Structural Health Monitoring (SHM) expressing a measure of the structural integrity and damage evolution during operation i.e. flight.

The novelty of the thesis lies on the gradual integration of the employed NDE techniques which were performed in different system levels: in typical composite laminates, in bonded composite repaired laminates, in representative coupons and, finally, in a real wing structure.

The current work accomplished two targets: i) to address the presence of damage in (hybrid) composite laminates and composite repaired plates (composite laminates and metals), ii) to monitor the initiation and propagation of damage in hybrid composites, bonded composite repaired laminates and bonded composite repaired structures, in real time, using a variety of non-destructive techniques.

Fundamental principles related to composite materials, bonded composite repairs in aircraft and NDE techniques are reported in Chapter 2. A brief theory of composites is outlined, along with general considerations related to the benefits of novel bonded repair methodology. The basic non-destructive techniques mainly employed in aircraft are presented and analyzed.

The 3rd chapter of the thesis expands on the use and implementation of novel non-destructive techniques for the identification of damage in hybrid composites as well as in bonded composite repaired laminates. Various optical thermographic methodologies were used for the identification of damage in composite laminates as well as in bonded composite repaired aluminum and composite plates. In particular, Pulsed, Pulsed Phase and Lock-in thermographic techniques were employed. Optical (incandescent) lamps were employed as heat sources in purposely made thermographic set-ups with a view to identifying damage in composites as well as composite repaired plates (both composite and aluminum). Moreover, a new mode of phase thermography was developed for the first time. It deals with the thermal excitation of a material by injecting direct electrical current. In this way, the inherent properties (electrical) of the material are exploited for the propagation of the electrical current. Due to Joule effect, a temperature gradient is generated on the surface of the material, which is detected with a thermal sensitive camera. The CNT effect on the electrical and, consequently, on the thermal properties of CFRP laminates was also interrogated with the thermal camera. CNTs were found to improve the electrical conductive network of the laminate forming additional electrical contacts in the material. The advantage of such incorporation was a uniform temperature distribution in the material improving the accuracy of the thermographic methodology. The CNT effect was also examined when mapping the electrical potential values of CFRP laminates in order to pin-point internal damage. Electrical potential mapping is a stand-alone technique based on the damage induced electrical anisotropy of the material. According to the methodology, the electrical network of the CFRP laminates was interrogated through electrical potential measurements along the surface and cross-section of the plates. Inherent damage alters the electrical properties by deforming the "electrical grid" of the laminate. With respect to the efficiency of the technique, it was considered as a promising NDE tool. However, the technique is affected by secondary parameters, such as surface of the investigated material and the electrical contacts. Regarding all the aforementioned stages of the chapter, C-scan imaging was adopted for the benchmarking of the particular evaluation methods.

The 4th chapter is concerned with the use of NDE techniques in on-line conditions. Electrical resistance /potential change technique, Lock-in thermography and acoustic emission techniques were applied in various specimens and structures for the monitoring of service - induced damage and bonded repair efficiency. The Electrical Potential Change Monitoring (ERCM) technique was developed to monitor the deterioration of CFRP and GFRP laminates. In the CFRP aspect, CNTs were dispersed in the epoxy matrix. The CNT effect on the sensing properties of the materials was verified by comparing reference and CNT modified CFRPs. Another investigated approach involved employing ordered all-CNT structures in the form of fibres in the structure of GFRPs. The electrically conductive fibres were embedded in bulk GFRP specimens, so as to follow the bulk deformation of the material. Electrical resistance measurements indicated the CNT fibres exhibited piezoresistive properties upon deformation. Together with the CNT fibre deterioration, stiffness loss of the GFRP laminates was estimated. The embedded CNT fibres were proved to operate as internal strain gauges. In the same chapter, LT is employed for the monitoring and characterization of service-induced damage in bonded composite repaired materials. In this case, both composite and aluminum strips with artificially induced damage were tested. The damaged areas were repaired with the bonded repair methodology and, consecutively, the patched materials were submitted to dynamic mechanical loading. Lock-in images were recorded during testing. As was observed, the integrity monitoring of the bonded repair was feasible. Critical and subcritical damage was monitored in real time. AE, as a complementary real time assessment technique, was also employed in a combined NDE system which constituted of EPCM, LT and AE, all combined towards the efficient Structural health monitoring of bonded composite repaired specimens. The deterioration profile of bonded repairs was recorded in real time using all three techniques simultaneously. After a complete testing series, the combined NDE system was used to monitor service damage in representative small scale components. Double overlap fatigue and skin doubler aluminum substrates were examined in dynamic and quasi-static loading conditions. The components targeted in testing the combined NDE system in order to study typical loading conditions taking place at the vicinity of repaired region. The integration of structural health monitoring was achieved with a system level shift in large scale structures. An aluminum wing was tested under dynamic mechanical testing. The tested structure was artificially damaged with a frequently encountered form of damage i.e. a crack. In sequence, the damaged region was repaired. LT was successfully applied to monitor the deterioration of the patch /parent skin interface during bending fatigue mechanical loading.

A conclusive summary of the work is presented in the 5th chapter. All non-destructive assessment systems analyzed in the pages of the thesis are characterized and evaluated. The conclusions of the thesis follow future suggestions and recommendations related to the field of the study.

CHAPTER 2

Background

2.1 Introduction to Composite materials and bonded repairs

Composite materials consist of two or more physically or /and chemically distinct phases appropriately combined together in order to provide a new material with improved predefined properties. Typically, composite materials consist of two phases: the reinforcement (dispersed) and the matrix (continuous). Depending on the intended usage, the engineer can design the composite material in order to optimally adapt it to the needs of a particular application. The chemical, physical and mechanical characteristics of the two phases remain the same after their combination. Potential types of reinforcement are fibres (short or long) or particles. Carbon, Kevlar, and Glass are examples of fibre reinforcement. As is obvious, in the case of fibre reinforcement, enhanced mechanical properties exist in the direction of the reinforcement. In the case of a particulate - reinforced composite, the reinforcement direction is random and always a function of the mixing process and technique. As far as the matrix is concerned, it can be a polymer, ceramic or metal. The reinforcement is typically stiffer and higher in strength compared to the matrix. The common area between the reinforcement and the matrix is the interface. The strength of the interface dominates the strength of the composite material [1, 3]. The scheme below (Fig.2.1) represents schematic configurations of different types of composite materials.

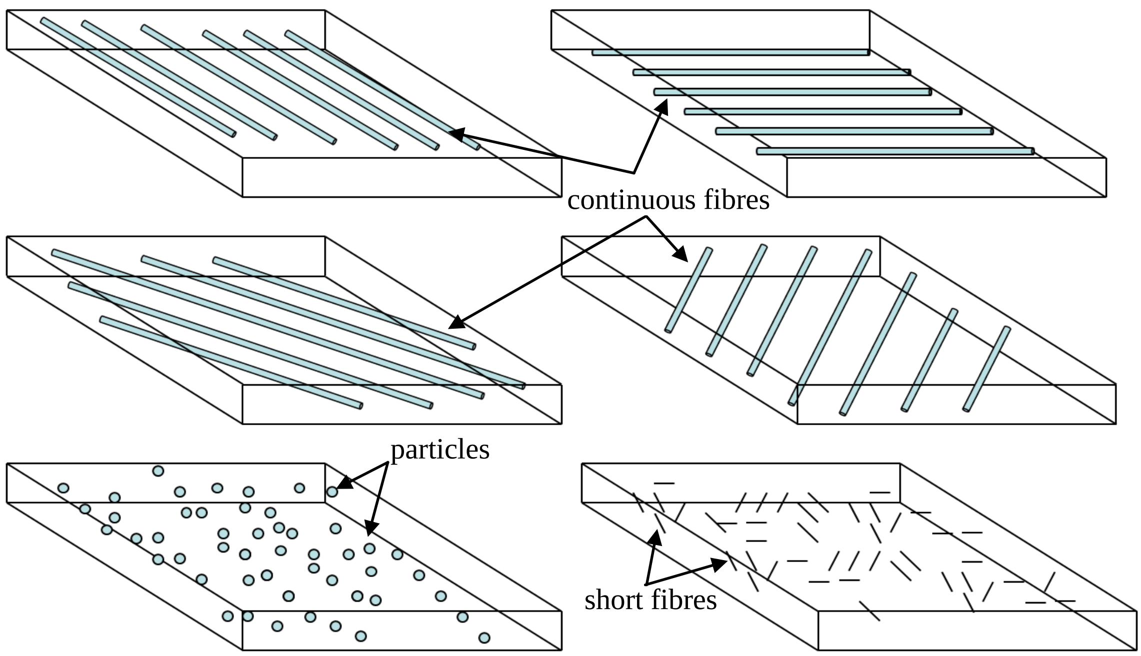

Figure 2.1 *Schematic representation of composite materials.*

Two or more different layers of a reinforcement embedded in a matrix, compose a laminate. A lamina is a single layer or ply of a laminate. It is then well understood that the bonding degree between the particular laminas control the total stiffness of the laminate. The main advantage of advanced composite materials over metals is the light weight. This benefit goes together with the increased specific strength, stiffness and modulus of elasticity.

The first composite materials were developed in 19^{th} century by wood fibres and natural resins for the matrix such as pitch. However, the mass production of composite materials only started at 1930. Initially, composite materials were confined to aerostructures, chemical and naval industries due to their high fabrication costs. Nowadays, there is a vast variety of the applications of composite materials. Some examples are sports (bikes, helmets, skis etc), cars (formula 1, motorcycles), medicine (teeth, artificial ligaments etc), ships, all kind of aircraft etc. [4, 5]. Composite materials became gradually more popular and replaced metals and metal alloys in several applications. Currently, the aeronautical industries absorb the 75% of composite materials production [6, 7].

From the mechanical point of view, composites are anisotropic and inhomogeneous materials. Their anisotropy leads to the initiation and propagation of different "damage entities", often acting /interacting at distinct scales. Composite laminates fail with a complex behaviour which usually is not self-evident. For example, a single crack in metals is usually predictably propagating leading to catastrophic failure. However, this is not always the case in composite laminates, where, delaminations, fibre-matrix cracking, fibre breakage are frequently encountered [1, 8]. Typical to composites is that a combination of the aforementioned failure modes is active most of the times. When pertaining to the instigation of damage in composite laminates, it is more convenient to first refer to their particular life stage. Critical phases of their "life" are the manufacturing, assembling and service life. During manufacturing misaligned fibres, matrix cracking due to residual stresses, resin-rich regions, porosity and discontinuities in general, are common failure sites [9-11]. These sites expand during the service life of the materials and may lead unexpectedly to catastrophic failure. Combined with the above parameters, mechanical stresses and environmental factors act cumulatively [1, 8]. Regarding mechanically induced stress fields, periodic loading such as fatigue, is considered to be the most important structural degradation loading case. In the case of fatigue, the fiber-matrix interface and the polymer matrix mark the durability of the composites [12, 13]. With respect to environmental degradation, such parameters as large temperature variations (i.e. from 30 ^{0}C to -75 ^{0}C) and humidity are crucial damage sources in composite materials [14, 15]. Last but not least, composites are prone to impact damage. Impact damage can be induced during manufacturing, assembling and service (operation and maintenance). Impact damage instigates dangerous forms of damage, such as delaminations, matrix and fibre cracking. In particular, the propagation of impact - induced damage is directly linked to the mechanical loading of the impacted structure. In this case, the prospective consequence is the catastrophic failure of the structure [16].

Fatigue as well as stress corrosion have always been a major problem for metallic aircrafts. In most cases, a crack, which is invisible to the naked eye, may develop catastrophically. A crack or defect can occur during the manufacturing process, assembling, during flight or even during the scheduled repair of an aircraft [17, 18]. The replacement of a damaged section is the last resort for the rehabilitation of the aircraft. At the same time, the increased aging of the airborne structures has increased the need for new maintenance methodologies which would guarantee airworthiness. With respect to aircraft repair, an efficient method has been proposed by Baker A. A. in Australia [18], which refers to the bonded repair methodology. This technique takes advantage of the properties of composite materials i.e. CFRPs, in order to repair a cracked component. CFRP patches are directly applied on the surface of the damaged material. Being more expensive than conventional repairs [17], the bonded repair methodology exhibits considerable benefits compared to the mechanically fastened repair technique. The fibrous composite materials which are used in the bonded repair concept offer increased specific stiffness, which minimizes the weight penalty for the primary structure. The improved stiffness is coming along with other properties inherent to composite materials, such as improved fatigue resistance. In bonded repairs, mechanical load is uniformly transferred on the substrate. As the cracked component is not replaced, there is no need to introduce secondary notches /cracks by drilling in order to fasten a patch on the primary structure. Last but not least, the interface is completely sealed and thus fretting, crevice corrosion and galvanic corrosion effects are minimized [19]. Fig.2.2 depicts an applied composite patch on an aluminum cracked surface.

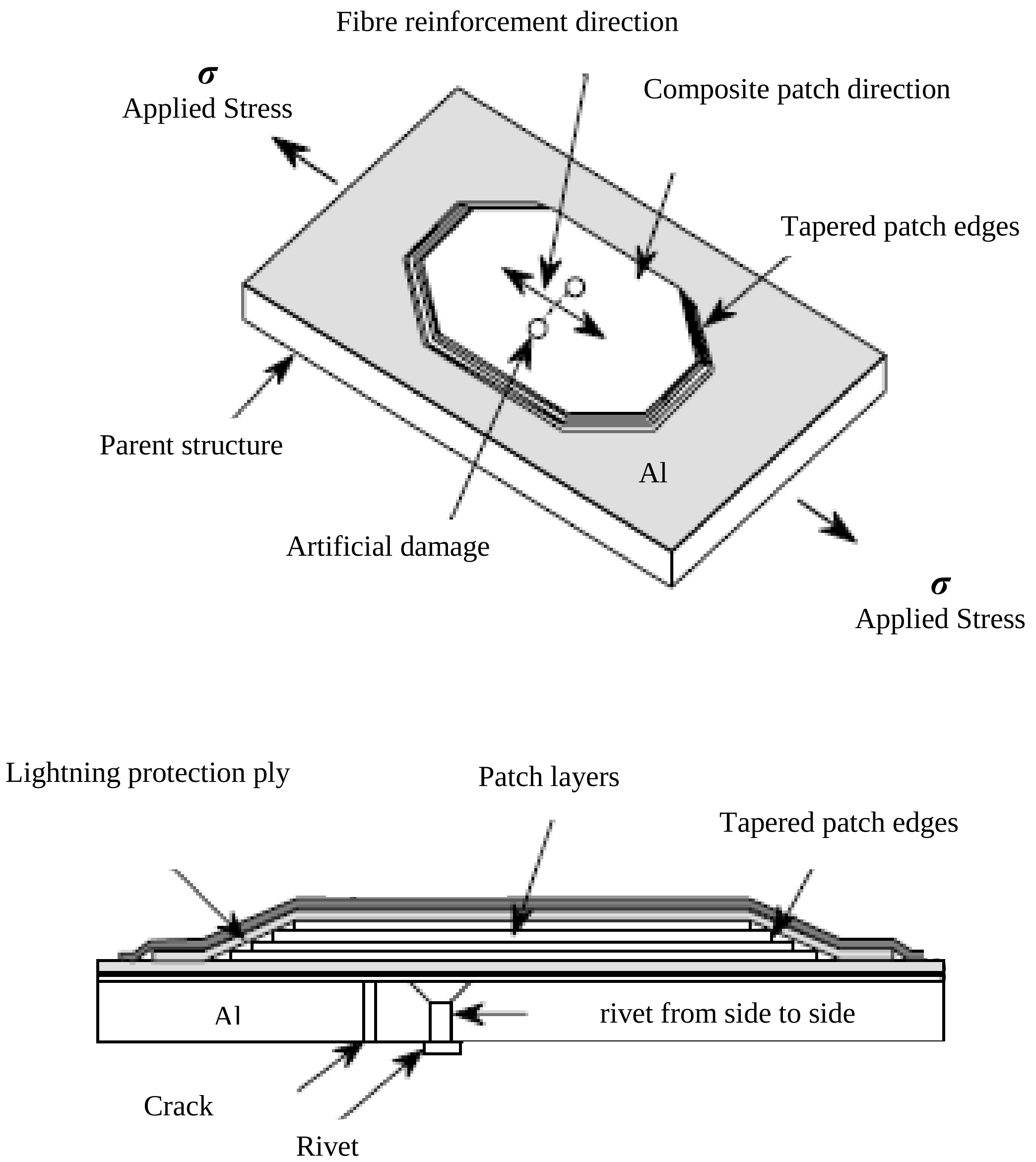

Figure 2.2 *Schematics of the top and cross-section of a bonded composite repair patch [20].*

In summary, distinct advantages of the bonded composite repair approach include:

1. Bonded repairs help to relieve the residual stresses brought on by traditional fastened repair methodology. The adhesively bonding concept eliminates stress concentrations, and new dangerous crack initiation sites, caused by additional fastener circular holes.

2. Bonded repairs allow for rapid, coherent joining of materials. Load transfer occurs over the entire footprint of the patch /adhesive. The patch edges can be tapered to gradually introduce the reinforcing effect. This greatly reduces stress concentrations associated with discretely

fastened repairs. The more uniform load distribution provided by bonded repairs improves fatigue life.

3. The bonded repair method provides localized support around the damaged region thus providing better crack mitigation than traditional repairs.

4. Composite patches can be tailored to meet specific anisotropy needs hence eliminating the undesirable stiffening of a structure in directions other than those required. The directional stiffness of composite patch can appropriately be designed to address the critical loads so that reinforcement is applied only in the desired direction(s).

5. Adhesively bonded patches perform better than bolted patches, as the effect of the low shear strength of the adhesive layer is superseded by the large contact area.

6. This repair resists corrosion which may eliminate the onset of stress corrosion cracking.

7. Composite laminates are “flexible” permitting the repair of irregular and geometrically complex structures.

8. Non-aggravation of the primary structure as the composite patch possesses a very low weight and very low thickness. These two factors have a positive effect on fuel consumption as well as aerodynamics design.

9. Composite bonded repairs can be performed very fast; therefore economic advantages stem primarily from repair time having a secondary effect on reduced aircraft downtime.

The efficiency of bonded repair over conventional fastened repair one is well demonstrated in [21] and schematically shown in Fig.2.3. Differences between the fastened and bonded repair methodologies as presented in [22] are juxtaposed and compared in Fig.2.3.

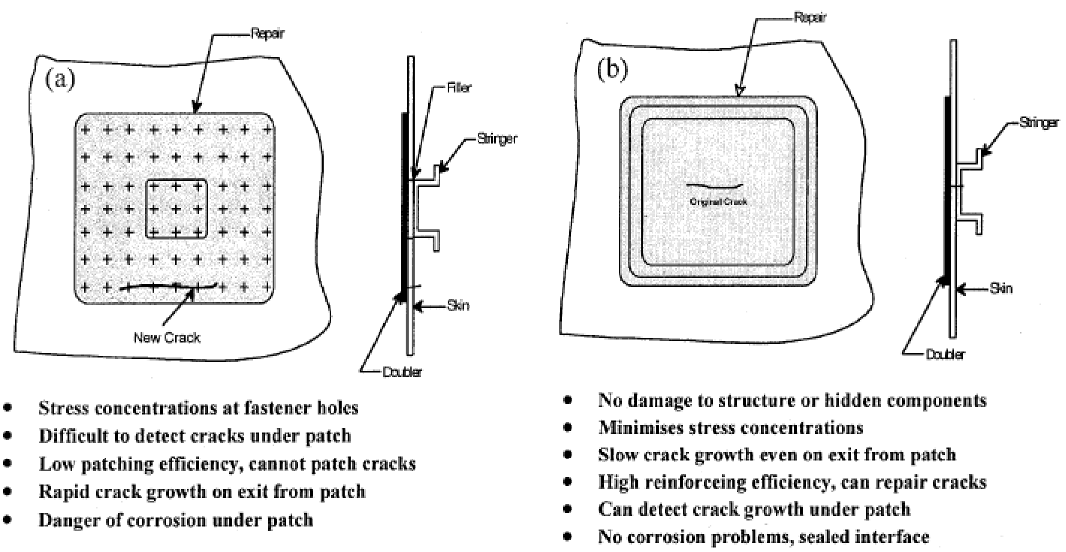

Figure 2.3 *Fastened repair vs. bonded composite repair methodology [22].*

It is also clear that, irrespective of the static performance of the repaired component, fatigue loading may lead to crack initiation from fastened holes, which are typically loci of stress concentration. The improved efficiency of bonded versus mechanically fastened repair is clearly demonstrated experimentally [7]. As explained in Fig.2.4, composite patched aluminum edged notched panels exhibited clearly superior behavior to fatigue loading than the mechanically fastened method, as the crack propagation under the patch is significantly delayed when the doubler is bonded and practically sealed on the substrate. Fig.2.4 manifests the crack arrest phenomenon when a crack evolution meets an applied bonded patch.

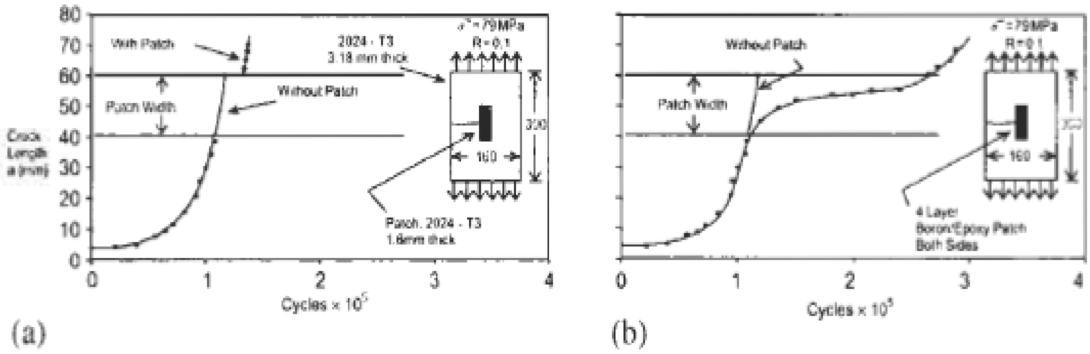

Figure 2.4 *Comparison of crack growth performance of patching efficiency between a) a mechanically fastened mechanical repair, and b) an adhesively bonded composite repair [23].*

The efficiency of the adhesive layer defines the sustainable factor for bonded repair methodology. The limitations posed by current adhesive technology lead to the endorsement of mechanically fastened patches by aircraft manufacturers, at least for structurally critical component repair. Typical failure mechanisms of bonded composite repairs comprise (i) patch /substrate interface failure and (ii) delaminations between the patch layers. A combination of fatigue loading conditions and environmental degradation mechanisms can be detrimental to the repaired structure mechanical properties [20, 23]. Baker's pioneering work [18] presented a significant analysis regarding the repair of cracked metallic surfaces with bonded repair methodology. Composite patch reinforcement, such as boron and carbon fibres, is discussed. These two reinforcements are considered to meet the requirements of ideal materials for crack patching [24, 25]. Ouinas et al. examined the effect of the boron and carbon /epoxy repairs on the reduction of the Stress Intensity Factor (SIF) at the crack tip [26]. The reduction of SIF was more prominent in the case of boron /epoxy than in the carbon /epoxy patching. Bachir Bouiadjra B. et al. [27] showed the dependence of the SIF on the possible adhesive disbands, especially when a transverse disband is encountered. It is known that the adhesive thickness dominates the SIF value [28]. The lower the thickness of the adhesive is, the lower the SIF value is. However, there is a limit in the adhesive layer thickness as the lower the thickness gets, the higher the risk of adhesive failure can be. Additionally, a major concern in composite repair is that of the use of a different material for repair than that of the mother structure. The difference of the Coefficient of Thermal Expansion (CTE) between the two materials is bound to cause thermal stresses [24]. Usually, the differential CTE leads to the generation of residual tensile stresses after the repair installation. Boron and carbon /epoxy material possess low CTE values compared to metals. Nevertheless, in the case of a composite parent structure i.e. Airbus A380 /A350 XWB /Boeing 787, this concern is redundant.

As aforementioned, the main advantage of bonded repair is the elimination of the Stress Concentration (SC) at the crack tip. This elimination increases the fatigue life of the component. In most cases, the patch repair is applied in a single side of the cracked surface. Although the double sided or symmetric repair is far more effective, it is rarely feasible. In such a case, the symmetric repair methodology is used. This leads successively to generation of bending stresses and a SIF increment at the crack tip. The value of SIF in this case is higher than that of the unrepaired material. This bending stress field is the Achilles heel of the asymmetric patch repair. Many researchers use the Finite Element Method (FEM) in order to calculate the SIF at the crack tip, with a view to estimating the behavior of a patched crack. FEM results confirm that the symmetric (double-sided repair) excels in the elimination of the SIF at the crack tip compared to the unsymmetrical repair [28, 29]. Dae-Cheol Seo and Jung-Ju Lee employed 3D FEM models in order to calculate the SIF of a crack repaired with a bonded composite patch [30, 31]. They reported the difference between the symmetrical and unsymmetrical repair patches. The problem was also addressed by Duong et al. [32] who modeled a geometry which proposes gradual increase of the patch thickness. This practice– commonly referred to as “tapering” in patch repair processes-minimizes the bending and the shear stresses at the edges of the repair and, consequently, reduces the SIF at the crack tip [33-35].

2.2 Non-destructive assessment

2.2.1 General considerations

With respect to the many stages of life of a composite aircraft material or structures, a variety of defects may be induced. Critical phases are the manufacturing and assembling as well as its operation life which includes the scheduled repair during downtime. During all these life steps, various defects may be caused and under certain conditions propagate. Local discontinuities usually develop catastrophically when the structure is mechanically loaded. It is evident that NDE techniques used for the inspection and monitoring of the structural integrity of materials and structures are of primary significance. They could be characterized as vital for their secure operational life. Generally the term NDE includes all techniques that are used to examine a material or structure without impairing its usefulness [36]. There are some distinct terms which descry the particular NDE techniques regarding the time of their usage. Typical terms are the Out-of-service, In-service, Off-line and On-line. The Out-of-service refers to the inspection at the manufacturing and after assembling processes or else when the material or structure is not officially used. The In-service quality assessment concept takes place when the material or structure is in operation, including both maintenance and flight time. The Off-line term represents inspection when the structure is not loaded and particularly including (i) manufacturing, (ii) assembling, and (iii) maintenance. Finally, the On-line term refers to those techniques that can be applied during its purpose made function i.e. of an aircraft structure. The on-line inspection is often identified with real-time and SHM. As aforementioned in *Chapter 1*, NDE techniques in “off-line” and “on-line” conditions are within the scope of the current thesis.

Conventional NDE techniques are used to periodically inspect a structure. Innovative NDE techniques can work on-line, providing instantaneously a “snapshot” of the internal condition of a structure and thus enabling SHM [37-39]. Effective non-destructive evaluation techniques are of primary importance as they serve the dual purpose of preventing catastrophic failure and extending the operational life of structural components. It is beyond doubt that new materials and processes as in the case of composites and bonded composite repairs require protocols that will certify their integrity for their safe in service operation.

Due to the fact that NDE methodologies have limitations and “weak” points, a combination of NDE techniques is the optimum way for structural integrity assessment providing a complete inspection or SHM of a structure. Some of the most frequently employed NDE techniques are listed as follows:

- **Acoustic Emission (AE)**
- Acousto-Ultrasonics (AU)
- Liquid penetrates
- Eddy Currents
- **Thermography**
- Holography
- Tap Testing
- Acoustic Microscopy
- Visual inspection
- Replication
- Radiography
- Visual Inspection
- Radiography (Gamma, X-rays)
- **Ultrasonics**
  - A /B-scan
  - **C-scan**
  - L-scan (Guided /Lamb Waves)
- **Electrical Methods**
  - **Electrical Resistance /Potential Change Monitoring technique**
  - **Electrical Potential Mapping**
- Shearography
- Magnetic Measurements
- Laser Interferometry
- Flux Leakage
- Magnetic Particle

Most of the NDE techniques listed above are often employed by the aircraft industry, but not all of them are fully qualified for in service testing. The NDE techniques studied within the scope of this work are marked in bold. NDE is essential in many applications such as: civil structures [40], marine structures [41, 42], oil industry [43, 44], aerospace industry [45], automotive [46], food [47, 48] as well as in medicine [49, 50]. Moreover, NDE techniques can be divided in “scanning” and “full-field” techniques (Fig.2.5). This differentiation is directly linked to the field of view (FOV) of a specific imaging methodology. The reduction of the FOV improves the resolving power of the technique in the expense of the image size. Scanning techniques perform a 1D, 2D or 3D image reconstruction from individual signals. In this respect, all imaging techniques may be employed in scanning of full field mode. The following flow chart (Fig.2.5) depicts various techniques usually categorized as scanning, full field and those capable of SHM.

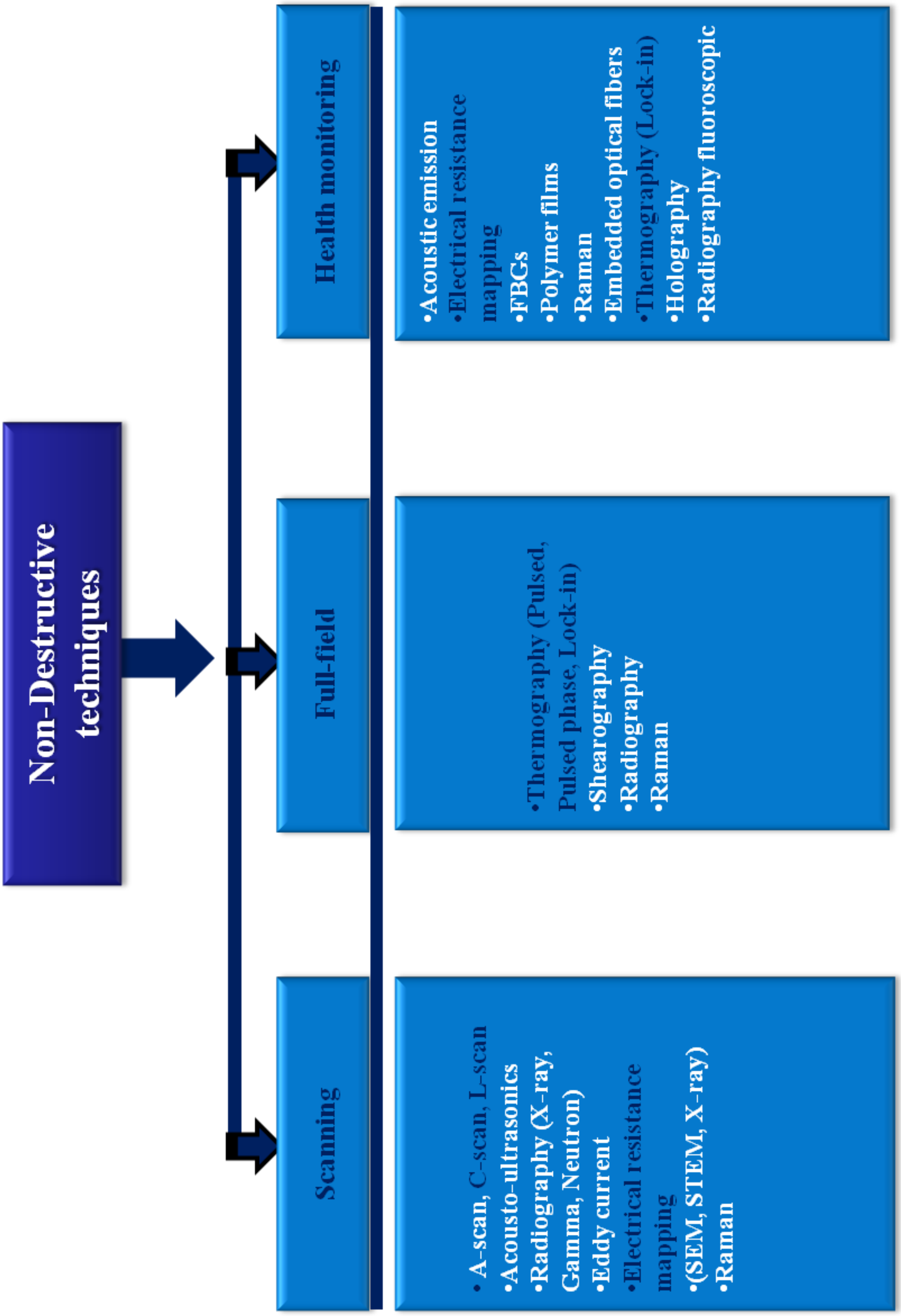

Figure 2.5 *Non-Destructive Evaluation techniques; Scanning, Full-field and SHM.*

According to DIN EN 4179 (2011-02 /Aerospace series-Qualification and approval of personnel for non-destructive testing; German and English version EN 4179:2009), in aerospace applications prospective types of defects in aerostructures made of composites are: foreign body inclusion, voids, porosity, resin-rich and lack of resin areas, debonding, delaminations, impact damage, water in honeycomb composites. The application of an NDE technique usually follows optical inspection by specialized staff. In most cases, once a flawed area is visible, more specialized NDE techniques are usually employed. Typically the employed protocol is as follows: after visual inspection, tap testing is performed. Tap testing is effective for defects close to the surface. When a damaged area is tapped, sound in different frequency than the surrounding region (intact) is generated. Afterwards, Ultrasonics, X-rays and Eddy Currents follow. When the inspected structure is made of ferromagnetic material, magnetic particle and Liquid penetration testing are also employed.

Further down, common NDE techniques are outlined. Basic characteristics of the most frequently used techniques are presented, while the NDE techniques utilized in the framework of this study (various deployments of Infrared Thermography, Electrical Resistance Change Monitoring, Electrical Potential Change Monitoring, Electrical Potential Mapping, Ultrasonics (C-scan) and Acoustic Emission) are analyzed in detail.

2.2.2 Holography

Holography is a full field imaging technique based on small displacements in the order of ¼ of the wave number used in the case of a laser. Local increased displacements indicate the presence of damage. Holographic magnitude and phase imaging of the reflected - from the structure - light are recorded. Surface and sub-surface discontinuities can easily be detected. Perfect alignment of the experimental setup is crucial as it is susceptible to external vibrations [51, 52].

2.2.3 Shearography

Shearography is a full-field imaging technique based on laser displacement changes. The resulted fringe patterns are recorded using an image-shearing camera. The technique has shown to be more effective in identifying stress concentrations than cracks or voids. In addition, strain analysis is feasible [53, 54].

2.2.4 Radiography

Radiography is a full-field imaging technique. In the radiographic imaging mode, X and γ-rays are induced on the surface of the material under investigation. The method is based on the absorption variations due to differences in physical characteristics, thickness, density, etc. The non-absorbed irradiated energy is printed on a film or recorded by sensors revealing the presence of damage. Crack and voids can be identified [55].

2.2.5 Eddy Current technique (EC)

EC technique uses alternating currents through a conducting coil employed in adjacency with the inspection surface. In response, the inspected material generates internally eddy currents in reverse to the alternating current of the coil. The generated eddy currents can then measured by a coil or appropriate magnetic field sensors. Variations in the induced eddy currents field may be attributed to inherent changes of the material electromagnetic properties and /or geometrical variations, i.e. cracks, discontinuities. EC technique is efficient in identifying surface cracks as well as for the estimation of electrical conductivity and coating thickness. However, EC has a limited use in electromagnetic materials and thus inspection of i.e. glass /epoxy composites is not feasible [56, 57].

2.2.6 Infrared Thermography

Infrared Thermography (IrT) is a thermal stimulating technique which uses thermal variations in order to evaluate the inherent characteristics i.e. defects and flaws of materials and structures. The principle of IrT is based upon the transformation of the surface thermal gradients of the investigated materials into an image, through a thermal-sensitive sensor, like an Infrared (IR) camera. The thermal variations on the surface of a material can be monitored optically via its infrared energy radiation. The encountered defects are projected on the thermal properties of the material surface; defects generate local thermal differences which result into differential thermal transfer between the flawed and flaw-free regions. Characteristic defects are due to corrosion, delaminations, cavitations, moisture, impact damage etc. [58]. IrT is based on the fact that every material in a temperature higher than the absolute zero always emits energy. This energy radiates to all directions. All thermographic setups require a thermal sensitive camera, a dedicated system to analyze the thermal images and a heat source when the material is not physically in different temperature than the ambient. IrT is categorized in two distinct approaches; the active [59] (Fig.2.6) and the passive [60]. In the passive protocol, the material is physically in different (usually higher) temperature than the ambient, whereas in the active, a heat source is necessary to thermally stimulate the material. Fig.2.6 demonstrates the active approach of IrT.

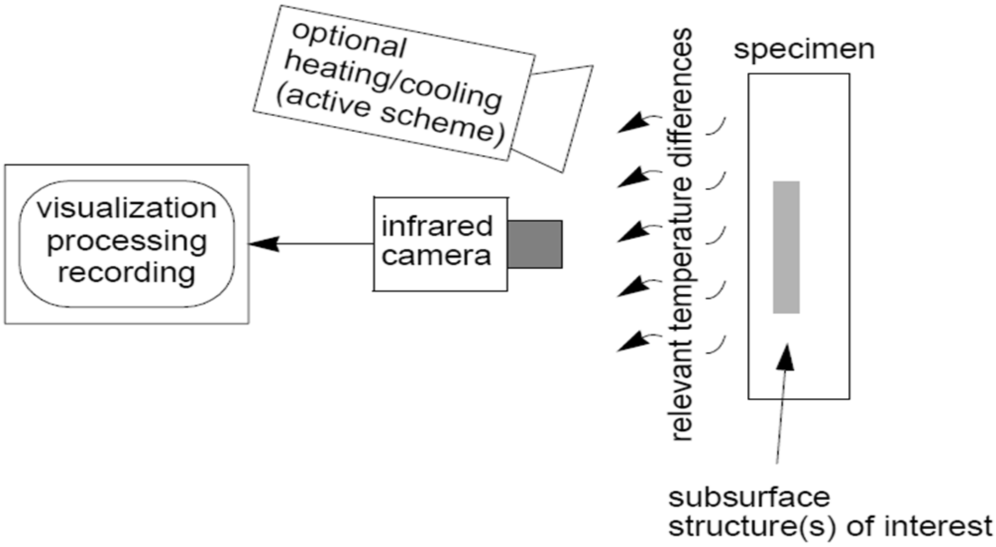

Figure 2.6 *Active infrared thermography [60, 61].*

There are different modes for heat transfer: conduction, induction and radiation. The radiation is the heat transfer mode which is exploited for inspection with thermography [62]. Characteristic benefits of infrared thermographic technique are (i) the non-contact inspection, (ii) the capability of fast inspection of large surfaces (full-field method), (iii) 2D image acquisition. Usually, a black mat paint is applied on the material surface under examination in order to render the materials surface properties (emissivity) close to that of the black body's ($\varepsilon = 1$) [62]. At high stimulation frequencies, a secondary thermoelastic effect is generated due to the diffusion delay from the material to the paint and vice versa, which allows for the calculation of the locally induced thermoelastic stresses [63, 64]. With respect to the active protocol and depending on the different mode of thermal excitation, various thermographic techniques are found in the literature. Characteristic thermographic modes are:

- Step-Heating Thermography-SH
- Vibration Thermography-VT
- Current injection phase thermography – CIPT (the method was developed for the first time in the framework of the current thesis – *see Section 3.3*)

In Step-Heating Thermography - SH approach, the material is thermally stimulated and the increase of the material temperature is monitored. It is usually also called as Time - resolved Infrared Radiometry - TRIR [60, 65].

In Vibration Thermographic mode - VT, an external vibration source is used for the thermal excitation. In that case, mechanical energy produces the necessary thermal gradient. The generated thermal energy is reflected from regions where defects are present [60, 61, 66].

Current Injection Thermography – CIT is a novel active thermographic concept. Typical active thermography uses optical (incandescent or flash lamps) thermal excitation in order to create the necessary thermal gradient on the surface of the material. In the case of CIT, electrical current is injected through the thickness of the inspected material. Thus, the material is heated via the "Joule effect" and thermographic images are recorded in the transient regime. The method is in detail described in *Section 3.3*.

With respect to the active approach and depending on the different post processing procedures of the recorded thermal transient, various thermographic techniques are found in the literature. Characteristic methodologies are:

- Pulsed Thermography-PT
- Pulse Phase Thermography-PPT
- Lock-in Thermography-LT

Pulsed Thermography-PT is a widely employed technique, mainly used in aerospace applications [60, 67]. PT is a thermal stimulation technique where the surface under investigation is heated via a thermal pulse (square). Thermal images are recorded during the cooling down process.The period of the heating pulse depends on the thermal conductivity of the material and varies and from some milliseconds (metals) to a few seconds (composites) (Fig.2.7) [61].

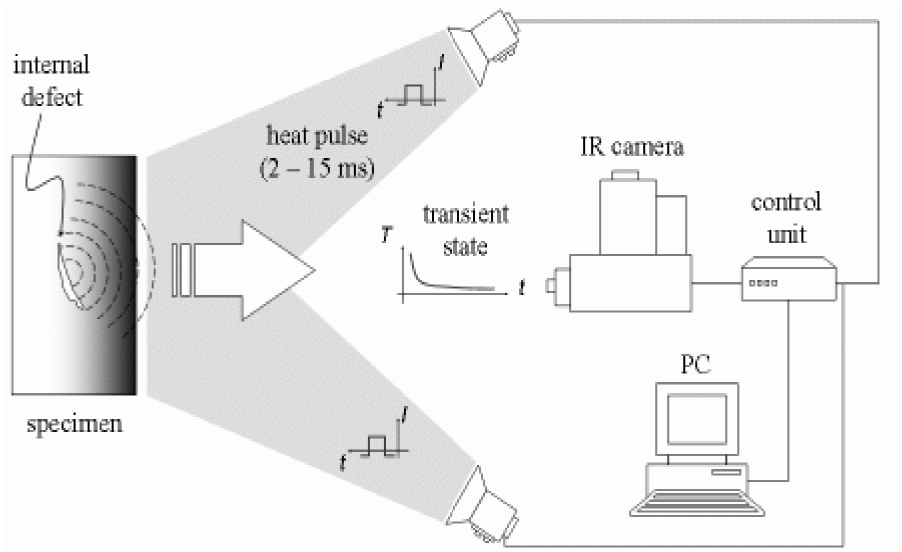

Figure 2.7 *Pulsed thermography [60].*

The resulting thermal gradient at materials surface is monitored using a thermal camera [68]. Vavilov et al. [69] discussed the principles of thermal NDT and illustrated the ability to provide quantitative information about hidden defects or features in a material. There are various properties of the material that need to be taken into consideration such as conductivity, diffusivity emissivity etc. These properties are critical in the inspection with thermography. For example, when a material possesses voids or pores in its structure [70], its thermal conductivity and density decreases; at the same time, its thermal diffusivity is altered and, as a result, the conduction of heat within the material is affected [66]. PT has been implemented by several groups worldwide. The potential of the technique for detecting and imaging subsurface defects has improved [60, 71-77].

Pulse Phase Thermography - PPT is a thermal stimulation technique which offers phase and amplitude images (Fig.2.8). In this mode, the inspected material is heated with a square pulse as in PT. The frequency of the thermal waves generated on the surface of the material is being analyzed via the Fast Fourier Transformation (FFT) during the cooling down process pixel by pixel [60, 61, 66, 72, 73]. The Fourier analysis provides a more accurate data processing protocol, which is highly sensitive to the various types of subsurface flaws. In addition, it offers the possibility of a quantitative evaluation of a wide range of materials. The computed phasegrams are ideal for the visualization of hidden defects. These hidden defects may exhibit low sensitivity to non-uniform stimulation heating, as parasitic reflection of surrounding area and background results in signal distortions [61] which usually inhibit their detection [78, 79].

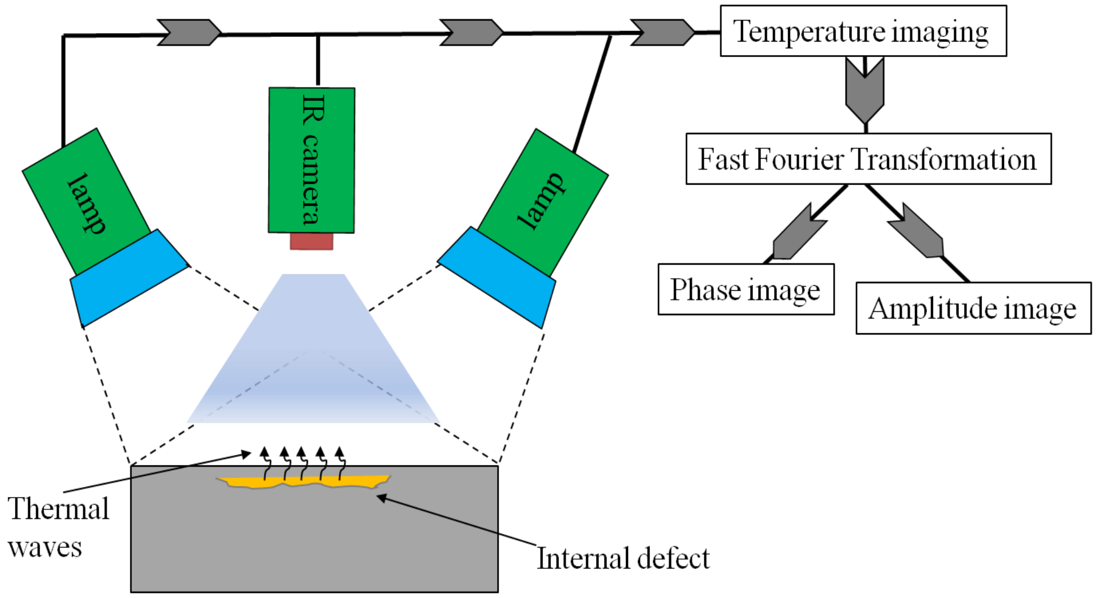

Figure 2.8. *Pulsed phase thermography; optical excitation mode.*

Lock-in thermography - LT (Fig.2.9) is based upon the generation of thermal waves on a material surface under examination when it is subjected to periodical thermal stimulation.

When the periodical stimulation is sinusoidal, the frequency of the obtained thermal waves varies in a sinusoidal way [71]. When a specimen is subjected to sinusoidal thermal wave excitation, attenuated and dispersive waves irradiate from the near surface region (Fig. 2.9).

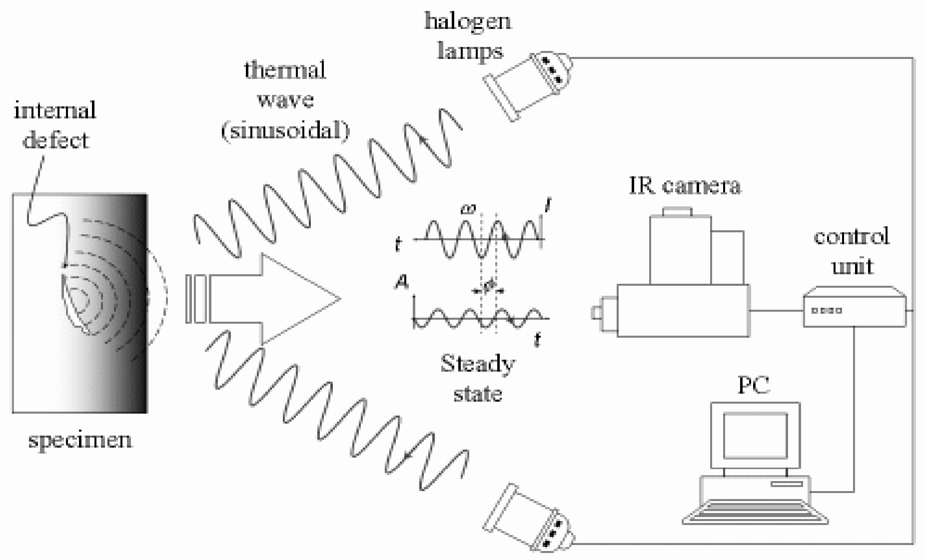

Figure 2.9 *Lock-in thermographic approach [60, 61].*

These waves are described by a position and time temperature modulation. The lock-in principle is linked to the exact time interdependence between the output signal and the reference input signal, i.e. the oscillating - also called modulated - heating. The resulting oscillating temperature field, which results from the oscillating thermal stimulation in the stationary regime or after the transient regime, is remotely recorded via the IR emission from the interrogated material. LT provides both phase and amplitude images. Thermal images (PT) correspond to the mapping of the emitted thermal IR power while phase images are related to the propagation time and amplitude images are related to the thermal diffusivity [61, 71-73, 80]. Typical applications of LT are for the detection of corrosion, vertical cracks and delaminations [61, 73]. For the excitation of thermal waves there are various methods based on acoustic, optical, and thermal effects [81]. In the case of cyclic mechanical loading [82, 83], the oscillating stress may be directly be followed by monitoring the temperature variation [84-86]. In this case, internal stresses are the source of thermoelastic waves. If there is a stress gradient due to the presence of stress raisers e.g. notches, this will be manifested as a local variation both in phase and amplitude images. Fig.2.10 demonstrates the principle of LT when a material is periodically mechanical loaded. A detailed analysis on the thermoelastic effect when a material is periodically mechanical loaded is presented in *Section 4.1*.

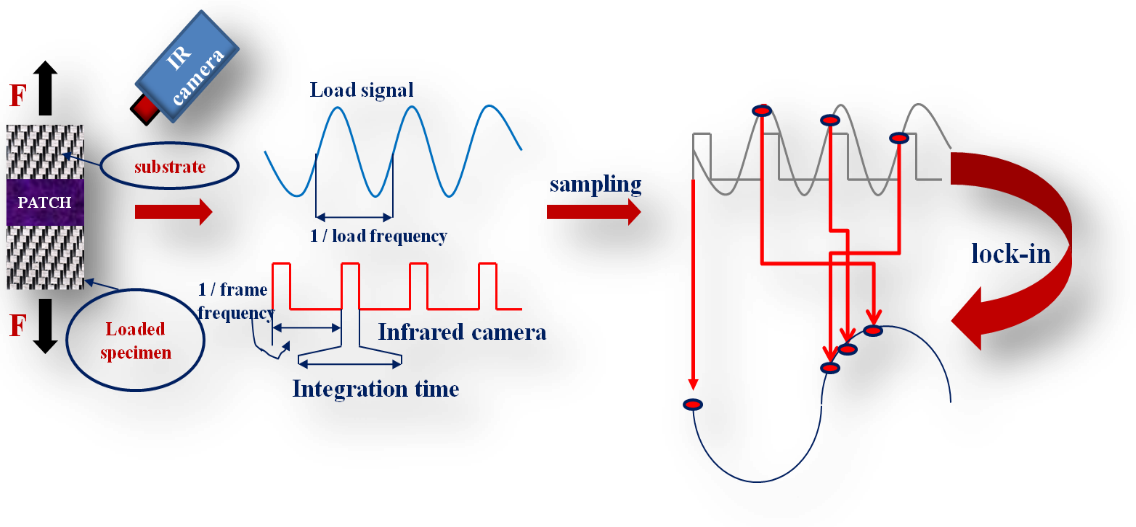

Figure 2.10 *Principle of lock-in thermography.*

2.2.7 Ultrasonics

The Ultrasonic testing (US) is based on the detection and the interpretation of the ultrasonic waves reflected by defects [87]. Typically, the ultrasonic wave frequency ranges from 100 kHz to 40 MHz. Ultrasonics are commonly generated via electrical stimulation of a piezoelectric element. The information obtained from propagation and reflection from the inspected material is used for its structural characterization. The ultrasonic data are collected with the reverse process; the acoustic signal is transformed into electric. The ultrasonic technique is able to detect defects like delaminations and debonds with high resolution. Ultrasonic inspection methods may employ the same transducer for the emission and the reception of the ultrasonic wave, or two different transducers. After the collection of ultrasonic data, they can be displayed in different ways. Common representation modes are: A-scan, B-scan and the C-scan. A-scan is the representation of the recorded ultrasonic energy in time. As it is usually the practice in A-scan inspection, the received signal from a material surface is compared with a reference one in order to characterize the structural state or the severity of damage. The advantage of A-scan is its portability for on-site non-destructive inspection. In the B-scan mode the cross-section of the material is available. A typical B-scan inspection displays the time – of – flight (TOF) of the recorded signal that is plotted against the position of the transducer. The most interesting form of the US technique is the C-scan imaging. Appropriately set time-gates allows for time-window mapping of the received waveform. The amplitude and TOF of the reflected from the material wave is recorded with an automated scanning system. Usually, in the C-scan deployment the amplitude or TOF intensity of the recorded signal is plotted in a 2D image representation in a color scale. In typical US (C-scanning) setups, either the reflected wave or the wave after passing through the object under review is monitored. Two methods may be employed:

1. Through Transmission (Shadow method),
2. Echo method and Double - Through Transmission.

In the first method both a transmitter and a receiver are used. These are either placed opposite to each other or side by side. The transmitter /receiver method is the so-called pulse /echo technique. Its advantage lies in the fact that the relative time difference between the two reflections can be measured. Provided that the location of the reflector and the speed of sound in the medium are known, the calculation of depth is feasible. In this way, it is possible to monitor the size, the form and extend of the imperfection with high resolution. The disadvantage of this method is that it requires relatively smooth and parallel surfaces. A variant of this method is the Double - Through Transmission. In this case, another reflector is used, e.g. a plate of glass /Plexiglas under the specimen, forcing the signal to pass two times through the interrogated material (Fig.2.11). In this thesis, both pulse-echo with longitudinal waves at normal incidence and double - through transmission modes were used in order to detect and locate defects in the composite structure of the manufactured laminates [72]. Typical US testing setups consist of a water bath filled with water. Water is utilized as ultrasonic wave coupling medium, whilst the material is immersed into the water during inspection process. The water bath employs an automated moving system. The transducer(s) is (are) appropriately connected with a PC for data acquisition. Fig.2.11 shows a typical US experimental setup:

Figure 2.11 *C-scan experimental setup.*

The following figure (Fig.2.12) depicts multiple wave reflections from a material. The time difference between two reflections is the required time for the ultrasonic wave to travel from the transducer to the back surface of the inspected material and vice versa back to the transducer. The amplitude of the wave reduces exponentially with time.

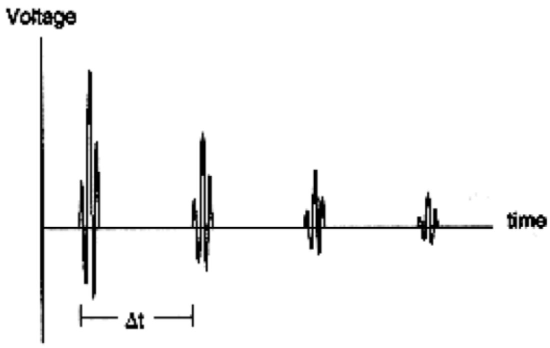

Figure 2.12 *Reflected signal from a material [72].*

The wave velocity can be determined by the time difference between two reflections and the thickness of the investigated material.

$$c = \frac{2d}{\Delta t} \qquad (2.5)$$

where *c* the wave velocity, *d* is the thickness of the material and *Δt* the time – difference [87-91]. As outlined from the aforementioned discussion, US technique is applied in off-line conditions. The US approach is a well established methodology in the aerospace industry.

2.2.8 Acoustic Emission

The Acoustic emission (AE) technique is as a real time method used to monitor damage in materials and structures in operational conditions (on-line). AE is used to define the elastic waves that are emitted from a material during crack propagation incidents. In general, when a crack occurs, energy is released causing the propagation of US waves in the material. These can be detected using sensitive piezoelectric sensors. With respect to composite laminates, fibre breakage, matrix cracking, delaminations and debonding are common acoustic emission sources. Piezoelectric transducers placed on the surface of the material capture the elastic waves (AE hits) released during crack propagation incidents [92, 93], and transform it into an electric waveform which is digitized and stored for analysis. Combined information of the different hits includes the location of the cracking source (by comparing the acquisition time from different positions), estimations on the crack density, as well as the severity of the materials condition [94, 95]. Additionally, AE indices may be connected to the dominant cracking mode. For most materials and loading scenarios, tensile cracks are developed at the early stages of loading, while shear cracks follow. This has been shown for reinforced concrete members that undergo bending and cross-ply composites. In concrete members, the initial cracking comes from transversely to load cracks due to their brittle nature, whereas in composites transverse cracking is followed by delaminations [96, 97]. Therefore, the characterization of the cracking mode may lead to early assessment of the cracking condition offering an early warning against final failure. In the case of a crack propagation incident, acoustic emission waves are generated and acquired by the employed transducers on the material. In order to determine the exact point of the crack or else to locate the crack point, the time-difference in acquisition of the signals from the two sensors can be measured. In this case, the acoustic incident is an “event” and represents the source of the acoustic stress wave [98]. Hence, the number of events coincides with the number of cracks and is a representation of the topography of damage in the material. The typical characteristics of the acoustic waveform such as the amplitude, rise time, average frequency etc., are termed as descriptors. It has been shown that a crack propagation incident exhibits different acoustic emission signature depending on the mode of the crack. The tensile mode of crack which includes opening movement of the crack sides results in AE waveforms with short rise time and high frequency. On the contrary, shear type of cracks usually result in longer waveforms, with lower frequency and longer rise time [99]. This is mainly due to the larger part of energy transmitted in the form of shear waves, which have lower velocity than longitudinal waves. Thus, the maximum peak of the waveform after the onset of the recording is delayed. This has been demonstrated in a variety materials, like concrete [97, 100] and fibre composites [96, 101]. The connection between AE signature and mechanical loading is well described by the Kaiser and Felicity effect [102]. According to the Kaiser effect, when a material is loaded to a value and then unloaded, no acoustic emission activity is recorded until the previous maximum load value is reached. However, when the applied load is high enough, significant emissions may be recorded even though the previous maximum load is not reached. This phenomenon is known as the Felicity Effect. This effect can be quantified using the Felicity Ratio, which is the load where considerable AE resumes, divided by the maximum applied load (F/D). The Felicity ratio is reported to directly correspond to structural deterioration [103]. Fig.2.13 shows a typical AE waveform after a crack propagation event. One of the crucial parameters which are influenced by the mode of crack according to the above discussion is the average frequency, AF, which is the ratio of threshold crossings (counts) over the duration.

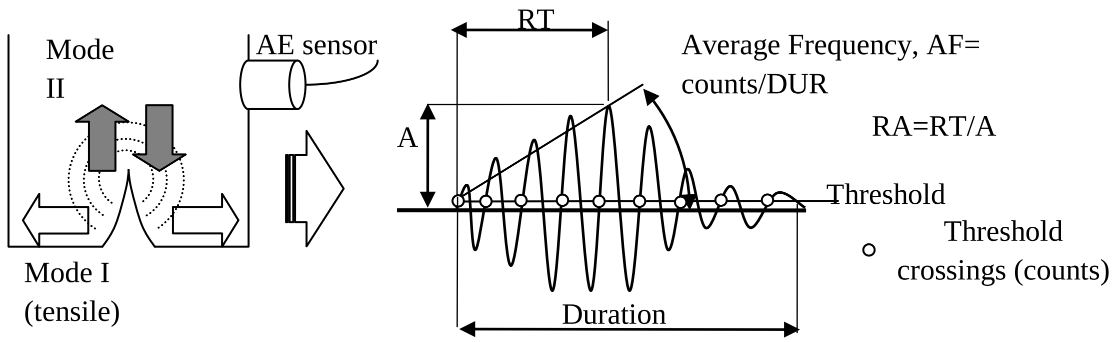

Figure 2.13 *Typical fracture modes and AE waveform [104].*

Another crucial parameter is the RA value which is the rise time (RT, delay between the onset and the maximum amplitude) over the amplitude, A. AE energy [105] is the area under the rectified signal envelope. Results of AE measurements show that the emissions during the early tensile damage stage exhibit higher AF and lower RA, AF decreases and RA increases while as the material is led to final failure. In the case of a bonded repaired patch [104], the failure process of the plates with the composite patches include different modes such as matrix cracking as well as delamination between the plate and the patch, and AE may be employed with the aim of characterizing the different processes. To summarize, compared to other non-destructive assessment methods, AE is a fast and cost efficient NDE method. AE is capable of providing real time monitoring of damage without using external stimulation sources as long as the structural deterioration process provide signal input to the AE sensors. Although the AE sensors are quite sensitive to noise, crack development and propagation incidents whose energy is relatively low, usually go “undetected”. One of the main shortcomings of the AE methodology is the difficulty of quantifying the acoustic activity in terms of s AE cannot provide quantitative inspection as Ultrasonics or thermography [106].

2.2.9 Structural health monitoring: electrical property based methodologies

Structural Health Monitoring aims at continuous sensing of the structural state of materials. The suitable sensing technique depends on the interrogated material or structure. The efficiency of the sensing technique is always a function of the region under inspection, the number of sensors or sensing elements, the possible necessary electrical power supply and the system complexity.

The sensing techniques which are employed for structural health monitoring are capable of observing i) the induced mechanical stresses using electrical resistance strain gauges [38, 107, 108], piezoelectric films [38, 109] and optical fibres which are appropriately embedded /fitted in the structure or are simply attached on the surface of the inspected structure, ii) the residual mechanical strain using electrical resistance - based strain gauges [107, 110] and optical fibres iii) electromechanical impedance using piezoelectric sensors [111, 112] and iv) internal structural degradation using Micro Electrical Mechanical systems (MEMs) [110]. Fibre Bragg Grating sensors or FBGs are the most famous sensors in the category of Optical Fibre Sensors. FBGs are used usually used embedded in a structure in order to provide SHM through load and strain entities. Curing monitoring [113, 114], disbond [115], cracks [116, 117] and impact damage [118] have been reported to be successfully examined via the use of FBGs. Typical piezoelectric sensors are made of Lead Zirconate Titanate (PZT). These sensors transform the mechanical signal into electric and vice versa, enabling the identification and quantification of internal damage. Apart from pure PZT, piezoelectric sensors can be made by powder dispersed into polymer matrices, forming a functional composite [119]. Strain gauges, MEMs and piezoelectric films are categorized in the list of the “electrical sensors”. The term “electrical sensors” refers to the sensors which relate to the physical changes of a material by measuring its electrical properties i.e. electrical resistance, electrical potential, electrical capacitance or induced current loss. The following graph (Fig.2.14) depicts the most popular self-sensing techniques and the corresponding sensors as well as power suppliers.

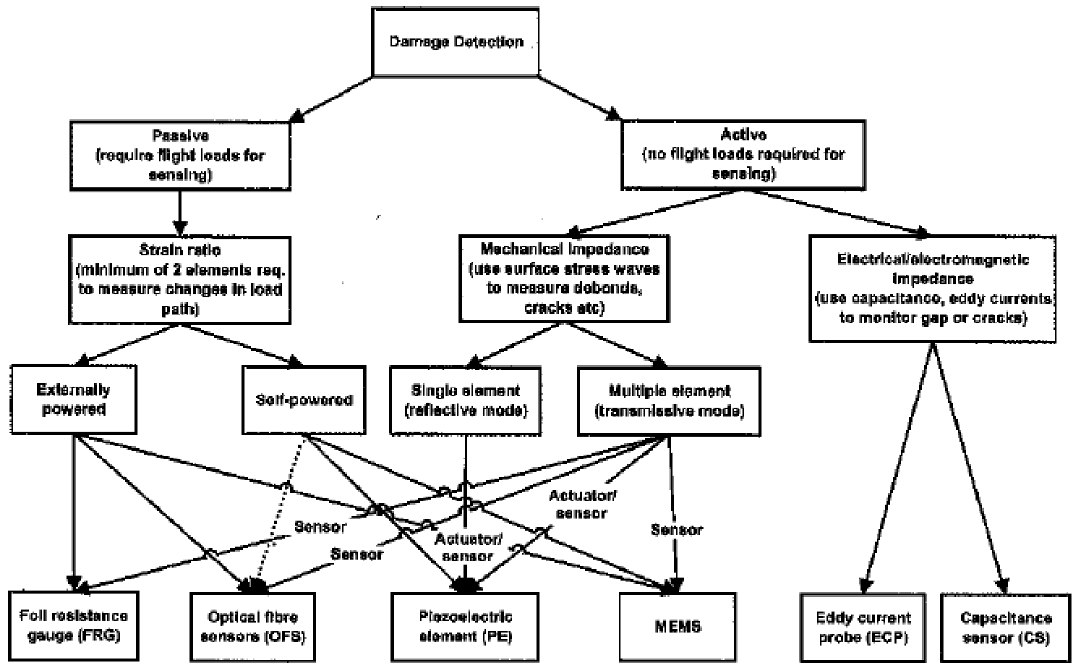

			Transducer					
Source	Device	Storage	FRG	OFS	PE	ECP	CS	MEMS
aircraft power			Y	Y	Y	Y	Y	Y
manufacture time		primary cell	Y	Y	Y	Y	Y	Y
strain energy	PZT	capacitor/secondary cell	N	N	Y	Y	Y	Y
interrogator	RF	capacitor/secondary cell	N	(Y)	Y	Y	Y	Y
solar	PV	capacitor/secondary cell	Y	(Y)	Y	Y	Y	Y

Figure 2.14 *Flow diagram showing damage detection techniques with possible corresponding transducers and power sources [120].*

A new attractive methodology that could be added in the category of electrical sensors exploits the inherent physical characteristics of the investigated material in order to obtain information about its structural integrity.

The electrical properties of materials are closely related to damage accumulation. Therefore, monitoring the electrical properties of the material itself provides information about its structural state. Moreover, a map of the electrical properties of a shell or laminate would potentially provide the topology of internal damage. This SHM concept is usually referred to as "self-sensing" since the employed sensor is the material itself. This is by definition the most attractive choice considering SHM, as was initially presented by Kemp et al. [121]. In addition, the ideal sensor should be small in size and lightweight along with increased sensitivity [122]. Electrical self-sensing methods can be applied either off-line (activated on demand) or on-line (real time monitoring-SHM). In the off-line protocol, the electrical properties of the material are appropriately measured following a prescribed algorithm. The acquired electrical data are extracted from the material surface or via its cross section allowing for the mapping /tomography of its internal structural state. For monitoring damage during service loads (on-line protocol – real time monitoring - SHM), appropriate experimental setups provide direct electrical recording in real time [123-125]. As is obvious, the efficiency of the electrical SHM concept is always dependent on the electrical properties of the material. In that respect, Carbon Fibre Reinforced Polymers (CFRPs) are ideal material for such a sensing technique. Various hybrid CFRP and hybrid GFRP composite laminates have been interrogated employing this self-sensing concept both in the on-line and off-line protocol. Nano-enhanced carbon /epoxy composites have been compared in terms of damage sensing with reference (plain matrix) carbon /epoxy laminates. Additionally glass /epoxy composite laminates have rendered from insulators into conductive materials via the addition of secondary phases such as Carbon Nanotubes (in the form of fibres or powder) [123, 126], iron [127], Polyaniline [128] and Carbon Black [129].

Carbon nanotubes are found as multiple (MWCNTs), double (DWCNTs) or single (SWCNTs) graphite layers or “walls” appropriately rolled forming a tube. An enormous list of recent works document the distinct electro-mechanical properties of Carbon Nanotubes (CNTs) [130]. Within the scope of the present work, is the incorporation of CNTs in the structure of composites to produce advanced hybrid composites (nanoenhanced composites /nanocomposites).

In the current thesis, CNTs as a nanophase in hierarchical advanced composite materials are primarily employed to enhance the conductive properties of advanced composites in order to develop self-sensing techniques. As is well known CNTs possess impressive properties such as increased mechanical strength and modulus of elasticity, high thermal and chemical stability, outstanding electrical and thermal conductivity, all these escorted by low weight and density. The exploitation of their unique properties has been the aim of extensive research effort within the scope of nanoenhancing the electro–mechanical properties of aerospace composites. However, the production of nanoenhanced advanced composites with properties close to those theoretically predicted is as yet far from achieved as many issues have arisen, concerning, mixing of CNTs with the polymer matrix, type of polymer matrix, proper amount of CNTs etc [131].

In the case of CFRPs, electrical conductivity of the primary reinforcement e.g. carbon fibres is already electrically conductive, and as a result the in situ monitoring of the change of electrical properties is feasible (on-line). As should be noted, conduction is by definition efficient along the reinforcing fibres, but can be significantly less in other directions, rendering the composite electrically anisotropic. In the absence of secondary reinforcement, the conductive grid in other directions than the reinforcing ones e.g. in the through thickness direction is formed primarily by the adjacency of carbon fibres. Therefore, although the epoxy matrix is an insulator, it does not inhibit conduction in all directions of the laminate [132, 133]. As is reported by Louis et al [134], the electrical conductivity of a plain CFRP is relevant to fibre - fibre random contacts which are a function of the fibre volume fraction of the laminate. Carbon fibres themselves has been shown to possess piezoresistive properties as has been shown in the pioneering work performed by Owston in 1970 [135], who directly related resistance changes to strain induced by mechanical loading. In a later study, Schulte and Baron [136], examined the potential of employing conductive reinforcement such as carbon fibres as sensors together with their typical mechanical reinforcing role in the composite structure. Irving and Thiagarajan [137] correlated the electrical resistance changes to matrix and fibre damage caused by the application of mechanical load. The electrical response of composites to strain and damage was the object of several other studies that followed [133, 138-142]. Luo and Chung examined the efficiency of CFRPs to work as capacitors [143], and Wang and Chung [144] carbon /epoxy composites as sensors for light and temperature. In another work, the advantages of the electrical property based technique over other embedded sensors are also reported [142]. In the case of unidirectional CFRPs, the through - thickness conductivity is more than one order of magnitude, less than in the reinforcement direction [145]. In the case of delamination, the electrical resistance increases due to the loss of interlaminar electrical continuity [146]. In the case of unidirectional reinforcement, the longitudinal value of electrical resistance is increased with reinforcement failure [147]. Besides electrical resistance changes, electrical potential values have been investigated with a view to monitoring damage initiation and evolution. Todoroki et al. [148], and Angelidis et al. [149] examined the electrical potential changes for self-sensing in advanced composites [104]. The electrical potential technique is reported to supersede the electrical resistance based technique. In the electrical potential configuration, a fixed – amplitude electrical current is usually injected and the potential values or potential difference along the material surface is measured, whereas, in the electrical resistance configuration, electrical resistance changes are monitored via the alteration of electrical current under fixed potential values. In the work by Kupke et al. [150], the electrical potential technique is examined this time by means of alternating (AC) and direct current (DC). It was documented that the capacitance of the composite decreases with load, and thus damage accumulation monitoring is feasible.

Apart from the on-line mode of damage sensing (continuous monitoring), considerable work has been dedicated in the off-line (detection on demand) assessment of the electrical properties of carbon /epoxy composites. Electrical properties are measured along the surface of materials and structures in order to provide a map of its internal structural state. Resistance tomography /mapping is a widely accepted technique and fundamental to the assessment of geophysical underground state as well as in identifying underground water or landslides [151-155]. In the case of advanced composites materials, the same idea is applied, albeit in smaller scale. Similarly to the on-line case, electrical resistance or electrical potential differences are measured. Electrical current is used in order to electrically stimulate the investigated material. In the presence of internal damage, the electrical grid formed by the reinforcement is both deformed and disrupted affecting the electrical current path along the bulk material. Resistance or potential value mapping has proved very efficient in identifying intrinsic damage [123, 125, 139, 149, 150, 156-159].

Apart from the structural integrity monitoring, the electrical properties of the conductive reinforcement have been exploited for the curing of carbon /epoxy materials [160]. Joule /resistive heating has been adopted for curing composite panels [161, 162] and is typical for removing the ice from the skin of aircrafts [163]. Resistive heating has also been used for heating building, driveways, for plastic welding and for the demolition of concrete structures [164-171]. Additionally to these studies, resistive heating of self-healing composites has been successfully applied in order to activate the “healing” process of the polymer matrix [172-175]. As stated by Fosbury et al. [176], up to 100% energy conversion from electrical to thermal may be achieved. The basic principle of resistive heating or “Joule heating” is that electrical power is converted as heat when current is injected through an electrically conductive material i.e. the carbon /epoxy laminate. Grammatikos et el. reported the use of resistive heating for the identification of impact damage in carbon /epoxy composites. Direct electrical current was used to thermally stimulate carbon /epoxy composite laminates. The thermal gradient on the surface of the material was monitored with a thermal sensitive camera [177]. Suzuki et al. [178] examined through point-by-point resistive heating, the thermal behaviour of CFRPs with a view to identifying indentation damage .

More recently, breakthrough sensing technologies were introduced exploiting Carbon Nanotube (CNT) electrical [179] and mechanical [180, 181] properties. As aforementioned, CNTs have been very popular throughout the last years in the aircraft industry for their distinct properties [131]. CNTs are electrically conductive [182], and may be employed in order to render insulating matrices electrically conductive. When small volume fractions of carbon nanotubes (0.1-1 %w/w) are added into a polymer matrix, the electrical properties change significantly. Thostenson et al [183, 184] suggested the mechanical enhancement of composites provided by carbon nanotubes. When CNTs are dispersed in a polymer matrix, they form a percolating network within the polymer. It is noteworthy that the CNT loading needed to render the nano - polymer conductive is an order of magnitude less than in the case of carbon-black [185]. This is attributed to the deformation-sensitive percolating network formed at low concentrations [186, 187]. Current research has proved that the conductivity of hybrid composite systems relates to their real time strain state as well as their damage state [124, 188]. As Kostopoulos et al. [180] and recently Gkikas et al. reported [189], CFRPs modified with carbon nanotubes doped matrix material exhibit a spectacular improvement in fracture toughness, significantly higher damage tolerance and increased fatigue life expectancy. Improved compression after impact behavior was observed when 0.5% MWCNT was added [181, 190].

Apart from CFRPs, Glass fibre reinforced polymers are widely employed in the aerospace industry as they possess improved specific properties combined with significantly lower cost. GFRPs are non-conductive composite laminates. Dispersed carbon nanotubes and embedded carbon nanotube fibres (CNFs) are used to render GFRPs electrically conductive. Hence, multifunctional GFRPs may meet the requirements for damage sensing. As demonstrated by Fiedler et al. [145] and Thostenson et al. [172, 191] the addition of dispersed carbon nanotubes in the epoxy matrix allows for damage sensing and damage accumulation monitoring in GFRPs. In [192] a glass /modified with CNTs vinylester and in [193], damage accumulation in GFRPs were studied by means of electrical sensing during mechanical loading. More recently, Liu et al. studied the interlaminar shear strength of a CNT-modified GFRP by means of electrical resistance measurements [194]. Apart from the scenario of dispersed CNTs in composite matrices, CNT fibres have been embedded to sense damage in glass /epoxy composite laminates. Carbon nanotubes in PVA (Poly -Vinyl - Alcohol) matrix in the form of fibres with very low diameter (in the order of 10 to 20μm) have been embedded in non-conductive glass /epoxy composite laminates. The sensing properties of CNT fibres have been exploited and correlated with the failure of the composite. Most importantly, the low diameter of the CNT fibres does not impose any degradation to the initial mechanical properties of the composites after embedding. PVA-CNT fibres have been manufactured by Vigolo et. al [195, 196], where nanotubes are appropriately injected in a polymer solution and via coagulation spinning process, CNT fibres were available. The pioneering idea of embedding a conductive fibre for damage sensing in glass /epoxies was presented in early 2001 by Muto et al. [197], where a carbon fibre in a glass /epoxy composite was embedded. However, the observed results were not as promising as expected. Typically, damage sensing in such configurations is achieved via the electrical resistance monitoring of the conductive fibre which acts as a strain sensor. The embedded CNT-fibres follow closely the deformation of the composite induced by mechanical loading. Induced damage as manifested by the stiffness loss of the material is correlated with the recorded electrical resistance change.

Unlike embedded carbon fibres in GFRPs [197], CNT-fibres were found to be more effective in monitoring load induced damage [123].

Repair technologies offer a new exciting field for the application of the aforementioned novel material concepts for sensing the repair integrity, as they are non intrusive and can mirror the damage state of the patch/ substrate system through simple electrical resistance or electrical potential monitoring. This may be performed both in real time and at scheduled intervals. Bonded composite repairs pose a great challenge in the electrical property based techniques to address induced damage. A first approach towards reaching the goal of the off-line approach was presented by Ampatzoglou et al. [198]. Composite laminates were repaired with the bonded patch repair methodology. Various PTFE artificial damages were interrogated using an electrical potential and resistance mapping system. The damage sensing philosophy was evaluated with finite elements. Aiming at the on-line repair integrity monitoring of bonded repairs, Vavouliotis et al. [199] and Grammatikos et el. [104] used the electrical potential change monitoring system in composite patch /composite substrate systems. Circular notches in the middle of the laminates were repaired with tapered repaired patches and the repaired structure was subjected to fatigue loading. Vavouliotis et al. [199] assessed the electrical behavior results with concurrent measurements of AE signals. Grammatikos et al. [104] exploited, besides acoustic signals, the irradiated thermal gradient caused by patch debonding.

The aforementioned concepts which combine intrinsic material properties with advanced hybrid composite systems exhibit a large potential for their application in aircraft technologies. The in-service monitoring of the ’structural health’ of a repaired component is of primary importance, as it reduces overall functional costs and guarantees safety. Improved structural integrity capabilities together with multifunctionality have always been the key issues for advanced aerospace structures. More importantly, both Airbus and Boeing aircraft industries have performed a significant leap by advancing from metal to advanced composites as structural material, manufacturing their first airborne structures (Airbus A350 XWB and Boeing 787 Dreamliner) with more than 50% composite materials.

In Table 2.1 the NDE techniques usually employed in the aerospace industry along with a summary of their ability to identify common types of damages in composites are shown. Tables 2.2 to 2.7 summarize distinct advantages and disadvantages of common NDE techniques; Shearography /Holography, Ultrasonics, Thermography, Acoustic Emission and Self-sensing electrical methodologies are highlighted. Finally, Table 2.8 juxtaposes self-sensing NDE techniques with thermography, acoustic emission and ultrasonics.

Table 2.1 *Common type of defects, damage along with Non destructive assessment techniques.*

Type of damage	Non destructive techniques							
	Ultrasonics	Radiography	Eddy current	Acoustic emission	IrT	Holography	Electrical Resistance /Potential Change Monitoring	Electrical Potential Mapping
Voids	√	√	-	-	partial	partial	√	√
Debonding	√	partial	-	partial	√	√	√	√
Delamination	√	partial	-	partial	√	√	√	√
Impact	√	√	√	-	partial	partial	√	√
Resin-rich areas	√	partial	-	-	-	-	-	-
Fractured fibres	√	partial	√	√	-	-	√	-
Fibre misalignment	√	-	√	-	√	-	-	-
Matrix cracking	√	partial		-	√	√	√	√
Bad curing	√	-	-	-	-	-	-	-
Moisture	√	√	-	-	√	-	-	-

Table 2.2 *Shearography /Holography.*

Shearography / holography	
Detects: internal defects, delaminations, impact damage, voids, cracks, defects due to corrosion, residual stresses	
Full field & in-service	
Advantages	**Disadvantages**
Optical	*Hard to interpret – skilled staff requirement*
Non-contact	*Safety rules necessary (laser)*
Mechanical strain evaluation through displacement measurements	*Material need to be stressed in order to identify the presence of cracks*
Physical properties measurements	*Heavy equipment*
Fast and portable system	*Quantitative structural assessment*
2D and 3D representation of damage	*Prone to environmental conditions*

Table 2.3 *Thermography.*

Thermography	
Detects: internal defects, delaminations, impact damage, voids, cracks, defects due to corrosion, residual stresses	
Full field & in-service and on-line	
Advantages	**Disadvantages**
Fast and portable system	*Surface emissivity – black mat paint is necessary*
Real time assessment	*Problems with polymers with low thermal conductivity*
Easy interpretation	*Difficult the quantitative evaluation*
Optical	
Non-contact	

Table 2.4 *Ultrasonics.*

Ultrasonics	
Detects: Internal discontinuities, delaminations, impact damage, cracks, voids, porosity, thickness measurement, residual stresses measurement	
Scanning method	
Advantages	**Disadvantages**
2D image representation	*Difficult to interpret when A-scan format is used*
High sensitivity and resolution	*Skilled staff*
High reliability and easy to interpret	*Limitations in complex material geometries*
Localization of damage with enhanced resolution	*Limitations at low depths due to attenuation*
Useful in manufacturing process	*Very slow*
Portable	

Table 2.5 *Eddy current.*

Eddy current	
Detects: Cracks, delaminations, impact damage, voids	
Scanning method	
Advantages	**Disadvantages**
High resolution	*The material has to be conductive*
Non-contact	*Sometimes hard to interpret*
Dimension of damage inspection	*Slow method*

Table 2.6 *Acoustic emission.*

Acoustic emission	
Detects: Internal defects, delaminations, discontinuities, cracks. Resin curing monitoring	
Scanning method, on-line	
Advantages	**Disadvantages**
High sensitivity	*Mechanical loading necessary*
Portable	*No image representation*
Directly relevant to damage	*Cannot define the type of defect*
Straightforward inspection	

Table 2.7 *Self-sensing electrical methodologies.*

Self-sensing electrical methodologies	
Detects: Internal defects, delaminations, impact damage, cracks	
Off-line & on-line	
Advantages	**Disadvantages**
Portable	*Limited in conductive materials*
Very cheap	*Hard to adapt the measurement electrodes*
High sensitivity	*Low resolution and sensitivity in some cases*
Self-sensing	*Very difficult to interpret the exact type of damage*
Non-aggravation of the structure with external sensors and devices	*Difficulties in image construction*
Fast inspection	*Non-reliable as is still being under investigation*
2D Image representation	

Table 2.8 *NDE particular characteristics.*

Type of damage	Non destructive techniques				
	Ultrasonics	Electrical Potential Mapping /Tomography	Electrical Resistance Change Monitoring	Acoustic emission	IrT
Feasibility	easy	difficult	difficult	moderate	easy
Portability	x	√	√	√	*Depends on which methodology
System level (On line monitoring)	√	x	√	√	√
Non-contact	√	x	x	x	√
Off-line	√	√			√
Integrated sensing	x	√	√	x	x

CHAPTER 3

Off-line damage identification in composite materials using innovative NDE

3.1 Identification of artificially induced damage using optical thermographic methodologies

3.1.1 Introduction

Over the last three decades, composite materials have been widely used in aircraft applications. Fibre reinforced polymers (FRP's) possess high strength and Young's modulus combined with low density, and, therefore they are the most attractive structural materials for the aircraft industry, along with metal matrix composites (Fibre Reinforced Metal Laminates) and advanced aluminum alloys. In particular, FRPs are ideal as repair materials due to their inherent modularity. Alternative materials, such as FRPs, are increasingly being used in aircraft repair operations, in the place of metal patches. When pertaining to bonded composite repairs, outstanding fatigue and corrosion resistance, as well as the stress shielding of the damaged area, are some of the distinct repair features. Moreover, their potent specific properties eliminate extra weight aggravation of the airborne structure [23]. Carbon Fibre Reinforced Polymers are currently the most attractive high performance structural as well as repair materials for aerospace applications [200]. The development of new materials demands an effective way of non-destructive assessment in order to pin-point internal defects and critical and subcritical damage. The latter are in most cases invisible to the naked eye. Various Non-Destructive Evaluation techniques (NDE) have been documented to detect damage in composite laminates. Radiographic [201], ultrasonic [202], and lamb wave [203, 204] methods have been effectively used to localize damage with high resolution and accuracy. Electromagnetic properties of composites pose an additional challenge in NDE for the assessment with eddy current based methods [205]. Together with the aforementioned methodologies, Infrared thermography (IrT) is particularly appealing for its ability for relatively simple and fast quantitative full-field damage detection. IrT is a non-contact NDE technique, which exploits the irradiated thermal gradient of the examined surface, in order to analyze its physical and intrinsic characteristics [62, 206]. The applicability of IrT has been utilized to detect damage, such as delaminations, voids, debonding etc., in a wide range of materials i.e. carbon /epoxy and glass /epoxy laminates as well as sandwich structures [207]. Depending on the particular application, appropriate modes of active [61] thermography have been proposed such as Vibrothermography – VT, Pulsed Thermography – PT [208], Lock-in thermography – LT, Pulsed Phase Thermography – PPT [209], Pulsed Eddy Current Thermography [210, 211] – PECT and Ultrasonic thermography – UT [61, 212].

PT is a thermal stimulation technique where the sample surface is instantaneously heated via a thermal pulse. In optical PT, either incandescent or flash lamps may be used. In the presence of subsurface flaws, heat diffusion is delayed. This resulting thermal transient on the surface is captured using a thermal camera. PT provides thermal images [60, 62, 71, 72, 77, 208] [213]. In PPT mode, the material is heated identically to PT. In this concept, a Fast Fourier Transformation (FFT) of the original recorded signal is applied so that the thermal data in the frequency domain can be analyzed. FFT analysis provides a more accurate data processing protocol, which is highly sensitive to the various types of subsurface flaws. In addition, it offers the possibility of a quantitative investigation in a wide range of materials. PPT offers phase and amplitude images [61]. LT is based on thermal waves generated onto a specimen surface when submitting it to a periodic thermal stimulation [71]. LT allows for the observation of the amplitude and phase shifts of the thermal waves from the surface of a specimen. The thermographic images obtained from such a setup are different from the thermograms acquired via PT. Phase images are time-dependent while amplitude images refer to the thermal diffusivity. Nevertheless, PT is considered to be more powerful compared to LT in identifying defects close to the surface [214]. This is basically attributed to the blind frequency effect which is encountered in phase images. These excitation frequency band do not induce phase shifts in the presence of some flaws and, thus, these defects go undetected [215, 216]. A proposition to overcome the blind frequency effect was reported by [217] where a frequency modulated thermographic mode is presented. In this mode, the excitation spectrum is square and thus the energy is irradiated at all excitation frequencies. The observed magnitude and phase - related images possess higher resolution compared to the observed ones through PPT [218]. The strong point of LT is the synchronization of the thermal sensitive camera with the excitation source which allows for lock-in images to be extracted at modulated frequencies or at the same frequency with the excitation source [61, 71, 219].

Besides thermography, ultrasonic imaging is a reliable NDE technique and capable of interrogating induced defects in composite materials. It is the most broadly employed inspection technique. As ultrasonics is a good way to provide quality assessment with high accuracy, it can be easily employed to benchmark thermographic data. Ultrasonic testing is based on the detection and interpretation of ultrasonic waves reflected by internal defects as well as of surface anomalies [87]. The ultrasonic imaging technique is able to detect defects like delaminations and disbonds with high resolution. The multiplicity of applications gave rise to the development of more than one ultrasonic inspection methods, such as “Through Transmission”, “Echo method” and “Double-Through Transmission” (employing a reflective plate) [87, 220, 221]. Ultrasonic imaging (C-scan) uses a water bath with the material immersed into the water, which works as wave couplant [55]. This experimental setup can be automated providing fast and effective inspection. Nevertheless, the methodology is weak for complex geometries. For that reason, multi-axial ultrasonic systems have been developed

[222], which continuously spray water in between the material /transducer area so that the inspection is feasible. Moreover, for structures where water injection is prohibited, as in the case of honeycomb core within a laminated structure where water infiltrates in the core area, air coupled ultrasonic transducers are developed [223]. It is reported that the usage of water as propagation medium allows for 75% energy transfer. In the case of air as coupling medium, the energy transfer is very low and approximately 0.03%. [224].

Within the aim of the current section, different modes of optical IR thermography were investigated in the framework of the off-line identification of damage. In particular, pulsed, pulsed phase and lock-in thermography were employed. The studied materials were i) CFRP laminates which included different artificial simulated modes of damage using PTFE-Teflon tapes, ii) repaired Aluminum (Al) surfaces which included simulated artificial defects using PTFE-Teflon in the patch /substrate interface, iii) repaired composite and Al plates, which included PTFE artificial defects in various dimensions and locations in the patched structure. IrT proved capable of identifying low dimension artificial defects with high accuracy. The results of IrT were benchmarked via ultrasonic imaging (C-scan).

3.1.2 Materials

Distinct material configurations were manufactured and examined in order to evaluate the performance of infrared thermography in identifying material damage. Three different types of laminates were interrogated. The examination protocol involved three cases. Hereunder, the employed materials are presented in detail.

Case 1: Two different CFRP laminates, which included artificial defects in a variety of dimensions in the bulk material, were manufactured in the laboratory (Fig.3.1.2 and 3.1.4). The unidirectional carbon fabric (provide by R&G) was used as a reinforcement. In Table 3.1.1, the carbon fabric properties are listed.

Table 3.1.1 *Case 1 carbon fabric properties.*

Unidirectional carbon fabric, plain, width 100 cm (R&G)	
Weight	140 gr/m^2
Resin Consumption	154 g/m^2
Laminate ply thickness	0.215 mm
Laminate ply weight	294 g/m^2

The Araldite LY 5052 /Aradur 5052, cold curing epoxy system provided by Huntsman International LLC was used as a matrix. The manufacturer recommended curing cycle for curing and post-curing of the matrix was employed i.e. curing for 24 h at 23 ^{o}C and post curing for 4 h at 100 ^{o}C. The embedded artificial defects were PTFE tapes of 75 μm thickness in various dimensions and shapes. The thickness of the artificially induced defects was varied by introducing a number of overlapping Teflon tapes.

1. The carbon fabric orientation of the 1st CFRP laminate was $[0, 90]_3$ (Figs.3.1.1-3.1.2). The laminate was manufactured by hand lay-up and its dimension was 250x250 mm^2. PTFE defects with varying thickness ranging from 75 μm up 525 μm were placed between the 3rd and 4th plies of the composite laminate as shown in Fig.3.1.2. The defects had a standard width of 12 mm (Fig.3.1.2). The laminates were cured in a vacuum bag under 700 mbar vacuum pressure.

2. The 2nd plate was a unidirectional $[0]_6$ CFRP laminate (Fig.3.1.4). This laminate was fabricated using the infusion method in dimensions 200x220 mm^2. The artificial defects were inserted (i) between the 3rd and 4th and (ii) between the 4th and 5th plies with varying thickness ranging from 75 μm to 300 μm and varying width, as can be seen in Fig.3.1.3. Again, the laminates were cured in a vacuum bag under 700 mbar vacuum pressure.

In Fig.3.1.1, the manufacturing sequence of the 1st laminate is presented. After the Teflon tapes placement at the prescribed locations, the remaining layers of the laminate were laid up on top and subsequently vacuum pressing was applied.

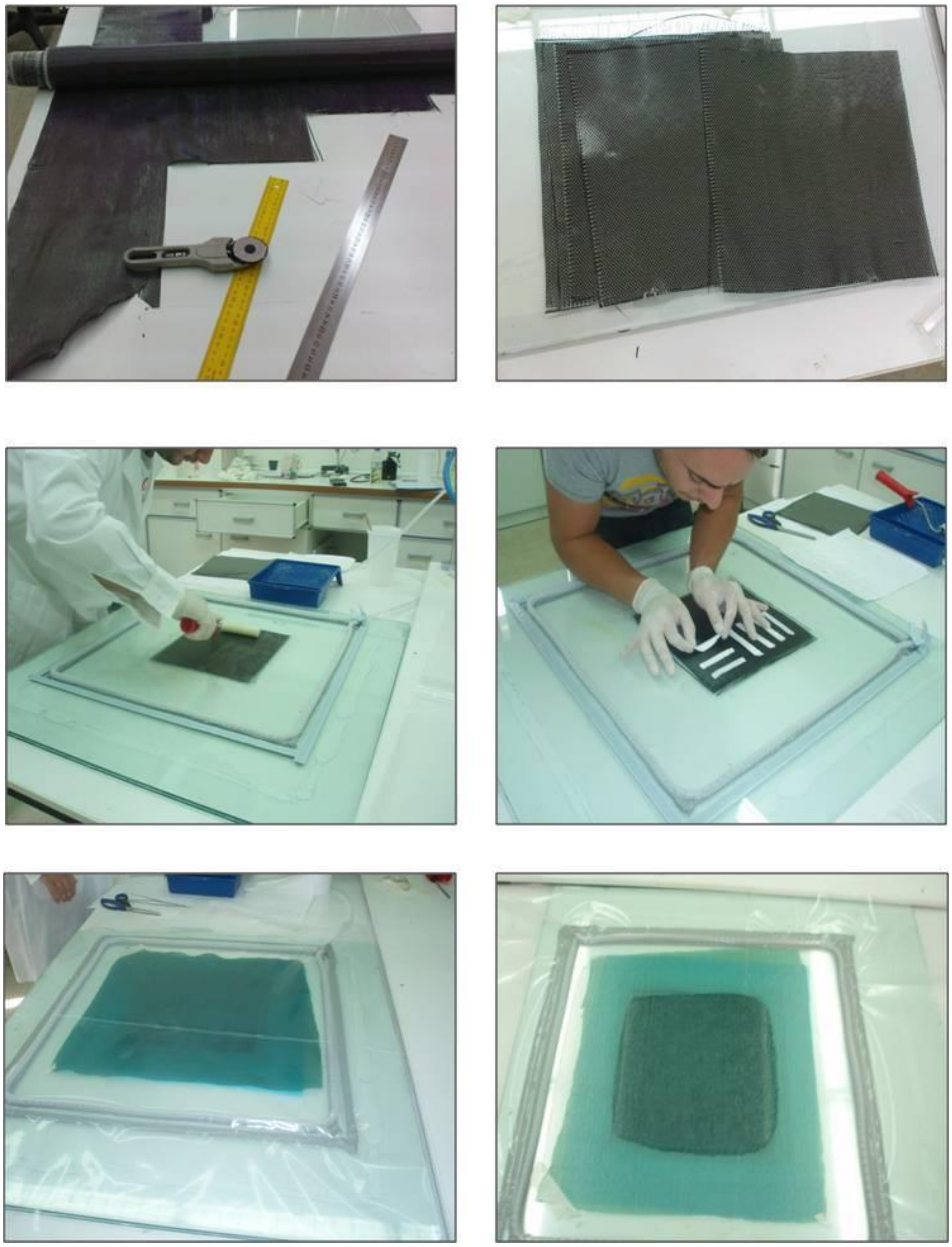

Figure 3.1.1 *Case 1 - typical manufacturing procedure; 1st CFRP laminate.*

The following sequence of snapshots (Fig.3.1.2) depicts the schematic configuration of the artificial Teflon-simulated defects juxtaposed to the laminate well as an image of the composite laminate after the post-curing process.

Fig.3.1.2 also shows the location and dimension of the inserted artificial defects. As is depicted in the scheme, a typical distance of 20 mm between the Teflon inserts was adopted. This would inhibit the interference between the thermal imprints of the particular tapes when interrogated with thermography.

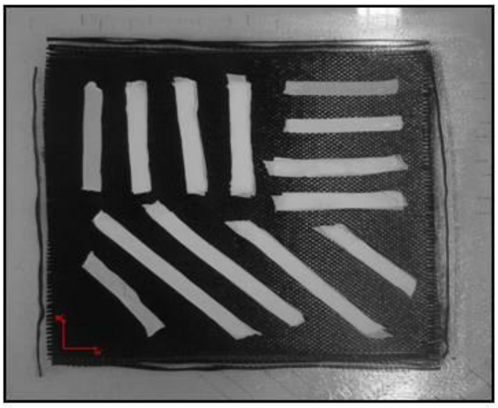

(a)

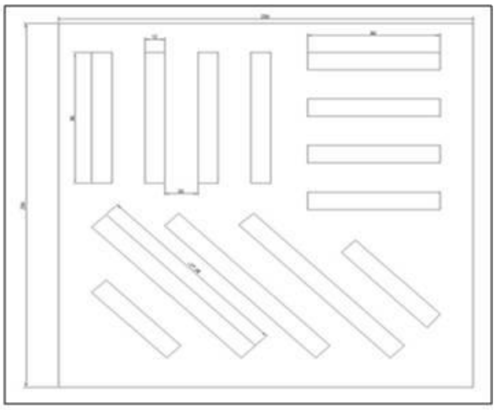

(b)

(c)

Figure 3.1.2 *Case 1 - 1st CFRP laminate (a) manufacturing snapshot, (b) location and dimension and configuration of the PTFE inserts, (c) CFRP laminate after post-curing process.*

Fig.3.1.3 illustrates the complete manufacturing process of the 2nd CFRP laminate. In this scenario, infusion was adopted as fabrication methodology. Infusion was chosen as an alternative to wet hand lay-up, as it was more convenient to precisely place the particular Teflon tapes at the prescribed locations, without being inhibited by the presence of resin. After the lamination process and the positioning of the Teflon inserts, resin was transferred in the mold using vacuum. As aforementioned, the artificial defects were inserted in two distinct interlaminar surfaces, i.e. in the 3rd -4th laminae interface and in the 4th – 5th laminae interface.

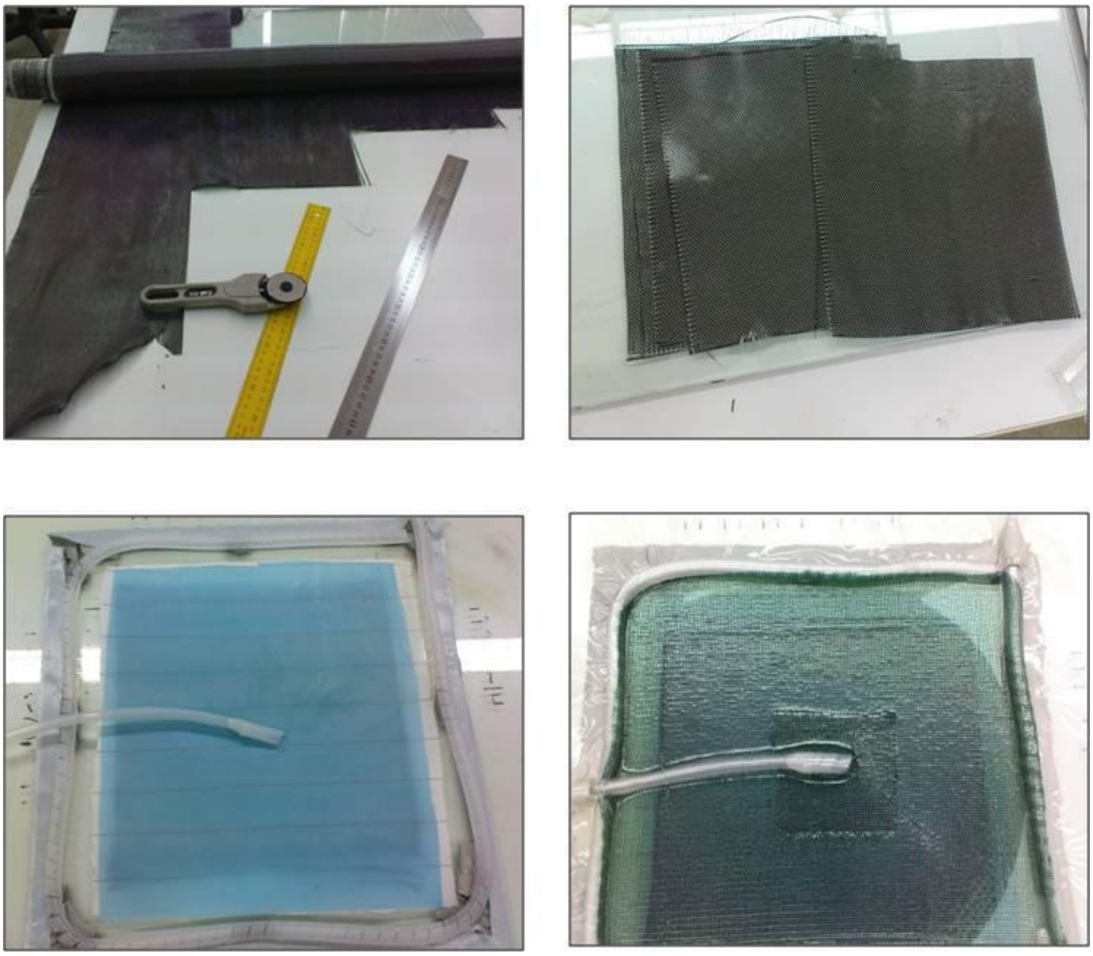

Figure 3.1.3 *Case 1 – typical manufacturing procedure; 2nd CFRP laminate.*

The following sequence of images (Fig.3.1.4) shows two snapshots taken (3rd and 4th layer) during manufacturing process, the schematic configuration of the artificial Teflon-simulated defects as well as an image of the 2nd CFRP laminate after post-curing. In addition, in Fig.3.1.4 the location and dimension of the induced artificial defects can be distinguished. As was also the practice for the 1st CFRP laminate, the distance in between the particular Teflon inserts was kept constant at 20 mm. As can be seen in Fig.3.1.4d, the infusion process induced a longitudinal flaw on the center of the laminate, which unavoidably interfered with the intentionally inserted flaws during the thermographic interrogation.

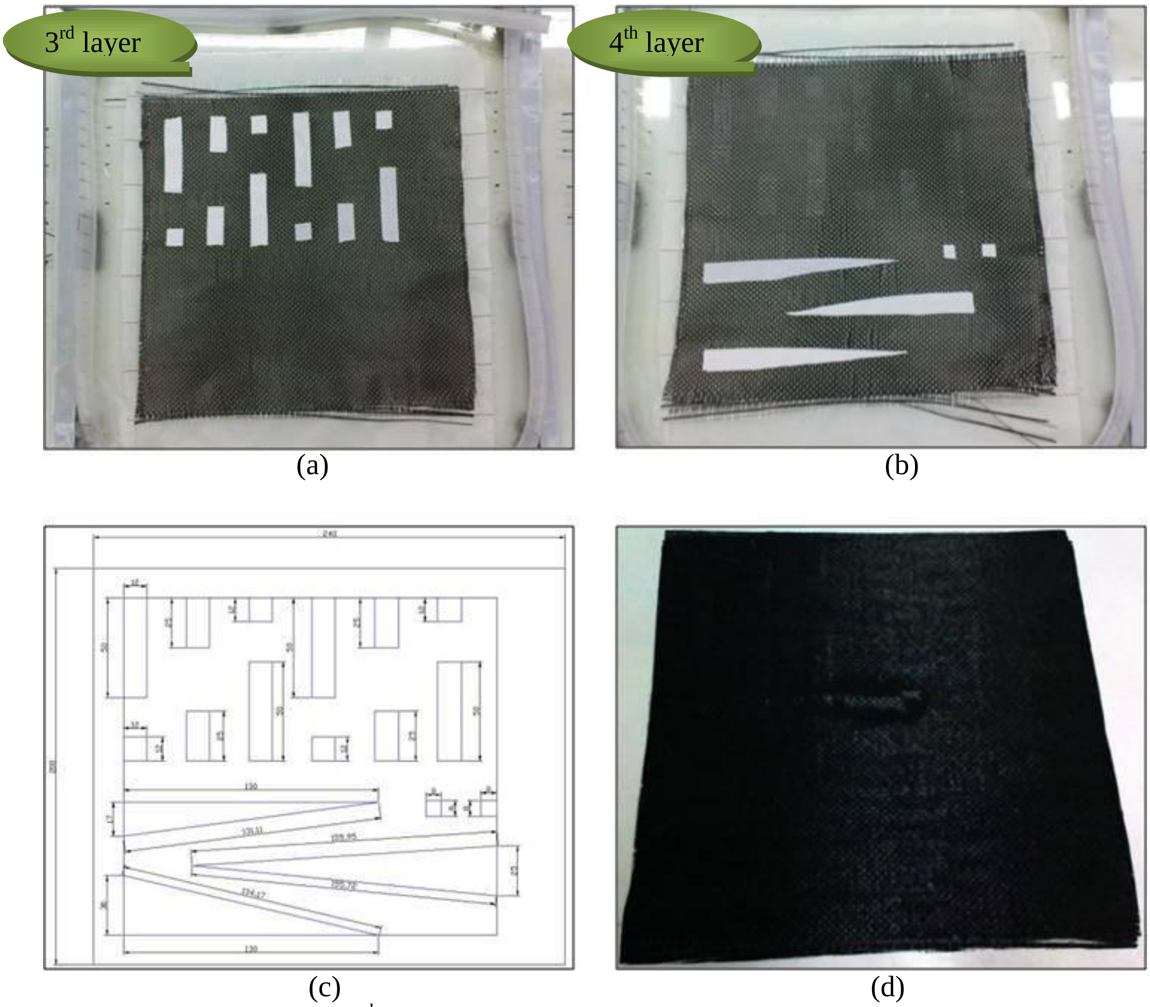

Figure 3.1.4 *Case 2 - 2nd CFRP laminate (a, b) manufacturing snapshots, (c) location, configuration and dimensions of the PTFE inserts, (d) CFRP laminate after post-curing.*

Case 2: Unidirectional (UD) CFRP patches in dimensions 100x100x1.29 mm^3 and orientation $[0]_5$ were positioned on 300x100x1.22 mm^3 aluminum substrates to simulate patch repair. A twill weave carbon fabric provided by R&G was employed. The table below shows the biaxial fabric properties (Table 3.1.2). PTFE inserts were placed at the edges of the patch and in the centre, as shown in Fig.3.1.5 (100x6x0.075mm^3). In the following image sequence (Fig.3.1.5), a CFRP repaired aluminum coupon is presented. For the manufacturing, the wet lay-up method was employed. Fig.3.1.5 depicts the location of the induced Teflon “damage-initiators”. The substrate material was non-anodized Aluminum 2024 T3. The preparation of the aluminum surface was solely abrasion with a 150 grit emery cloth and, subsequently, cleaning it with de-ionized water and acetone. Before the application of the patch repair, the Al strips were left to dry in an oven in 30 ^{o}C for 3 h. Table 3.1.3 lists the substrate material properties.

Table 3.1.2 *Case 2 carbon fabric.*

Twill weave carbon fabric (R&G)	
Weight	160 gr/m^2
Resin Consumption	184 gr/m^2
Laminate ply thickness	0.257 mm
Laminate ply weight	344 g/m^2

For the matrix, the Araldite LY 5052 /Aradur 5052 cold curing epoxy system was adopted provided by Huntsman International LLC. Curing of the matrix was 1 day at 23 ^{o}C followed by post-curing for 15 h at 50 ^{o}C. A low temperature post-curing procedure was chosen over the high one in order to eliminate the possibility of inducing additional thermal stresses. The embedded artificial defects were PTFE tapes of 75 μm thickness.

Table 3.1.3 *Case 2 aluminum.*

Aeronautical Aluminum, Al 2024 T3	
Thickness	1.22 mm
Young's modulus	70 GPa

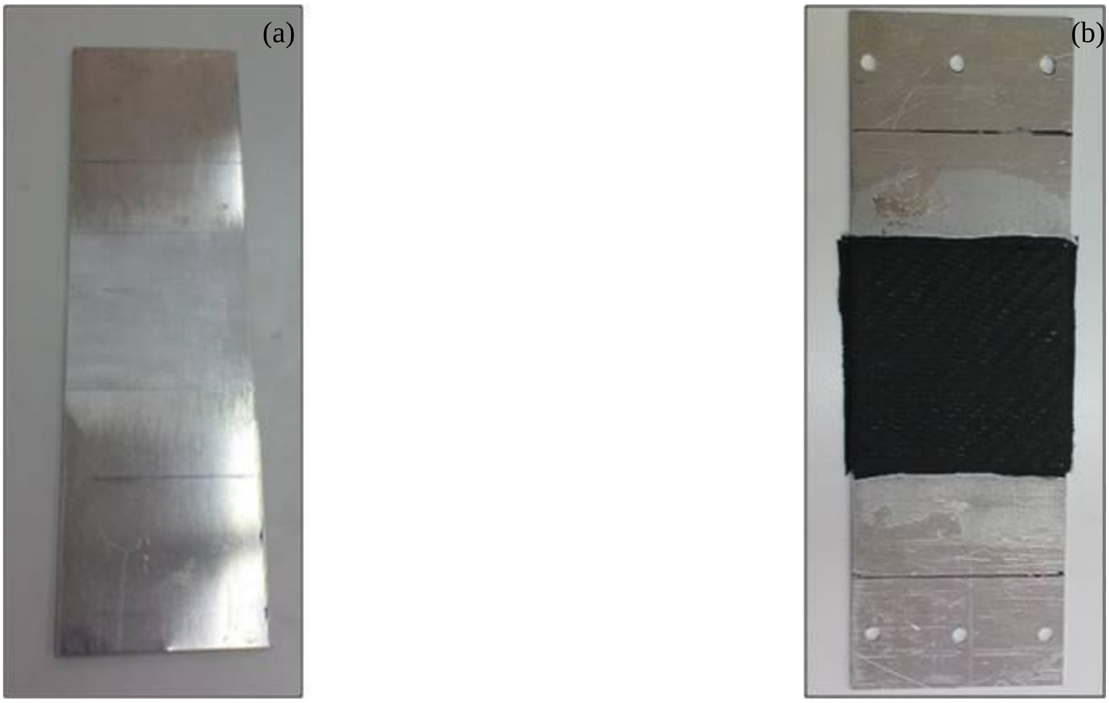

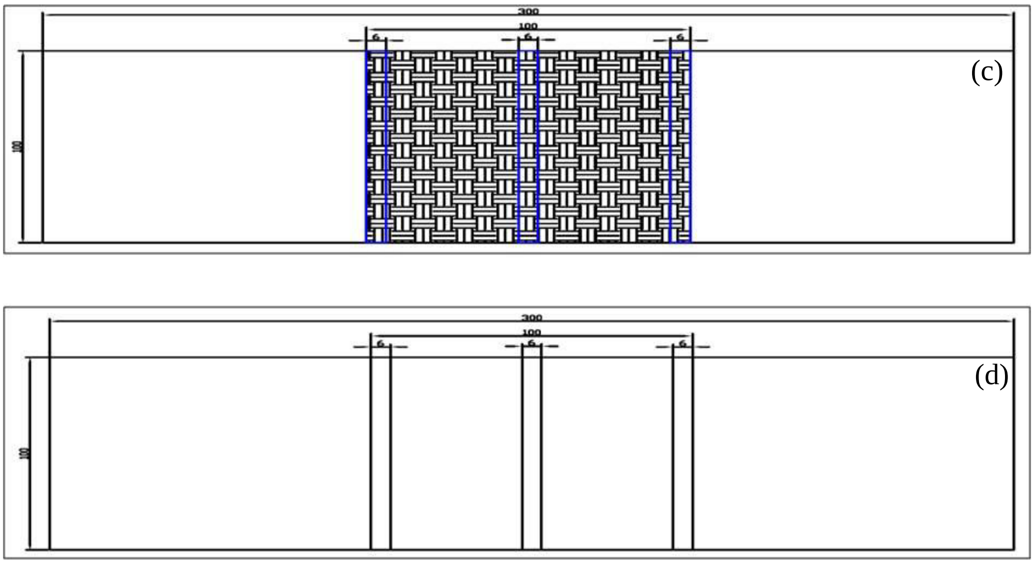

Figure 3.1.5 *Case 2 – (a) Al surface, (b) repaired Al surface, (c, d) configuration and location of patch and Teflon inserts.*

Case 3: As is shown in Figs.3.1.7 to 3.1.10, Al and composite plates were repaired with CFRP patches. These consisted of i) six aluminum substrate coupons repaired with five-ply CFRP patches and ii) six composite substrate coupons repaired by five-ply CFRP patches. For the patch manufacturing, an identical repair and defect protocol was followed in both substrate cases. A satin weave fabric provided by (5H SATIN 43280) HEXCEL was employed for patch reinforcement and Epocast 52 A/B for the patch matrix. Patch matrix was modified with 0.5% w/w MWCNTs. CNTs were dispersed in the epoxy matrix via sonication for 2 h, using the ultrasonic processor UP400S (400 W, 24 kHz) by Hielscher at 50% amplitude, which was found to yield optimal fracture toughness properties for 0.5% w/w CNT /matrix ratio [189]. The orientation of the patch reinforcement was 0/90°/0/90°/0. The impregnation of the fabric layers was performed on a heated table surface (60 °C) in order to obtain low viscosity conditions. Impregnation was performed with carbon fabric and resin within two plastic sheets so as to facilitate the impregnation process and plies cutting. The matrix was initially applied on the centre of each fabric layer (Fig.3.1.6a) and then impregnation was carried out from the centre towards the whole fabric layer area (Fig.3.1.6b to e). The followed curing process was 4 h at 95°C in an oven under -700 mbar vacuum pressure. As far as the Al substrate is concerned, it was anodized with chromic anodization and afterwards the CYTEC BR127 primer was applied. The thickness of the substrate was 1.6mm. In the case of the composite substrate, the reinforcement was provided by a pre-preg (MTM®56-cure cycle: 30 min at 120 ^{0}C) woven carbon fabric (199 g/m^2) by ACG (UK). The final thickness was approximately 1.6mm. The preparation of the composite substrate before the application of the patch comprised grinding with 180 grit abrasive paper on the smooth side of the plate and subsequently cleaning with diestone DLS.

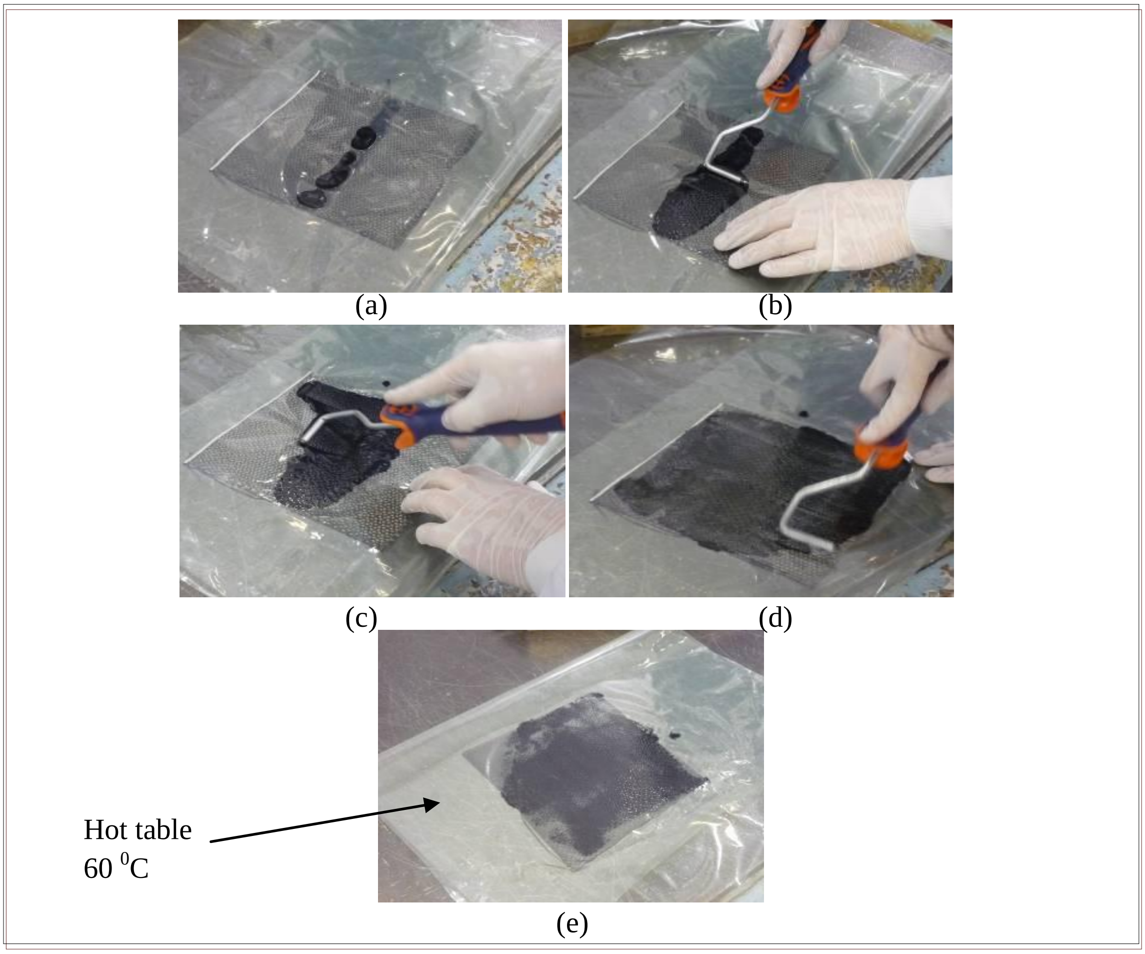

Figure 3.1.6 *Patch fabric layer impregnation procedure*[1].

The pre-defined artificial damages included the following scenarios:

1. Configuration 1: undamaged coupon
2. Configuration 2: one centered point with no adhesion
3. Configuration 3: 4 areas with no adhesion between substrate and first impregnated ply
4. Configuration 4: 4 areas with no adhesion
5. Configuration 5: triangular no adhesion area between substrate and first impregnated ply
6. Configuration 6: 50% “bad” adhesion between the patch and the substrate.

No adhesion was obtained by locally inserting a Teflon film /flake cut to prescribed dimensions whereas bad adhesion occurred by painting the surface with a multipurpose oil

[1] The repaired plates of *Case 3* were manufactured by Daher industry (France) for the purposes of Iapetus EU project (WP2).

"WD-40". The following images (Fig.3.1.7 - 3.1.10) represent the particular configurations of all the interrogated artificial damages regarding the repaired plates of *Case 3*.

Al substrate *Composite substrate*

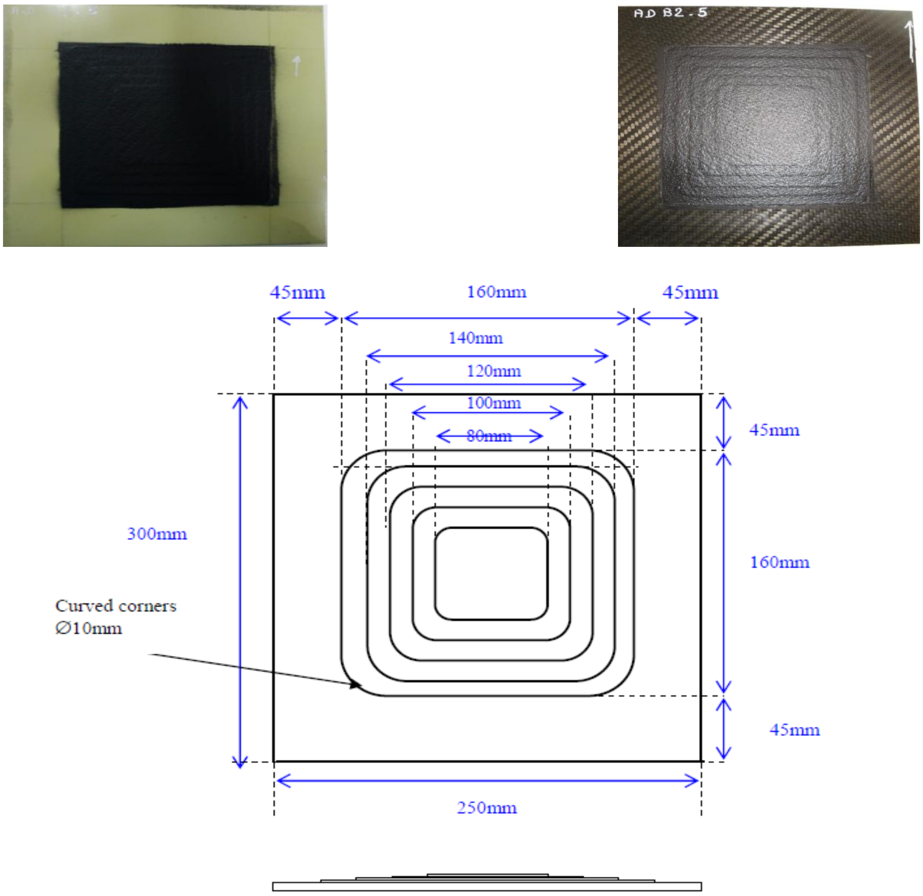

Figure 3.1.7 Geometry of the manufactured coupons.

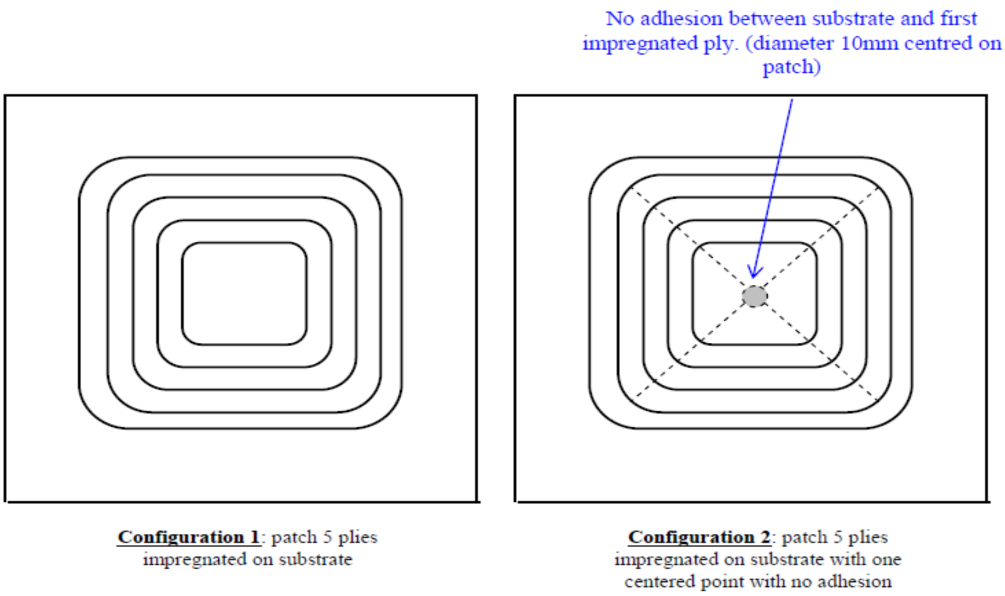

Figure 3.1.8 *Specimen configuration 1 (left) and 2 (right).*

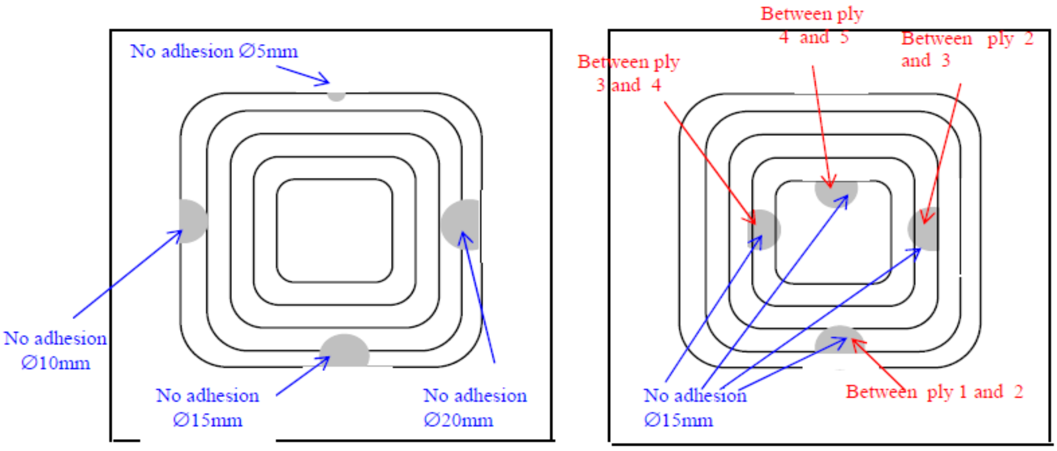

Configuration 3: patch 5 plies impregnated on substrate with 4 areas of no adhesion between substrate and first impregnated ply

Configuration 4: patch 5 plies impregnated on substrates with 4 areas of no adhesion

Figure 3.1.9 *Specimen configuration 3 (left) and 4 (right).*

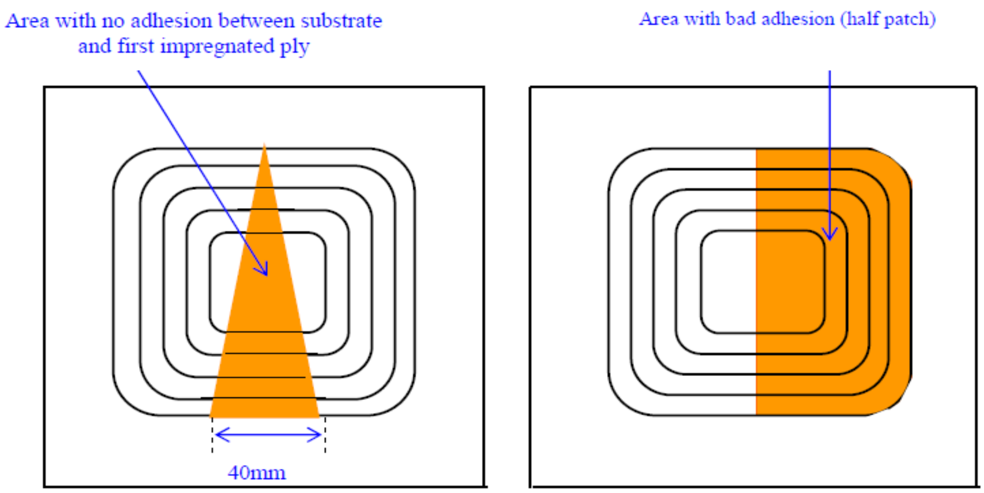

Configuration 5: patch 5 plis with triangular no adhesion area between substrate and first impregnated ply

Configuration 6: patch 5 plies with half surface of "bad" adhesion

Figure 3.1.10 *Specimen configuration 5 (left) and 6 (right).*

3.1.3 Damage assessment

The experimental setup of optical infrared thermography comprises an excitation source (optical incandescent lamps) and an infrared camera. The thermal source was a 4 optical-lamp array (1kW each). The Jade 510 (manufactured by CEDIP) medium wave infrared camera was employed. The camera uses a cooled indium antimonide detector (3–5 mm) with a frame rate of 50-150 Hz and a focal plane array pixel format of 320 (H) 240 (V). The position of the lamps and the infrared camera depended on the minimum focal length of the employed lens and the desired Field Of View (FOV). The specimens were appropriately fixed on a specimen holder. Initially, for the thermographic inspection, PT was employed. Subsequently, PPT and LT were applied. In *Case 1* materials, the whole CFRP plates were inspected. However, in *Case 2* and *3* coupons, merely the patched areas were examined. Various combinations of voltage frequency and distance were tried in order to define the optimum experimental parameters. In Fig.3.1.11, the experimental setup for the implementation of the off-line damage inspection is depicted. As can be seen, it includes the excitation source, the pulse generator, the thermal camera, the lock-in amplifier and the PC. In all material cases, a commercially-available black mat paint (ε=0.97) was used in order to render the emissivity of the material surfaces close to that of the black body (ε=1).

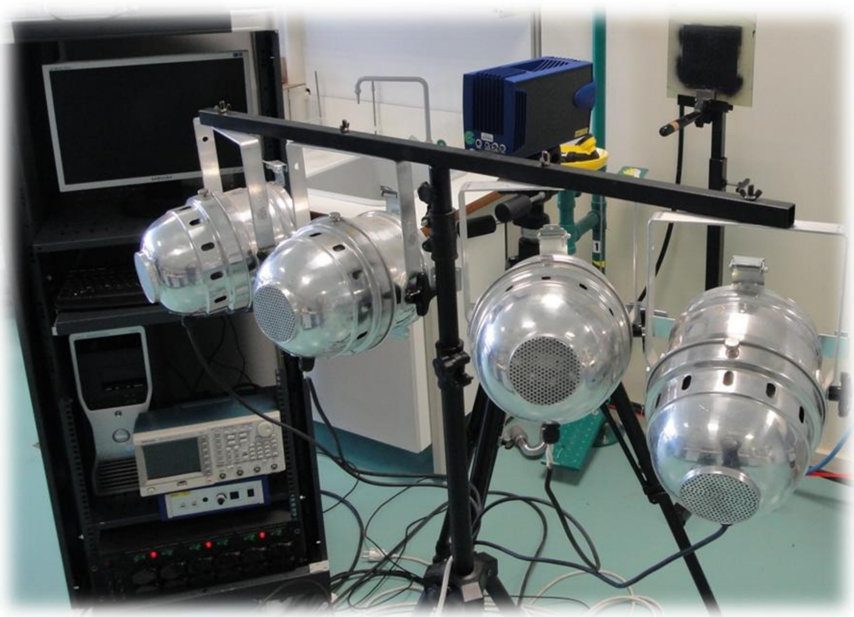

Figure 3.1.11 *Experimental setup of off-line infrared thermography.*

As aforementioned, the thermographic assessment of the interrogated materials was preceded by the examination via ultrasonics. C-scan imaging was used as a benchmarking technique for the obtained thermographic results. For the implementation of the ultrasonic inspection, an immersion tank shown in Fig.3.1.12 was used. A 10 MHz pulser–receiver piezoelectric transducer was employed. As can be seen in Fig.3.1.12, the experimental setup includes a single bridge ultrasonic system (Physical Acoustics) which employs an automated motion allowing for the transducer to translate along the xyz axes.

Figure 3.1.12 *Representation of the employed c-scanning method.*

Since the material in C-scan is completely immersed into the water, air bubbles were observed on the surface of the all CFRP laminates. This effect was attributed to surface roughness. A paint brush was used to remove the air-bubbles from all interrogated material surfaces, as would certainly impede on the inspection process and consequently reduce the image resolution. Two different ultrasonic modes were performed to verify the results of IrT: pulse-echo and double-through transmission. Optimization of the ultrasonic method was achieved via appropriately setting the ‘time gates’ on the proper time - windows of the received waveforms. Multiple attempts were made in order to suitably adapt the time gates on the reflected waveform and optimize the c-scan image.

3.1.4 Results and discussion

With regard to damage assessment via IrT, there is a temperature constraint which refers to the maximum temperature that the material can be subjected. For the interrogated polymer matrices, the 80 ^{0}C was chosen to be the maximum inspection temperature regarding its post-curing degree which was 100 ^{0}C. After this temperature the increased heat is expected to degrade the material matrix and subsequently to deteriorate the overall composite. Moreover and as initial trials indicated, above this temperature, a steady state temperature was reached over the surface of the specimen with no noticeable thermal gradients on the specimen surface, and thus thermographic damage detection was not feasible. To that respect, all NDE testing was implemented in lower than 80 ^{0}C surface temperature. Practically, this temperature limit was not found to be an impediment, as optimum damage information was obtained in temperatures lower than 50 ^{0}C. In all thermographic inspection approaches, proper experimental parameters were set in order to observe optimum identification potential.

Case 1 and 2 materials

3.1.4.1 Pulsed thermography

The selected experimental parameters followed for the implementation of the pulsed thermographic assessment of *Case 1 & 2* materials, are shown in Table 3.1.4:

Table 3.1.4 *Experimental parameters of thermographic evaluation.*

Method	PT	PPT	LT
Specimen	1st CFRP laminate	2nd CFRP laminate	Patch
Frequency/Hz	1	0.05	0.05
Voltage/V	5	5	2
Distance/m	1.56	1.79	0.92

As is the usual practice in PT, the surfaces of the interrogated laminates were subjected to square heat pulses using the optical lamps. Thermal images were captured during the cooling down process. The raw data of the images correspond to an arbitrary intensity value (calibrated to temperature, amplitude or phase values) attributed to each one of the 2D array of pixels. Following the intensity values along straight lines provides the resolving ability of the thermographic imaging along an axis. As can be seen in Fig. 3.1.13, such lines were drawn using the software of the IR camera. In the depicted mode i.e. PT, the straight lines track temperature variations on a pixel by pixel basis. The raw data of the straight lines (temperature shift) are plotted against the length of each line (pixels). Thus, when a line meets a defect, it is clearly shown as a step increase in the respective temperature - pixel graph.

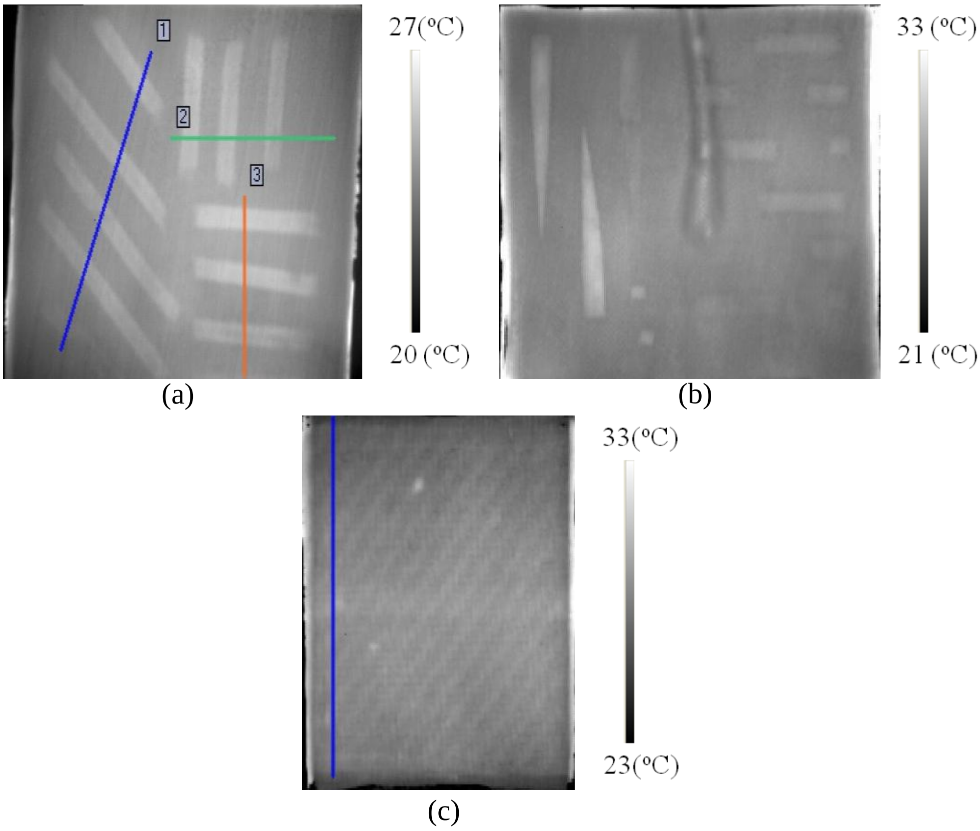

Figure 3.1.13 *Thermal images: (a) 1st CFRP laminate, (b) 2nd CFRP laminate, (c) CFRP patch on Al substrate.*

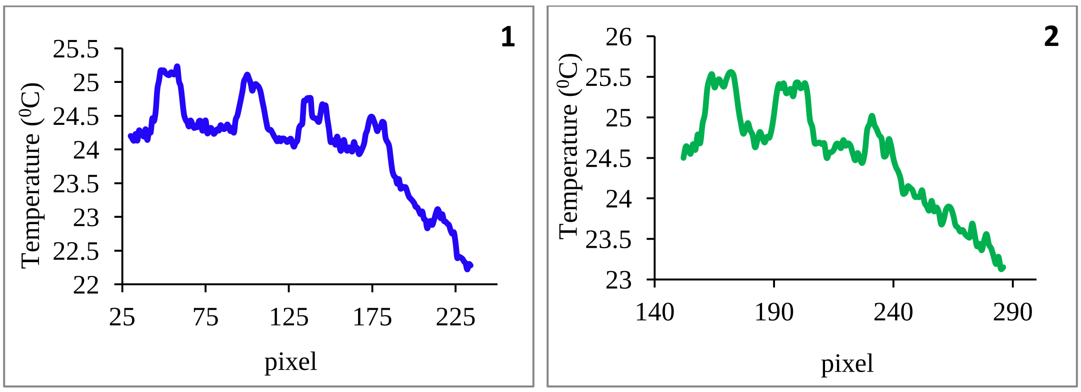

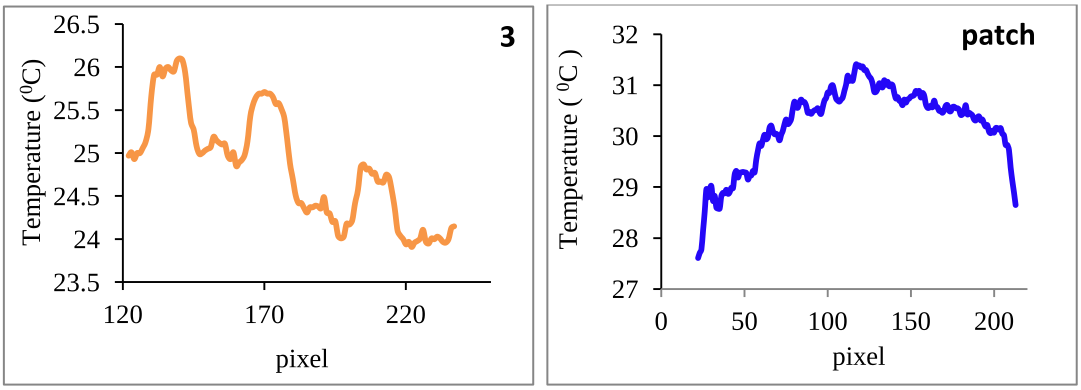

Figure 3.1.14 *Temperature – pixel graphs for the: 1st CFRP laminate (1, 2, 3) and the CFRP patch on Al substrate.*

Figs.3.1.14 depicts the recorded temperature variations as a function of pixels of the straight lines of Fig.3.1.13, for the different material cases (1st CFRP plate and CFRP patched Al strip). Practically, this representation indicates that the artificial defects (Teflon tapes) are in higher temperature than the rest of the laminate, or act as heat traps which locally delay the cooling down process. This is due to the fact that the thermal diffusivity between the specific examined materials is different (PTFE – carbon /epoxy) and as a result, IR thermography can conveniently detect the artificial Teflon-defects.

The examination of the thermal images in Fig.3.1.13 provides information on the resolving ability of the method, as some of the induced defects are not clearly visible. This is primarily due to the thickness of the artificial flaws. In all cases, the barely visible flaws possess the lower incorporated thickness which was equal to 75 μm. In the patch - Al case, the Teflon tapes at the edges of the patch are barely visible or almost invisible (Fig.3.1.13c). In this case there is a strong difference in the inspected materials thermal conductivity (CFRP–Al-Teflon). A closer look at the thermal images indicates that in the case of the patched coupon, the weave pattern is also visible. In the 2nd CFRP laminate, a longitudinal defect can be clearly distinguished which is attributed to the resin infusion plastic hose used in the manufacturing process. It should also be reported that in the case of CFRP laminates, the Teflon tapes exhibited one degree higher temperature than the ambient Figs.3.1.4 (1,2,3) whereas in the case of the CFRP patched Al strip, a three Celsius degrees higher temperature was recorded between the edges and central patched area. This may be attributed to the presence of the aluminum CFRP interface (Figs.3.1.4 (patch)).

As Fig.3.1.14 indicates, the noise level as manifested by the variation amplitude away from the defect is approximately 0.15 to 0.20 ºC. The maximum temperature difference induced by the defects is of the order of 1 ºC, whereas there are defects that are within the noise level. In order to increase the detection ability of the thermographic imaging, PPT and LT were subsequently employed.

3.1.4.2 Pulsed Phase Thermography

Table 3.1.5 lists the selected experimental parameters for the implementation of the inspection with PPT, of *Case 1* & *2* materials:

Table 3.1.5 *Experimental testing parameters for the 1st CFRP laminate, 2nd CFRP laminate and the CFRP patch on Al substrate, respectively.*

Method	Pulsed Phase Thermography		
Specimen	1st CFRP laminate	1st CFRP laminate	PATCH
Frequency/Hz	0.3	0,1	0.30
Voltage/V	3	5	5
Distance/m	1,66	1,70	0.92

In PPT mode, the material is heated similarly to PT. The frequency of the thermal waves generated onto the materials is mathematically analyzed by a FFT. As a result, PPT provides phase and amplitude images. The observed phase images were in all cases clearer than the amplitude ones. For that reason, solely the phase images are presented.

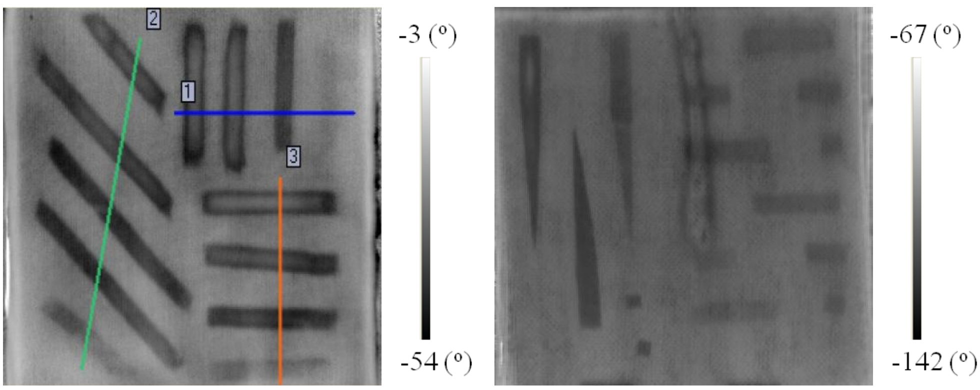

(a) (b)

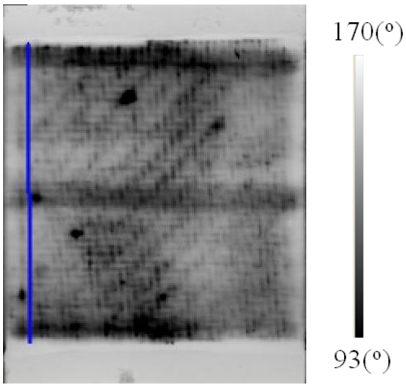

(c)

Figure 3.1.15 *Phase images: (a) 1st CFRP laminate, (b) 2nd CFRP laminate, (c) CFRP patch on Al substrate.*

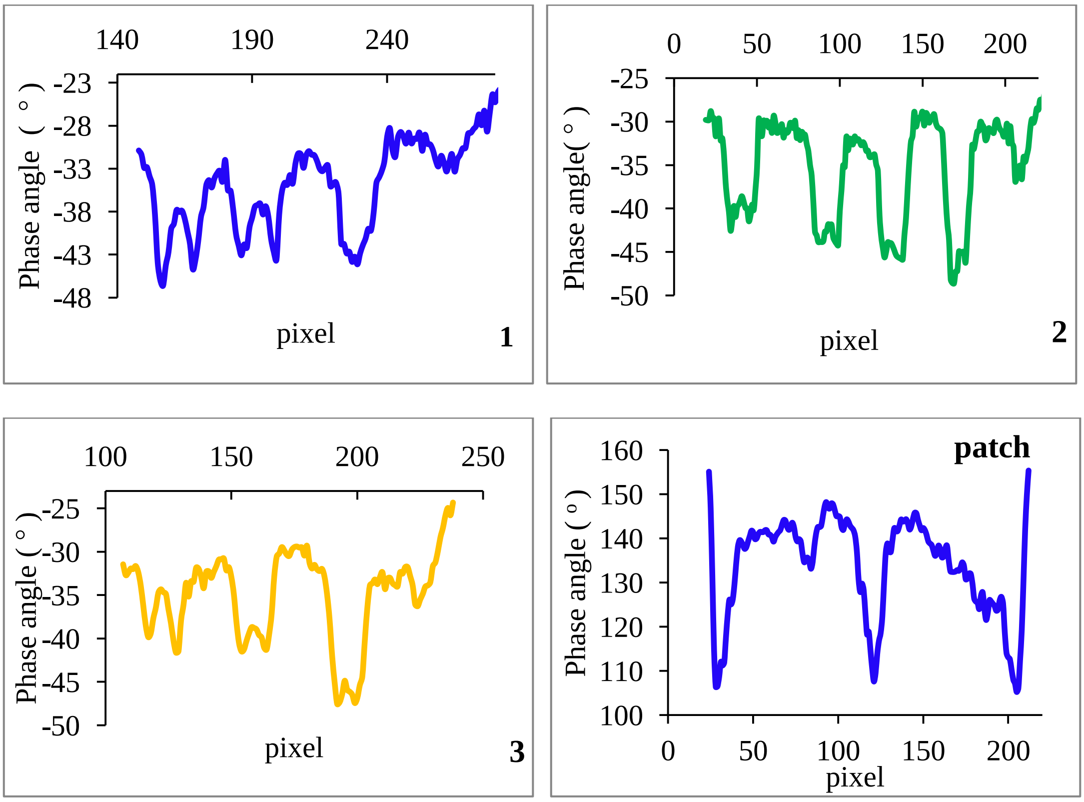

Figure 3.1.16 *Phase angle – pixel plots for: 1st CFRP laminate (1,2,3) and CFRP on Al substrate.*

As it is obvious from the phase images of Fig.3.1.15, the artificial defects are recognized. This is also verified by the phase angle shifts vs. pixel graphs (Fig.3.1.16), where the difference in phase is noticeable and much higher than the noise of the system. In the respective graphs, remarkable peaks /drops, respectively, are shown in the presence of a defect. Closer examination of the phase images can confirm that in the case of the patched coupon, the weave pattern is distinguished along with some flaws which are possibly small masses of fragmented fibres. It is noteworthy that recorded phase shift in the presence of damage (PTFE tape) in the CFRP laminate is higher compared to the repaired Al case (Fig.3.1.16).

3.1.4.3 Lock-in Thermography

Table 3.1.6 lists the employed experimental parameters for damage inspection of *Case 1* & *2* materials with LT:

Table 3.1.6 *Experimental testing parameters for the 1st CFRP laminate, 2nd CFRP laminate and the CFRP patch on Al substrate, respectively.*

Method	**Lock-in Thermography**		
Specimen	1st CFRP laminate	1st CFRP laminate	PATCH
Frequency/Hz	0.2	0.2	0.2
Voltage/V	2	2	2
Distance/m	1,66	1,70	0.92
Periods	2	2	3

In the case of LT, the thermal camera was synchronized with the frequency of the lamps. Thermographic images are juxtaposed to the results from the c-scan and are correlated (Fig.3.1.16a to 3.1.16i).

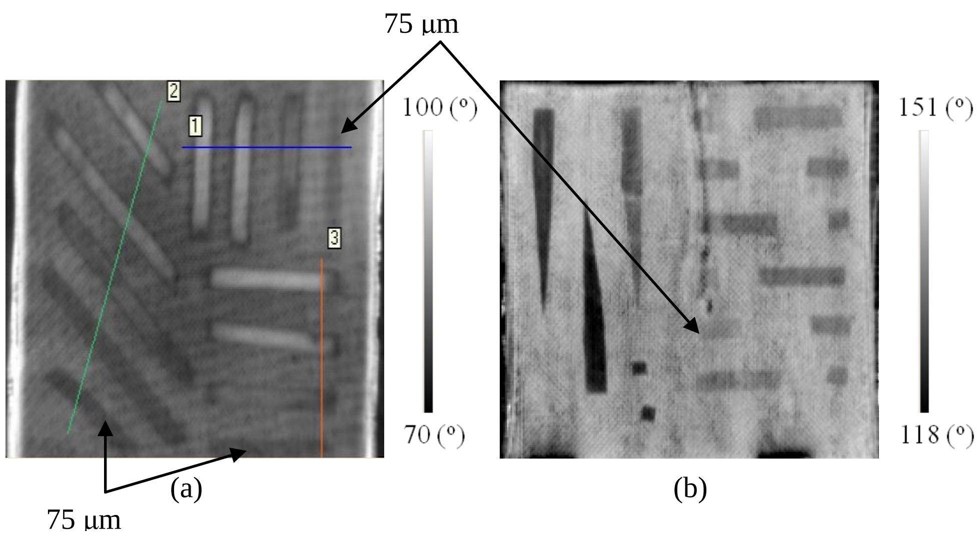

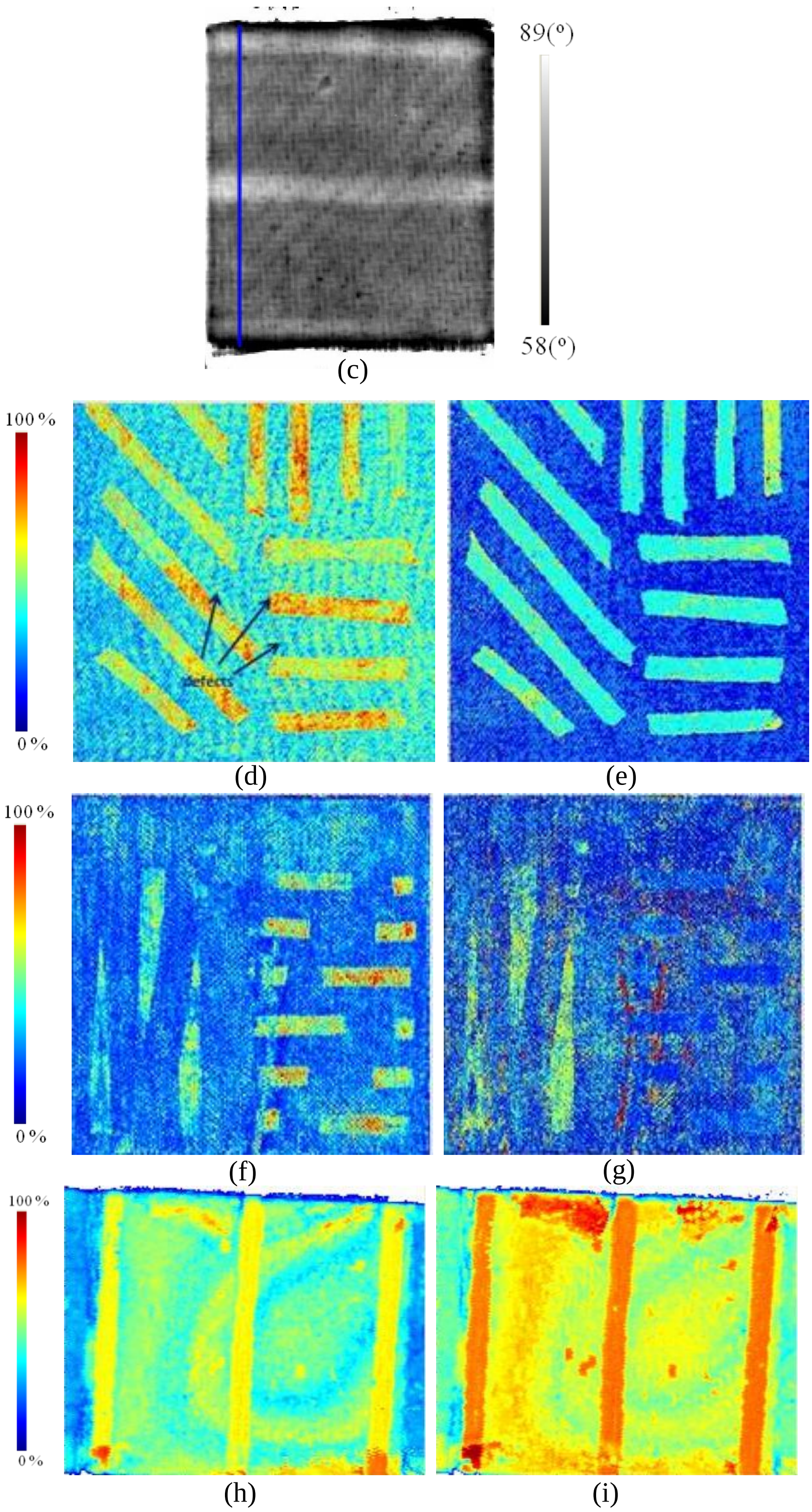

Figure 3.1.17 *Phase images: (a) 1st CFRP laminate, (b) 2nd CFRP laminate, (c) CFRP patch on Al substrate, (d, e) C-scan images of the 1st CFRP plate (Case 1), (f, g) C-scan images of the 2nd CFRP plate (Case 2), (h, i) CFRP patch on Al substrate (Case 2).*

Regarding phase-related images (Figs.3.1.17a, b and c) the resolution of the method has considerably increased. The observed images clearly pin-point all the included simulated defects. Figs.3.1.18 show the phase angle shift as a function of the pixel of the straight lines observed on the phase images (Figs.3.1.17 (a, b, c)). It is evident, that LT may provide higher quality images compared both to PT and PPT, as all artificial flaws could be detected, including those of minimum size and thickness (75 μm). This result may mainly be attributed to the synchronization of the thermal camera with the excitation source. In the case of the 2^{nd} CFRP laminate, the defect created during manufacturing is not as visible as it was in the case of PPT and PT (Fig.3.1.13b and 3.1.15b). With respect to the patched coupon, additional defects are identified with black colors and are also attributed to the manufacturing process. In all respects, the weaving pattern is clearly distinguished and the fabric type can easily be discriminated (unidirectional (Figs.3.1.17a & 3.1.1.7b) or biaxial (Fig.3.1.17c)). In addition, the value of thermal diffusivity is always dependent on the material characteristics of the constituted phases. Type and orientation of the reinforcement as well as the material used for matrix, affect significantly the thermal properties of the material. This difference is always noticeable and increases when “passing” from cross-ply laminates (Figs.3.1.17a) to unidirectional (Figs.3.1.17b) and then to composite repaired Al surfaces (Figs.3.1.17c).

In the 2^{nd} CFRP laminate case, the tapes shown with darker color possess higher thickness than those with brighter color Fig.3.1.17b. As aforementioned, the method was capable of detecting the 75 μm inserted tapes, albeit with lower resolution. Moreover, in the case of the patched Al (Fig.3.1.17c), the tapes are quite easily distinguished even if their thickness is the lowest interrogated, equal to 75 μm. This is considered to be a complementary effect due to the higher thermal conductivity of the substrate over the composite patch. Although this differential thermal conductivity was expected to mask the presence of the PTFE tapes, it enhanced their detectability.

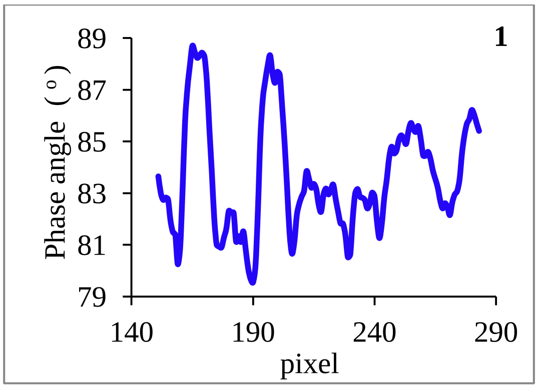

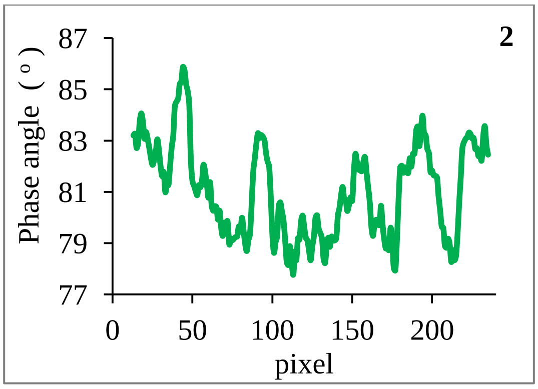

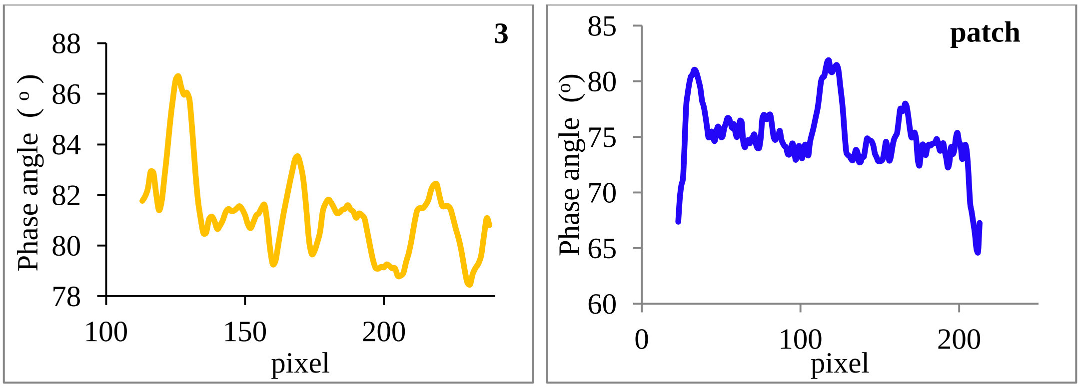

Figure 3.1.18 *Phase angle – pixel plots for: 1st CFRP laminate (1, 2, 3) and CFRP on Al substrate.*

Figs.3.1.17 represents the C-scan images observed for the *Case 1 & 2* interrogated specimens. As it is verified from the presented images, IR thermography was as efficient in damage detection as C-scanning, and in some cases even performed better (compare Fig. 3.1.17b to Figs.3.1.7f & g). Concluding, lock-in thermography proved to more efficient technique compared to PT and PPT as it exhibited the best resolving ability. Therefore, lock-in thermography was chosen for damage inspection in *Case 3*.

Case 3 materials

As mentioned previously, LT was selected among the three thermographic assessment methodologies as the most efficient in identifying simulated discontinuities for the *Case 3* scenario. In the following section, LT phase images of both the Al and composite repaired substrates are presented. C-scan images of the Al substrate repaired materials are juxtaposed with the phase thermographs in order to benchmark the efficiency of LT technique. Table 3.1.7 lists the selected experimental parameters applied for the interrogation of artificial damage in *Case 3* materials.

Table 3.1.7 *Experimental parameters.*

Method	**Lock-in Thermography**				
Configuration	1	2	3	4	5
Frequency/Hz	0.01	0.1	0.01	0.05	0.05
Voltage/V	3	2	3	2	2
Distance/m	1.18	1.18	1.18	1.18	1.18
Periods	2	5	2	3	4

Figs.3.1.19 – 3.1.24 show in sequence the (a) simulated damage configuration, (b) phase image of the aluminum substrate plate and (c) phase shift image of the composite substrate patched laminate, (d) c-scan image of the aluminum substrate repaired plates. Besides c-scan, b-scan ultrasonic imaging was also employed for Configurations 2, 5 and 6. As discussed in chapter 2, b-scan mode captures the cross-section of the material in a 2D representation.

Configuration 1: *patch 5 plies impregnated on substrate*

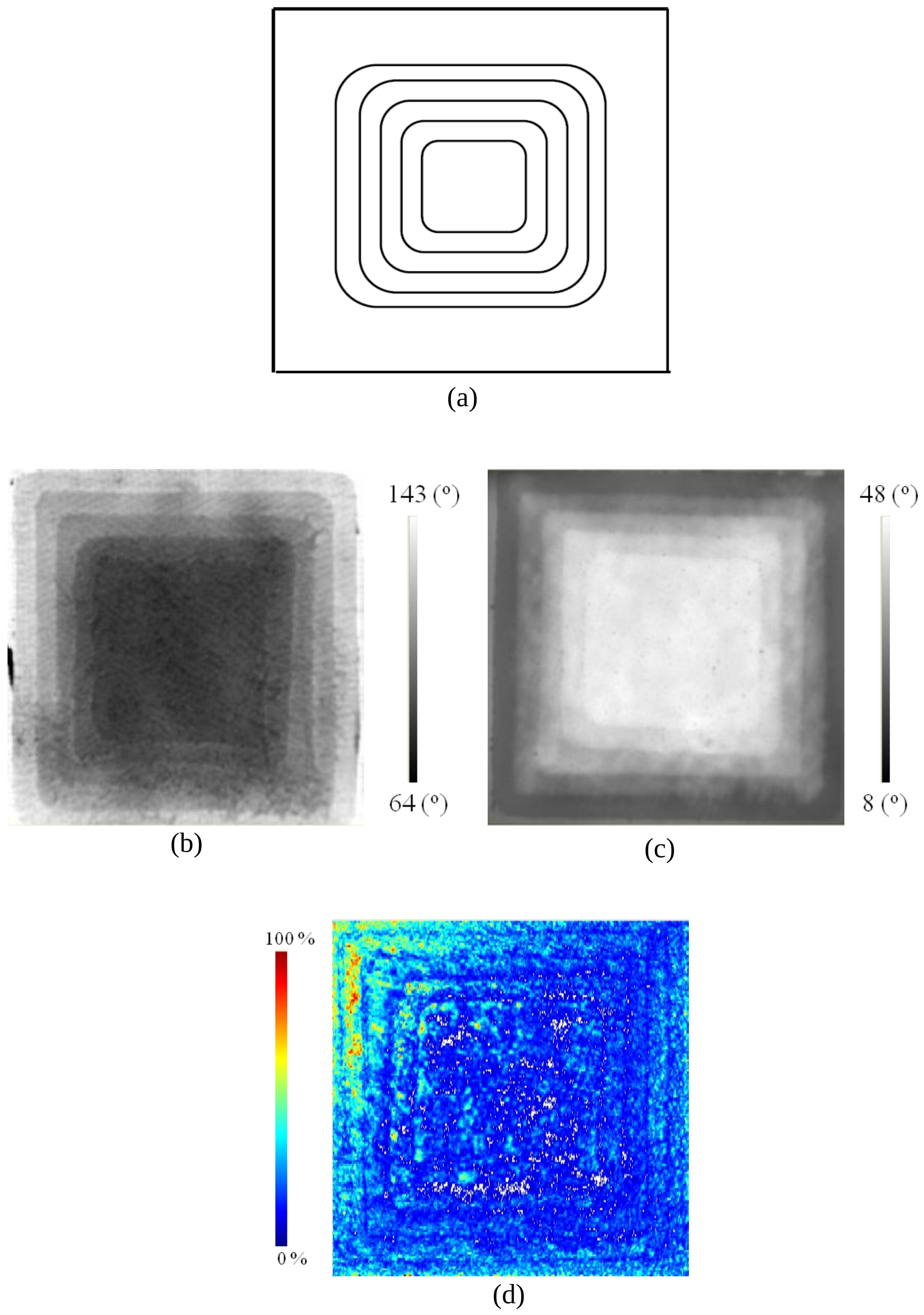

Figure 3.1.19 *No defect. (a) Coupon configuration. Phase images by lock-in thermography. (b) Al substrate, (c) Composite substrate, (d) C-scan image of the Al substrate repaired plate.*

Configuration 2: *one centered point with no adhesion*

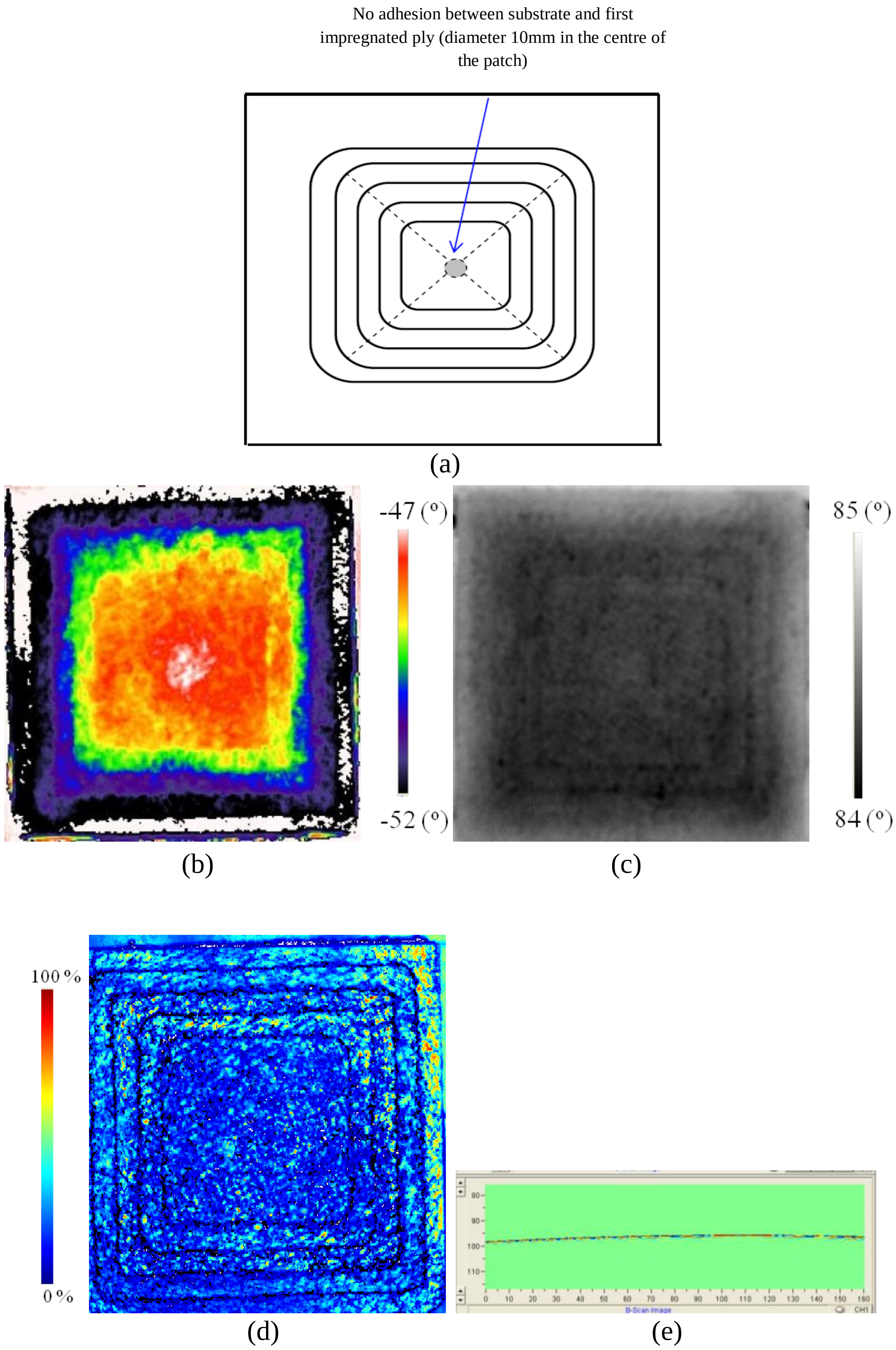

Figure 3.1.20 *Centre ∅10mm disbonding; (a) Coupon configuration. Phase images by lock-in thermography. (b) Al substrate, (c) Composite substrate, (d) C-scan image of the Al substrate repaired plate, (e) B-scan image of the Al substrate repaired plate.*

Configuration 3: *four areas of no adhesion between substrate and first impregnated ply*

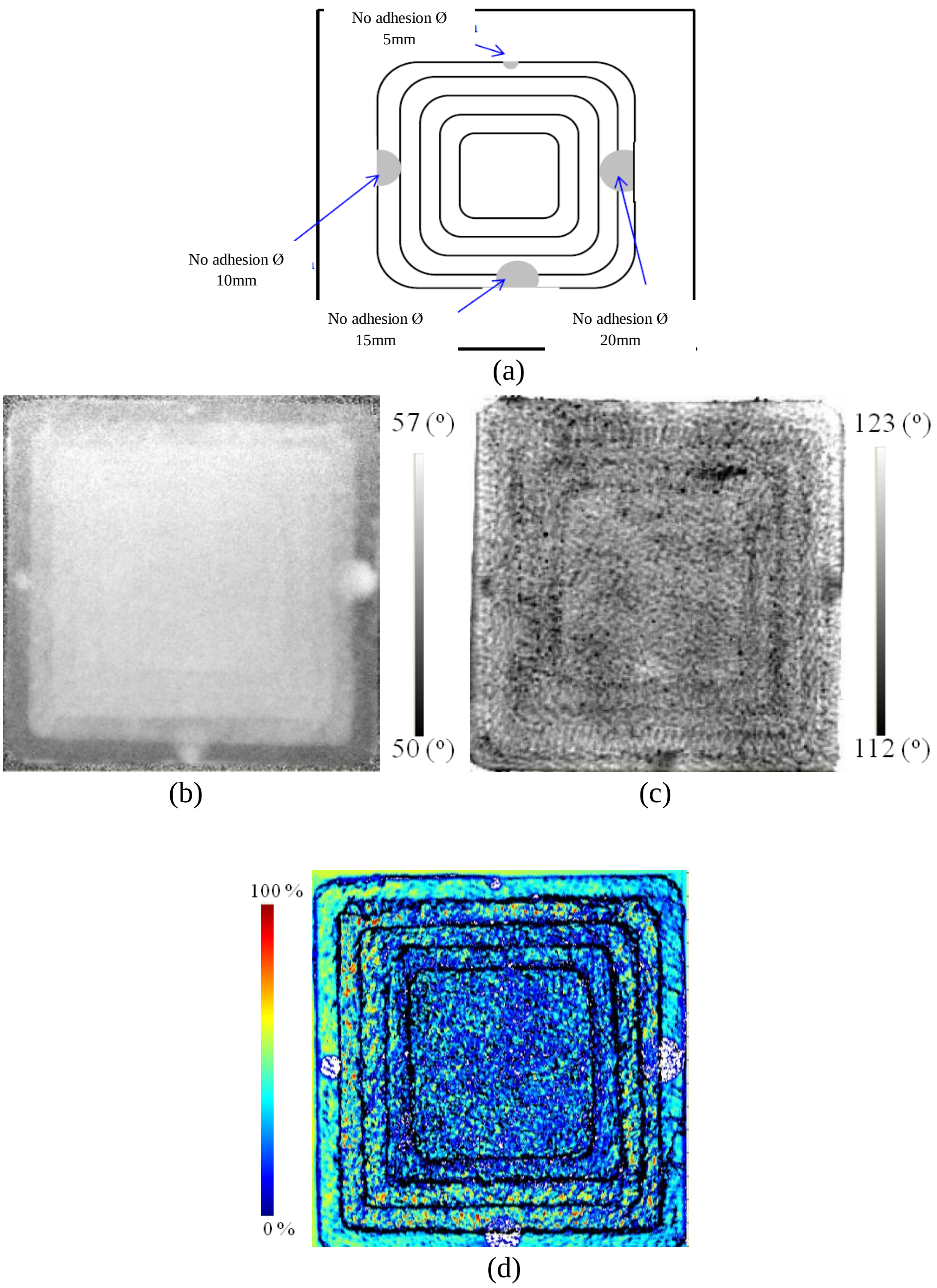

Figure 3.1.21 *Patch substrate disbonding: (a) Coupon configuration. Phase images by lock-in thermography. (b) Al substrate, (c) Composite substrate, (d) C-scan image of the Al substrate repaired plate.*

Configuration 4: *four areas of no adhesion*

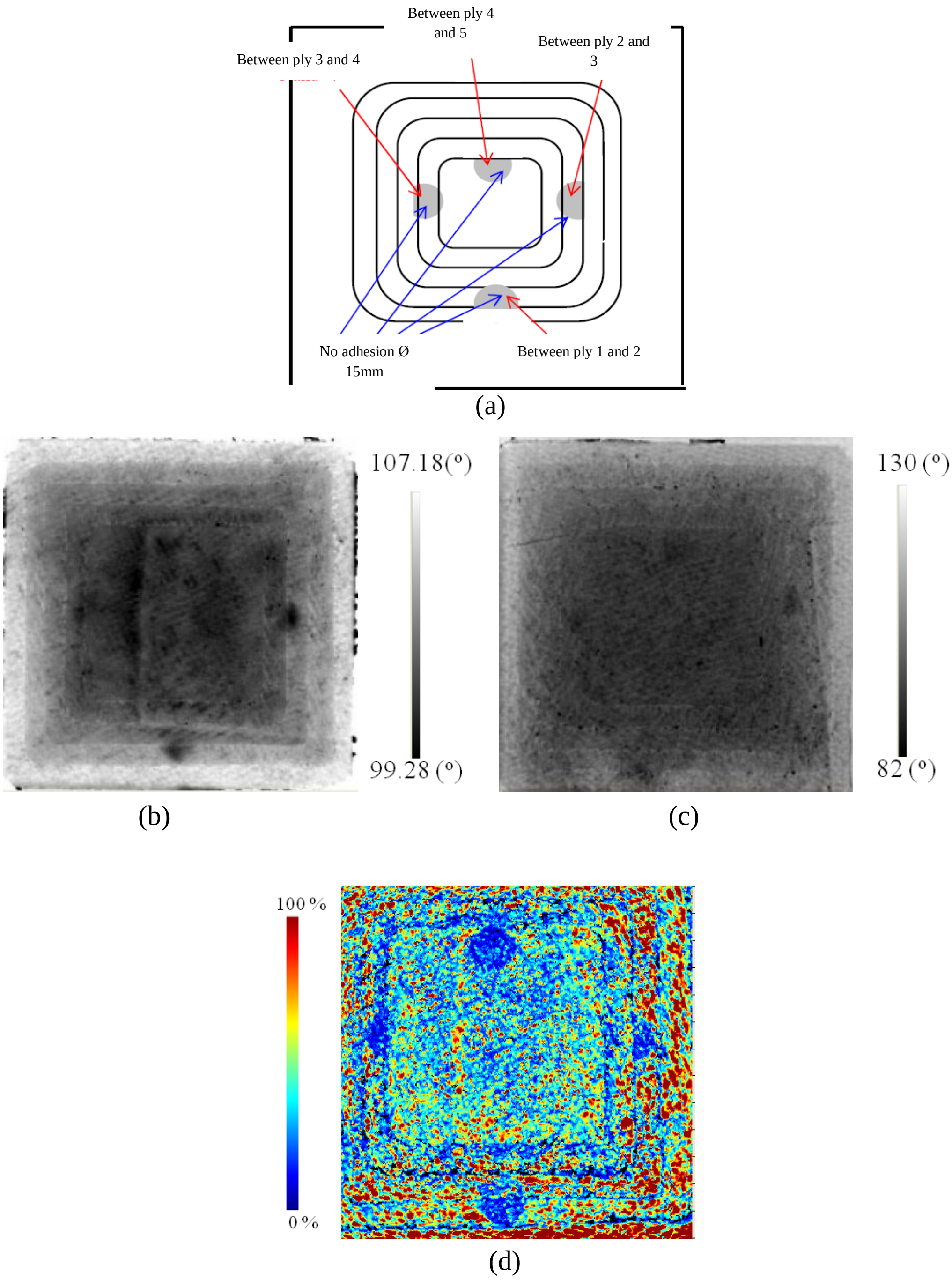

Figure 3.1.22 *Delamination between patch layers: (a) Coupon configuration. Phase images by lock-in thermography. (b) Al substrate, (c) Composite substrate, (d) C-scan image of the Al substrate repaired plate.*

Configuration 5: *triangular no adhesion area between substrate and first impregnated ply*

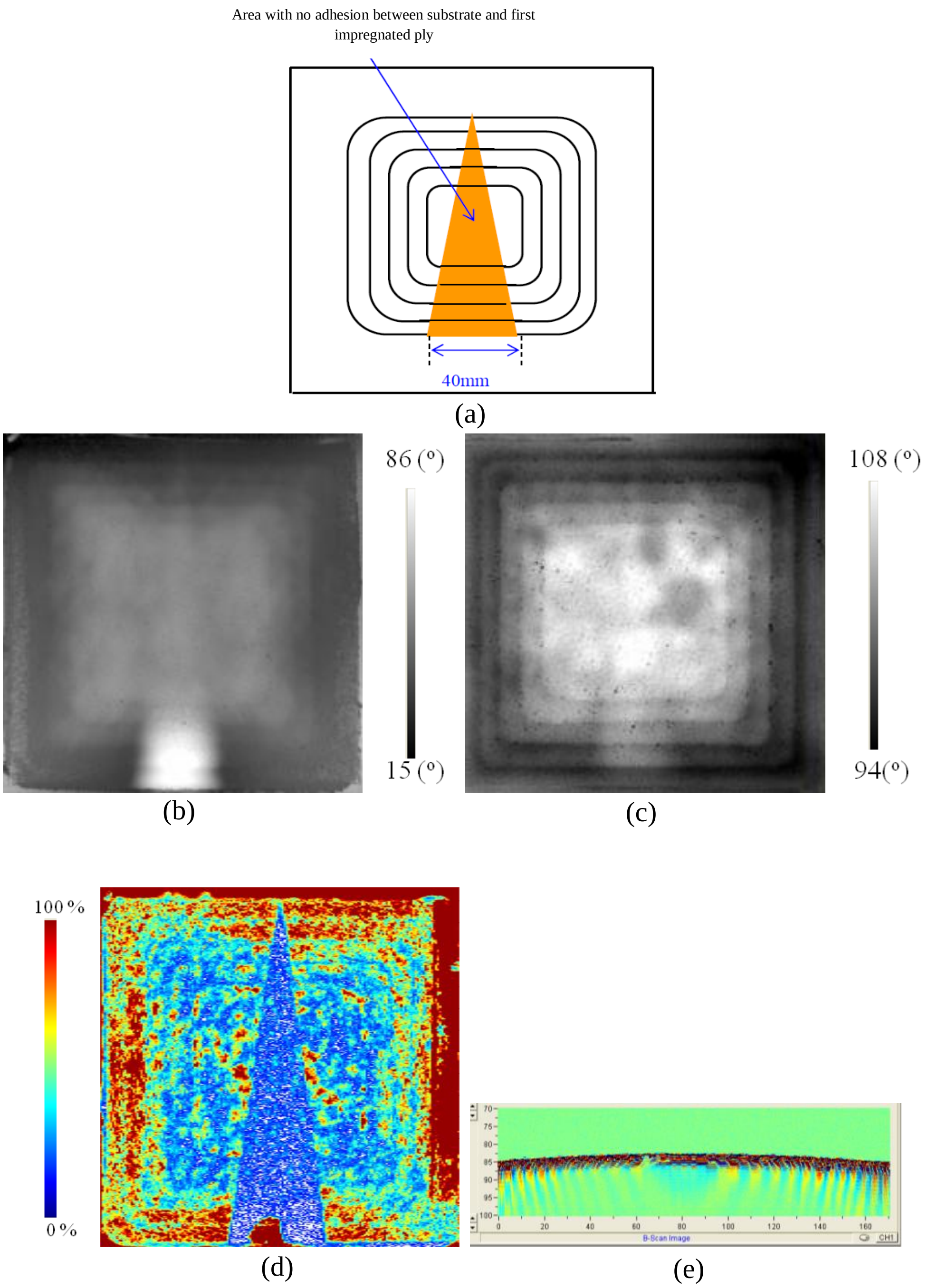

Figure 3.1.23 *Triangular debonding: (a) Coupon configuration. Phase images by lock-in thermography. (b) Al substrate, (c) Composite substrate, (d) C-scan image of the Al substrate repaired plate, (e) B-scan image of the Al substrate repaired plate.*

Configuration 6: *half interface of "bad" adhesion*

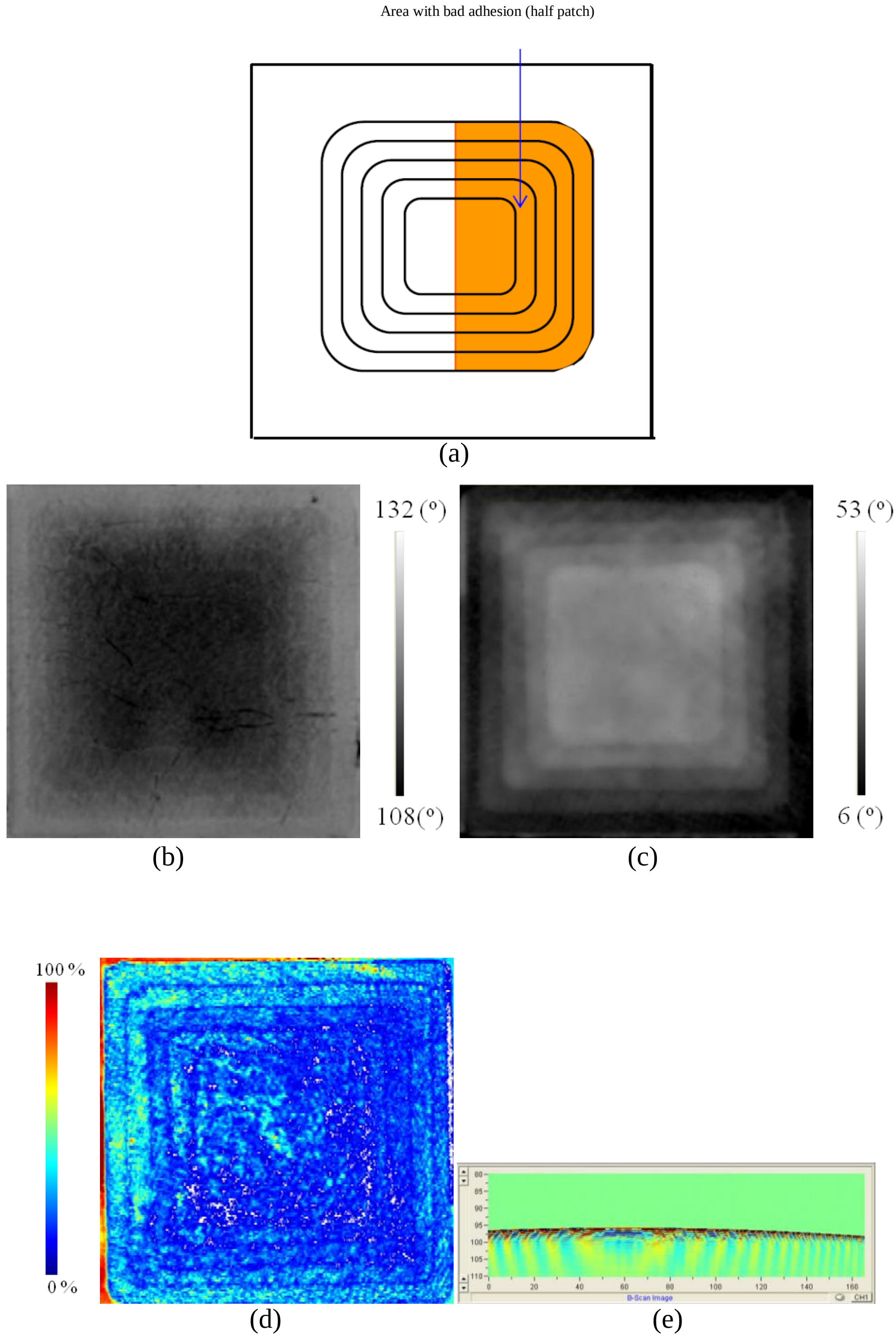

Figure 3.1.24 *50 % bad adhesion. (a) Coupon configuration. Phase images by lock-in thermography; (b) Al substrate, (c) Composite substrate, (d) C-scan image of the Al substrate repaired plate, (e) B-scan image of the Al substrate repaired plate.*

With respect to lock-in images, configurations which employed damage using PTFE tapes (Figs.3.1.20 to 3.1.23) were effectively revealed using LT and were verified throughout ultrasonics. However, concerning Al substrate plates, the identification of the Teflon flake in the case of centre damage (Fig.3.1.20) with ultrasonics, was not feasible. In this case, thermography proved more efficient. In addition, regarding Configuration 6 which included half interface of bad adhesion, no indication of damage was observed by both thermal and ultrasonic testing. This could be an indication that bad adhesion was not achieved, and possibly the whole patch /substrate interface remained intact or that the changes in both thermal diffusivity /acoustical impedance were negligible. As the b-scanning indicates (Figs.3.1.20e, 3.123e and 3.1.24e), it is obvious that thermal stresses induced a curvature in the interrogated plates. This effect posed an additional constraint on the identification capability of both methods. In the case of thermography, the focal distance of the camera was adjusted in a middle distance in order to detect all defects. In the case of c-scan, the focal distance between the transducer and plates could not accurately be set due to the curvature of the plate. In some cases better resolution was achieved by thermography than C-scan imaging. On the other hand, this is to the expense of lateral resolution, which in the case of ultrasonic inspection is better, as indicated by the b-scans. The above conclusion stems directly from the fact that IrT is a full field method compared to c-scan which is a scanning method. For *Case 3*, PTFE were more clearly identified in the case of aluminum substrate. Identical behavior was also noticed in *Case 2* patched aluminum strips (Fig.3.1.17c). This is again attributed to the differential thermal conductivity between substrate - patch – Teflon insert. In contrast, simulated Teflon defects in the case of composite substrate plates were not as detectable as in the case of Al substrates plates. It is noteworthy that the thickness of the Teflon defects was smaller than the other 2 cases (*Case 1 & 2*). In this scenario, the thickness of the tapes was equal to 50 μm. This additionally impeded the discerning capability of the inserted defects. Summarizing, all simulated defects were visible with LT, except for the last configuration (50% bad adhesion).

Section conclusions

The goal of the current section was to prove and benchmark the efficiency of Infrared Thermography as a NDE technique for off-line structural integrity evaluation of composite materials, as well as of bonded composite repaired materials. Initially, 2 different CFRP laminates were manufactured. Between the particular layers of the CFRP laminates artificial defects in the form of Teflon tapes simulated delaminations. In both laminates, various combinations in location and dimension were incorporated. Secondarily, bonded CFRP patches were applied on Al substrates for repair. In between the interface of the ‘parent material’ and the patch, PTFE tapes were inserted as a matter of damage initiators. Lastly, aluminum and composite plates were repaired with bonded composite patches. Six different configurations of damage were examined using Teflon tapes in various locations and dimensions. In addition, WD-40 was applied in the last configuration to simulate bad adhesion. Various thermographic techniques were employed for the inspection of the simulated damages. Pulsed, pulsed phase and lock-in thermography were successively employed for inspection. The observed results were in-between compared and evaluated. For verification and benchmarking of the observed thermographic data, ultrasonic C-scanning was performed.

In thermography, the value of thermal diffusivity always depends on the material characteristics of the constituted phases. In particular, the material and orientation of the reinforcement, as well as the matrix material, basically affect the thermal properties of the material. This difference is always noticeable and increases when “passing” from cross-ply laminates to unidirectional and then to composite repaired Al surfaces (Figs.3.1.17 a, b and c).

LT exhibited the optimum results in defect detection compared to PT and PPT. PT was not always successful in identifying artificial defects with low thickness and also the tapes at the patch edges in the case of the patch repaired Al strip.

Moving from PT to PPT and then to LT one may observe the following:

- increase of the detection capabilities of the method,
- deeper interrogation in the composite material with less energy,
- increase of the resolution of the method.

In all cases, simulated damage areas (Teflon tapes) exhibited higher temperatures than the defect free areas, due to a slower cooling rate in the vicinity of the particular defects. This statement was attributed to the difference in the material thermal diffusivity. Regarding *Case 3* materials, damage in aluminum substrate plates was more detectable than in the case of composite substrate plates. This was also encountered in *Case 2* scenario and attributed to the high difference in thermal conductivity. However, all inserted artificial defects in the form of Teflon were detected in both Al and composite substrate cases.

In addition, bad adhesion in Configuration 6 (using WD - 40) was not identified either by both thermography or by ultrasonics (Fig.3.1.24b, c & d). One possibility is that WD – 40 multipurpose oil did not lead to reduced adhesion and allowed for patch bonding. As indicated by the B-scan of the specimen (Fig.3.1.24e), “bad adhesion” does not inhibit the curvature of the plate induced by thermal stresses or in other words there is stress transfer between the substrate and the patch. In Configurations 2, 5 and 6 of *Case 3*, the cross-section of the interrogated plates exhibited a curvature attributed to the differential thermal expansion coefficient between the substrate and the patch. This curvature posed a secondary detectability impediment. This effect was not noticed in the case of composite substrate plates. Concerning the experimental part, it was not feasible to detect defects after prolonged heating, because this resulted in a uniform temperature on the whole surface of the material. The material in that case reached a steady state and no information was available. These demonstrate that off-line optical IrT possesses a large potential as a method for damage inspection in aircraft materials as it provides a wide field, non-contact NDE methodology that can easily be applied on site.

3.2 Structural integrity assessment of aerospace materials by implementing an electrical potential mapping method

3.2.1 Introduction

Most flaws and defects generated during the service life of a composite structural component primarily originate from Low-Velocity Impact (LVI) damage and secondarily from corrosion or bad manufacturing [225, 226]. LVI is usually invisible or barely visible to the naked eye. Although impact damage may leave a mark or spot on the surface of the damaged part, under most circumstances the surface of the damaged structure appears intact. It is found that low velocity impact mostly initiates delaminations [16]. The difference of the elastic properties in the laminae of a laminated plate reflect the impact induced waves causing out of plane strains which, in their turn, lead to delaminations. Thus, the inspection of impact damage is of primary importance for layered structures are by nature susceptible to this type of damage [16, 225]. Electrical potential or resistance mapping /tomography are a widely accepted techniques and fundamental to the assessment of geophysical parameters as well as in identifying underground water or landslides [151-155]. Recently, Karhuhen et al. used a tomographic concept to inspect damage in concrete structures [227] with very promising results. Baloch et al. developed an electrical resistance tomography system to inspect a solid object in a metallic vessel, filled with water [228]. When pertaining to aircrafts, the general idea is identical, however in a smaller scale. Electrical current is used in order to electrically stimulate the investigated material. In the presence of inherent damage, the electrical grid is changed, deformed etc. [123, 125, 139, 149, 150, 156-159]. Electrical potential mapping (EPM) technique does not require expensive external devices and, consequently, allows a fast and low-cost inspection [122, 133, 137, 140, 229-235]. Basic requirements of the method are simply i) an electrical current supplier and ii) a digital multimeter [148, 228, 232, 236-239]. Schueler et al. reported the pioneering work in damage inspection of CFRPs by means of electrical conductivity mapping [139]. Interesting studies have been documented by Angelidis et al. [149] who addressed damage using an electrical potential 2D mapping methodology and Todoroki et al. [240] who examined delaminations in CFRPs using the electrical resistance change technique. Recently, Baltopoulos et al. developed an electrical tomography methodology to inspect drilled damage and indentation in CFRPs. The observed results were compared with finite element models [159]. In Fig.3.2.1 a schematic configuration of the proposed methodology can be seen. It is a common LVI damage case which can occur during maintenance; a tool is unintentionally dropped from a mechanic. Appropriately positioned electrical contacts may be used in order to examine the electrical continuity of the damaged area, extracting an image representation of its structural inherent state. Changes in the electrical conductive path are indicative of damage beneath the surface.

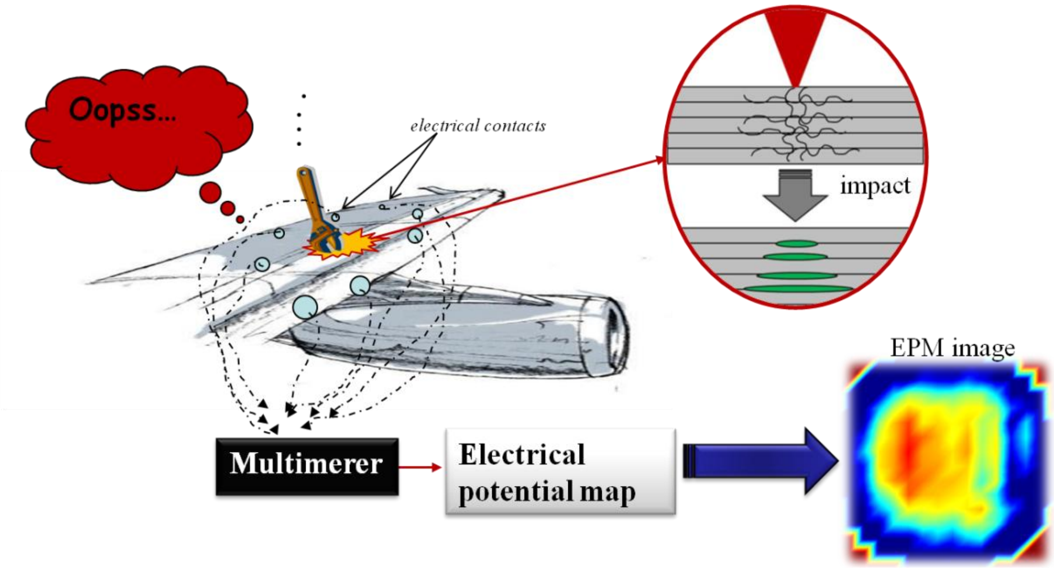

Figure 3.2.1 *Schematic representation of low velocity impact damage case; invisible impact damaged structure and electrical potential mapping inspection system.*

Within the scope of this section an electrical potential mapping technique (EPM) was developed in order to identify induced damage in aircraft materials. Rectangular CFRP plates subjected to low velocity impact damage as well as a plates with a circular notch, were examined using EPM. In the case of the impacted specimens, conventional c-scan imaging was employed in order to validate the results observed from the EPM system.

3.2.2 Experimental

3.2.2.1 Material

For the purposes of the current study, cross-ply CFRP laminates were manufactured in the laboratory using the hand lay-up technique. A unidirectional carbon fabric G0947 1040 by Hexcel (France) was employed for the reinforcement. The laminae orientation was (0,90,0,90,0) (Fig.3.2.2). For the matrix, the Araldite LY 5052/Aradur 5052 by Huntsman International LLC (Switzerland) was used. The employed curing cycle was 23 h at room temperature conditions followed by 4 h at 100 ^{0}C. The tested CFRPs were square laminates in dimensions 60x60x1mm^3 as is clearly shown in Fig.3.2.2. As aforementioned, i) a 5mm drilled hole [139, 159] and as well as ii) 3J and 5J impact damages [241] were the three investigated damage scenarios. The achieved fibre volume fraction was approximately 50%, measured with an optical microscope and image processing software.

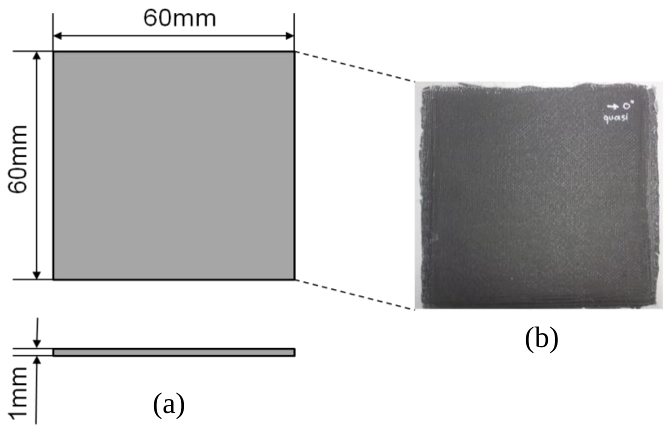

Figure 3.2.2 *(a) CFRP specimen configuration, (b) CFRP laminate.*

3.2.2.2 Artificial damage

The circular notch was drilled using a diamond drill in the centre of the specimen. The LVI was imposed using an Instron (CEAST 9340) drop-weight round impactor, as can be seen in Fig.3.2.3. For the material impaction, a 1.5mm diameter semi-spherical impactor was in all cases employed. Before the impact, the specimens were appropriately clamped on the testing machine. The performed impact energy levels did not lead to penetration of the employed composite laminates.

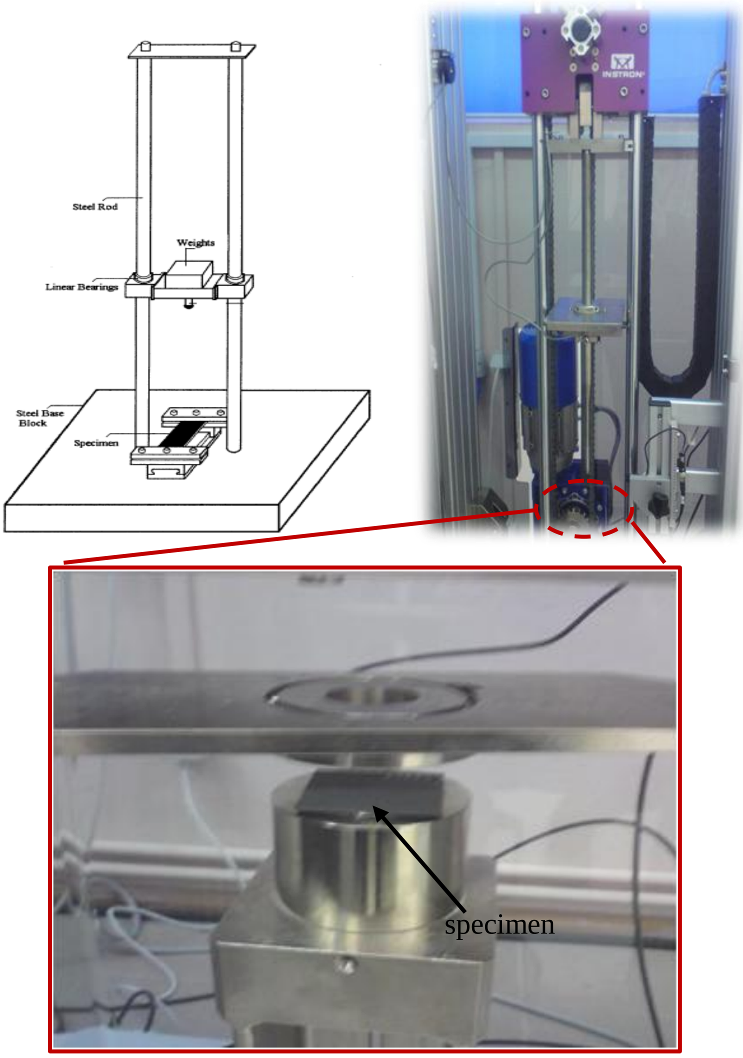

Figure 3.2.3 *Drop-weight impact setup configuration.*

3.2.2.3 EPM system implementation

For the purposes of the electrical potential mapping, two different measurement scenarios were developed. More specifically, a) surface mapping and b) through-thickness mapping were adopted. For the surface mapping 16 electrical copper contacts were manufactured onto the surface of the coupons (Fig.3.2.5a and Fig. 3.2.7b and 3.2.7e) via electrochemical platting. Akira Todoroki [242] reported a convenient copper plating method for manufacturing electrical contacts in CFRPs. The same approach was adopted for the purposes of the study. For copper plating, the employed electrochemical cell purposely made for this study is shown in the following picture (Fig.3.2.4).

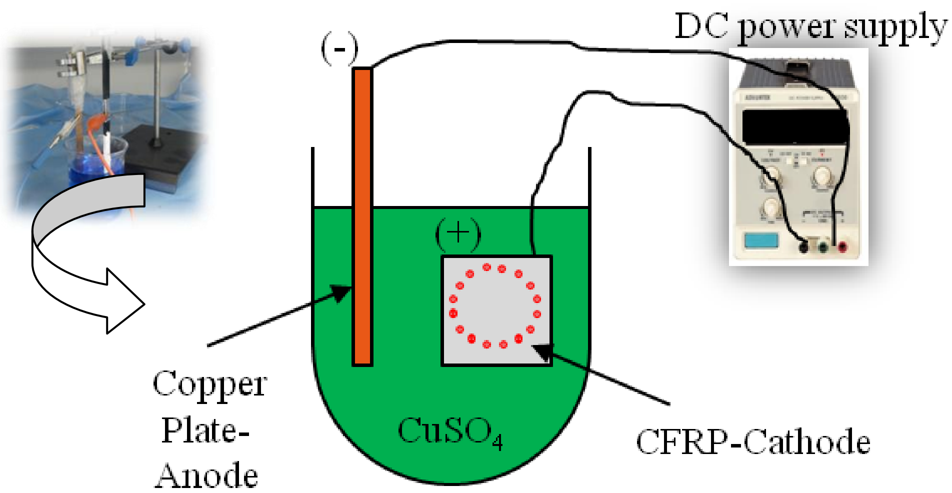

Figure 3.2.3 *Electrochemical cell for copper plating*.

As it is depicted in Fig.3.2.4, in the employed electrochemical cell, the copper plate is the anode and the CFRP specimen the cathode. This method allows for copper particle deposition on the exposed electrically conductive region of the surface of the CFRP coupon. In order to apply the contacts at the desired area, a commercially available polymer masking film (Sadipal) was adhered to the surface of the specimens. The masking film covered the whole material surface except from those areas where electrical contacts were about to deposit. The preparation sequence for the copper plating implementation is as follows:

1. Grinding with a 150 grit emery cloth of the electrode area
2. Cleaning with de-ionized water and acetone subsequently
3. Masking of the unpolished area
4. Removal of the matrix using concentrated sulfuric acid and hydrogen peroxide
5. Waiting for 30 sec or more in order to remove the whole matrix from the fibres
6. Cleaning with de-ionized water and acetone subsequently
7. In the case of remaining matrix on the surface, iteration of steps 4-6

As soon as the epoxy matrix was fully removed from the material surface, the specimen was immersed into the copper sulfate solution for copper plating. The electroplating parameters of the current work comprised 7,2A DC injection for 10min and additional 21,6A for another 10min. For the measurement protocol, appropriate electrodes were attached on the contacts. For the demonstration of the through-thickness scenario, 16 electrical contacts were manufactured on the cross-sectional region using a commercially available silver paint (RS-Components) (Fig.3.2.5a, 3.2.5c and 3.2.5d). In this case, silver paint was used instead of copper plating, to minimize contact resistance and provide a highly conductive interface with the material. Copper measurement wires were bonded on the silver painted regions using silver paste and directly connected with the multimeter and power supply cables (Fig.3.2.5c, 3.2.5d), respectively.

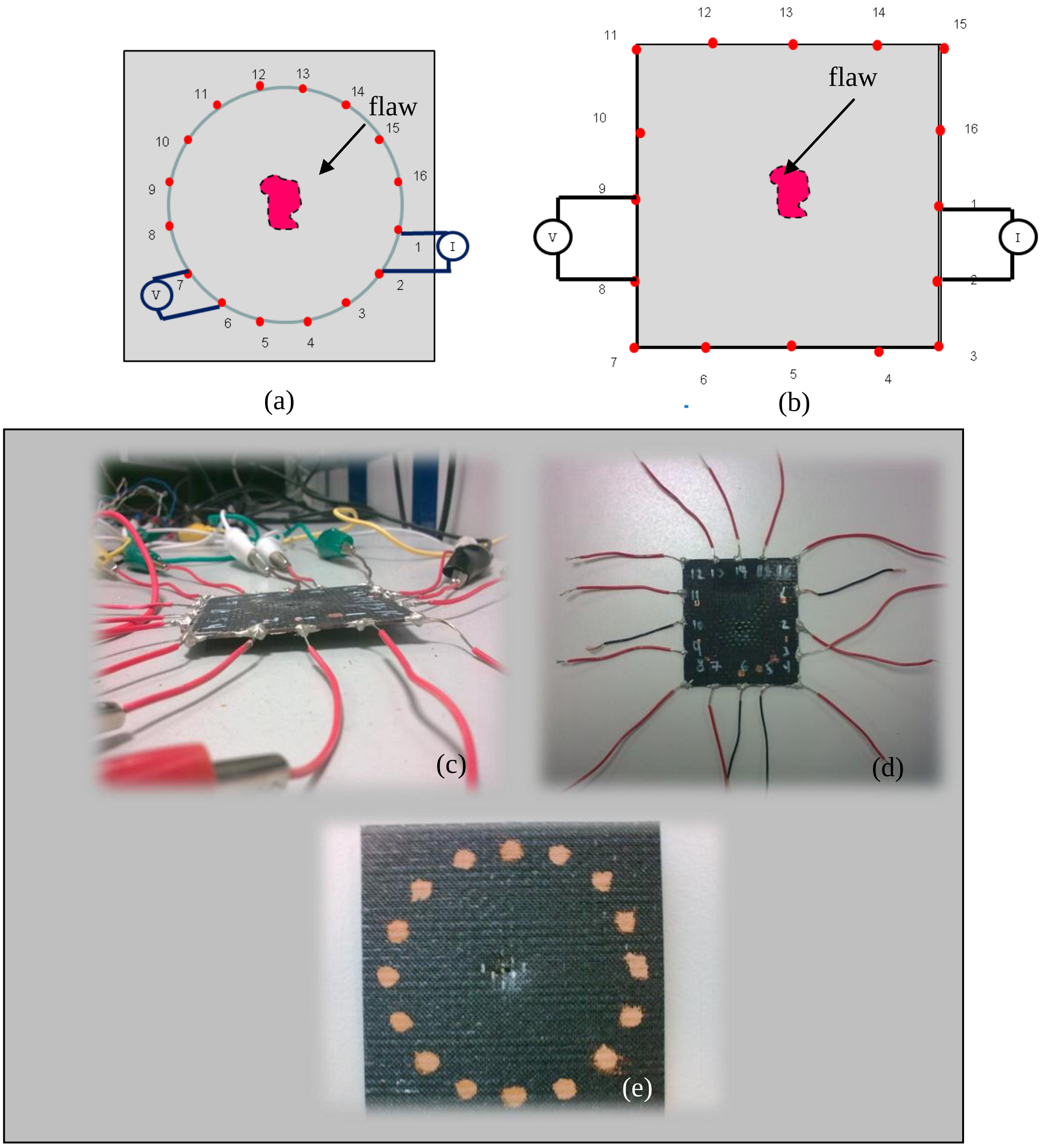

Figure 3.2.5 *(a, c, d) Bulk potential mapping, (b, e) Surface potential mapping.*

In Fig.3.2.5a and 3.2.5b the two different mapping scenarios are manifested. Figs.3.2.5a and 3.2.5e show the surface measurement scenario. In Fig.3.2.5e, copper contacts can be seen. Figs.3.2.5b, 3.2.5c and 3.2.5d depict the through-thickness (bulk) measurement approach with the measurement cables properly bonded on the cross-section surface.

The measurement strategy (Fig. 3.2.6), as described in [228], was adopted for all measurements. In Fig.3.2.6 a measurement cycle of one current injection pair can be seen. After the completion of the first cycle, the injection pair is moved to the next pair and continues until all the injection and measurement combinations are covered. More specifically, 16 available input combinations multiplied by 13 remaining electrode pairs give 208 total measurements.

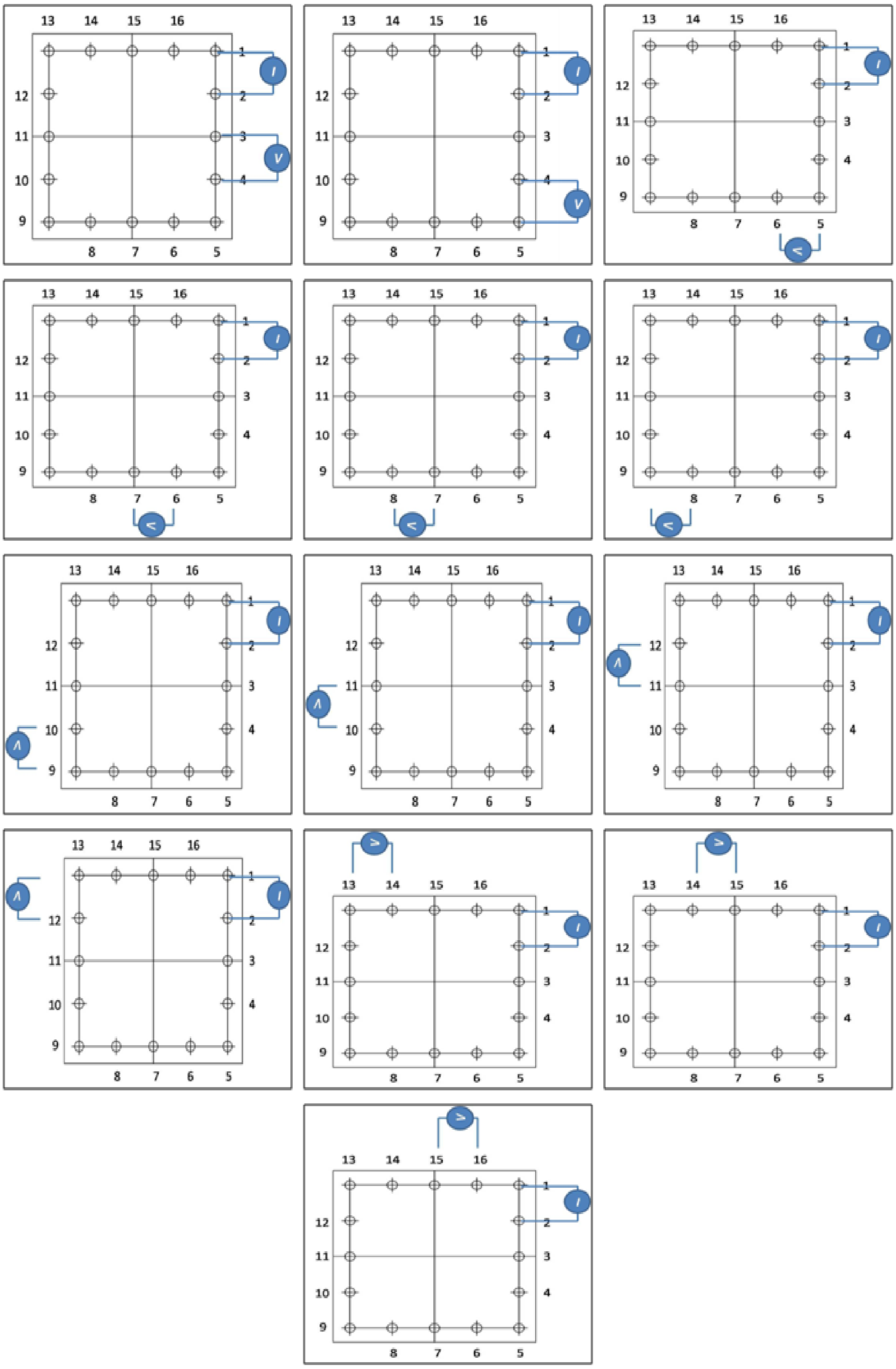

Figure 3.2.6 *Electrical potential mapping-one measurement cycle.*

In Fig. 3.2.7 the EPM experimental setup and the measurement protocol are depicted. 150mA DC current was injected through an electrical contact pair. The voltage between all the remaining electrical adjacent contact pairs was subsequently measured using the digital multimeter (Fig.3.2.7a). The same measurement sequence was followed by moving the pair of the injecting electrodes and measuring the voltage at all the respective remaining electrical contacts.

As it is shown in Figs.3.2.7 and 3.2.5e, the electrical contacts on the surface of the investigated coupons draw a circle which was segmented in separated cells. In specific, a square of 16x16 cells was formed in excel. Every cell represents an average of electrical potential measurements. Further on, the two lines which connect the input and output pair of electrodes in the grid representation define the cells that will be include in the average of each cell (Fig.3.2.7b); According to the employed protocol, when more than 1/3 of the cell is included in between the lines (Fig.3.2.7b), then this cell is included in the total average measurements.

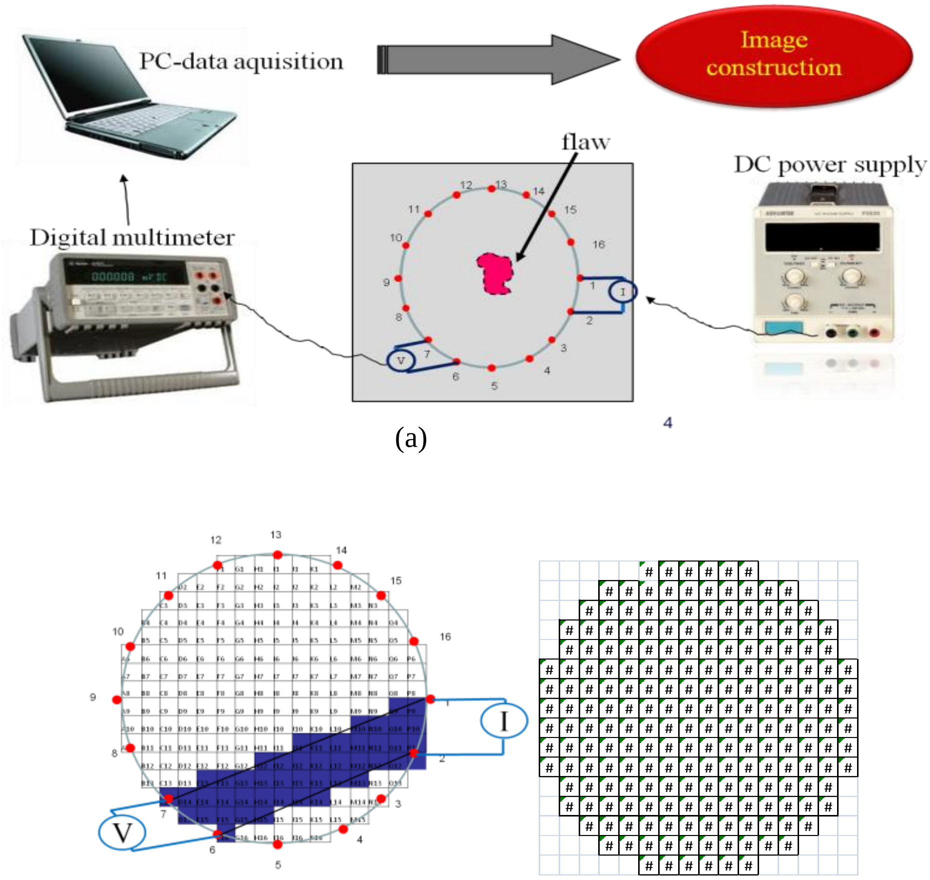

(a)

(b) (c)

Figure 3.2.7 *Mapping protocol EPM surface measurement (a) experimental setup, (b, c) EPM*

A simple algorithm was built in a typical worksheet environment for data acquisition and manipulation. After data processing, image reconstruction was performed in MatLab® environment via a purposely made matrix.

3.2.3 Results and discussion

Figs.3.2.8-10 depict in sequence the optical, C-scan and EPM images of the investigated specimens. As aforementioned, the impact energy levels employed for LVI did not lead to penetration. In some case (Fig. 3.2.8a), the impactor induced visual damage on the specimen surface. Initial surface and through-thickness electrical resistance values were measured with the two probe method [124]. In both cases, the measured resistance values prior to impact were in the order of 1 Ohm. After impact induced damage, through-thickness electrical resistance values did not change significantly compared to the surface. Post impact surface electrical resistance was unaffected away from the impacted area and presented higher values when "moving" towards the central area where impact had induced delaminations.

Fig.3.2.8a shows the picture of the impacted plate against the employed NDE methods for the 3J impact, which indicates that the damage is visible in the form of a semispherical dent at the impact site. As can be seen in Fig.3.2.8b, the induced damage by the round impactor is within the resolving power of the C–scan image. Fig.3.2.8c shows the EPM image acquired by the surface measurement protocol while Fig.3.2.8d the one extracted via the through-thickness potential mapping. The exhibited color differentiation on the images indicates that both surface and bulk measurements identify damage in the centre of the specimen. However, in the surface case image, these color variations are found to be symmetrically around the centre of the specimen, where impact damage is present.

In Fig.3.2.9a an optical snapshot of the 5J LVI damaged specimen is presented. In this case, damage is barely or invisible to the naked eye. Fig.3.2.9b shows the caused impact damage through an amplitude C-scan image. Figs.3.2.9c and 3.2.9d show the EPM images for the surface and through-thickness measurements respectively. Concerning the EPM image, the deterioration of the material is expected to be identified in the centre based on the ultrasonic testing. The surface-EPM snapshot indicates a variation in the centre whereas the bulk-EPM imaging implies a similar response with a slight deviation from the centre. Comparing EPM images of specimens damaged with 3J and 5J impact energy, it could be reported that a more uniform damaged area is observed in the 5J impact case. This could be attributed to the higher applied energy. In both EPM images (Fig.3.2.8c and 3.2.9d), the differentiation on the images reflects the presence of induced damage i.e. delamination around the impaction point.

Fig.3.2.10 depicts the damaged material with the 5mm drilled hole. In this case C-scan testing was not necessary. In Fig.3.2.10b the differentiation in color in the centre of the image represents the presence of the artificially induced drilled hole in the centre of the specimen. Bulk EPM measurement protocol (Fig.3.2.10c) was not as informative as the surface case.

It is evident that in all cases the surface EPM image identifies a difference on surface potential values. The top reinforcement layer governs the electrical potential measurements when estimating the surface electrical potential values. In other words, the direction of the surface carbon fibres complicates damage identification, increasing the uncertainty of the method. It is likely that the trough-thickness measurements are not affected by the surface material conditions i.e. carbon fibre orientation. For that reason images in Fig.3.2.8d and 3.2.9d and Fig.3.2.10c are less indicative of damage compared with EPM images of Fig.3.2.8c and 3.2.9c and Fig.3.2.10b.

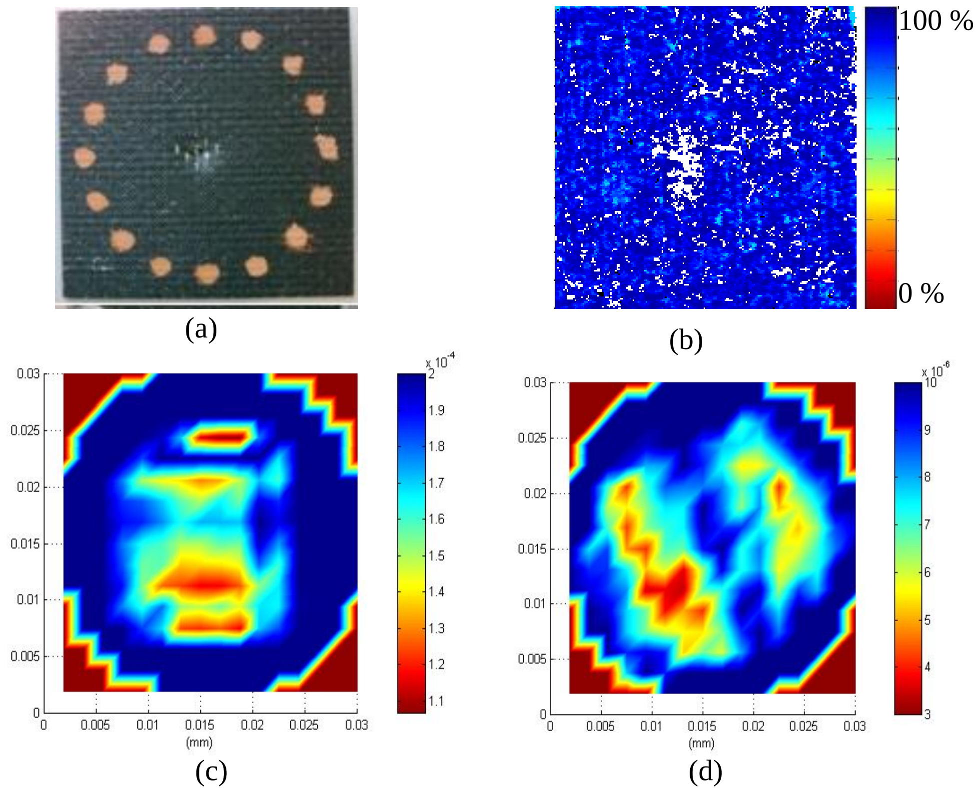

Figure 3.2.8 *(a) Cross-ply CFRP-3J LVI, (b) C-scan (c) Surface EPM, (d) Through-thickness EPM.*

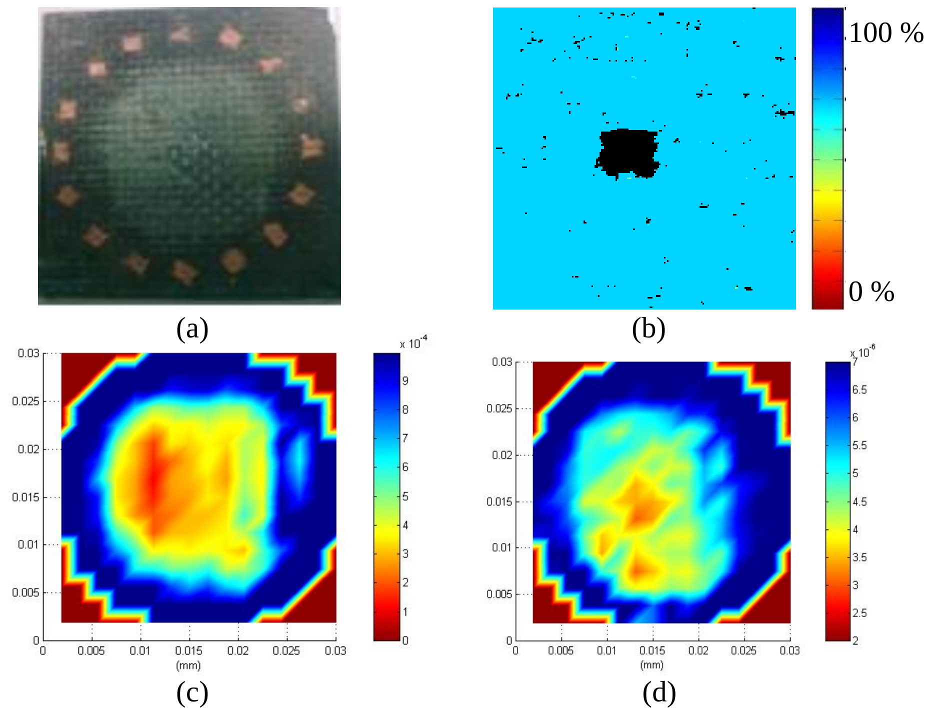

Figure 3.2.9 *(a) Cross-ply CFRP-5J LVI, (b) C-scan (c) Surface EPM, (d) Through-thickness EPM.*

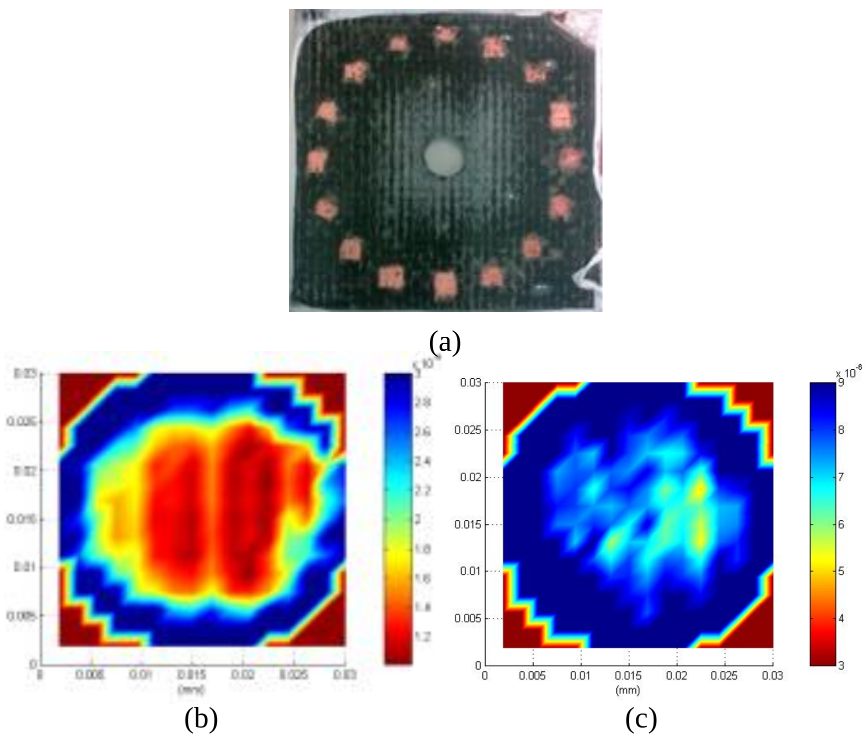

Figure 3.2.10 *(a) Cross-ply CFRP-5mm drilled hole, (b) Surface EPM, (c) Through-thickness EPM.*

It is noteworthy to say that the orientation of the top layer of the composite plate may govern surface electrical conduction. When electrical current is injected through a material, it ‘prefers’ to pass through the path which possesses the lower electrical resistance value. In the case of a single unidirectional layer or surface measurement of a composite, the direction of the carbon fibres reinforcement possesses the highest electrical conductivity. As aforementioned and is also shown by the schematic below (Fig.3.2.11), current conduction is realized via the primary reinforcement as well as the random contacts of the reinforcement phase. Electrical resistance is increased at the loci of internal damage. Through-thickness and transverse electrical conductivity always possess lower values than the longitudinal conductivity or that of the reinforcement. However, through-thickness electrical resistance values do not change significantly in the presence of internal damage i.e. impact, and thus damage inspection is inhibited. For that reason, the through-thickness was not as informative as the surface one. Fig.3.2.11 shows a schematic representation of the electrical behavior of a CFRP. Every fibre-layer can be represented by an array of electrical resistances.

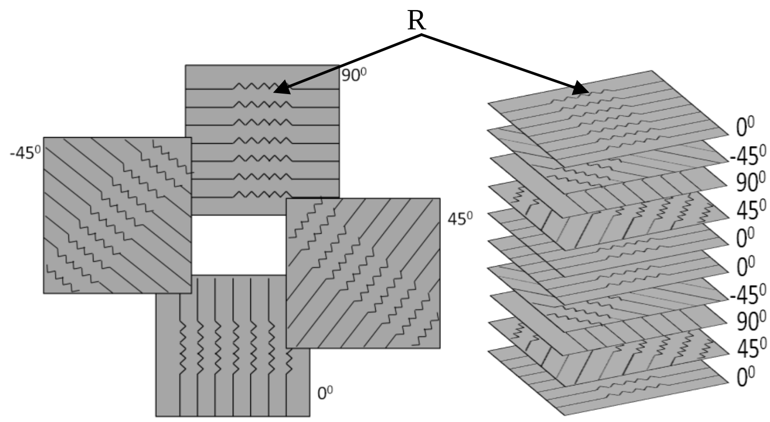

Figure 3.2.11 *Schematic representation of the CFRP electrical behavior.*

Section conclusions

The scope of the work described in this section was to develop an electrical potential mapping (EPM) system with a view to identifying induced damage in composite laminates. Preliminary results on this task proved the ability of the technique to identify induced damage. For the purposes of the study, rectangle-shaped CFRPs were manufactured. A 5mm drilled open hole, 3J and 5J impact damages were the three interrogated types of damage. With respect to the EPM system, both surface and through-thickness measurement scenarios were performed. In the surface case scenario, 16 electrically conductive contacts were electrochemically plated onto the surface of the employed coupons. Subsequently, purposely designed electrodes were attached on the surface of the specimens connected with the cables of the multimeter and power supply. In the through-thickness scenario, flexible cables were directly bonded on the cross-section of the coupons. The attached cables provided connection with the measurement and power supply devices, respectively. The adjacent strategy was employed for all measurements. 150mA direct current was injected through a pair of electrodes and the electrical potential was measured between the remaining contacts. This process was repeated for all the remaining electrode pairs. Employing an averaging protocol, the interrogated area was separated with a grid and via an averaging process a distinct value of potential was attributed to each individual cell. The measured data were imported in Matlab environment for the image reconstruction. The employed damages were identified and compared to each other. The local variation of the calculated potential values is expected to be directly linked to the presence of delaminations imposed by the low velocity impact.

In the case of LVI damage, the surface-EPM snapshots indicated a color variation in the centre whereas the bulk-EPM imaging exhibited a similar response with a slight deviation from the centre. Comparing EPM images of specimens damaged with 3J and 5J impact energy, it can be postulated that a more uniform damaged area is observed in the 5J impact case. This could be attributed to the higher applied impact energy. In both EPM images, the differentiation on the images reflects the presence of induced damage i.e. delamination around the impaction point. In the case of the 5mm drilled hole C-scan testing was not necessary. In this damage concept, differentiation in color in the centre of the image represented the presence of the artificially induced drilled hole in the centre of the specimen. Bulk EPM measurement protocol was not as informative as the surface case as it exhibited a less affected by the damage area.

Summarizing the above, the implementation of the EPM technique proved promising in identified induced damage in composite laminates. The preliminary experimental results provided a strong motivation to further investigate the capabilities of the potential of the technique. The implementation of the proposed electrically-based methodology is still in progress and under investigation. An automated system has already designed for the automatic measurement of electrical potential values. This will allow for the system integration in structural components and even on line monitoring provided that, as a rule of thumb, the data acquisition frequency is more than one order of magnitude more than the loading frequency.

Acknowledgements

The author would like to thank Prof. Stefanos Zaoutsos for providing the impact damage facilities located at the Dept. of Mechanical Engineering of the Technological Educational Institute of Larissa, Greece.

3.3 Current injection phase thermography for low-velocity impact damage identification

3.3.1 Introduction

As highlighted in the previous section, LVI damage provides a challenging field for the application of a variety of non-destructive evaluation methods [85, 243-245]. Of the many non-destructive techniques, Infrared Thermography (IrT) has proved its efficiency in defect identification and material characterization processes[244]. A major technical difficulty (see also Section 3.1) with optical thermography is the uniform thermal excitation of the investigated structure in order to effectually pinpoint any present flaws [60, 62, 71, 73, 246]. Fundamental to a thermal stimulation protocol is the uniform excitation of the monitored surface for optimal detection of the emitted thermal waves with the concurrent minimisation of the thermal energy input. Non-uniform thermal excitation impedes damage inspection. Large thermal energy input is energy consuming and overheating may degrade the primary structure (particularly in the case of CFRP, where the composite matrix temperature should be relatively low). In the case of periodic thermal loading, the energy input should allow for uniform heating of the monitored component. At the same time a steady temperature state (compared to the excitation period) is not desirable, as the technique is based on the transient temperature profile monitoring.

An interesting approach to thermal stimulation is the exploitation of the conductive nature of CFRPs in order to use them as Joule heating elements. As analyzed in chapter 2 and Section 3.2, the electrical properties of composite materials and particularly of graphite /epoxy laminates have been widely studied for structural health monitoring or else real-time structural integrity assessment [123, 124, 126, 247]. Apart from the structural monitoring, the electrical properties of the carbon fibres have been exploited for curing carbon /epoxy materials [160]. Joule heating has been employed for curing composite panels [161, 162] and for removing the ice from the skin of aircrafts [163]. In addition, it is now well established that the electrical properties may be improved through the incorporation of secondary conductive phases in the insulating matrix i.e. Carbon Nanotubes (CNTs) in the epoxy matrix of the laminate [141, 234, 248, 249]. When electrical current is injected through a bulk material it passes, through the path which possesses the lower electrical resistance value [124]. Current conduction is realized via (i) the primary reinforcement i.e. the carbon fibres (ii) via the secondary reinforcement i.e. the CNTs and (iii) via the random contacts of the reinforcing phases. These random contacts are loci of increased electrical resistance and therefore nuclei of heat generation. More random contacts result to a more uniform heat generation in the volume of the material [176]. As a result, the inclusion of CNTs results to a more uniform heating front on the laminate, as current traverses the laminate. A carbon fabric layer may be represented as an array of electrical resistances (Figs.3.3.1a and 3.3.1b).

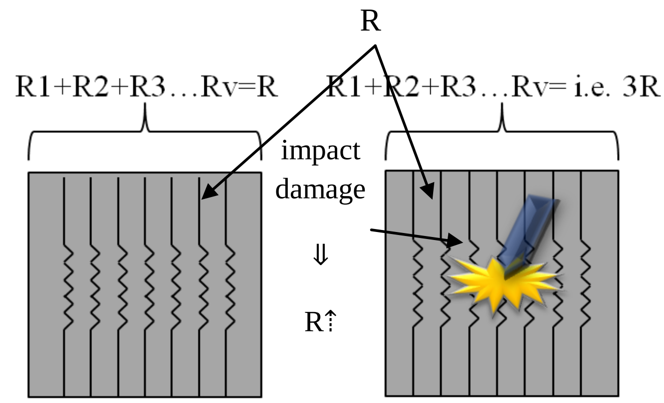

(a)

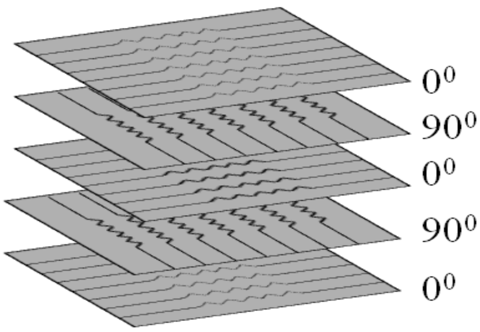

(b)

Figure 3.3.1 *Mechanical models of Carbon fibre fabrics; array of electrical resistances: (a) carbon fibre layers; intact case (1) and damaged case (2), (b) lay-up of a cross-ply CFRP laminate.*

The presence of any flaw, discontinuity or delamination reduces locally the electrical conductivity or even results to loss of electrical continuity. In this case, there is a preferential path of the electrical current via the route of maximum conductance. At the same time, as the electrical resistance at the damaged areas reaches high values, the joule effect should cause a temperature increase around the damaged region. This may be verified simply by assuming two cases of carbon fibre laminae: (i) a lamina with electrical resistance of $R_1 = R$ consisting of the resistances of the individual carbon fibres laid in parallel and (ii) a second mechanically damaged layer with resistance (increased due to mechanical deformation or obstruction of the electrical path) $R_2 = n*R$ (n>1). By employing the 1st law of thermodynamics, the Ohm's and Joule's law the following considerations are obtained:

$$P = \frac{Q+W}{t} \qquad (3.3.1)$$

where P is the power (W), Q is the heat (J), t is the time (sec) and W (J) the work. In the case of electrical current injection through a material, the differentiation in the volume is negligible (*ΔV=0*) and thus the work is zero. In that sense, the power is:

$$P = \frac{Q}{t} \qquad (3.3.2)$$

The Joule generated heat is given by:

$$Q = I^2Rt \qquad (3.3.3)$$

where I is the electrical current (A), and R the electrical resistance (Ω).

From Eq.3 for the two particular cases:

$$P_1 = I^2R_1 \qquad (3.3.4)$$

$$P_2 = I^2R_2 \qquad (3.3.5)$$

By dividing Eqs.3.3.4 and 3.3.5 for given electrical current I and time t we obtain the following:

$$P_1 = \frac{1}{n}P_2 \text{ or } P_2 = nP_1\text{, n>1} \qquad (3.3.6)$$

From Eq.3.3.6 it is obvious that higher material electrical resistance results in higher power throughput and consecutively higher Joule heating. However, in the absence of electrical continuity there is no power throughput, In that case the "damaged" area is expected to remain cooler than the surrounding material. This temperature variation in the presence of a flaw is the "key point" of the proposed technique. The differentiation in temperature can be detected via the use of a thermal infrared camera. The novelty of the method lies on the fact that the local material properties will define the electrical current path and reveal the internal damage.

Considering electrical current injection, it is clear that appropriate electrical contacts are necessary in order to homogeneously distribute the current through the whole cross section of the bulk material. The minimization of contact resistance is indispensable in order to avoid Joule effects in the electrode/ material interface. These would inhibit the observation of damage induced temperature fluctuations. High contact electrical resistance results to a non-uniform thermal stimulation (hot edges - cooler central area) which may lead to unstable temperature gradients as well as catastrophic degradation of the epoxy matrix material due to overheating.

As should be added at this point, it is expected theoretically and shown experimentally [250] that for most materials including CFRPs, the temperature increase results to a proportional change of the electrical resistance of the inspected material. However, carbon fibres, possess a positive coefficient of thermal expansion (CTE) in the transverse axis and negative in the longitudinal, whereas typical epoxy matrices possess a positive CTE [251, 252]. This complicates the thermoelastic behavior of the composite. In general, temperature increase results to an electrical resistance increment (Eq.3.3.7):

$$R = R_0(1 + a(T - T_0)) \quad (3.3.7)$$

where R is the electrical resistance (Ω), R_0 the electrical resistance at room temperature conditions, (T_0 =20 ^{0}C), a the CTE (10^{-6} /^{0}C for carbon fibre) and T the temperature (^{0}C). Takahashi et al [253] examined the dependency of the electrical resistance of a graphite /epoxy polymer on temperature. They reported a 0.3% decrease in electrical resistance value in the reinforcement direction when the temperature increased from room conditions up to 60 ^{0}C. Concluding, typically the temperature increase is antagonistic to damage along the fibre direction. However, the resulting change in the electrical resistance is negligible compared to the local resistance change due to damage.

Within the scope of this section, a novel thermal stimulation technique is developed. For this purpose, rectangular CFRP quasi isotropic plates were subjected to LVI. Two different energy levels were employed for LVI in order to assess the ability of the method to identify various defect sizes. Modulated electrical current was injected through the composite specimens in order to impose the necessary thermal gradient around the damaged area which was monitored using PPT. The anisotropic electrical conductivity and thermal diffusivity of the composite laminate makes the damage identification and quantification with PPT a challenging and demanding task. Within the framework of the present study, heat excitation was provided by a square electric pulse injected in the bulk of the laminate with low frequency and thermal stimulation was achieved via the Joule effect. LVI induced damage was successfully identified for two impact energy levels and compared with typical optical IR stimulated PPT imaging, as well as traditional ultrasonic imaging (C-scan).

3.3.2 Experimental

3.3.2.1 Materials

For the purposes of the study, $(0, 90)_{2s}$ six-layer cross-ply rectangular CFRP plates were fabricated using the hand lay-up method. Both plain and Carbon Nanotubes (CNTs) enhanced CFRPs were employed. The unidirectional carbon fabric 43280 (160 gr /m^2) by Hexcel (France) was employed as reinforcement and the Epocast 52 A/B epoxy system by Huntsman International LLC (Switzerland) as matrix. For the CNT enhanced laminates, 0.5% w/w CNTs were added in the epoxy matrix. Dispersion of the CNTs in the epoxy matrix was performed via sonication for 2 h using the ultrasonic processor UP400S (400 W, 24 kHz) by Hielscher at 50% amplitude. This dispersion protocol was found to yield optimal fracture toughness properties for 0.5% w/w CNT/matrix ratio [254]. Lamination was performed using wet hand lay-up. The curing cycle was 2 h in an oven under vacuum conditions (-700 mbar) at 95 ^{0}C. The final fibre volume fraction was approximately 50%, as measured by an optical microscope and image processing software for both laminates.

Square coupons of 60x60x1mm^3 dimensions were cut from the manufactured laminates (Fig.3.3.2a, 3.3.2b). Contact resistance was of prior importance [124], so special care was taken for the realisation of appropriate electrical contacts for the current injection. The edges where current would be injected were slightly ground with a 150 grit emery cloth in order to locally remove the epoxy matrix from the material surface. Then the material was thoroughly cleaned, first with deionised water and subsequently with acetone. The specimens were left to dry in an oven at 50 ^{0}C for 4 h in order to remove any moisture. Silver paint (Fig.3.3.2c and 3.3.2d) was applied on the abraded cross sections in order to eliminate electrical contact resistance (Fig.3.3.2c-3.3.2f). The electrodes for the current injection were connected with the cross section of the coupons using silver loaded adhesive tape (Fig.3.3.2e and 3.3.2f). Further minimization of the contact resistances was achieved by applying 80 bar pressure on the specimen injection edges, a process that increased the contact area between the tape and the specimen and consequently decreased the contact resistance [3, 255]. Experimental trials indicated that a maximum value of 1 Ω through-thickness resistance was sufficient as a threshold for efficient current injection, in order to avoid overheating at the electrode contact area. The initial through-thickness resistance measured at the edges of the coupon via the 2-probe method was approximately 2 Ω. After the pressure application, the resistance dropped to less than 1 Ω for both plain and CNT modified matrix specimens.

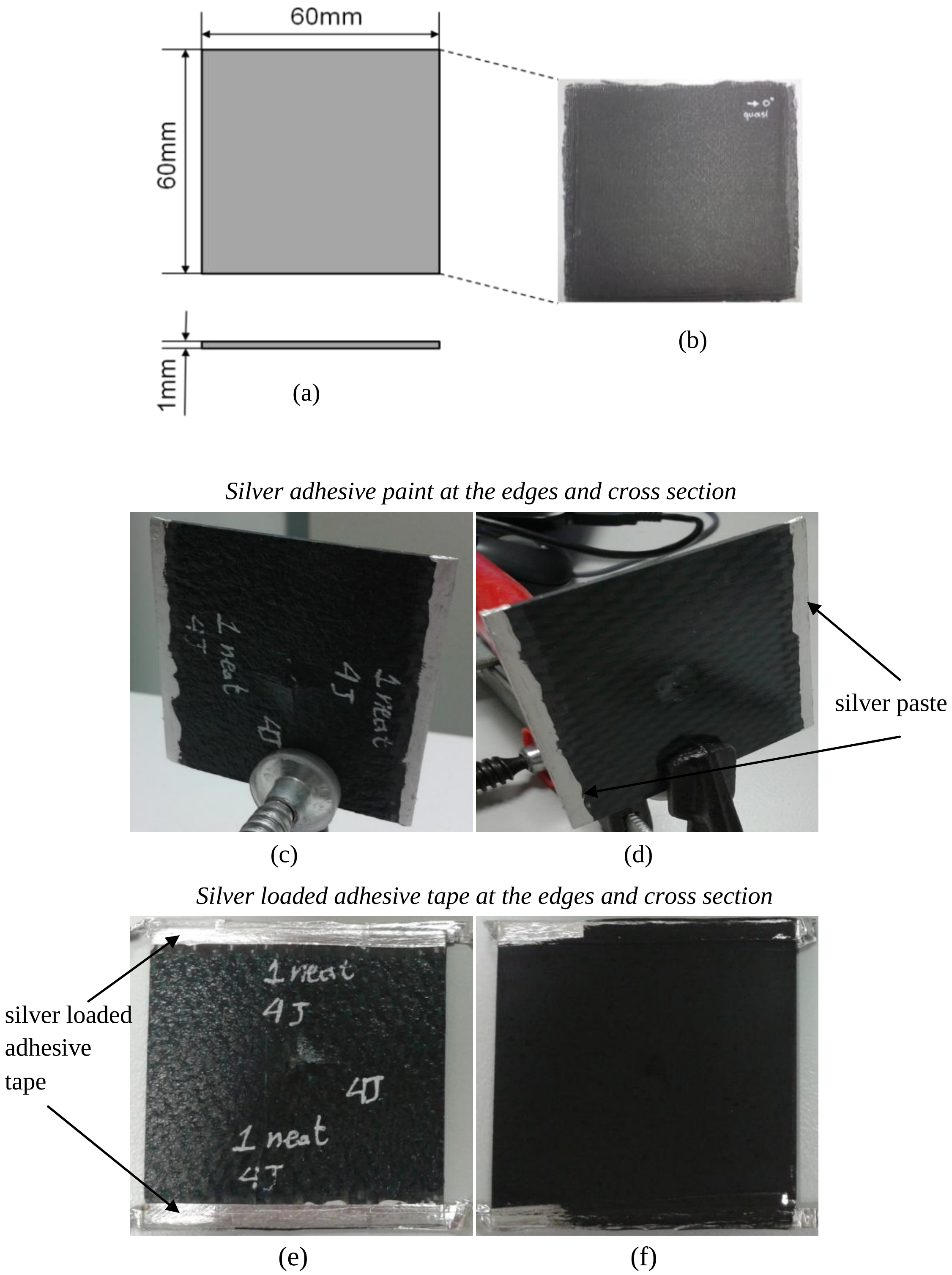

Figure 3.3.2 *(a) CFRP specimen configuration, (b) CFRP laminate (c-f) snapshot during specimen preparation.*

3.3.2.2 Impact damage

The LVI damage was induced using the CEAST 9340 drop-weight tower by Instron. A 1.5mm diameter semi-spherical impactor was employed. For impact testing, the specimens were appropriately clamped on the testing machine. The specimens were subjected to 3J and 4J impact energy. The employed impact energy levels were low enough in order to avoid penetration in all cases.

3.3.2.3 Non-destructive evaluation methodology

With respect to the thermal camera, the same model with section 3.1 was used. A 50 Hz frame rate was selected for the present study. In order to render the emissivity (ε) of the specimen surface close to that of the black body (ε=1, for optimal recording of the thermographic signals), the monitored surface was painted with a black mat paint (ε=0.97).

The camera was employed in both live and pulsed phase mode. The experimental setup which was developed in order to perform the novel current injection thermographic technique is shown schematically in Figs.3.3.3 and 3.3.4. As current flows through the material, Joule heating flows from the edges (current injection locations) towards the centre (cooler locations).

For the live mode, 10A electrical current were injected to the specimens for 60 sec via the DC power supply and then the materials were left to cool down in air for another 150 sec. The current injection was interrupted at approximately 60 ^{0}C maximum temperature. As was observed, after that temperature, the material reached steady temperature state throughout its surface and as a result, in the absence of temperature gradients, no internal features could be discerned. Under all circumstances, heating of the material in temperature higher than 80 ^{0}C was avoided, as it could affect the properties of the epoxy matrix.

For the pulse phase mode, the camera was connected with a pulse generator through a lock-in amplifier. As can be seen in Fig.3.3.4, the signal of the pulse generator was amplified through a DC amplifier. The infrared camera was positioned at appropriate distance of the coupon at approximately 30 cm. This distance corresponded to resolution of 0.18004 mm /pixel. Amplitude and phase images were available during the thermal excitation of the CFRP materials. In this case, a square current pulse of fixed amplitude was injected for a fixed period of time in the specimens. In this case, various attempts were performed in order to assess the optimum electrical current input that would steadily heat the materials with simultaneous minimisation of the required energy input. Finally, an amplitude of 200mA (0.5 V electrical voltage) for 50 seconds was chosen as excitation so as to uniformly induce thermal waves upon the specimens. As should be noted, the PPT current injection configuration was successful in identifying LVI damage with considerably less current amplitude.

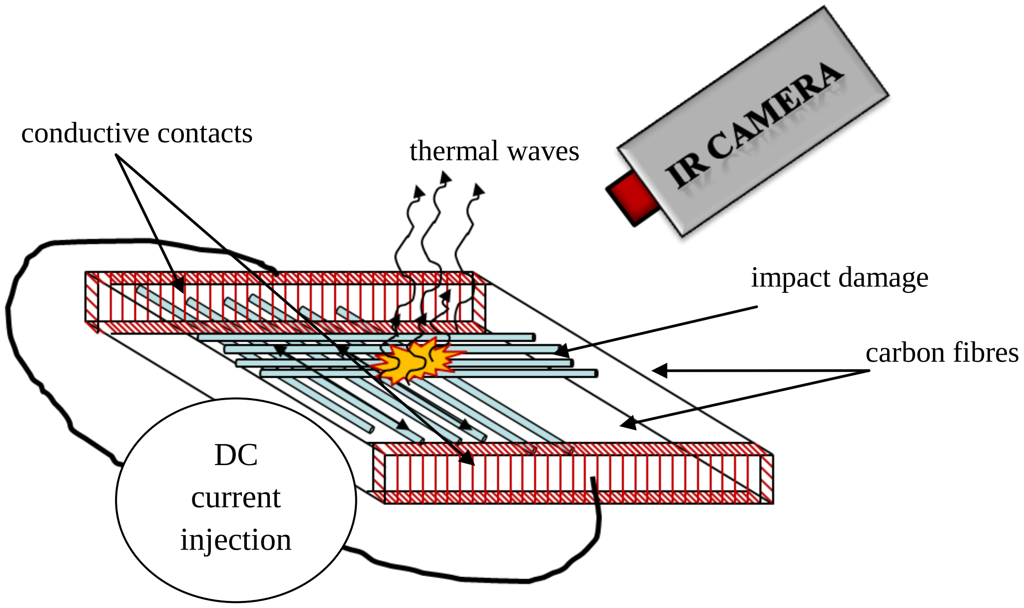

Figure 3.3.3 *Current injection experimental setup configuration.*

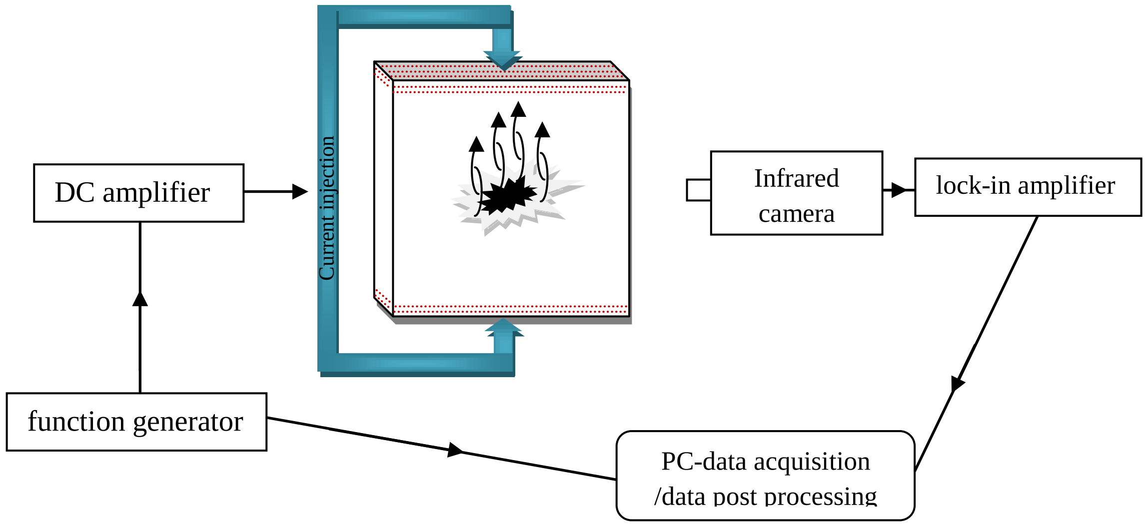

Figure 3.3.4 *Outline of the experimental setup.*

In order to render the emissivity (ε) of the specimen surface close to that of the black body (ε=1, for optimal recording of the thermographic signals), the monitored surface was painted with a black mat paint (ε=0.97).

3.3.3 Results and discussion

As aforementioned, both plain and CNT modified materials were subjected to 3J and 4J impact damage. The recorded force vs. time curves are depicted in Figs.3.3.5a, 3.3.5b, 3.3.5c and 3.3.5d. The evaluation of the impact performance of the laminates is not within the scope of this study, although the presence of the CNTs is expected to enhance the interlaminar, fatigue and impact properties of the composite [180, 181, 247, 256]

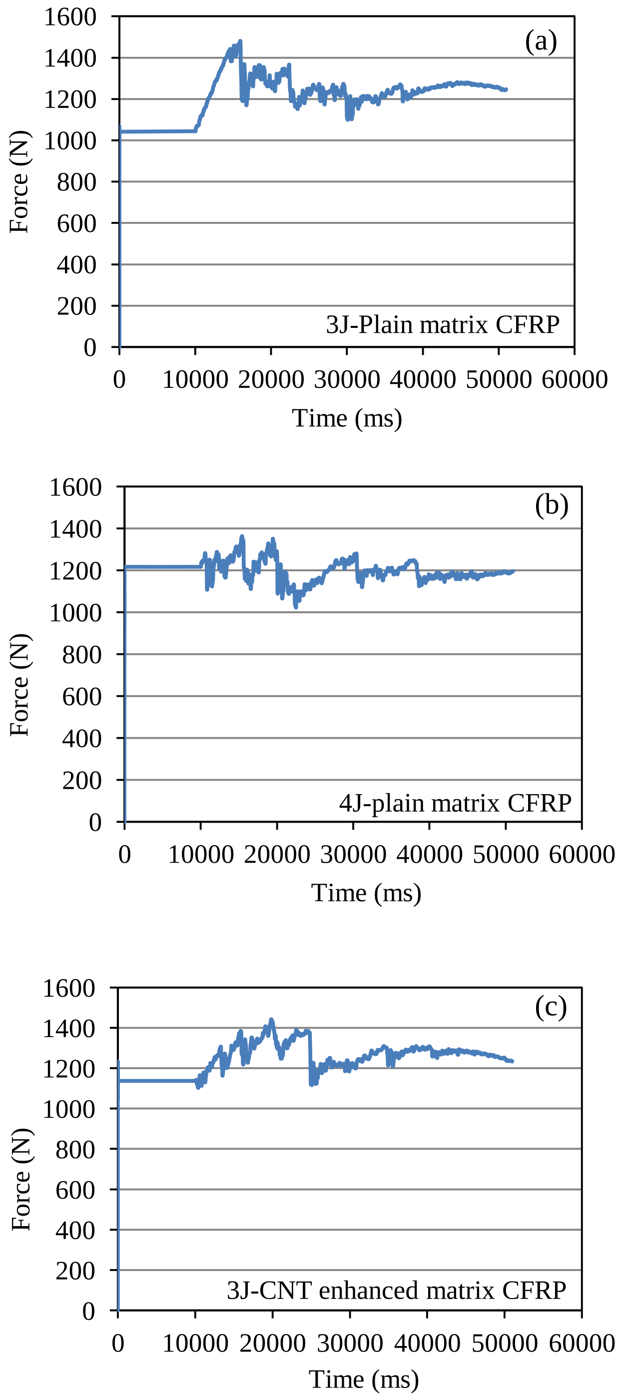

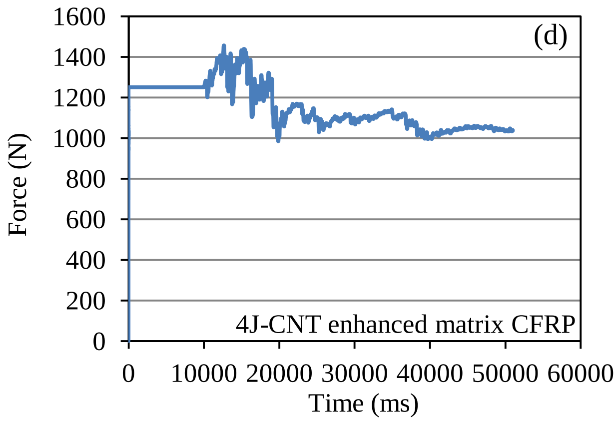

Figure 3.3.5 *Force vs. time graphs for both plain (a, b) and CNT modified matrix specimens (c, d).*

Initially, the thermographic inspection was performed in "live" mode. The 2D temperature distribution on the plate surface was simply recorded as a function of time. The material thermal response was recorded with the thermal camera, as both plain and CNT enhanced specimens were heated with resistance heating. In Fig.3.3.6 the employed thermal stimulation protocol is shown.

The following graphs (Fig.3.3.6) depict the temperature profiles (normalized to the initial mean value) of both CNT enhanced and plain matrix CFRPs. The series of thermographs shown were recorded during the heating (top series) and cooling (down series) phase. As was observed, delamination damage was more easily identified during the current injection i.e. the heating process, as around the damaged area, a temperature gradient on the specimen surface was observed; after the interruption of current injection, i.e. during the cooling process, impact induced discontinuities on the specimen were less discernible. This effect was attributed to the fact that, during the current injection, heat was preferentially generated along the injection path, whereas during the cooling down process, heat was dissipated along all edges of the monitored surface. As the specimen was a typical symmetric cross ply laminate, the aforementioned effect could not be attributed to the symmetry of the lamination, i.e. the thermal anisotropy of the material along its surface.

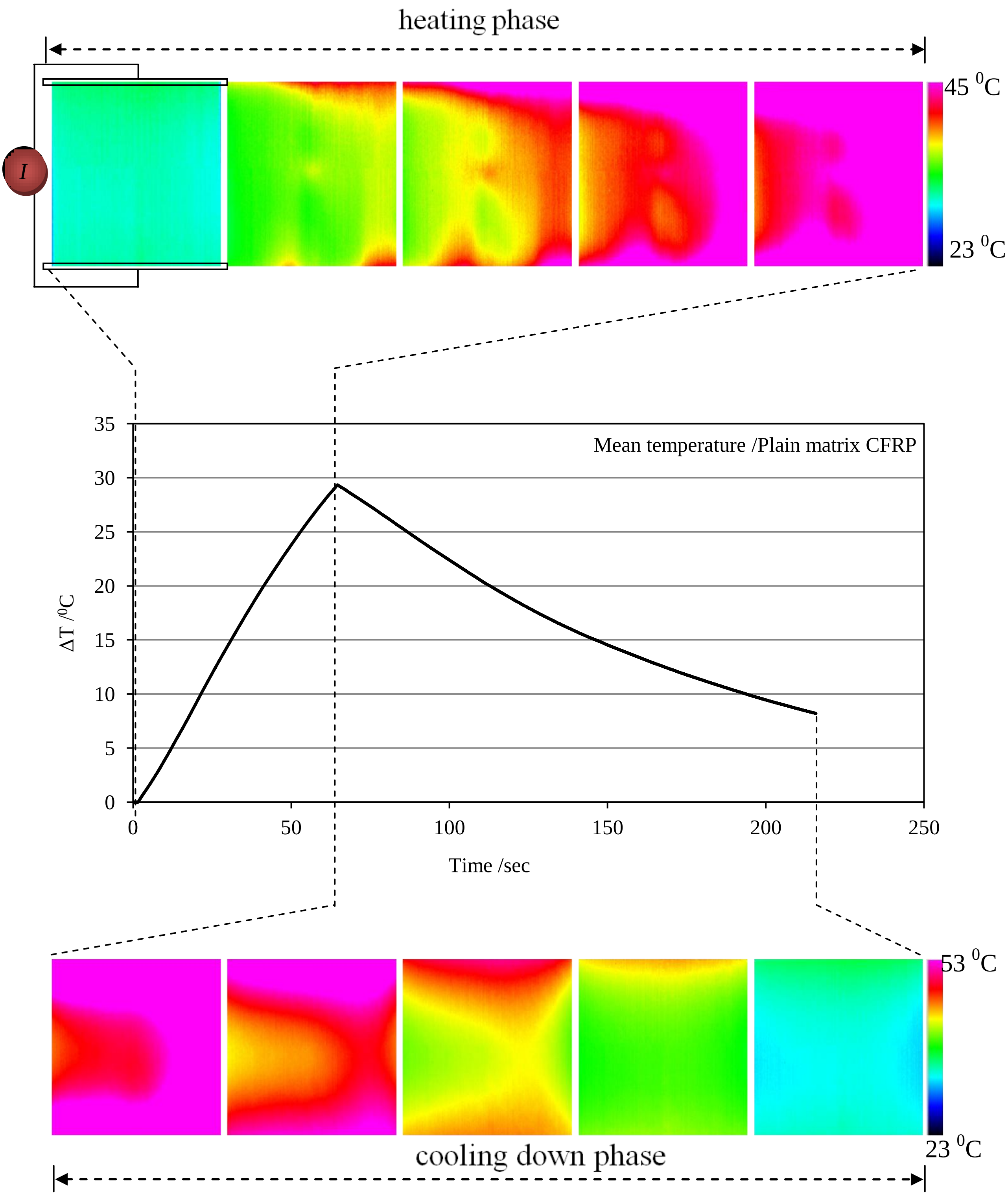
heading phase
45 ^{0}C
23 ^{0}C
I
Mean temperature /Plain matrix CFRP
35
30
25
20
15
10
5
0
ΔT /^{0}C
0
50
100
150
200
250
Time /sec
53 ^{0}C
23 ^{0}C
cooling down phase

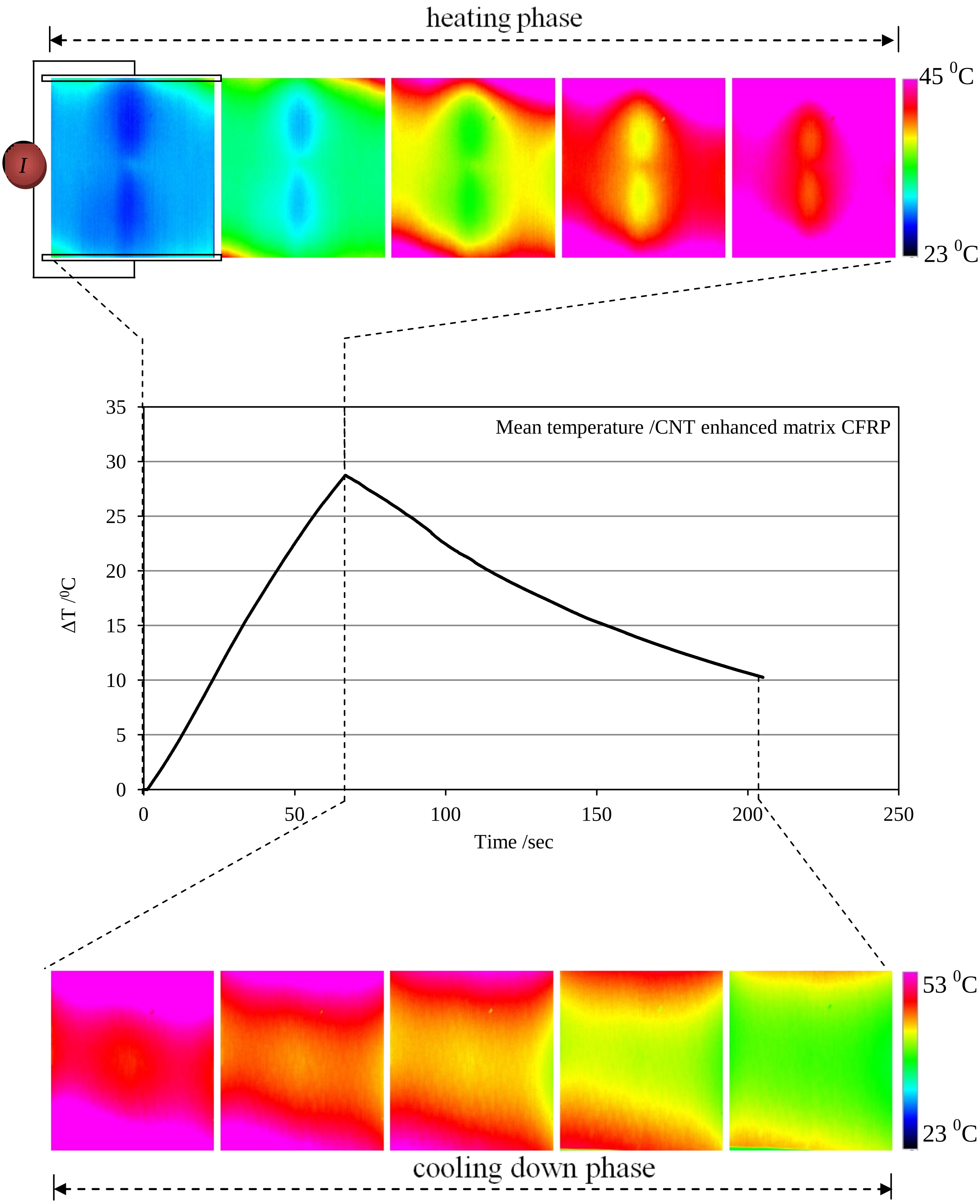

Figure 3.3.6 *Thermal stimulation procedure; temperature profile and representative thermographs (live mode) of the reference and CNT modified CFRP laminates when fixed - amplitude DC current is injected in the composites.*

It is worth mentioning at this point, that conventional IR active thermography is more efficient in identifying discontinuities during the cooling phase [72]. In contrast, current injection thermography is more efficient during the thermal simulation, a fact that is attributed to the preferential introduction of the thermal energy in the material. The above thermographs show that (i) the temperature distribution was practically symmetrical to both the mid width horizontal and vertical axes of symmetry of the plate and (ii) the delaminated area is optically enhanced by elliptical cold areas which lie on the same vertical axis as the delamination itself which coincides with the current injection axis.

More importantly, the addition of the CNTs is considerably enhancing the aforementioned effect. As is reported from previous studies, although the electrical conductivity remains practically the same along the conductive carbon fibres, it is at least an order of magnitude higher in the through thickness direction [126]. It can be postulated that, as the addition of the CNTs is globally enhancing the electrical conductivity in the through thickness direction, it is also facilitating the homogeneous heat transfer induced via the Joule generated heat between the individual laminae. In the absence of the conductive nanophase, through thickness conductivity is solely dependent on the carbon fibre random contacts. These contacts introduce random heat sources in the laminate which are independent of the current injection direction and mask the characteristic “butterfly pattern” observed in Fig.3.3.6 (heating phase).

Figs.3.3.7 to 3.3.10 show in sequence (a) the top (impacted) side, (b) the bottom side, (c) the C-scan image (d) the thermal IrT phase image and the thermal IrT phase image with optical excitation for both the 3J and 4J impact damaged plain and CNT modified CFRP coupons, respectively. As Figs.3.3.7d, 3.3.8d, 3.3.9d and 3.3.10d illustrate, the induced damage is identified with the proposed method. It is evident that higher impact energy results in wider damaged area. Delaminated regions are almost visible in the cases of 3J impact energy (Figs.3.3.7, 3.3.9 (a, b, and e)). However, significantly severe damage was induced by the 4J impact enforcement (Figs.3.3.8, 3.3.10 (a, b, c and e)). For reference purposes, IR excited optical PPT was performed using 2 optical lamps of 1 kW each (Fig.3.3.7e, 3.3.8e, 3.3.9e and 3.3.10e). In that case, the materials were heated for 10 sec (square pulse) with 5V energy. As is obvious, phase images observed by resistive heating (Figs.3.3.7d-3.3.10d) are similar to the phase images when stimulating with the optical lamps (Figs.3.3.7e-3.3.10e). The inspection of the IR optical PPT phase images reveal clearly the locus of the LVI damaged area. The current injection thermographic system to the inspection of LVI damage is providing considerable potential as (i) it does not require an external heat source as the material is directly heated via the Joule effect, (ii) the flow pattern identifies the resident axis of the defect with respect to the current injection and (iii) it is not affected by the surface morphology as the bulk laminate is heated via its cross sectional area and not via its interrogated surface and (iv) requires considerably less energy for the damage inspection; the total energy input for the LVI damage identification with current injection is 5 Joule compared to 20 kJ for the optical excitation. Conventional C-scan was also employed (Fig.3.3.7c, 3.3.8c, 3.3.9c and 3.3.10c) for the validation of both thermographic techniques. The C-scan images are juxtaposed with the optical images of the specimens for comparison purpose.

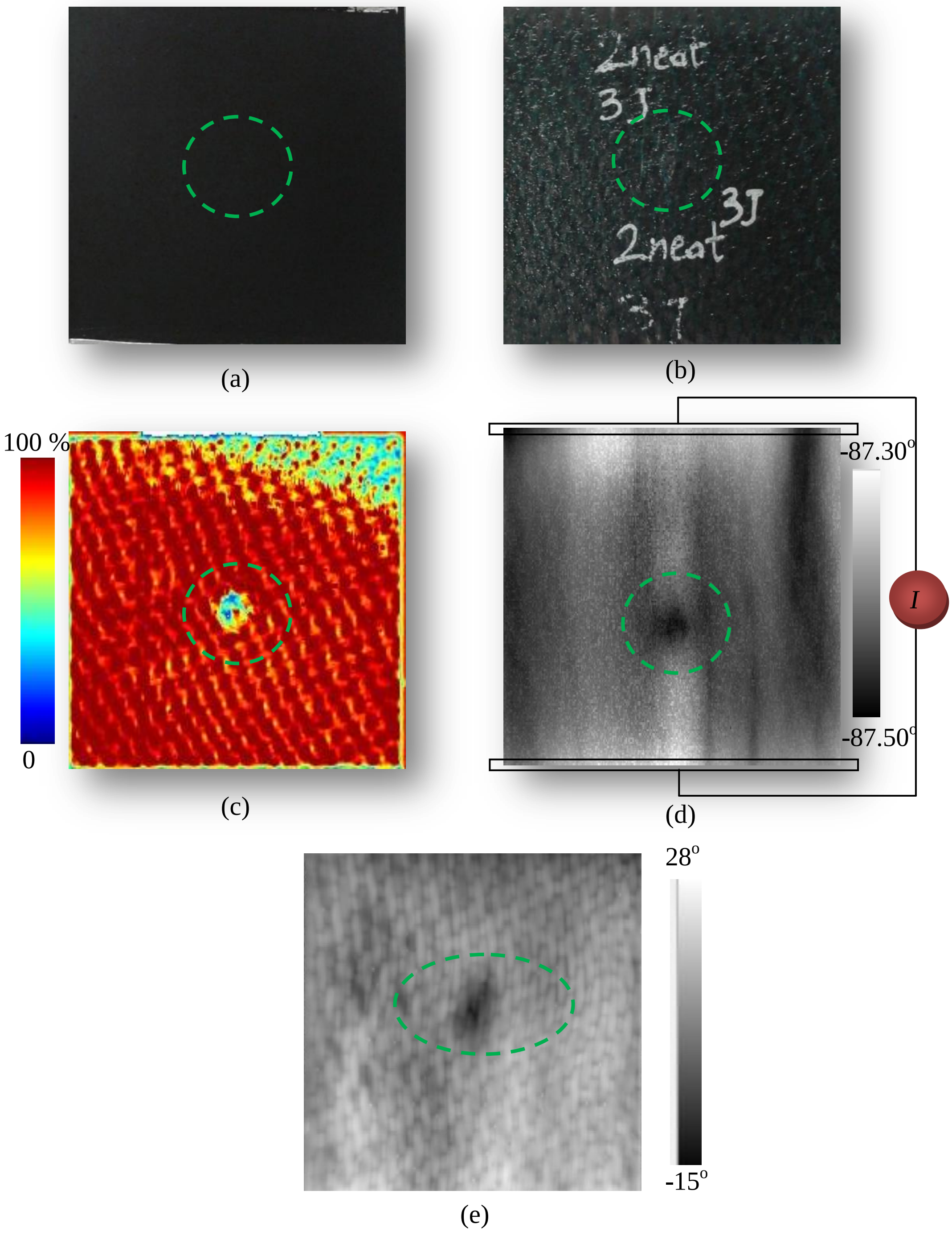

Figure 3.3.7 *Plain epoxy matrix CFRP - 3J impact damage; (a) Top (front) side of the coupon, (b) bottom (back) side of the coupon, (c) C-scan imaging, (d) IrT phase image (current injection excitation) (e) IrT phase image (IR optical excitation).*

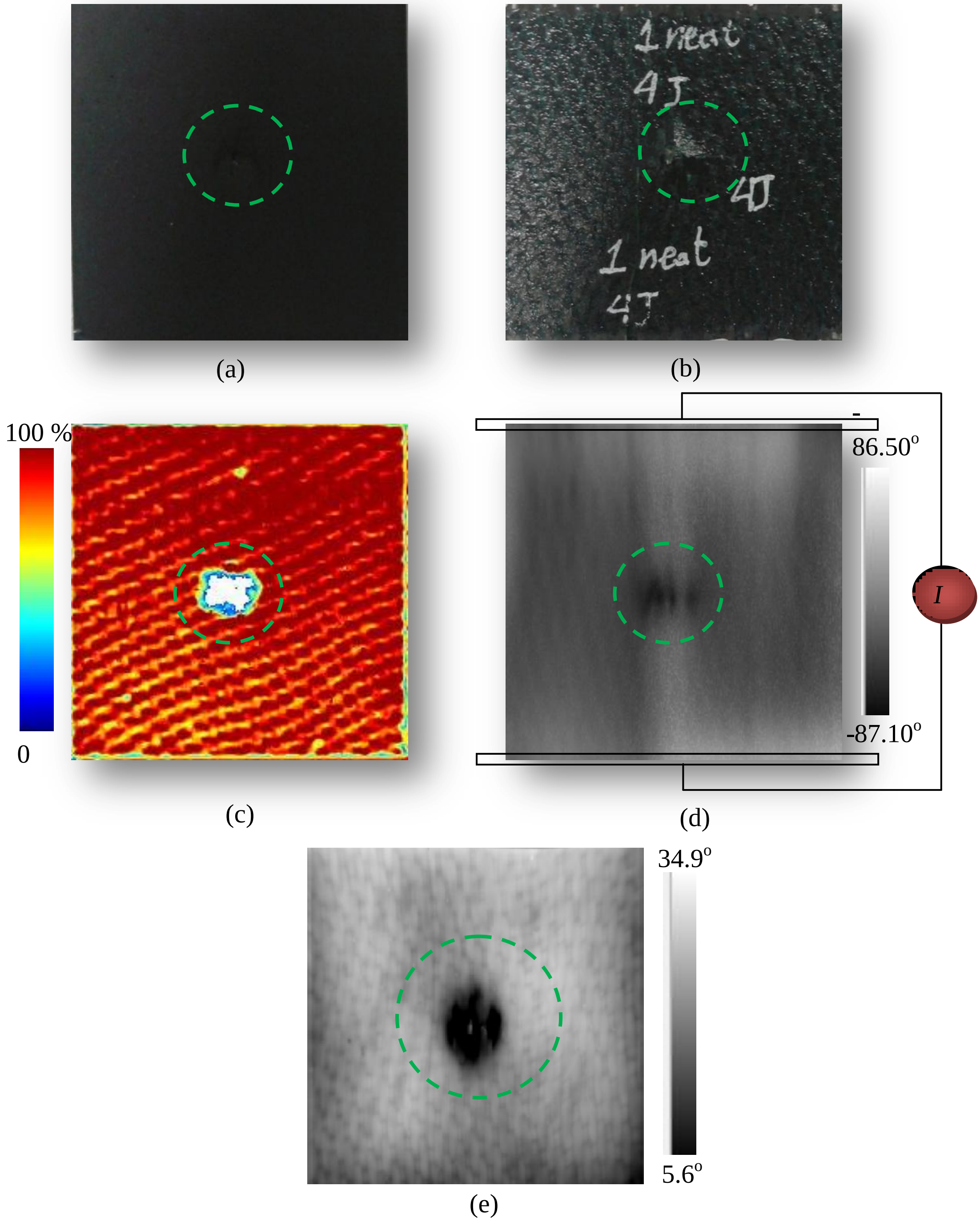

Figure 3.3.8 *Plain epoxy matrix CFRP - 4J impact damage; (a) Top (front) side of the coupon, (b) bottom (back) side of the coupon, (c) C-scan imaging, (d) IrT phase image (current injection excitation) (e) IrT phase image (IR optical excitation).*

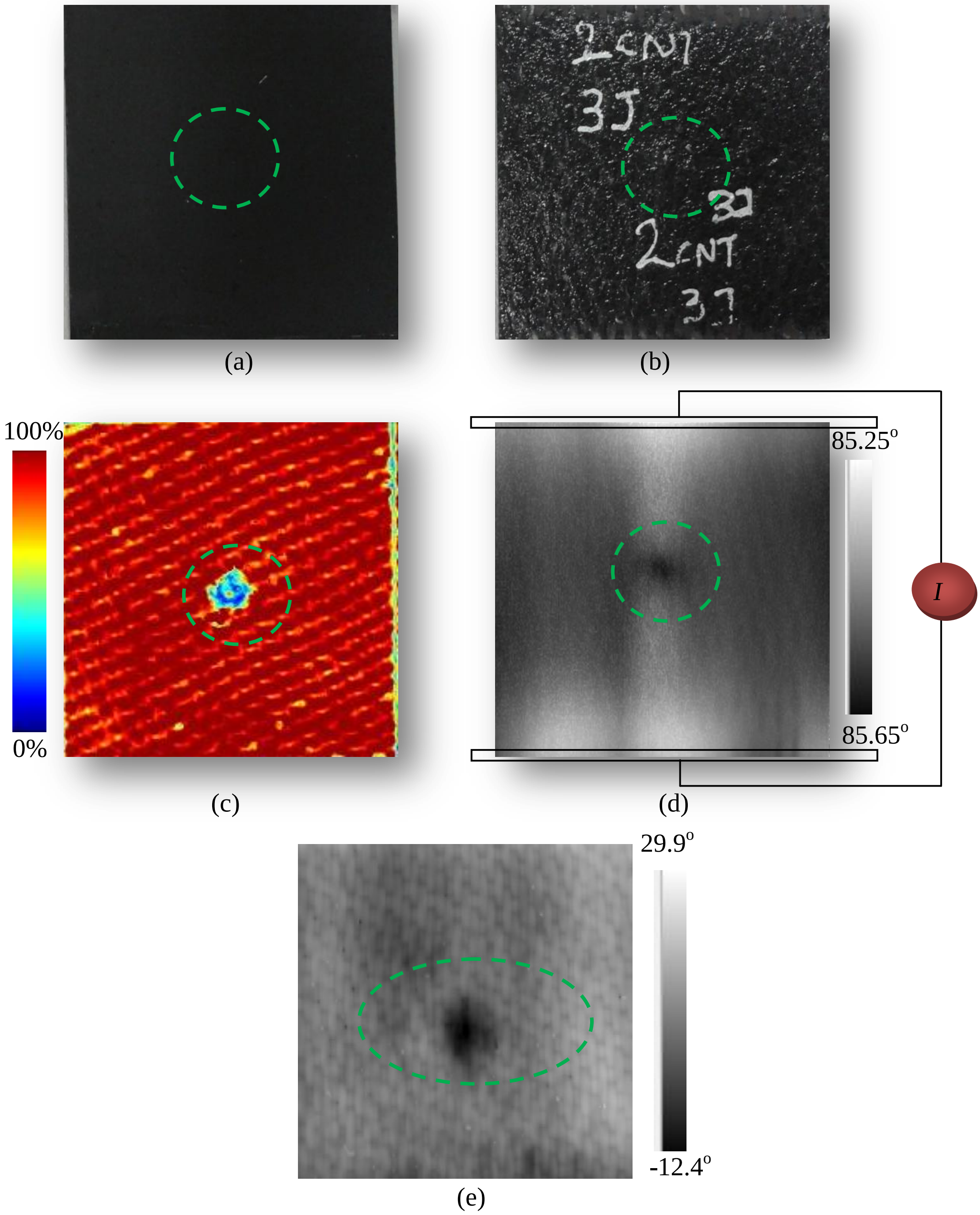

Figure 3.3.9 *CNT modified epoxy matrix CFRP - 3J impact damage; (a) top (front) side of the coupon, (b) bottom (back) side of the coupon, (c) C-scan imaging, (d) IrT phase image (current injection excitation) (e) IrT phase image (IR optical excitation).*

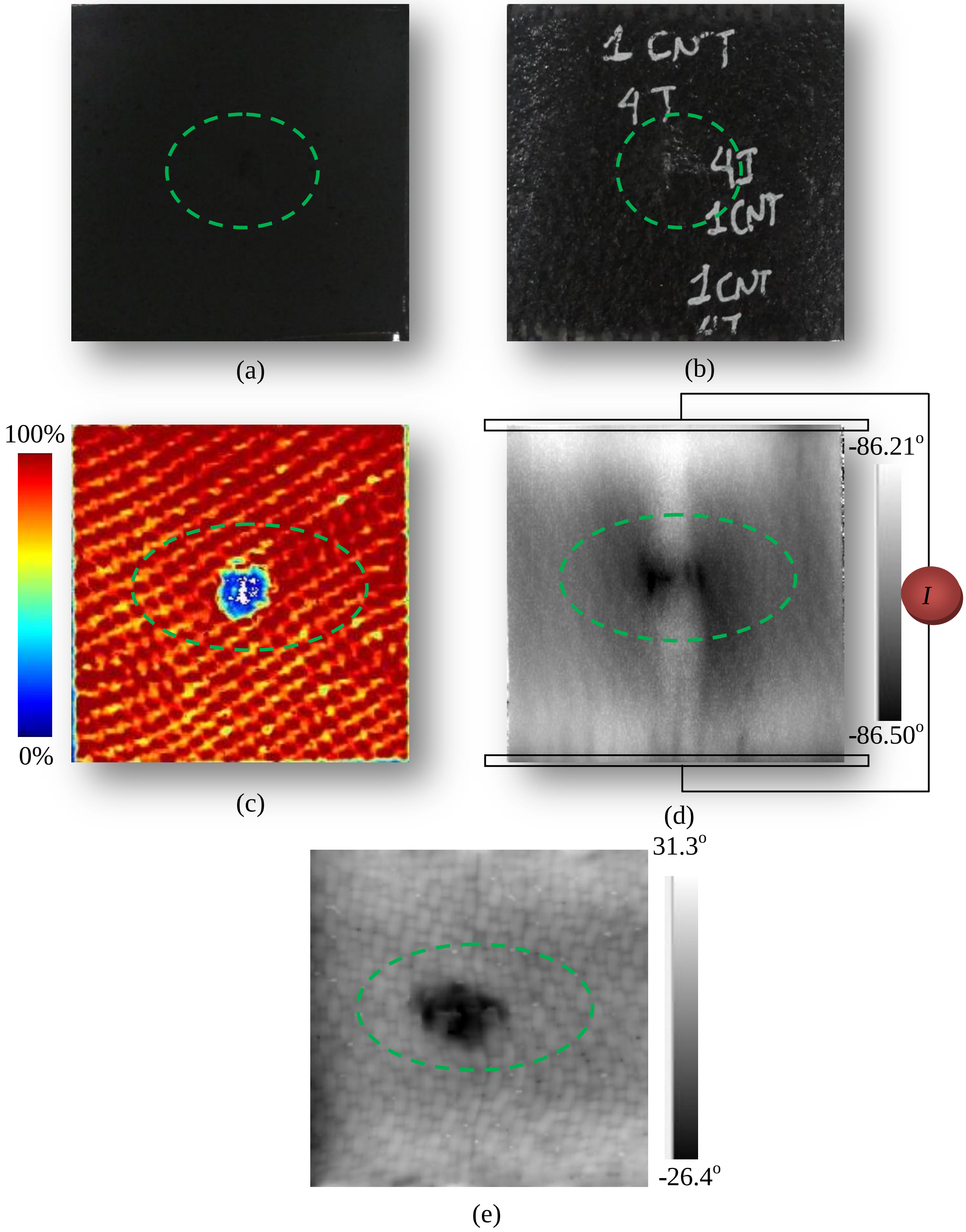

Figure 3.3.10 *CNT modified epoxy matrix CFRP - 4J impact damage; (a) Top (front) side of the coupon, (b) bottom (back) side of the coupon, (c) C-scan imaging, (d) IrT phase image (current injection excitation) (e) IrT phase image (IR optical excitation).*

For both 3J and 4J impact damage energies, the delaminations identified by the C-scanning method appear as dark areas with both thermographic methods. As expected, the 3J impact energy resulted to smaller damaged area than in the case of 4J impact (Figs.3.3.7d, 3.3.8d, 3.3.9d and 3.3.10d). Similar behaviour was noticed for both the plain and CNT modified matrix matters. In the case of the 4J impact damage, especially for the CNT modified specimen, the thermographic imprint of damage is manifested as two dark spots in the vicinity of the impacted area. As should be noted, the attainment of a uniform excitation field in the space domain through the optimisation of the current modulation protocol is indispensable. It is noteworthy that the directionality of the current path as dictated by the symmetry of the material was clearly observed in all the IrT current injection phase images (Fig.3.3.7-3.3.10d). More analytically, at the current injection sides, constant phase thermographs exhibit increased thermal wave emission. This is directly attributed to the contact resistance of the electrodes. Following, the phase images reveal reduced thermal wave activity on an envelope which surrounds the impact damage, revealing the thermal flow disturbance around the induced electrical discontinuity. It is believed that this effect is due to the combination of the plane electrical anisotropy of the material, i.e. the direction of the reinforcing fibres which define the paths of maximum conductivity and the current injection axis. It is also worth noting again, that the electrical induced thermal stimulation is not sensitive to the weaving pattern.

Section conclusions

The main objective of this part of the study was to develop a novel current injection thermographic technique for the detection of damage in composite laminates. The efficiency of the proposed methodology was tested in LVI damaged cross ply composite plates, and cross validated with optical thermography and C-scan. Both live and pulse phase thermography was employed.

The composite plates subjected to LVI of 3J and 4J.The performed impact energy levels did not lead to penetration of the laminates. In both impact energy level cases, the induced damage was identified. The major challenges for the application of the method were (i) the minimisation of the contact resistance at the current injection sites (ii) the uniform thermal stimulation of the composite structures so as to clearly pinpoint the internal characteristics which were imposed by LVI and (iii) the optimisation of the current injection protocol so as to avoid overheating and efficiently record the transient thermal gradient on the surface of the laminate.

Thermal stimulation was significantly affected by the electrical anisotropy of the composite laminates. The incorporation of the CNT conductive nanophase led in the clear thermal imprint of the current flow disturbance induced by the impact damage. This effect was manifested by two cold elliptical spots on either side of the impact location along the current flow axis, which was less obvious in the case of the unmodified laminates. This effect was attributed to the enhanced though thickness conductivity of the CNT enhanced laminate, and was particularly evident in the real time (or live) thermographic inspection of the transient temperature profile of the laminate surface during the current injection phase.

Appropriate current modulation was necessary in order to enhance the resolution of the phase images. The energy input required for the identification of LVI damage was three to four orders of magnitude less than the typical energy input required with optically excited PPT. The comparison of the current stimulated PPT images with typical optical PPT phase images as well as C-scans revealed that current injection is capable of pinpointing the damage. As in the case of live thermographic inspection, damage is manifested as a low excitation area within a ribbon of higher excitation, parallel to the path of the current injection.

Summarizing, a novel current injection thermographic technique developed in this work. The employed thermographic system proved its ability in identifying LVI damage in composite materials both in live and pulse phase modes.

Acknowledgements

The author would like to thank Associate Prof. Stefanos Zaoutsos for providing the impact damage facilities located at the Dept. of Mechanical Engineering of the Technological Educational Institute of Larissa, Greece.

CHAPTER 4

On-line damage assessment in composite materials using innovative NDE

4.1 Monitoring of damage initiation and development in Carbon Fibre Reinforced Polymers & Glass Fibre Reinforced Polymers using the Electrical Resistance Change Technique

4.1.1 Introduction

The application of bonded repair technologies for aircraft repair requires novel non-destructive techniques which will provide information on the repair efficiency throughout the service life of the component and subsequently enhance the credibility of bonded repair for aircraft structural components. More importantly, enabling non destructive technologies may also guide repair methodologies away from the widely accepted “repair and forget” principle. In this way (i) structural aggravation may be minimised [257] and (ii) smart structural health monitoring concepts can be benchmarked and reach the required technological readiness level for application [247]. In the case of bonded repair, an effective Non Destructive Evaluation (NDE) technique should guarantee the required operational safety levels for aircrafts [258]. Ideally, this NDE technique allow for the monitoring of any critical and subcritical damage propagation during the service life of the repaired structure. Critical damage is the failure of the bonded patch and subcritical damage is the propagation of damage underneath the patch, or the augmentation of the repaired flaw.

As is already presented in chapter 2, lock-in thermography is based on thermal wave generation into a structure which is subjected to periodical (usually sinusoidal) thermal excitation. In the case of cyclic mechanical loading [82, 83], the oscillating stress may be directly followed by monitoring the temperature variation [84-86]. In this case, internal stresses are the source of thermoelastic waves. If there is a stress gradient due to the presence of stress raisers e.g. notches [104], this will be manifested as a local temperature variation. LT mode (Fig.4.1.1) allows for the observation of both amplitude and phase shifts of the generated thermal waves of the specimen under investigation [60, 65, 71, 73, 259-261]. Phase and amplitude images are reconstructed via the FFT analysis of the real time recordings of the infrared camera.

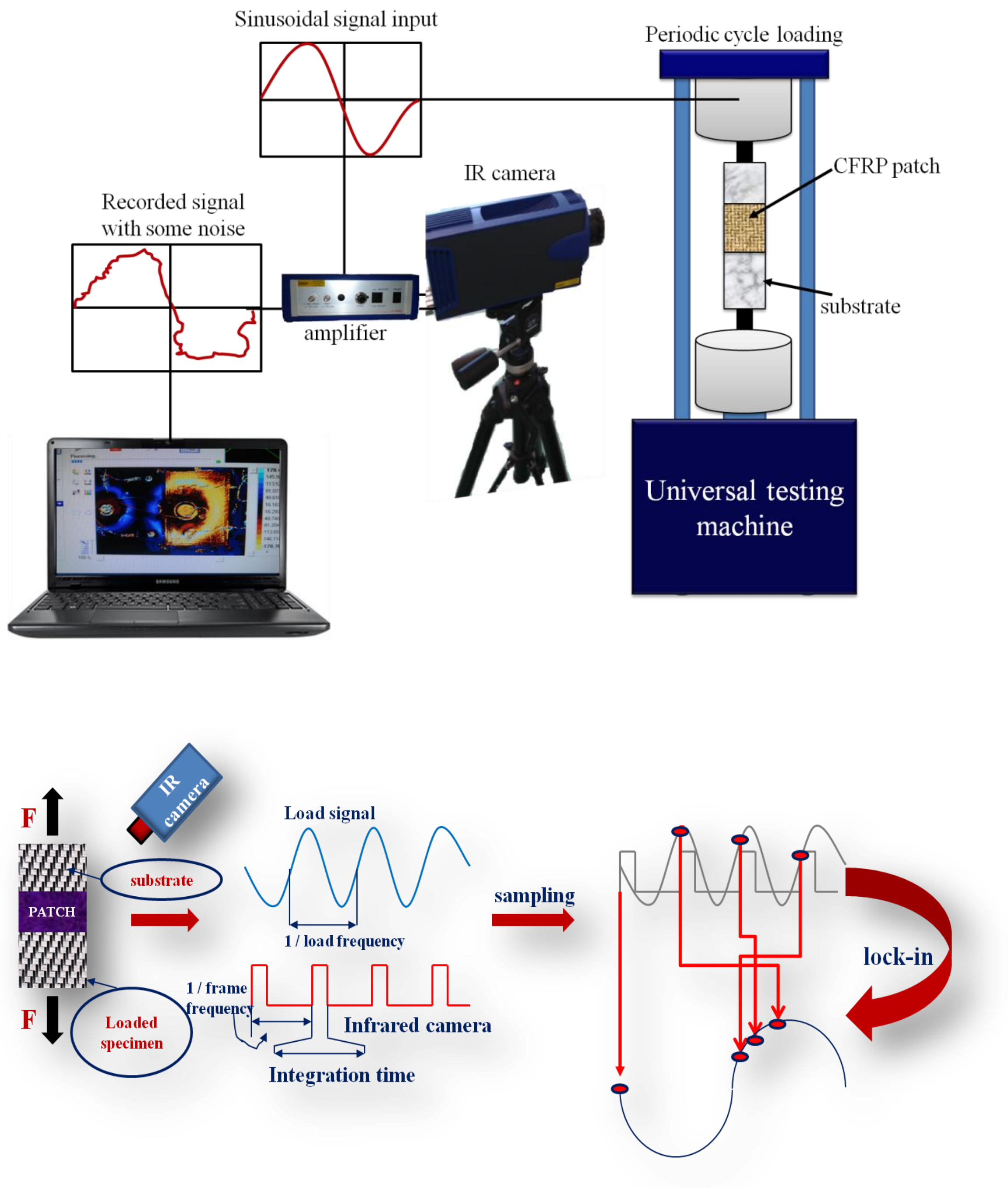

Figure 4.1.1 *Principle of lock-in thermography.*

As aforementioned, thermal waves are generated via thermomechanical coupling and detected by a synchronized thermographic system. Assuming reversible adiabatic elastic conditions for a thermally isotropic solid [82, 83], the well-known thermoelastic effect, may be described as (Eq.4.1.1):

$$\Delta T = (-\alpha / \rho C_p) T \Delta\sigma = \mathrm{K}_m T \Delta\sigma \qquad (4.1.1)$$

where ρ is the mass density, C_p the specific heat at constant pressure, α the Coefficient of Thermal Expansion (CTE), T the absolute temperature, ΔT the change in temperature in Kelvin degrees, K_m the thermoelastic coefficient and $\Delta\sigma$ represents the change in the sum of principal stresses. In the typical case of positive CTE, positive stress should result to a temperature drop in the material, as is the case of aluminum. On the other hand, carbon fibres are thermally anisotropic, as they possess a negative CTE in the longitudinal direction and a positive CTE in the transverse direction [251, 252]. In this case, the thermoelastic response of the material is different in the two principal directions and is more accurately described for plane stress conditions and an orthotropic solid (Eq.4.1.2):

$$\Delta T = -(\mathrm{T}/\rho C_p)(\alpha_L \Delta\sigma_L + \alpha_T \Delta\sigma_T) = \mathrm{K}_{mL} T \Delta\sigma + \mathrm{K}_{mT} T \Delta\sigma \quad (4.1.2),$$

where the subscripts L and T denote the longitudinal and transverse directions respectively. What is typically shown by Eq.4.1.2 is that the thermoelastic response of a loaded material is the sum of the thermoelastic response of the stresses in the two principal directions which cannot be distinguished.

Hence, depending on the sum of the terms in Eq.4.1.2, the temperature of a thermally anisotropic material may increase or decrease during tension and vice versa during compression [84, 86]. Another issue that is frequently raised relates to the imprint of the through thickness anisotropy to the surface temperature, which is of particular importance for a laminated structure. Melvin et al [262], concluded that the surface temperature differences are attributed to the whole laminate and not only to the top lamina of the examined multi-layered composite. In this case the thermal anisotropy as described in Eq.4.1.2 should be accounted for, even for orthotropic or transversely isotropic symmetries. In other approaches, the temperature gradient is attributed to the topmost layer which may act as a “strain witness” [263]. The strain witness layer may be related to the resin rich surface or even the black paint employed to simulate the emissivity of the black body.

In the case of orthotropic media, such as fibre reinforced laminates, the assumption that the thermograph of the material corresponds to the whole laminate is governed by Eq.4.1.2 whereas the “strain witness” hypothesis is governed by Eq.4.1.1. As $\Delta\sigma$ corresponds to the sum of principal stresses, in the more special case where the symmetry of the material allows it, as in the case of cross ply laminates equally reinforced in the two directions, Eq.4.1.1 can be employed.

It is well known that the thermoelastic phenomena prevail when the material is loaded in the elastic region. However, fatigue damage induces irreversible damage in structures which deteriorate their mechanical properties. This damage is manifested by heat release. During fatigue mechanical loading the temperature of a CFRP laminate generally increases and, the higher the applied stress, the higher the temperature increase is observed [59, 74, 208]. In the case of brittle fibrous composites, this monotonic temperature increase can be attributed to heat release due to the accumulating flaws in the structure which in the presence of irreversible processes may overcome the thermoelastic effect [262]. In the case of cyclic loading, the phenomenon of intense heat release that precedes catastrophic failure is usually recorded at the final cycles of the fatigue life of the material.

Within the scope of this study, Lock-in Thermography (LT) was employed during sinusoidal mechanical loading in order to assess the bonded repair integrity on composite and aluminium (Al) substrates. To define the stress level where debonding initiated and propagated in a stable manner, all coupons were tested under tension-tension fatigue which started from very low stress levels. The induced stress level was gradually increased until debonding initiated in a stable manner at the interface between the patch and the mother material. The level of load where debonding initiated, is directly relevant to the bonding efficiency of the applied patch repair. In the case of composite substrates, Carbon Fibre Reinforced Polymer (CFRP) laminates with circular notches in the middle were patched and subsequently tested under cyclic loading. Tapered patches were employed to minimize stress concentrations at the edges of the patch, as is usually the practice in bonded repair [264]. In the case of Al substrates, critical damage at the interface between composite patches and Al was simulated by thin PTFE films underneath the patch edges. Thus, the PTFE films acted as debonding initiators. The debonding process initiated from the edges of the repair, at the same loci where the maximum shear stresses were generated. Critical failure of the patch initiated at very low fatigue levels, i.e. at approximately 30% of the static strength of the un-patched plate. IrT was both successful in (i) monitoring the critical failure of the patch i.e. the initiation and propagation of the debonding process and (ii) identifying the subcritical damage i.e. the stress concentrations at the locus of the patched notch and its evolution.

4.1.2 Experimental

4.1.2.1 Materials and specimen preparation

Two different types of repaired materials (type I and II) were investigated. The first type (I) was designed to study the interaction between critical and subcritical damage for optimum bond strength. The MTM®56/CF0300 pre-preg (200 g/m^2) provided by ACG (UK) was used. The interrogated carbon fabric is a standard high strength material in twill weave format. The same material was employed for both the repair and the substrate. The performed curing cycle was step-by-step as following: (i) reaching of 0.98 bar vacuum condition, (ii) increase of vacuum pressure to 6.2 bar, (iii) increase of temperature at 120 ^oC with 3 ^oC /min rate, (iv) retain stable vacuum pressure and temperature for 10 min, (v) decrease of temperature at 80 ^oC with -3 ^oC /min rate and finally (vi) vacuum pressure release. The manufacturing procedure was as following (i) cutting of the pre-preg fabrics for both the substrate (8 layers) and the patch (4 layers) in the required dimensions, (ii) laying-up of the substrate layers, (iii) vacuum pressing of the substrate, (iv) curing of the substrate, (v) drilling of the circular notch, (vi) bonding of the patch layers, (vii) vacuum pressing of the patch, (viii) curing of the patch and (ix) cutting of the specimens in the appropriate dimensions. A 5 mm circular notch was drilled in the middle of each substrate using a diamond drill as a typical damage scenario. The notch is characteristic of the methodology employed to arrest/ retard the crack propagation by "stop drilling", both in the case of aluminum [265] and in the case of composite repair [266]. The patch edges were tapered bonded (Fig.4.1.2), in order to minimise the shear stress fields around the edges of the repair [264]. After specimen manufacturing, 50x60 mm^2 end tabs were attached on the composite coupon using high shear adhesive (Epibond 1590 A/B, Huntsman), to prevent failure at the gripping area. The examined configuration was chosen as typical of one sided repair of damaged panels In Fig.4.1.2 the final coupon dimensions and the employed CFRP patch configuration is shown[2].

In type II specimens scenario (Fig.4.1.2a), CFRP patches were applied on 2024 T3 aluminum (Al) strips. PTFE tapes were inserted in the patch /substrate interface, precisely at the sub-terminal edges of the patch, in order to initiate critical debonding. Additionally, the edges of the repair-layers were cut at the very same constant dimensions (there was no tapering), and thus critical debonding was in all cases promoted. Fig.4.1.2d depict the CFRP patch on Al substrate configuration. The location of the PTFE tapes at the edges of the CFRP patch is illustrated in Fig.4.1.2a (40x6x0.075 mm^3). Four ply CFRP patches with dimensions 80x40x1.03 mm^3 and orientation were fabricated using hand lay-up. The patch matrix was a cold-curing epoxy system Araldite LY 5052 /Aradur 5052 (provided by Huntsman with

[2] Type I coupon were manufactured by Tecnalia, Spain (FUNDACIÓN TECNALIA RESEARCH & INNOVATION), in the framework of WP2, of Iapetus EU project.

recommended cure cycle: 1 day at 23 ^{0}C and 15h at 50 ^{0}C) and the reinforcement a biaxial carbon fabric 160 g/m^2 (Twill weave) fabricated by Hexcel. The Al substrate was cut in dimensions of 300x40x1.22 mm^3 (Fig.4.1.2e), sanded with grade 200 emery cloth and cleaned using de-ionised water and acetone. The CFRP patches were placed on the Al substrate and were subsequently cured and post cured in an oven under -700mbar vacuum conditions. No end tabs were necessary to test this material configuration.

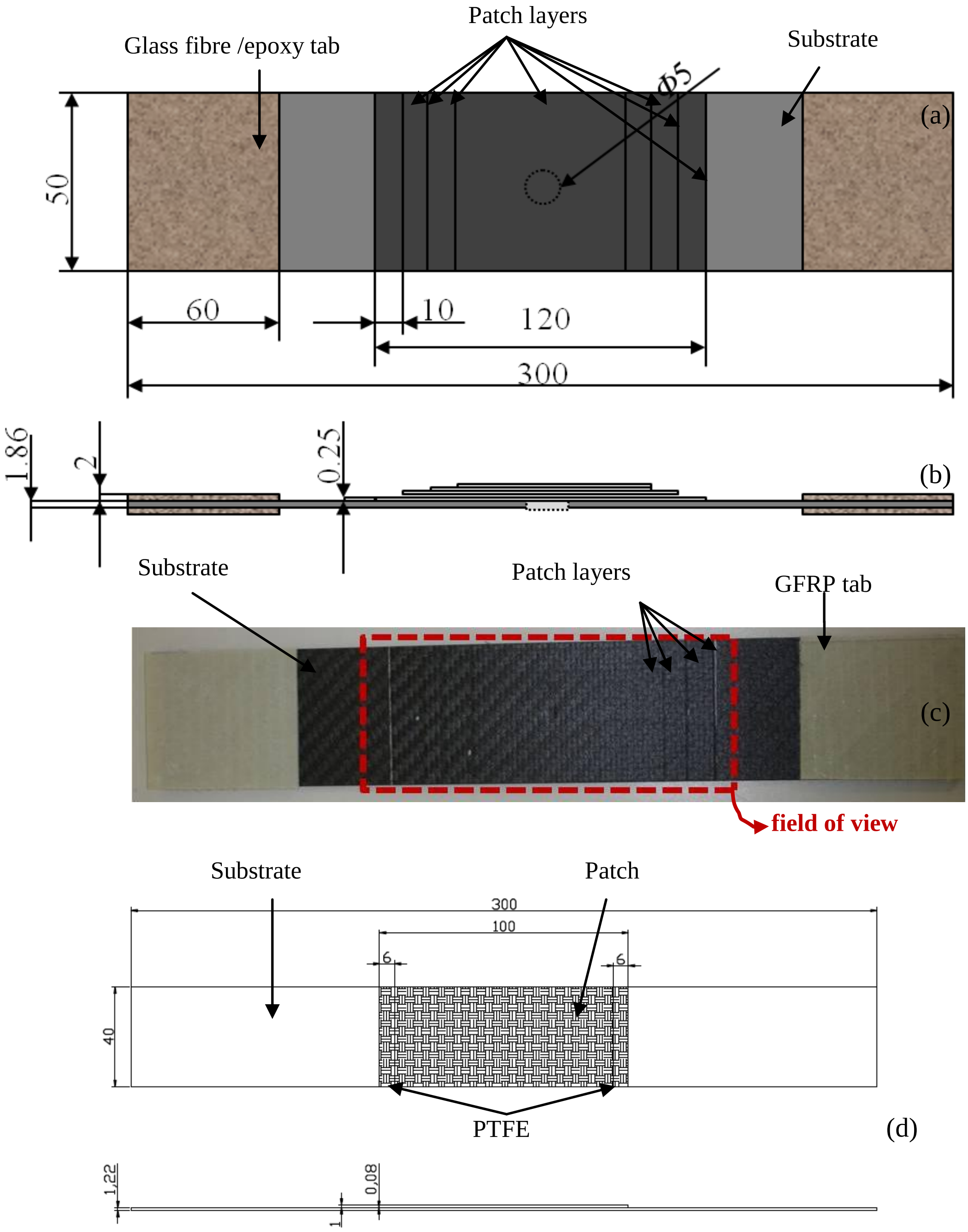

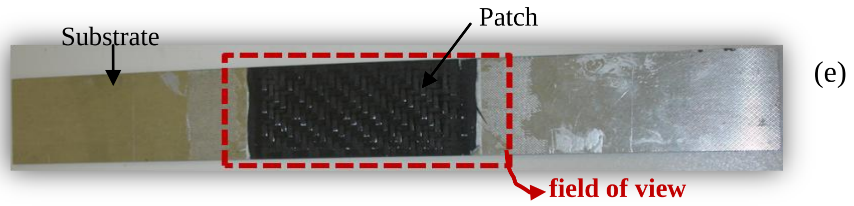

Figure 4.1.2 *CFRP patch on CFRP substrate configuration; open hole at the centre of the substrate: (a) front side, (b) lateral side, (c) CFRP patch on CFRP substrate view, CFRP patch on Al substrate configuration; (d) , and PTFE at the edges of the patch, (e) CFRP on Al surface snapshot*.

4.1.2.2 Thermographic assessment

For the thermographic inspection, the Jade 510-CEDIP-MIR infrared camera was employed (Fig.4.1.3). Information of the camera is reported in section 3.1. The camera was employed in lock-in mode at a frame frequency of 50 Hz.

The infrared camera was positioned at approximately 1 m distance from the specimen in order to include the whole patched area in the field of view of the camera (Fig.4.1.3a and 4.1.3b). At this distance the corresponding field of view was 208x156 mm^2 with a lateral and perpendicular resolution of 0.65 mm/pixel. The camera was connected with the Cedip R-9902 lock-in amplifier and the amplifier with the main servo hydraulic controller. The lock-in amplifier enabled the synchronization of the acquisition capture frequency with the IrT image by recording the exact propagation of time between the input and output signal [60].

For the purposes of the composite substrate testing, it was assumed that the material is thermally isotropic, i.e., Eq. 4.1.1 is valid. As aforementioned, this assumption holds for both the “strain witness” principle [263], and materials which possess a symmetry that is seen as isotropic by the thermal camera. In type I specimens, the composite substrate employed material is manufactured from a typical twill weave pre-preg with the reinforcing fibres in a 0º/90º configuration and the specimen loading in the principal material axis. As is analyzed in section 4.1.1, this material configuration is seen as thermally isotropic and Eq.4.1.1 is valid. In both specimen types, the un-repaired surface (side B: Fig.4.1.3b) of the coupons was monitored during the mechanical testing. All monitored surfaces were painted with a special black mat paint with an emissivity ε=0.97, close to that of the emissivity of a black body (ε=1).

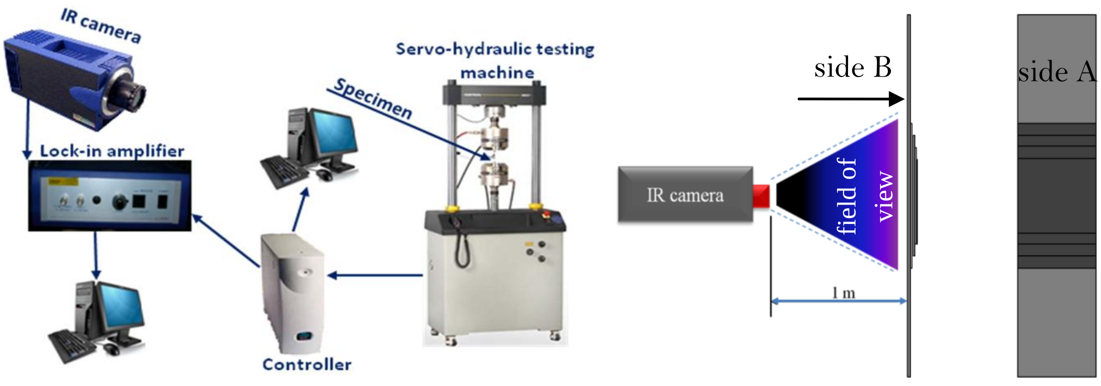

(a) (b)

Figure 4.1.3 *(a) On-line lock-in thermography; experimental setup, (b) recorded surface - field of view of the IR camera.*

4.1.2.3 Mechanical testing

An INSTRON 8801 servo-hydraulic testing machine with a maximum load capacity of ±100 kN was employed for the coupon testing (Fig.4.1.3). For the purposes of the current study, the strength of the undamaged laminate was chosen as a reference, based on the principle that the repaired structure should regain its initial strength. The ultimate tensile strength (σ_{uts}) of the undamaged CFRP and Al substrates, was determined by quasi static tension to be 600 ± 58 MPa and 483 ± 20 MPa, respectively, according to ASTM D3039 /D3039M - 08 (Standard Test Method for Tensile Properties of Polymer Matrix Composite Materials). In both type of specimens 5 Hz tension-tension fatigue and stress ratio R=0.1 was performed.

4.1.3 Results and discussion

4.1.3.1 CFRP substrate-drilled hole-CFRP patch

A total of three patched specimens were tested. Initially, fatigue testing was carried at very low stress level which was incrementally increased until debonding initiated and propagated in a stable manner. If no debonding were observed after 20 kcycles, a 10% step increase to the next stress level was performed. More analytically, tests at 20%, 30%, 40, 50%, 60%, 70% and 80% were performed. At the last load level (80% of the σ_{uts}), a stable propagation of critical failure or debonding of the patch from the substrate was observed with increasing fatigue cycles, starting from the edges of the patch. At the same stress level, considerable damage of the substrate at the edges of the drilled hole (subcritical damage) was observed. Critical failure was observed at 80% for all three coupons tested.

From Eq.4.1.1 and assuming that all other parameters are constant, the relative stress difference induced thermoelastically, is directly related to the relative temperature difference both for the local stress difference and temperature difference σ and T, respectively and the stress difference and temperature difference away from the notch $\Delta\sigma_\infty$ and ΔT_∞, respectively:

$$\Delta\sigma / \Delta\sigma_\infty = \Delta T / \Delta T_\infty \quad (4.1.3)$$

In other words, the recorded normalised amplitude gradient on the specimen surface is equal to the normalised stress gradient. In this way, all amplitude images may be transformed to stress intensity factor (SIF) maps simply by normalising the local amplitude values by the amplitude value away from the induced stress concentration, or the far field amplitude value.

In Fig.4.1.4, the typical stress intensity factor vs. position graph at the vicinity of the notch is analysed for the employed material. Fig.4.1.4a depicts the composite SIF vs. distance graph. This comprises the stress concentration that is due to the presence of the notch (dashed line) and the local stress variation that are due to the twill weave pattern of the interrogated material (solid black line). Fig.4.1.4b shows the interrogated axis on the repaired coupon. As should be stressed at this point, the stress variations due to the weaving pattern were consistently present in all thermographs. As they remained constant throughout the conducted experiments unless critical or subcritical damage altered the amplitude variation at the specific area, they are positively attributed to stress variations inherent of the interrogated system, and not noise. In this respect, the stress fields from both the notch (dashed line) and the weaving pattern (solid black line) are superimposed to result to the stress concentration depicted as the composite SIF (solid grey line). For the case under study, in order to calculate the SIF due to the presence of the notch, all local amplitude values were normalised by the mean amplitude value from the weaving pattern away from the notch σ_∞ (Fig.4.1.4b). As is obvious, the locally induced stress by the weaving pattern is cumulatively contributing to the SIF and the induced damage either constructively (e.g. left side) or destructively (e.g. right side). As the "weave induced" stresses are superimposed to the "notch induced" stresses, they increase the possibility of local failure where the stress intensity factor is maximum. As a result, the following analysis will be based on the cumulative stress concentration and not only on the "notch induced" stress concentration.

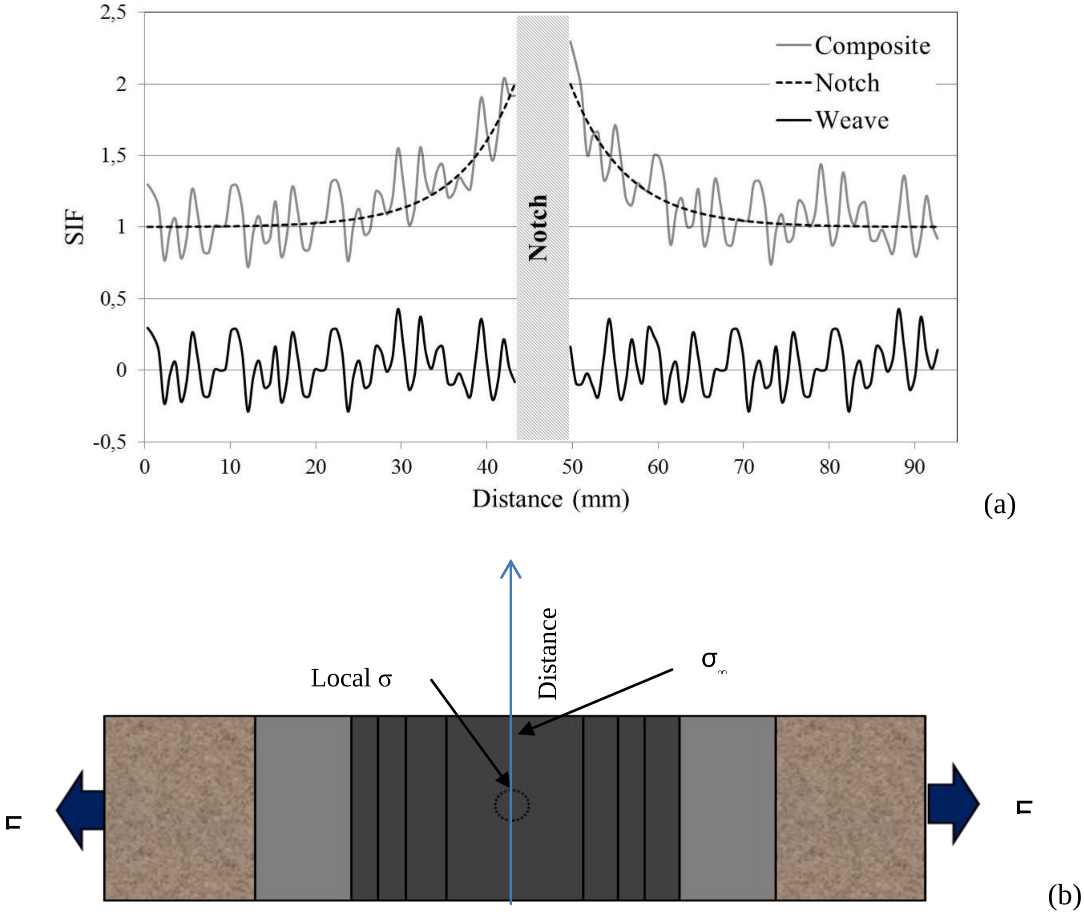

Figure 4.1.4 *$\Delta\sigma/\sigma_\infty$ vs. distance; (a) components of the composite graph: weaving pattern and notch induced SIF, (b) location of measurements.*

Figs.4.1.5, 4.1.7 and 4.1.8 represent amplitude snapshots at 40%, 70% and 80% load levels, as recorded by the thermal camera. In the case of 40% and 70%, the amplitude images did not change until the coupon was loaded to the next load level for all three tested coupons. On the contrary, in the case of 80% load level, the amplitude image changed characteristically during the fatigue loading until failure of the coupons. The deterioration trace of the interface (Figs.4.1.7 and 4.1.8) is highlighted by arrows on some of the images. In all three stress levels, stress concentration areas are depicted as bright spots in the corresponding snapshots around the circular notch or as bright areas at the edges of the patch, particularly at the loading (bottom) side of the test frame.

More analytically, Fig.4.1.5a is typical of the stress state at 40%, as no notable changes were recorded throughout the loading process. Stress concentrations can clearly be seen as bright spots on either side of the notch, where stresses are expected to be maximum. The application of higher stress level altered the stress distribution on the sample surface (Fig.4.1.5b) which also remained stable throughout the loading process at 70%. In the case of 80% load level, the amplitude image did not alter until approximately 20 kcycles. The typical amplitude image is shown in Fig.4.1.5c. As can be seen, the temperature disturbance at the vicinity of the notch clearly covered more extended area, with less prominent bright spots and characteristic dark areas which corresponded to unloaded (or less loaded) areas of the coupon.

The examination of these thermographs lead to the conclusion that stress concentrations caused initiation and propagation of stress-relief damage mechanisms, characteristic of the damage tolerant behaviour of the composite laminate: longitudinal splitting could be clearly seen on either side of the notch which at the same time reduced the SIF. This splitting occurred on the side of the specimen where the test frame applies the loading (bottom area in the thermograph). The same trend was observed in Fig.4.1.5c, where bright areas are less prominent at the edges of the notch and the extent of damage as manifested by the dark areas is slightly increased if not the same.

In Figs.4.1.5d, 4.1.5e and 4.1.5f the measured amplitude along the lines plotted on the Figs.4.1.5a, 4.1.5b and 4.1.5c is shown, normalised by the mean amplitude value away from the notch. This amplitude corresponds to the illumination received by the focal plane array sensor in the camera, and is directly proportional to the recorded temperature on the specimen surface. As was previously discussed, by normalising this amplitude to the recorded amplitude away from the discontinuity that induces the stress concentration will result to the SIF at the vicinity of the discontinuity (Eq.4.1.3).

In this way, the corresponding SIF at each stress level could be estimated and plotted as a function of the stress level. Figs.4.1.5d and 4.1.5e depict the transition from 40 % to 70% which leads to the relief of the cumulative SIF on the left side of the notch and its increase on the right side of the notch. This increase remains prominent at 80 % stress level (Fig.4.1.5f). It is interesting to note that the stress concentration pattern in Fig.4.1.5e and 4.1.5f remains almost the same, a fact that strongly indicates that the recorded stress variation is real and cumulatively due to the notch and the weaving pattern.

Fig.4.1.6a shows the SIF as a function of the stress level. In the specific geometry, the resolution of the amplitude picture was 0.65 mm /pixel. In Fig.4.1.6a the plotted curve corresponds to the binning of two pixel values at the centre of the notch, i.e. a resolution of 1.3 mm for a 5 mm notch. This was performed so that the diameter of the notch was always included in the measurements. Binning decreases the uncertainty in the amplitude measurements due to the inherent resolution limitations, but it may provide a slight underestimation of the measured stress intensity factor. However, this limitation does not affect the observations regarding the evolution of the stress intensity factor. The error bar corresponds cumulatively to the stress variation for the binning and the stress values on either side of the notch for all three tested coupons (a total of 12 values). There is initially a slight decrease in the mean value of the SIF which may be attributed to the local relief of the stress concentrations due to the longitudinal splitting, as was observed in the amplitude images. However, these changes are within the recorded variation in the system. In this respect, the SIF remains relatively constant at approximately 1.5. In addition, the thermographs remained unaltered during the fatigue loading suggesting that the damage induced heat is not significant compared to the thermoelastically induced variations, i.e. if hysteretic phenomena were dominant, the local temperature increase would mask the reduction in the stress concentration.

In Fig.4.1.6b the SIF is depicted as a function of the fatigue cycles at the 80% of the σ_{uts} for a single coupon that failed at approximately 30 kcycles. As observed for all tested coupons, the patch gradually debonded and the specimen failed catastrophically by a transverse crack at the vicinity of the notch. As for Fig.4.1.6a, the plotted SIFs include values of Figs.4.1.5a-c, Figs.4.1.7a-c and 4.1.8a-c and the equivalent SIFs plotted in Figs.4.1.5d-f, Figs.4.1.7d-f and 4.1.8d-f. It is interesting to note that for approximately 20 kcycles there is little or no change in the SIF and thereafter there is a substantial increase that reaches a maximum of approximately 2.5 and falls again to 1.5 at the time of the failure of the coupon at 30851 cycles. A closer examination of the amplitude images may justify the non-monotonic behavior of the SIF with cyclic loading. In Figs.4.1.7a-c and 4.1.8a-c the propagation of critical damage is manifested as areas of stress relief on the surface of the repaired composite coupon, or plainly dark unstressed areas that propagate towards the centre of the coupon with further cyclic loading. The critical debonding process was also monitored in a previous work for un-notched patched aluminum coupons [73]. The non-monotonic behavior of the stress intensity factor can be explained by the following mechanism: the gradual loss of lateral support due to the critical debonding results to the increase in the SIF which reaches a mean value of 2.5. At this stage, extensive longitudinal splitting (manifested as dark ribbons underneath the notch area) leads to the relief of the stress concentration. At the same time, the propagating critical failure gradually reaches the notch area (Fig.4.1.8f) leading to the catastrophic transverse failure of the coupon.

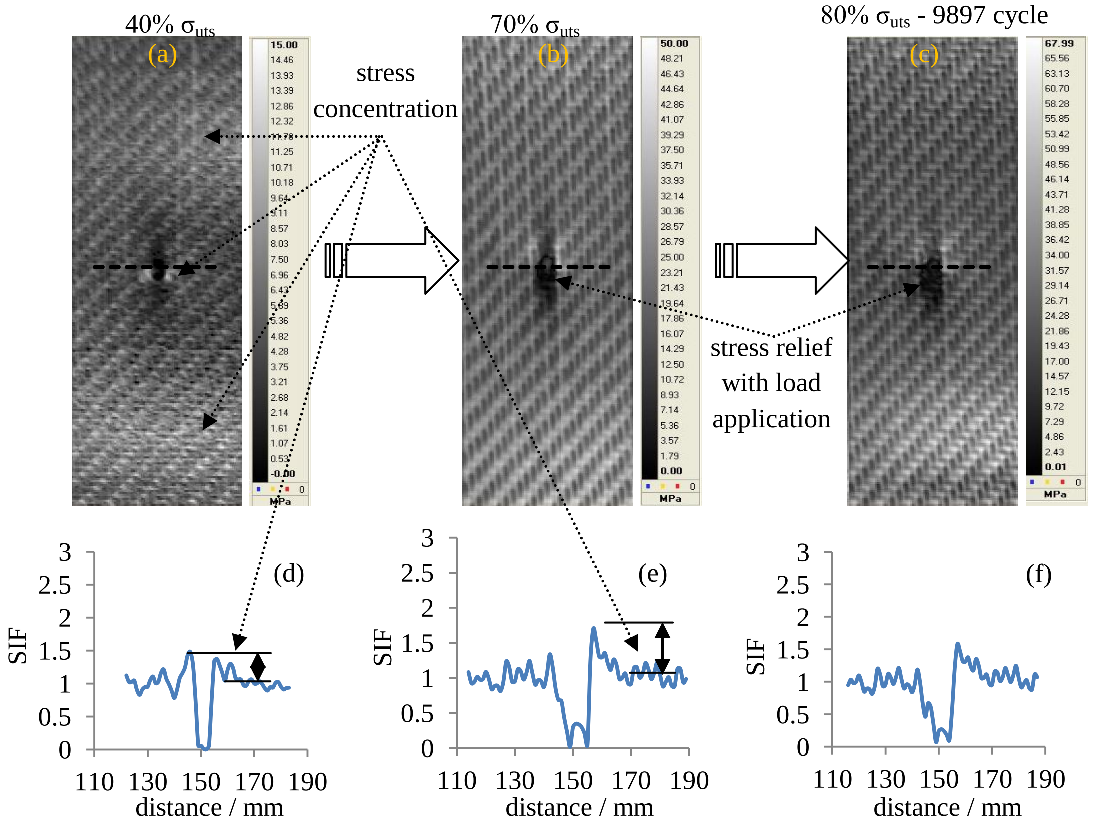

Figure 4.1.5 *SIF at the notch at low fatigue stress levels (prior to patch debonding). (a) 40% σ_{uts} (b) 70% σ_{uts}, (c) 80% σ_{uts}-9897 load cycle; respective normalized amplitude versus distance graphs.*

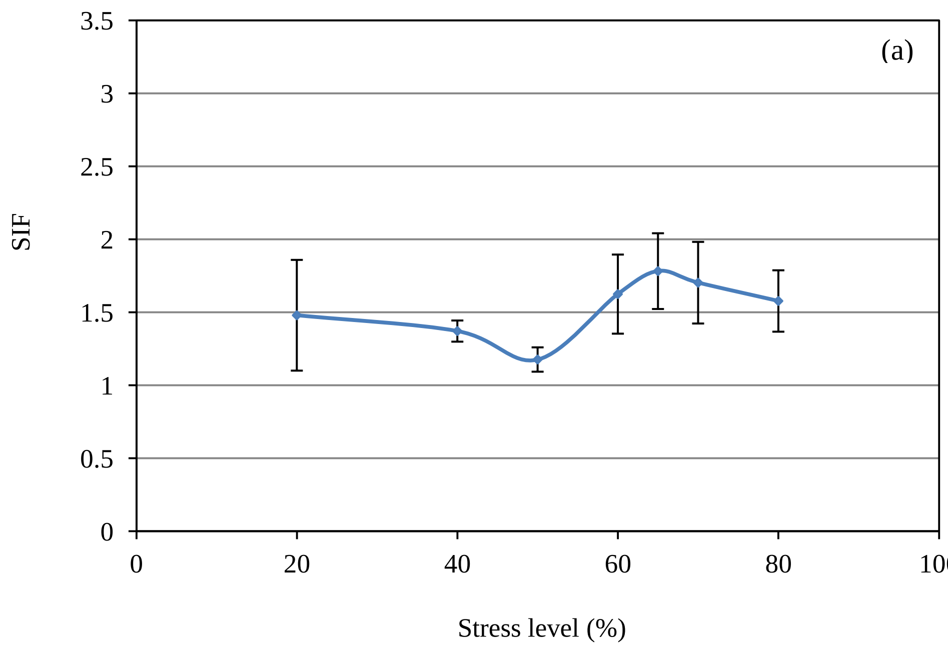

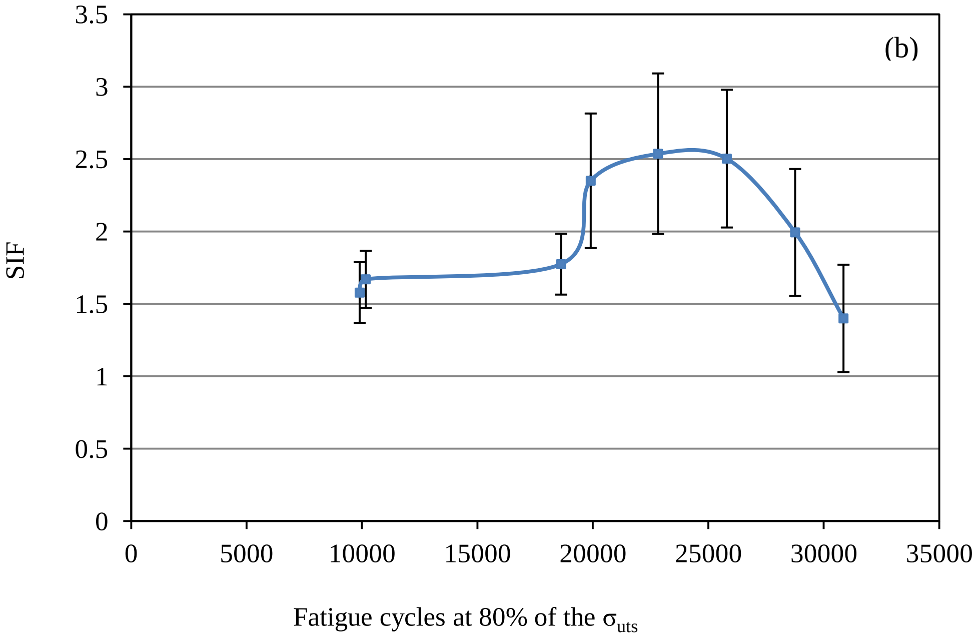

Figure 4.1.6 *(a) SIF vs. induced stress level, (b) SIF vs. fatigue cycles at 80% of the σ_{uts}.*

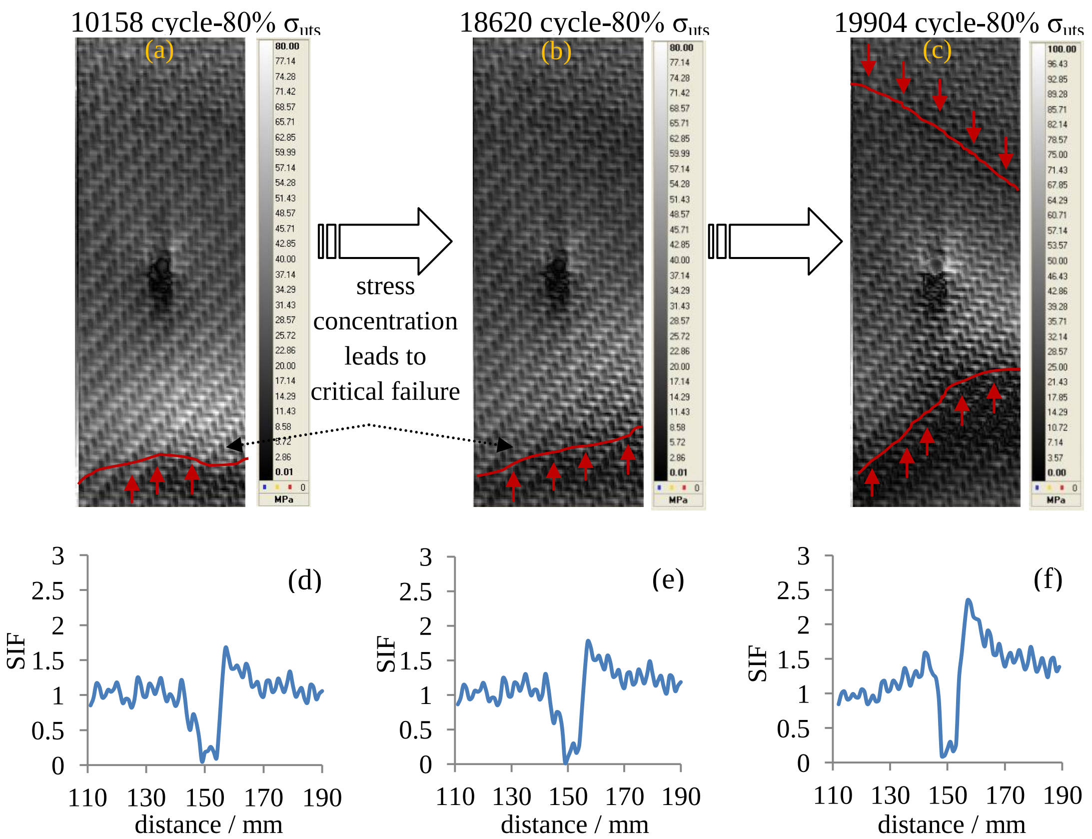

Figure 4.1.7 *Progress of delamination/separation/detachment of patch from the substrate during fatigue loading at 80% of σ_{uts}. (a) 10158 cycle, (b) 18620 cycle, (c) 19904 cycle; respective normalized amplitude versus distance (pixels) graphs.*

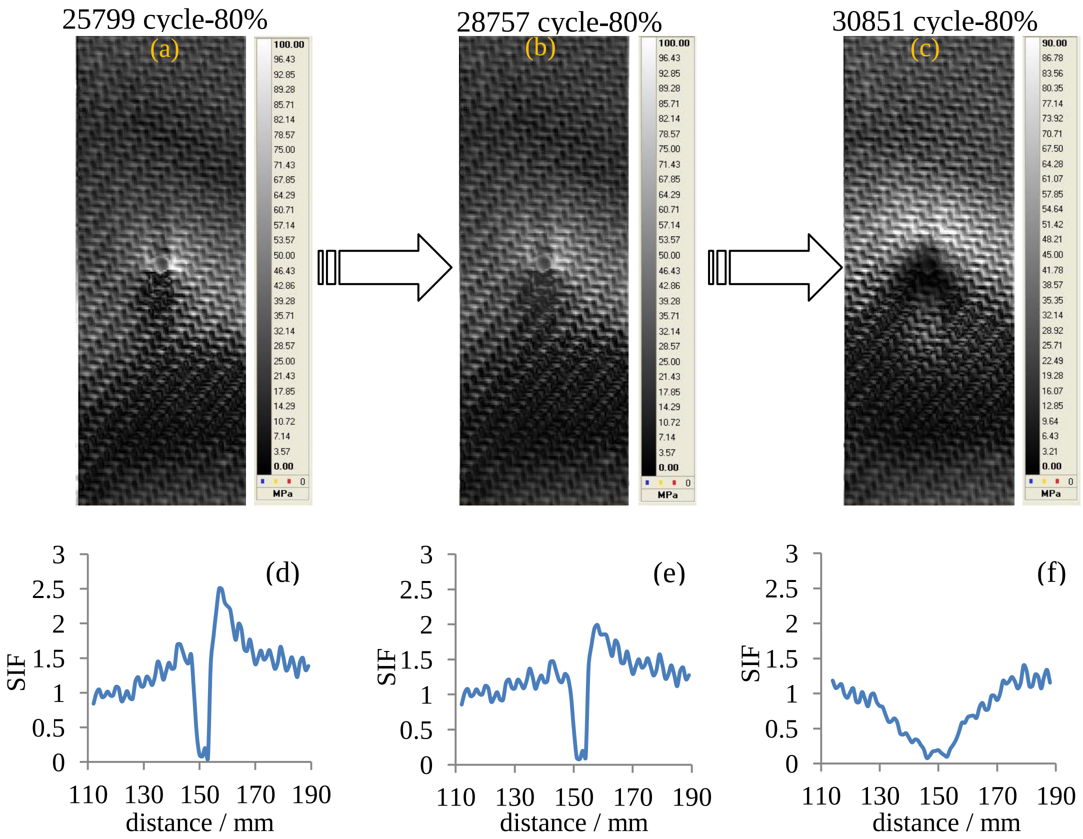

Figure 4.1.8 *Critical and subcritical damage monitoring in various load levels (a) 80% σ_{uts} 25799 cycles, (b) 80% σ_{uts} 28757 cycles and (c) 80% σ_{uts} 30851 cycles; respective normalized amplitude versus distance (pixels) graphs.*

In Fig.4.1.9, the sequence of amplitude images after damage initiation and propagation (i.e. after approximately 20 kcycles) is shown in order to exhibit the two distinct active processes. The bright areas on the top and bottom of the patch were clearly confined towards the middle of the specimen, denoting the onset and propagation of debonding. At the same time, the bright areas around the circular notch became more pronounced, as the localized stresses became gradually less inhibited by the failing patch. Further cyclic loading induced asymmetric debonding of the patch which significantly altered the stress distribution on the surface. Catastrophic failure took place at 30851 cycles when the debonding front merged with the notch induced stress concentration.

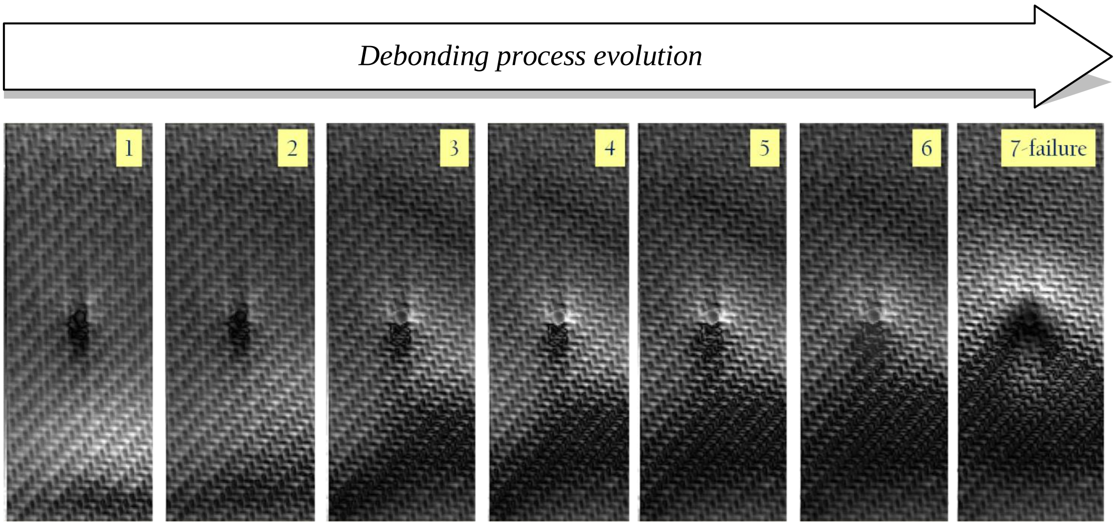

Figure 4.1.9 *Debonding process during the fatigue cycle mechanical loading.*

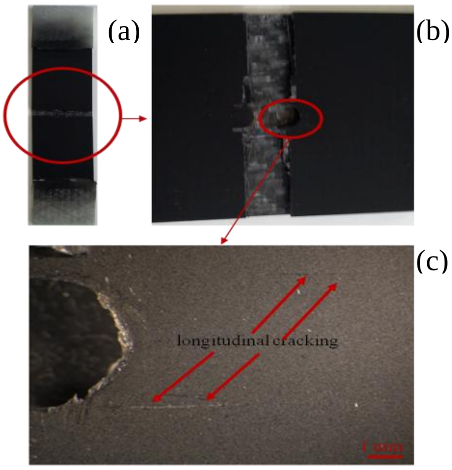

Figure 4.1.10 *(a, b) post failure images; (c) post failure stereoscopic image of the patched specimen.*

Post failure pictures of the coupon exhibiting the brittle failure exactly at its centre are shown in Fig.4.1.10. The magnification of the area of the notch (Fig.4.1.10c), revealed the existence of cracks parallel to the loading axis which decreased the stress concentration with the incremental increase of the load level (Fig.4.1.6a). The optical examination of the failed coupon also revealed the longitudinal cracks which led to the relief in the stress concentration shown in Fig. 4.1.6b after a maximum value for the SIF was reached at approximately 25 kcycles.

4.1.3.2 CFRP patch-Al substrate

The performed testing protocol was identical to type I specimens. Hence, in order to be able to monitor the debonding process of all investigated bonded repairs, the determination of the load level where debonding initiated and propagated was essential. To that respect, fatigue tests with gradually increased load level were carried out (5-30% of the ultimate tensile strength (σ_{uts}) of aluminium (~ 483MPa)). 5%, 10%, 15%, 20%, 25% and 30% are the stress levels which carried out. The synchronization of the infrared camera with the heat source (mechanical stresses induce thermal fields) resulted in the amplitude images of Fig.4.1.11a-g. Due to low contrast, the debonding trace is delineated on the images in order to assist the reader. The arrows indicate the direction of damage propagation. The PTFE inserts that acted as debonding initiators are represented with rectangles at the patch edges.

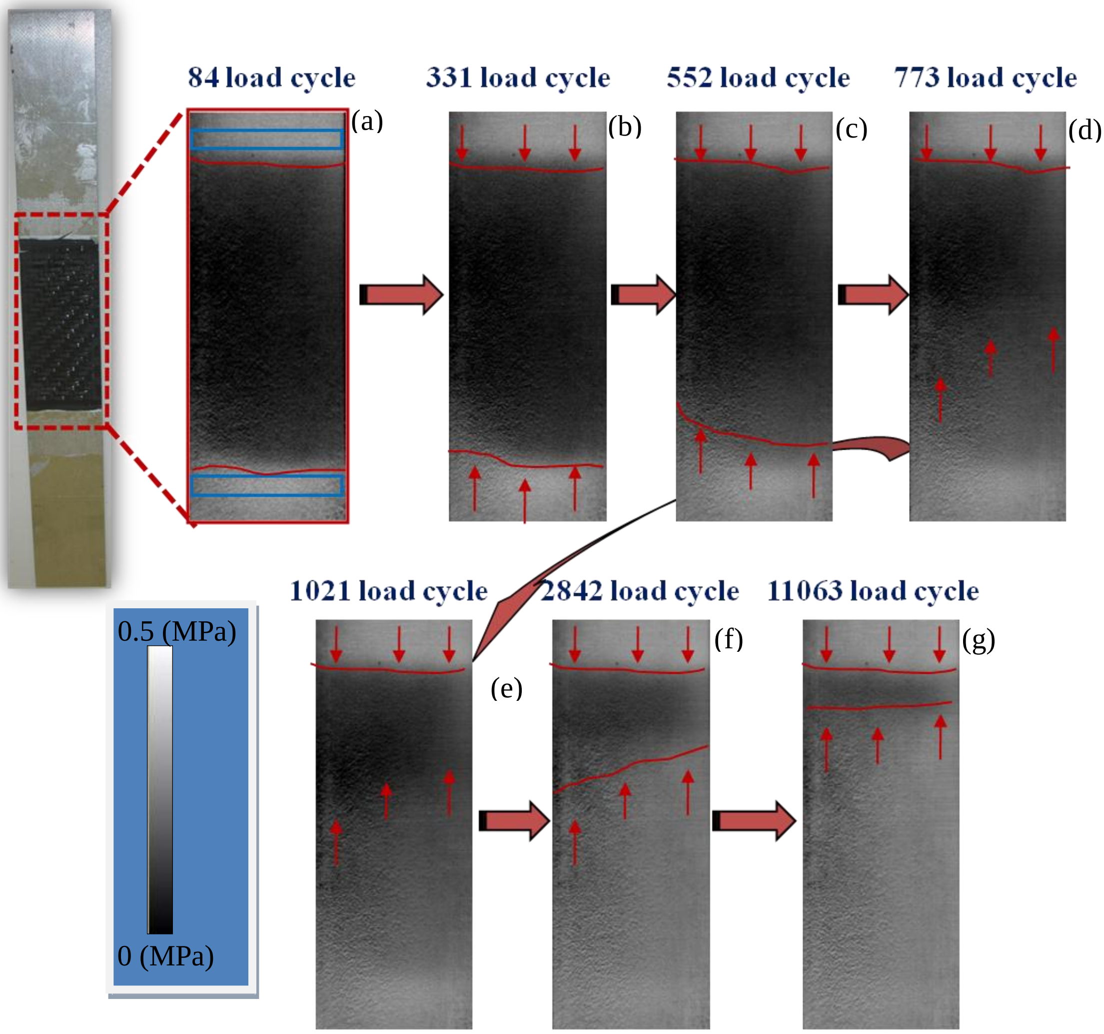

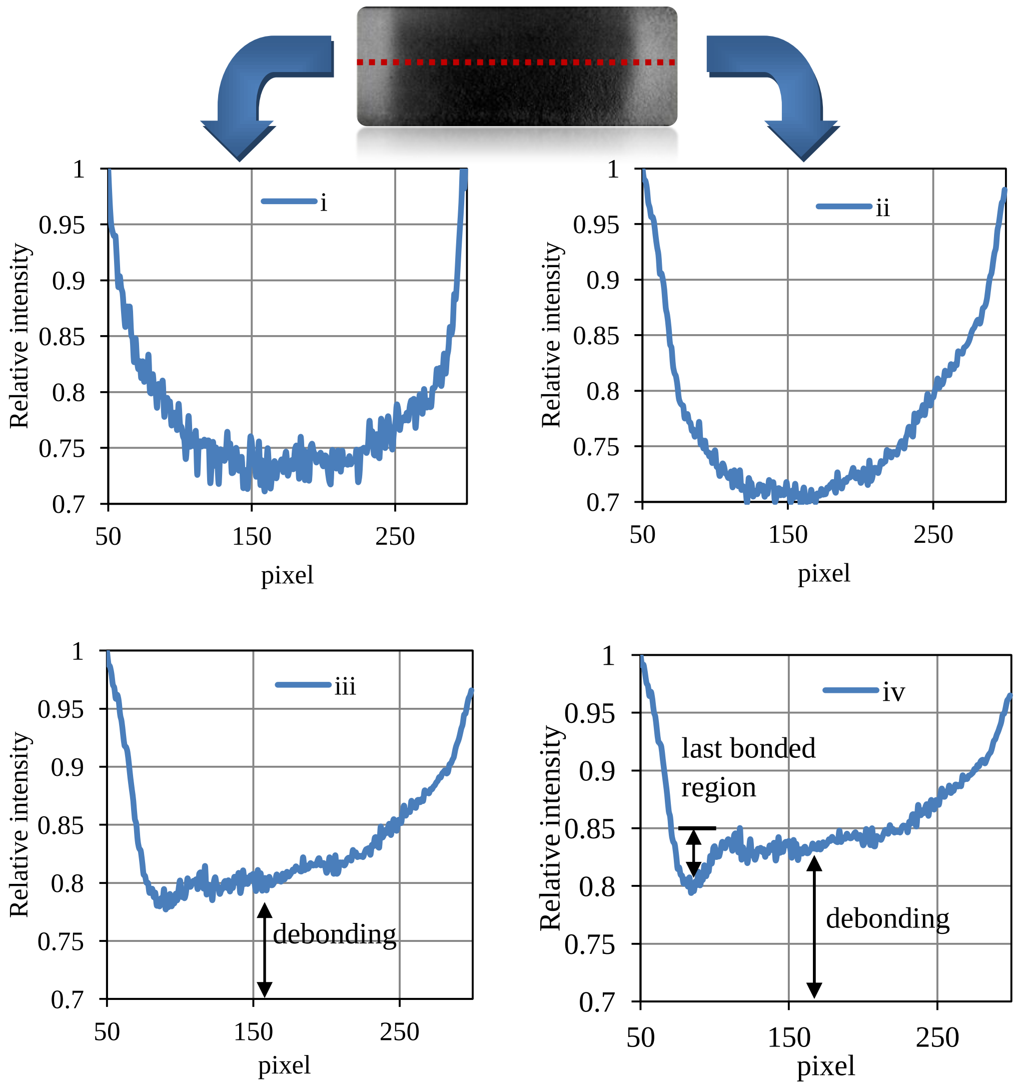

Figure 4.1.11 *Critical failure of the patch during fatigue loading (a) 84 cycles, (b) 331 cycles, (c) 552 cycles, (d) 773 cycles, (e) 1021 cycles,(f) 2842 cycles and (g) 11063 cycles, (i-iv) relative intensity vs. line pixels ((Type II (Figs.4.1.2d and 4.1.2e)).*

As was observed from the on-line thermographic testing (Fig.4.1.11a to 4.1.11g), the failure of the interface between the patch and the substrate is observed with the gradual brightening of the amplitude images. Thus, every dark region in the image corresponds to 'good bonding /sealing' between the patch and the mother structure while otherwise critical damage is observed. At approximately 30% of the σ_{uts}, the debonding of the patch from the substrate initiated and propagated in a stable manner, from the edges towards the centre. As is seen in Figs.4.1.11a-4.1.11g), the image became brighter next to the location of the PTFE tapes at approximately 84 cycles. This was an indication of critical debonding of the patch from the substrate from the very first stage of the fatigue testing. As fatigue loading continued, the image was becoming brighter at the debonding front i.e. after the initial crack (PTFE tape) and the edges of the CFRP patch. The dark region moved to upper regions and the shear stresses were building at different bonded locations tending to completely detach the CFRP patch from the Al substrate. At approximately 11000 cycles, only a small vertical dark region was present in the observed image. Further fatigue loading did not bring any change in the observed pattern. This was due to the fact that the bonded length was not enough to reach the necessary shear level to further propagate the damage. Figs.4.1.11i – 4.1.11iv illustrate the deterioration evolution of the patch /substrate interface by means of relative recorded amplitude /magnitude values. A straight line was created through the camera software in order to be able to plot the raw data of the magnitude images. As much, Figs.4.1.11i – 4.1.11iv depict the relative recorded amplitude values during arbitrary phases of mechanical loading as a function of the covered by the straight line, pixels. More analytically, Fig.4.1.11i corresponds to the early stage of testing at the very same time where the patch is still bonded on the substrate. In this graph, high relative intensity values (edges of the straight line) correspond practically to the areas outside of the patch region. The central area (Fig.4.1.11i) exhibits a large plateau with low relative intensity values (~0.75) which corresponds to the bonded region of the patch with the substrate. With the deterioration process of the patch (Figs.4.1.11ii to 4.1.11iv), the minimum relative amplitude values were minimized in the centre area (~0.82). At the same time, magnitude images gradually became brighter (Figs.4.1.11a-g) at the debonding front. The last bonded region shown in Fig.4.1.1g was graphically verified by Fig.4.1.11iv with a small drop. Mechanical testing of this type of specimens did not lead to failure of the coupon, but merely to critical damage of the repair from the substrate. Loading was below the fatigue limit of Al substrate, and the experiment was stopped at approximately 25 kcycles as there was no need to further mechanically fatigue the substrate up to its failure after the debonding of the repair did not propagate any further. As can be seen in Fig.4.1.11, the initiation and evolution of the debonding process was successfully monitored throughout the fatigue loading, even in the case of very modest bond strength, as it was for the model type I coupons.

After the loading, the coupon was carefully examined in order to verify the length of the remaining bonded area. This was performed by slightly bending the coupon and optically examining the bonded area under a stereoscope (Fig.4.1.12). In Fig.4.1.12 the last thermographic image (Fig.4.1.11g) of the test is juxtaposed with an optical image of the coupon cross-section, verifying the thermographically assessed remained bonded length.

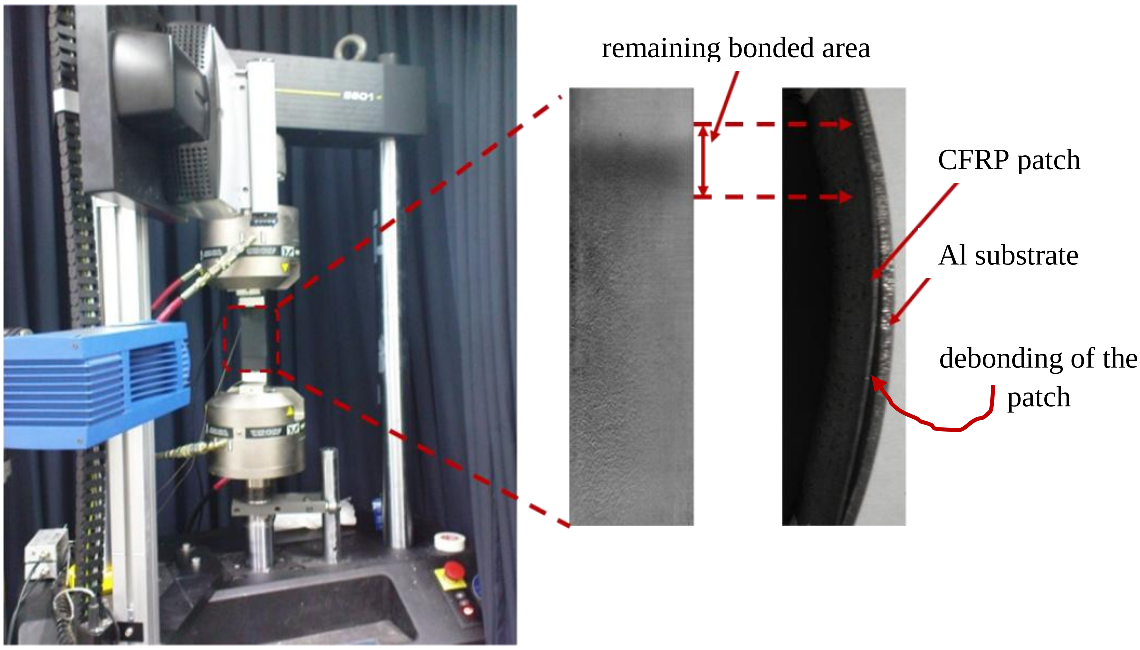

Figure 4.1.12 *Comparison between the optical and thermographically recorded images.*

Section conclusions

The main objective of the present paper was to evaluate lock-in IR thermography, as an effective non-destructive method for the on-line monitoring of the structural integrity of bonded patch repaired materials. The method was employed to monitor and quantify the initiation and propagation of critical and subcritical damage due to fatigue loading.

In order to obtain a more general overview of the bonded repair efficiency, two different combinations of materials were investigated; composite repaired (i) CFRP and (ii) Al substrates.

CFRP substrates with a circular notch were repaired using tapered CFRP patches (type I specimen). The relative amplitude variations at the vicinity of the crack were found to correspond to local stress variations. In other words, the relative amplitudes as recorded by the thermal camera are equivalent to the SIF at the locus of the discontinuity. These were identified and quantified by simply normalising the amplitude profile at the vicinity of the notch to the recorded amplitude away from the crack along a transverse straight line that dichotomised the crack.

The fatigue loading of the specimens at low stress levels showed that the local stress concentrations at the notch remained practically constant with increasing load level up to 80%. However, even at the early loading stages, longitudinal cracks on either side of the notch could be clearly observed in the recorded amplitude images, which possibly acted as a stress relief mechanism that led to an initial decrease in the stress intensity factor. These cracks delineated stress free or more precisely less loaded dark ribbons underneath the notch. However, at 80% fatigue level, debonding initiated and propagated. The debonding process was clearly identified thermographically. At the same time the evolution of the stress concentration at the vicinity of the notch was recorded. For approximately 20 kcycles, the stress intensity factor remained constant. Thereafter, the SIF at the notch exhibited a steep increase, reached a plateau at approximately 25 kcycles and decreased again to 1.5 when the coupon failed. This non monotonic behaviour was attributed to the critical debonding failure of the patch in combination with the damage tolerant behaviour of the coupon, where extensive longitudinal splitting led to the relief of the stress concentration.

In the second part on the current task (type II specimen), CFRP patches were attached to Al substrates and PTFE inserts were employed as debonding initiators. During fatigue at 30% of σ_{uts}, well bonded areas appeared darker than debonded areas enabling the monitoring of the critical failure process. After approximately 11000 cycles, no further debonding was observed. A dark region vertically to the loading axis was indicative of the last well bonded area. Further loading did not bring any further debonding, due to the fact that the bonded length could not generate the necessary shear stresses to further increase the critical failure degree.

Summarizing, on-line lock-in thermography was successfully employed to detect and quantify both critical and subcritical damage evolution in composite repaired substrates. The monitoring of the repaired materials was performed in real time fatigue loading, which simultaneously served for the thermal excitation of the specimen i.e. no external excitation source was required. Both the debonded area (type I and II) and the SIF at the vicinity of the notch (type I) could be quantified at all times during the loading of the coupons. This demonstrates that IrT possesses large potential as a method for the monitoring of the repair efficiency in aircraft materials, as it provides a wide field and non contact non destructive evaluation. IrT can be employed to provide qualitative and quantitative information in relation to the repair efficiency before the qualification of any bonded patch for aircraft application.

4.2 Monitoring of damage initiation and development in Carbon Fibre Reinforced Polymers & Glass Fibre Reinforced Polymers using the Electrical Resistance Change Technique

4.2.1 Introduction

Conventional non-destructive techniques offer the capability of periodical inspection; nevertheless they are unable to provide structural information in real-time conditions. Continuous health monitoring is the key issue to enhanced structural safety and minimization of maintenance time. The exploitation of the material properties for SHM purposes means that the material itself acts as a sensor, which further minimizes the structural aggravation by rendering all external sensing devices and systems redundant [122, 268]. Considerable research effort is currently focused on the variation of the electrical resistivity (or conductivity of composites and its relation to strain and damage. In the simplest case, the variation of the electrical resistance has been proven to provide real time information firstly on the strain and secondly on the damage accumulation of the composite [133, 135-142, 144]. As previously mentioned (chapter 2), the introduction of well-dispersed carbon nanotubes (CNTs) in CFRPs leads to modification of the epoxy matrix into an antistatic or a conducting phase increasing the total conductivity of the composite, particularly in other directions than those of the conducting reinforcement [180, 247, 269-272]. Also, non-conductive GFRP materials may acquire self-sensing properties via i) well-dispersed CNTs in the epoxy matrix [192] and ii) CNT fibres embedded at certain locations in the composite structure [123, 273]. More analytically, any increase in the applied strain is manifested as an increase in the electrical resistance of the composite. At a first approximation, strain and electrical resistance are linearly dependent and thus, electrical resistance changes directly yield real time strain fluctuations due to mechanical loading. These resistance fluctuations are due to the reversible deformations of the percolated conductive network which deforms following the global deformation of the composite. If accumulated damage results to the rupture of the conductive network at the locus of flaws, this should result to an irreversible increase in the electrical resistance of the composite. This irreversible electrical resistance change may be straightforwardly correlated to internal damage of the material [104, 123, 126, 148, 156, 183, 191, 230, 232, 233, 235, 240, 274-280].

The aim of this section is to exploit the electrical properties of both CFRP and GFRP materials as a means of identifying damage within the structural material. With respect to CFRPs, both conventional and CNT enhanced fibre reinforced polymers were examined with a view to identifying the sensing capabilities in terms of strain variation and global damage monitoring, especially in the case of multiscale reinforcement. Regarding GFRP materials, conductive CNT fibres embedded in the structure were monitored in terms of strain as well as damage monitoring. CNT fibres were appropriately embedded at specific locations between the layers of the glass /epoxy laminates. An Electrical Resistance Change Monitoring technique (ERCM) was employed to study damage evolution in all composite materials scenarios. In the case of CFRPs, the inherent electrical properties of have been examined as a self-sensing technique for internal damage of the material. In the GFRP complementary study, the CNT fibres worked as internal sensors allowing for strain monitoring during mechanical loading.

4.2.2 Materials

Regarding CFRPs, two types of unidirectional laminates (plain epoxy matrix and hybrid - CNT enhanced epoxy matrix) were manufactured using the infusion method (Fig.4.2.1b – 4.2.1j). In both CFRP cases the unidirectional carbon fabric G0947 1040 by Hexcel (France) was employed for the reinforcement. The epoxy matrix used was the Araldite LY 564 /Aradur 2954 by Huntsman International LLC (Switzerland). The employed curing cycle was 2h at 60^0 C followed by 4h at 120^0 C post curing. Multi Wall Carbon Nanotubes (MWCNTs) by Arkema (France) were employed as additives in the epoxy matrix for manufacturing of the hybrid composites at a 0.5% w/w CNT /matrix ratio. Dispersion of the CNTs in the epoxy matrix involved sonication for 2h using the ultrasonic processor UP400S (400 watts, 24kHz) by Hielscher at 50% amplitude (Fig.4.2.1a), which was found to yield optimal fracture toughness properties for 0.5% w/w CNT /matrix ratio [189, 281]. During dispersion, the mixture was kept in an ice bath to avoid overheating (Fig.4.2.1a). The fibre volume fraction was measured using an optical microscope and image processing software at approximately 56% for both laminates. A complete representation of the particular manufacturing steps regarding the infusion method is shown in the following image sequence (Fig.4.2.1).

- Cutting of the fabric layers at the desired dimensions
- Laying-up of the particular layers
- Release agent coating of the mold surface
- Laying-up of the bagging materials (release ply, green ply, omega flow, vacuum bag)
- Vacuum application (approximately -1Atm)
- Resin infusion
- Curing and post-curing of the matrix according to the recommended curing process of the supplier.

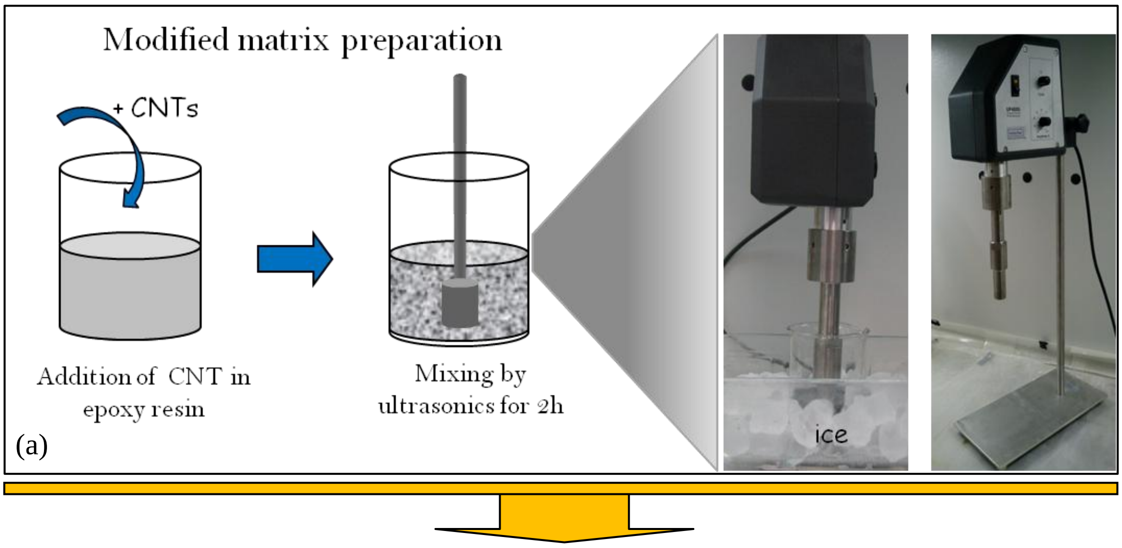

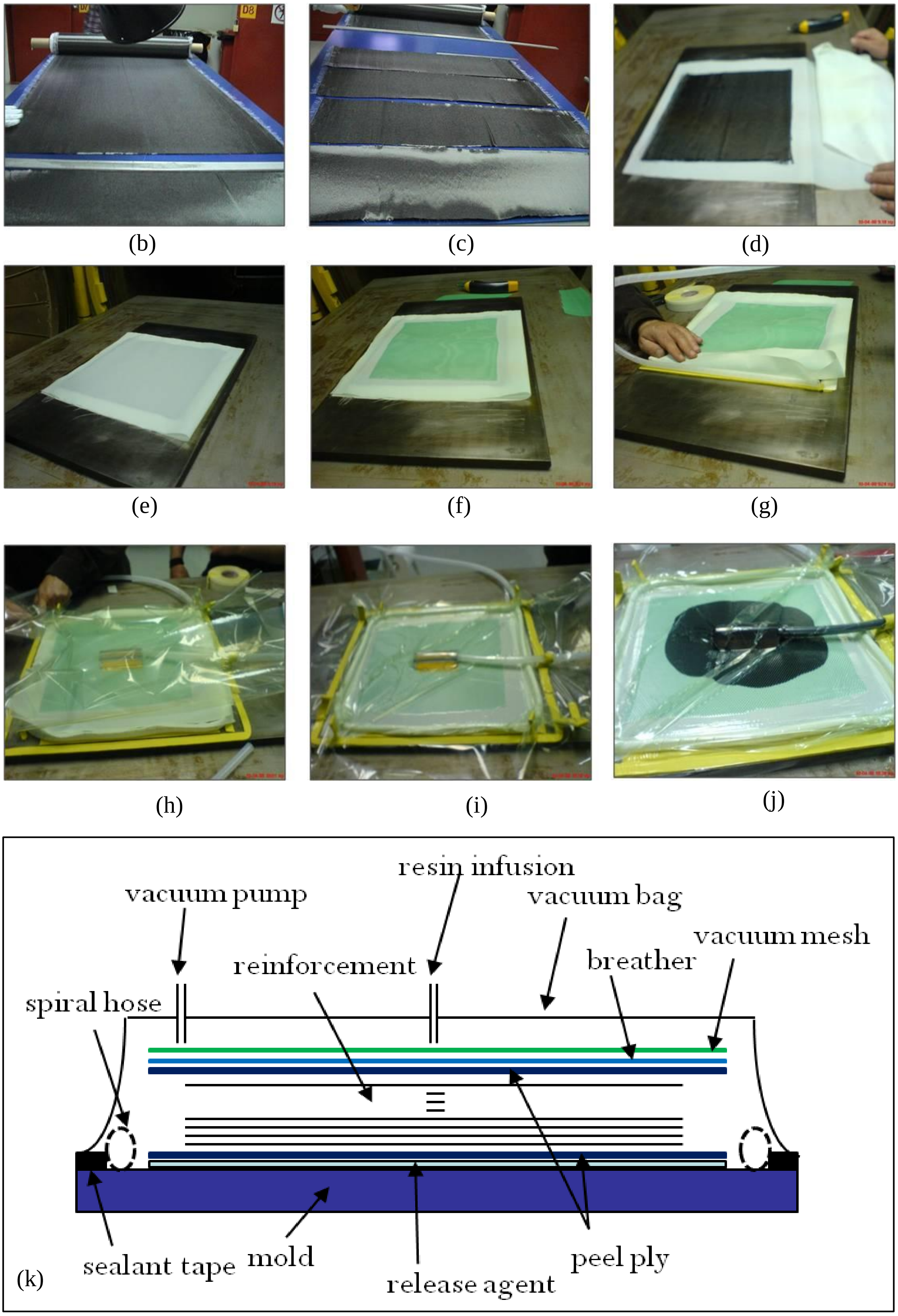

Figure 4.2.1 *CFRP specimen manufacturing procedure (identical to the GFRPs); (a) CNT mixing, (b-h) laying up, (i) vacuum application, (j) resin infusion, (k) infusion bagging.*

With respect to CFRPs, after curing phase, the preparation sequences followed tabs bonding and specimen cutting. Coupons in dimensions 15x250mm^2 (Fig.4.2.2) were cut from the cured laminates according to ASTM-STP3039. In order to ensure good electrical contact between the specimen and the resistance measuring device, the bottom and top edges of all specimens were lightly ground using a 200 grit emery cloth. The surfaces were subsequently cleaned with de-ionized water and drops of acetone. Following the cleaning process, the specimens were left to dry for 4h in 40^{0}C in a vacuum oven before the next preparation step. A small amount of silver paint was applied on the edges of the specimens to serve as conductive contact material. Electrically conductive adhesive tape was wrapped around the griping area. The copper leads of the 34401A digital multimeter by Agilent were directly connected to the electrical conductive tape using spring connectors. GFRP tabs were subsequently attached using high shear adhesive. GFRP tabs served also as insulating material to avoid short circuiting via the test frame. Using this configuration, the electrical circuit was closing within the gripping area of the loading frame, which offered the advantages of (a) preventing the connection cables from damage during mechanical loading and (b) ensuring that there were no strain effects on the electrical resistance measurements such as an increase in the contact resistance due to strain induced contact deterioration. The two-wire method was employed for resistance measurements. In Fig.4.2.2, a CFRP specimen as well as the electrical resistance measurement configuration are depicted.

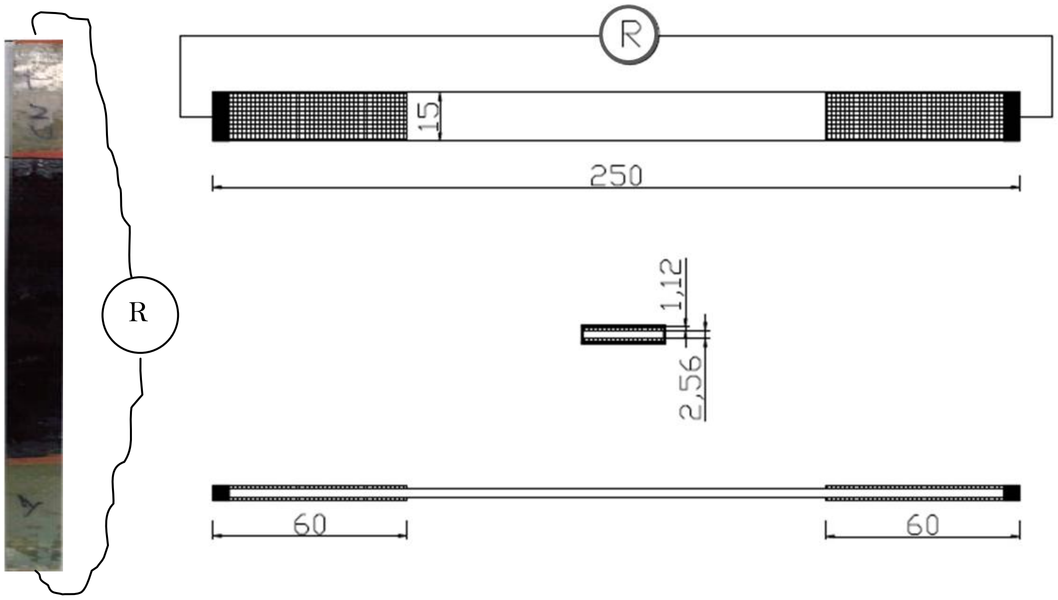

Figure 4.2.2 *CFRP plain/modified matrix specimen configuration; electrical resistance measurement protocol.*

The aforementioned CFRP manufacturing process was almost identical to the GFRP specimen case, with distinct differences, which involved the embedding of the CNT fibre instead of the uniform dispersion of the CNTs in the CFRP matrix. For such case, the matrix was an epoxy system Araldite LY 564 /Aradur 2954 (curing cycle 2h at 60^0 C and post-curing cycle 4h at 120^0 C) (Huntsman International LLC) and a woven glass fabric (S2, Style 6781, Fiber Glast Developments Corporation) in orientation $[0^0]_{12}$ for reinforcement. After the lay-up process, the infusion of the matrix followed. As should be noted, infusion was one-way option due to the addition of CNT fibres (Fig.4.2.4a). The respective manufacturing process is shown in Figs.4.2.3a and 4.2.3b.

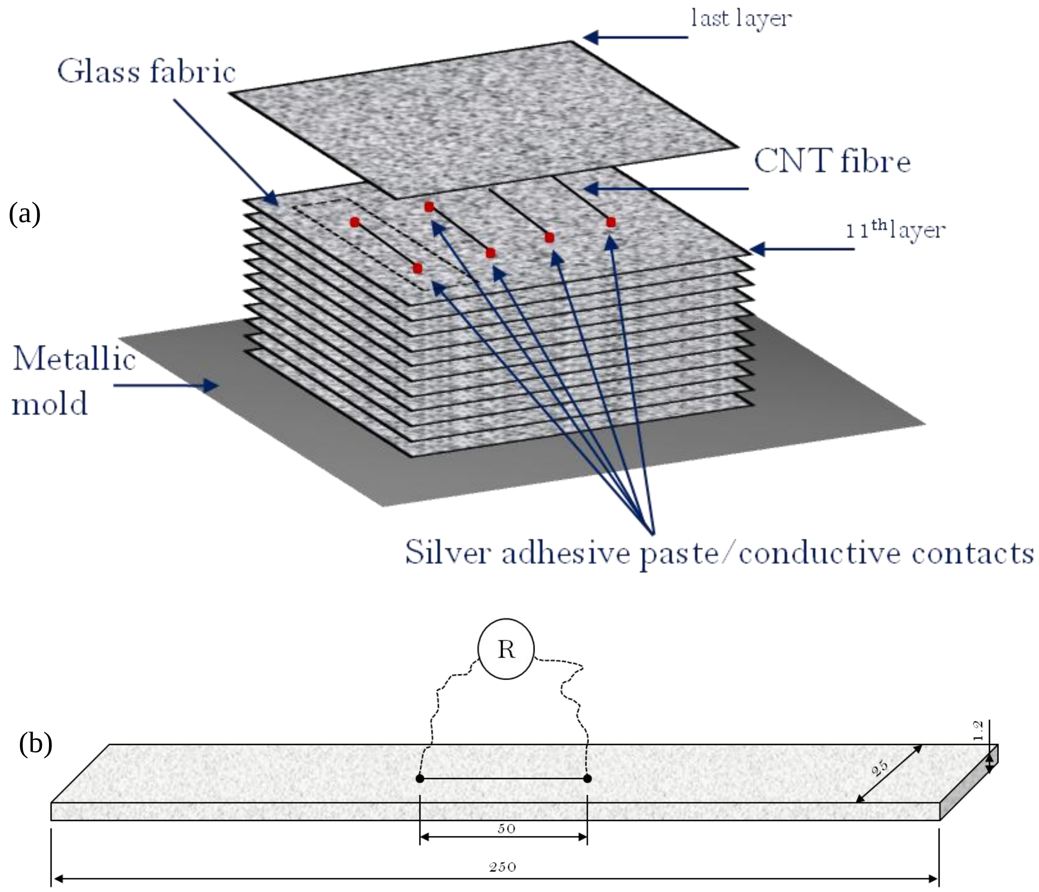

Figure 4.2.3 *(a) Lay-up process, (b) specimen dimensions and electrical resistance measurement protocol.*

The CNT fibres were provided by Centre de Research Paul Pascal, within the framework of the Noesis AST4-CT-2005-516150 European Project (FP6-STREP, Thematic Priority "Aeronautics and Space"). More analytically, MWCNTs (Arkema) were employed for the CNT fibres manufacturing and PVA polymer for the fibre matrix. These fibres possess excellent toughness and controllable electrical resistance response to load/ strain, albeit with reduced strength values. Details of the manufacturing and the optimization process may be found elsewhere [195, 196]. The CNT fibres were introduced at certain locations during the manufacturing process of the laminate. After specimen cutting, every GFRP coupon included one CNT fibre in its centre along the longitudinal axis (Fig.4.2.3a and b), working as a strain /damage sensor. The CNT fibres were located between the 11th and 12th layer of the laminate (Fig.4.2.3a) using an adhesive spray which did not affect the physical characteristics of the CNT fibres as well as the rest elements of the composite laminate. When the CNT fibres where laid on the 11th layer, small loadings of silver loaded adhesive paste were applied on both ends of every CNT fibre to enhance the electrical connection with the recording cables of the multimeter. These small quantities of silver paste impregnated a small zone of the last glass fabric layer (12th) and thus electrical connection access with the ends of the CNT fibres was feasible. CNT fibres were placed between the penultimate and final layer and before the resin infusion process. As was observed after the matrix curing process, the ends of the CNT fibres were pin-pointed as visible spots on the surface of the GFRP plate (Fig.4.2.4b and 4.2.4c). After specimen cutting, the CNT fibre edges (visible surface spots) were slightly ground with a 200 grit emery cloth and thoroughly cleaned using water and acetone subsequently. After specimen drying in an oven for 4 hrs at 40 ^{0}C, additional silver paste was used for the bonding of the copper flexible wires which provided electrical connection with the multimeter (Fig.4.2.3b). Fig.4.2.3a shows a schematic representation of the CNT fibre location in between the reinforcement layers as well as the areas were silver paste was placed. In Fig.4.2.4a the particular CNT fibres placed on the 11th layer are visible. Fig.4.2.4b and 4.2.4c present the cured GFRP laminates. Finally, specimens were cut from the cured plates (25x250 mm^2 ASTM-) and cables bonded on the top in between the gauge length (Fig.4.2.3b).

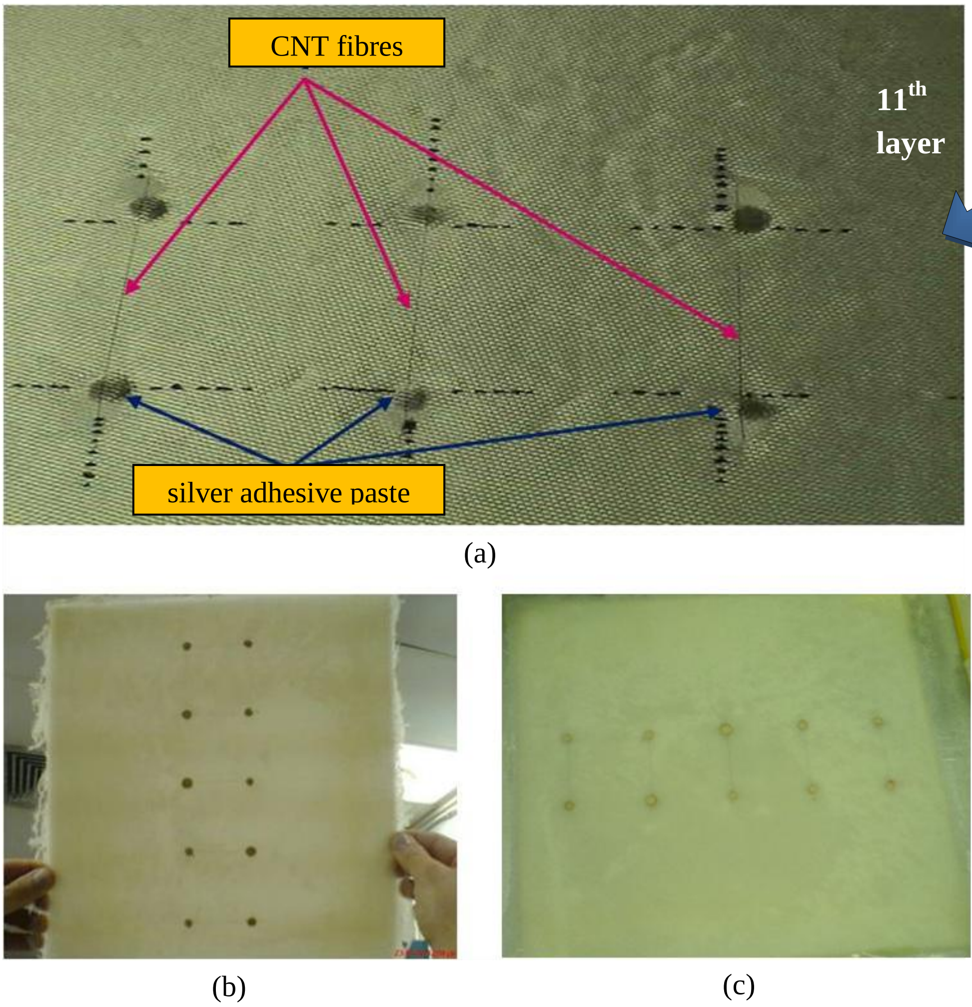

Figure 4.2.4 *(a) 11th layer, CNT fibres and electrical contacts at the fibre edges, (b, c) GFRP laminates after curing.*

4.2.3 Testing procedure

Loading-unloading tensile tests were performed for both CFRP and GFRP specimens in order to investigate their electrical resistance response to applied mechanical load. For all experimental testing an INSTRON 8801 universal testing machine equipped with 100 kN load cell was employed (Fig.4.2.5a).

With regard to CFRPs, the loading protocol involved incremental loading steps at load control mode with constant loading and unloading rate of 0.2 kN/s. The incremental loading cycles continued until the tensile failure of all specimens. The performed loading-unloading sequence is presented in Fig.4.2.5b. The increment of load for each consecutive step was 4 kN. GFRP embedded CNT fibre specimens were tested both in monotonic and loading–unloading testing. For the monotonic tensile tests, a constant 1mm /min rate was adopted. The loading unloading protocol of GFRPs was similar to that adopted in the CFRP case. The incremental stress step of the loading protocol was kept to 100MPa, as the GFRP laminate possessed lower stiffness and strength compared to the CFRP coupons. For all specimen configurations, loading-unloading testing was performed in 50% humidity and room temperature conditions. In all cases, electrical resistance measurements were recorded in real time during load-unload testing employing the inbuilt serial port of the Agilent multimeter (Fig.4.2.5a). The electrical resistance acquisition frequency was 2 Hz.

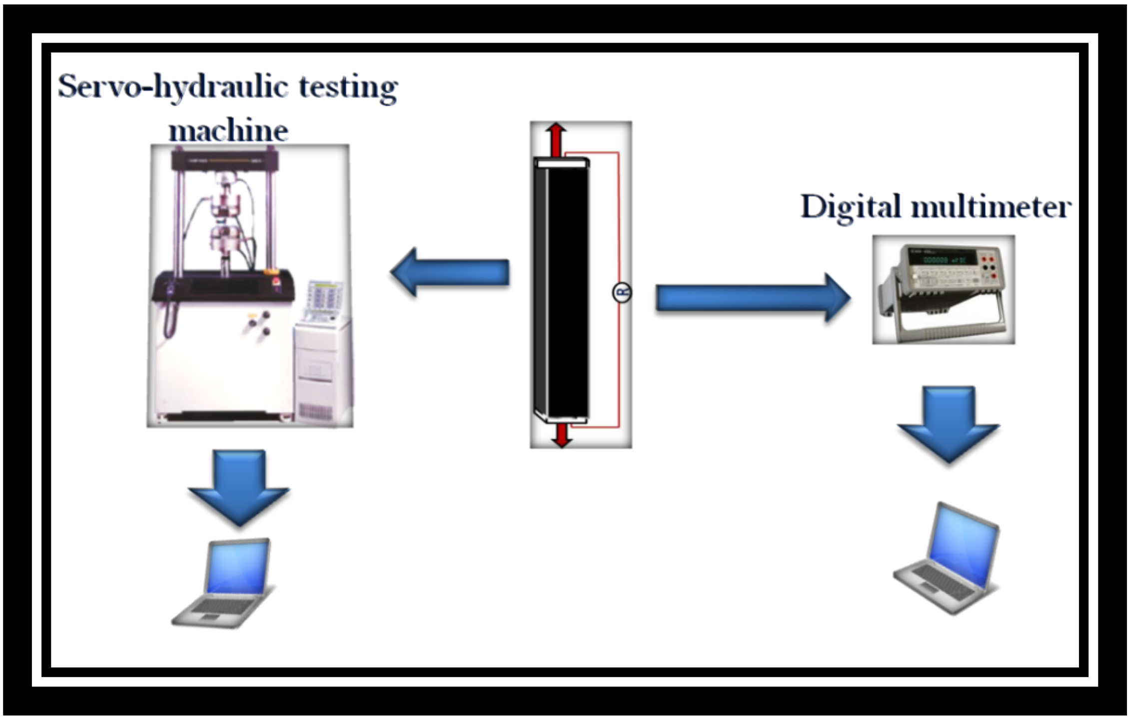

Figure 4.2.5a. *Experimental setup of electrical resistance change method.*

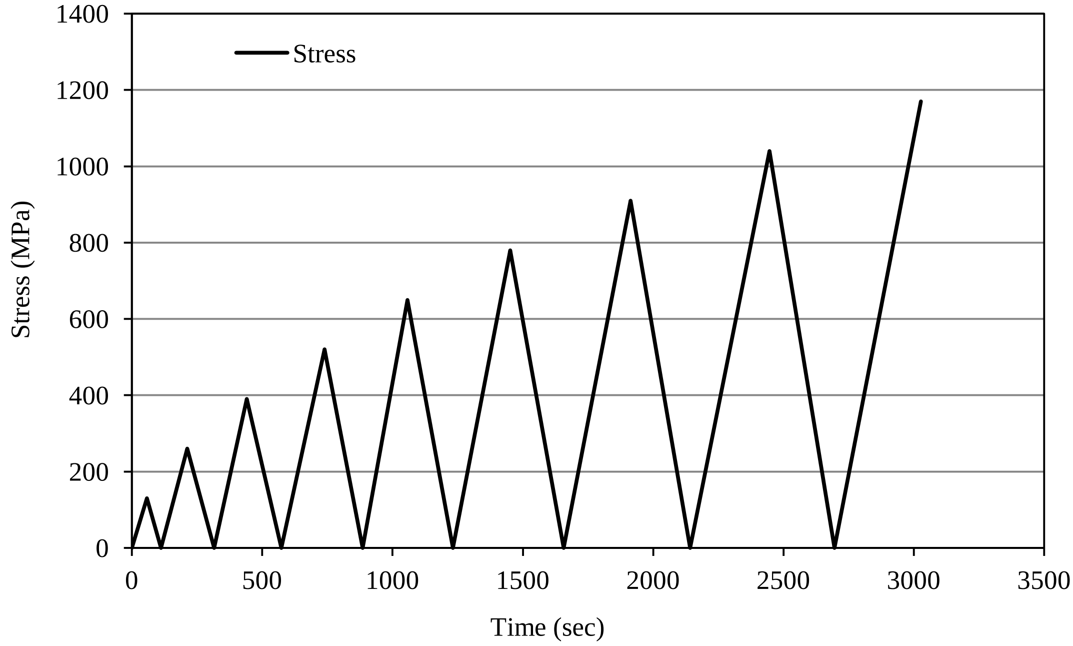

Figure 4.2.5b *Typical loading-unloading cycles (CFRP coupons).*

4.2.4 Results and discussion-CFRP laminates

4.2.4.1 Deterioration of mechanical properties

Fig.4.2.6a presents a stress-strain curve of the 9th loading cycle of Fig.4.2.8a. The calculation of the Young's modulus values was performed according to ASTM D 3039/D 3039M – 95a. Fig.4.2.6b depicts the normalized Young's modulus (E/E_0) as a function of loading steps. As seen in Fig.4.2.6b, the relative Young's modulus is increasing for both plain CFRP and modified matrix samples from the first cycle until the 7th cycle and the 8th cycle for the plain and the CNT-enhanced CFRPs, respectively. Both configurations exhibit four stages (i) an initial rapid increase, (ii) a plateau with a small increasing tendency, (iii) a secondary increase and (iv) a drop prior to failure. In all cases, the increase is attributed to the self-alignment of the longitudinal fibres to the loading axis reinforcement. The final decrease is attributed to cumulative damage that precedes the failure of the specimen.

Fig.4.2.6c depicts the residual strain at zero load versus loading cycles for both configurations. As expected, there is an increase in the residual strain, which is either due to the longitudinal fibre alignment which also results to the stiffening of the CFRPs, or cumulative damage in the composite coupons which results to stiffness loss. It may be argued that the contribution of cumulative damage is less prominent as this effect is saturated much earlier than the stiffening process i.e. at the 6th cycle for the plain CFRP and as early as the 3rd cycle for the CNT enhanced CFRP. After these points, the residual strain at zero load fluctuates around a constant value for both systems (Figure 4.2.6c).

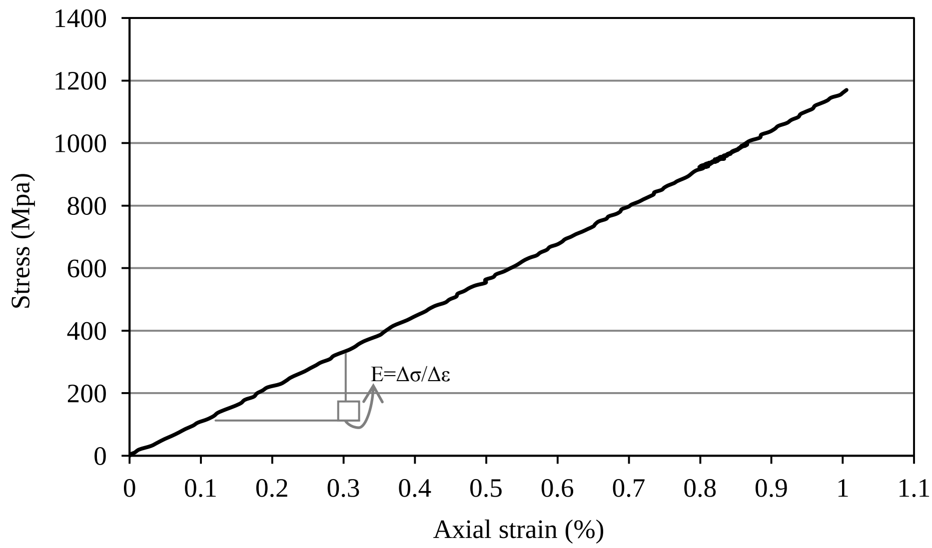

Figure 4.2.6a. *Typical stress-strain curve (9th loading step of the CNT enhanced specimen) modulus calculation.*

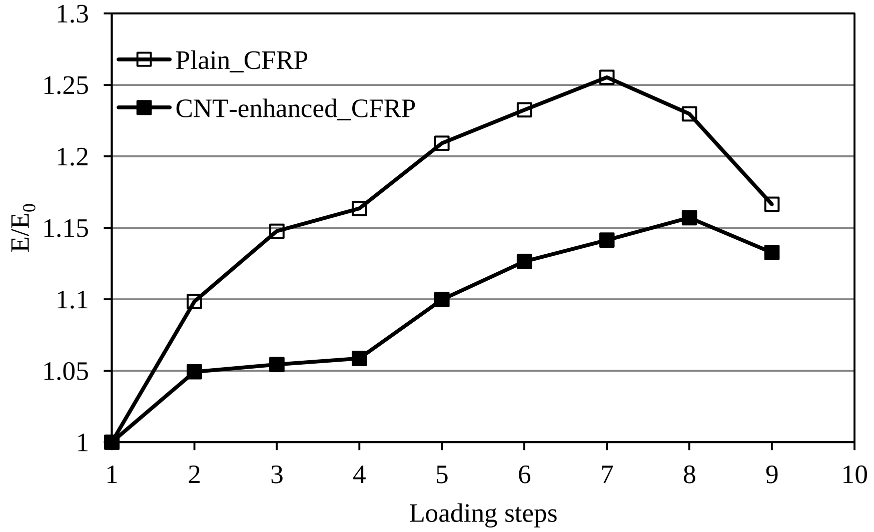

Figure 4.2.6b *Normalized Young's modulus vs. loading steps of CFRP modified-plain matrix.*

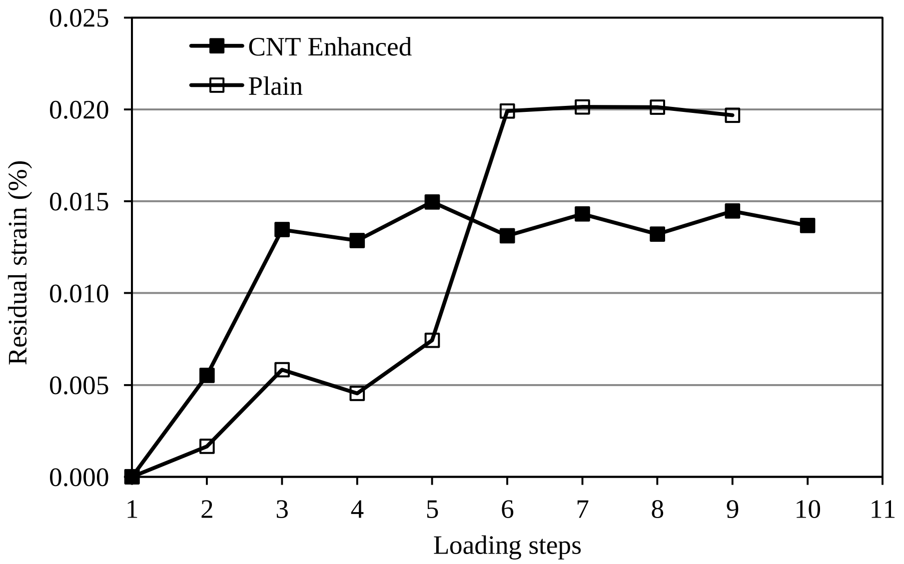

Figure 4.2.6c *Residual strain vs. loading steps of CFRP modified-plain matrix.*

4.2.4.2 CFRP specimen testing (plain matrix)

The electrical resistance technique as is applied in the employed configuration lies in measuring the bulk resistance changes of the specimens. The loading sequence employed for all CFRP specimens is shown in Fig.4.2.7a. The loading increment described in the previous section corresponded to a stress step of 130 MPa. In Fig.4.2.7a, the change of the electrical resistance normalized by the initial resistance ($\Delta R/R_0$) is also depicted.

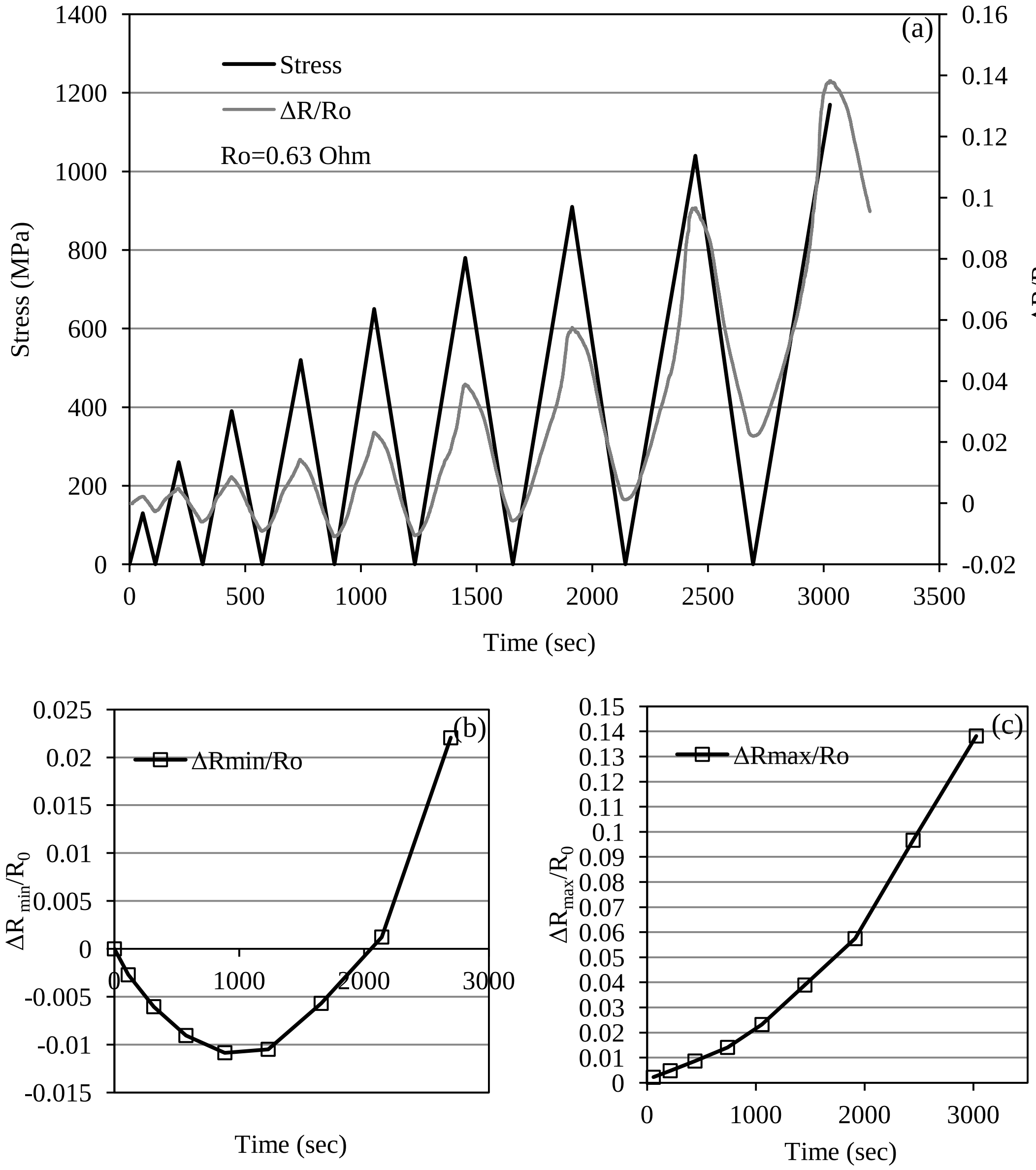

Figure 4.2.7 *Plain CFRPs: (a) stress & $\Delta R/R_0$ vs. time, (b) $\Delta R_{min}/R_0$ vs. time and (c) $\Delta R_{max}/R_0$ vs. time.*

As $\Delta R/R_0$ the resistance change normalized by the initial resistance is defined. As $\Delta R_{min}/R_0$ the resistance change normalized by the initial resistance at the end of each cycle or at zero load is defined. As $\Delta R_{max}/R_0$ the resistance change normalized by the initial resistance at the maximum load of each cycle (which corresponds to the maximum recorded resistance for each cycle) is defined. In Fig.4.2.7a, the triangular variation of the electrical resistance vs. time curve is seen to follow directly the load trace. In Fig.4.2.7b, $\Delta R_{min}/R_0$ at the end of each loading step is depicted as a function of time. $\Delta R_{min}/R_0$ does not exhibit a monotonic behavior as it decreases significantly for the first four load cycles, and afterwards exhibits an exponential increase. Fig. 4.2.7c depicts the evolution of $\Delta R_{max}/R_0$ as a function of time, which increases monotonically with the consecutive loading steps.

4.2.4.3 CFRP specimens (modified 0,5% w/w CNTs matrix)

As seen in Fig.4.2.8a, the change in the $\Delta R/R_0$ values is closely following the applied load by exhibiting the characteristic triangular shape of the loading protocol. $\Delta R_{min}/R_0$ as measured in the end of each loading cycle is depicted as a function of time in Fig. 4.2.8b. Interestingly enough, the minima of the $\Delta R/R_0$ are a monotonic function of time, indicating an irreversible increase in the remaining resistance.

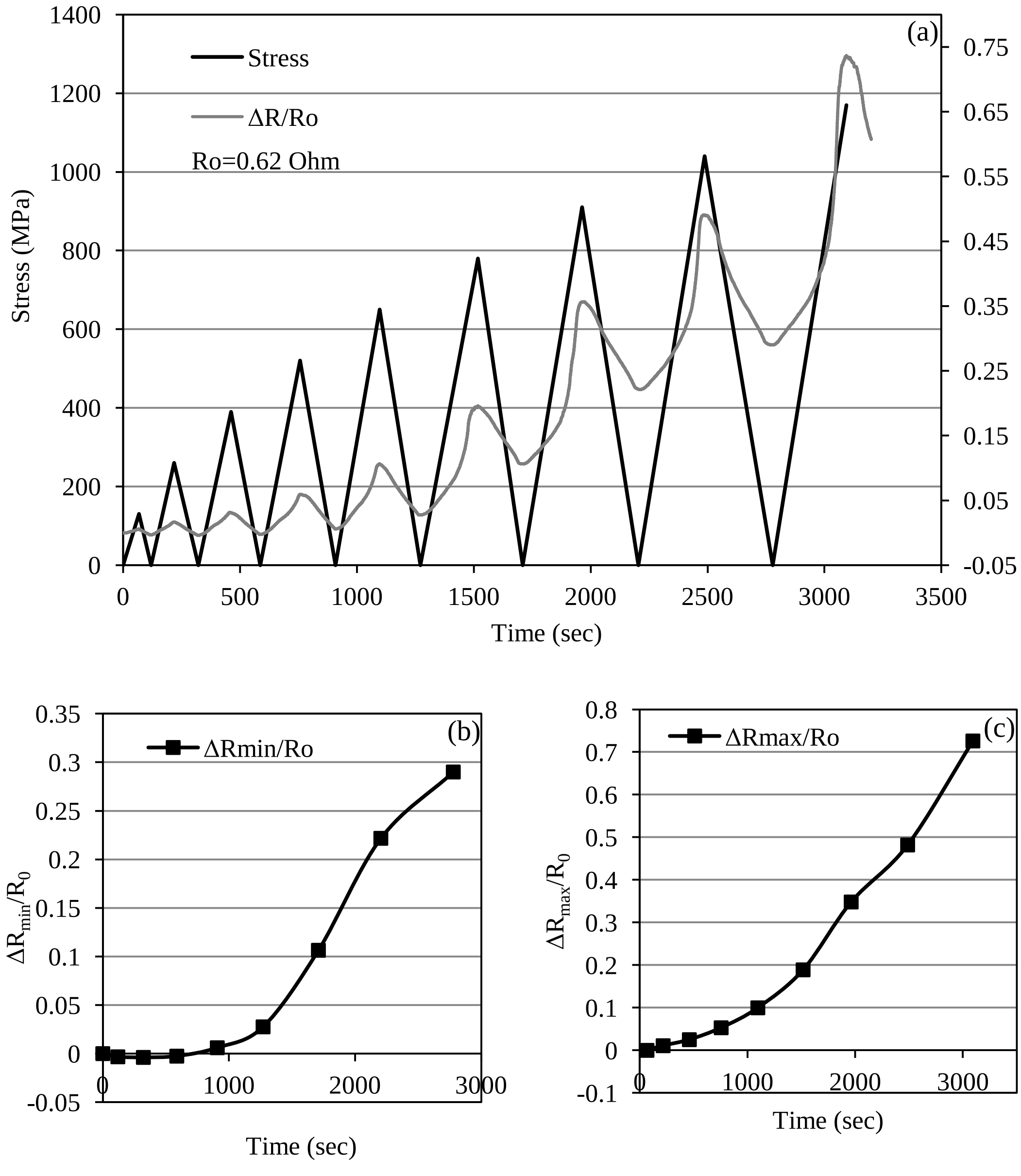

Figure 4.2.8 *CNT enhanced CFRPs: (a) stress & $\Delta R/R_0$ vs. time, (b) $\Delta R_{min}/Ro$ vs. time and (c) $\Delta R_{max}/Ro$ vs. time.*

Fig. 4.2.8c depicts the evolution of $\Delta R_{max}/R_0$ as a function of time, which increases monotonically with the consecutive loading steps.

4.2.4.4 Plain vs. CNT enhanced CFRPs; mechanisms of resistance changes

In both plain and CNT-enhanced CFRP specimens (Fig.4.2.7a and 4.2.8a), the change in the electrical resistance values follow closely the loading pattern. In all cases, $\Delta R_{min}/R_0$ (Fig.4.2.7b and 4.2.8b) corresponds to zero stress, and should be indicative of the structural state of the composite. Although the load induced damage would be expected to cause disruption of the conductive network followed by a monotonic increase in the residual electrical resistance at the end of each loading cycle, this is not always the case. In the case of the plain CFRP coupons, a notable decrease of the $\Delta R_{min}/R_0$ is recorded for the first cycles of the test. However after the 5^{th} loading cycle, a sharp increase in the residual resistance is observed until the last cycle which leads to failure of the sample. This increase is irreversible and may correspond to residual strain and/or damage accumulation due to mechanical loading.

The reduction of the residual resistance may be attributed to the following mechanism: in the case of plain matrix CFRPs the conductive phase is only the conductive reinforcement, or the carbon fibres. As the tested specimens are unidirectional, the electrical conductivity is maximum parallel to the reinforcement axis. The electrical conductance in the transverse direction is accomplished via the random contacts of the aligned carbon fibres. The initial decrease is attributed to the Poisson's ratio effect (Fig.4.2.9) which via the cross sectional reduction increases the possibility of random contacts creation between the longitudinal fibres. As a consequence, this short-circuiting leads to overall increase of conductivity or decrease of electrical resistance. The phenomenon is enhanced both due to the differential Poisson's ratio between the isotropic matrix and the highly anisotropic carbon fibre and the irreversible self-alignment of the reinforcing fibres along the loading axis. However, this effect comes to end after the 5^{th} load step which corresponds either to saturation of the stochastic electrical bridging phenomenon or to the fact that the damage induced increase in resistance becomes the dominant mechanism. Interestingly enough, the saturation of the stochastic bridging phenomenon coincides with the cycle where the residual strain reaches its maximum value for both plain and CNT enhanced CFRPs (Fig.4.2.6c) and not with the loading cycle where maximum stiffness is observed (Fig. 4.2.6b). As this occurs at a later stage, it may be directly concluded that the saturation of the stochastic bridging is taking place prior to the stiffening process. Summarizing, there are two overlapping and competing mechanisms that are dominant in different stages of the loading process. In the beginning, the resistance decrease due to the stochastic bridging phenomenon is dominant and the overall residual resistance decreases. At a later stage, the irreversible resistance increase due to damage becomes dominant and the overall resistance increases. The fifth cycle marks the turning point where the two overlapping mechanisms cancel each other.

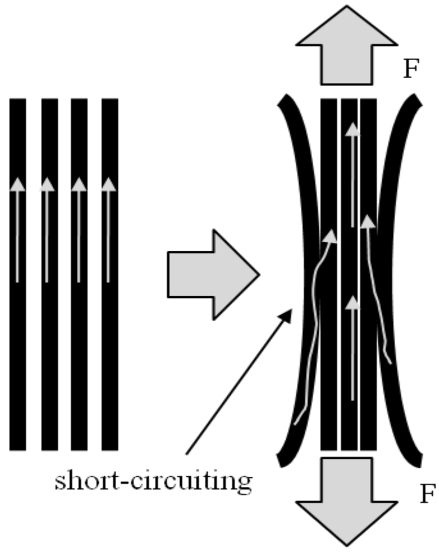

Figure 4.2.9 *Short-circuiting induced by the applied load to the longitudinal axis (Poisson's ratio effect).*

As far as CNT enhanced specimens are concerned, a different electrical response was recorded during the testing procedure. The $\Delta R_{min}/R_0$ changes were practically zero until the 5th cycle where a monotonic increase was observed. In contrast to plain CFRPs, there is no effect of the Poisson contraction. It may be postulated that the incorporation of the conductive nano-fillers created an electrically conductive network between the main reinforcement. In other words, as the electrical conductive phases are constituted by both the reinforcement and the nano-fillers, the nanotubes create a conductive network between the carbon fibres and essentially short circuit the main conductive phase. CNTs provide additional conductive paths to the random fibre contacts and thus the total electrical resistance is reduced in a value lower than the resistance at the saturation point of the plain-CFRP case. In this way, the incorporation of the CNTs allows for the application of the electrical resistance technique for damage monitoring by the elimination of artifacts caused by the creation of the random conducts between the longitudinal fibres. In addition, the sensitivity of the measurements as manifested by the relative change in the resistance values was significantly improved. For CNT enhanced CFRPs, the relative electrical resistance change throughout the loading protocol changed by approximately 5 times more than the plain CFRPs. According to measurements prior to the experiment, the through-thickness electrical resistance was measured to be 2.78±0.15 Ohm and 1.14±0.10 Ohm for the plain and the CNT enhanced coupon, respectively. In addition, the electrical resistance in the transverse direction was measured to be 3.01±0.10 Ohm and 1.98±0.22 Ohm for the plain and the CNT modified coupon, respectively. As is obvious the nano-induction has resulted in increased number of electrical contacts in the composite structures which is clearly reflected by the electrical resistance measurements in the bulk and also the through-thickness direction.

4.2.4.5 CNT effect on the remaining and maximum electrical resistance response

Figures 4.2.10a and c depict the variation of the $\Delta R_{min}/R_0$ and Figures 4.2.10b and d the variation of $\Delta R_{max}/R_0$ at the end of each loading cycle, respectively, as a function of the initial Young's modulus for the plain and for the CNT modified CFRPs. Figs.4.2.11a and c depict the variation of the $\Delta R_{min}/R_0$ and Figs.4.2.11b and d the variation of $\Delta R_{max}/R_0$ at the end of each loading cycle, respectively, as a function of the residual strain for the plain and for the CNT modified CFRPs. $\Delta R_{min}/R_0$ may be directly attributed to residual strain as it corresponds to the unloaded state of the structure and is closely related to damage. In contrast $\Delta R_{max}/R_0$ includes the effect from the additional strain imposed by the applied loading protocol.

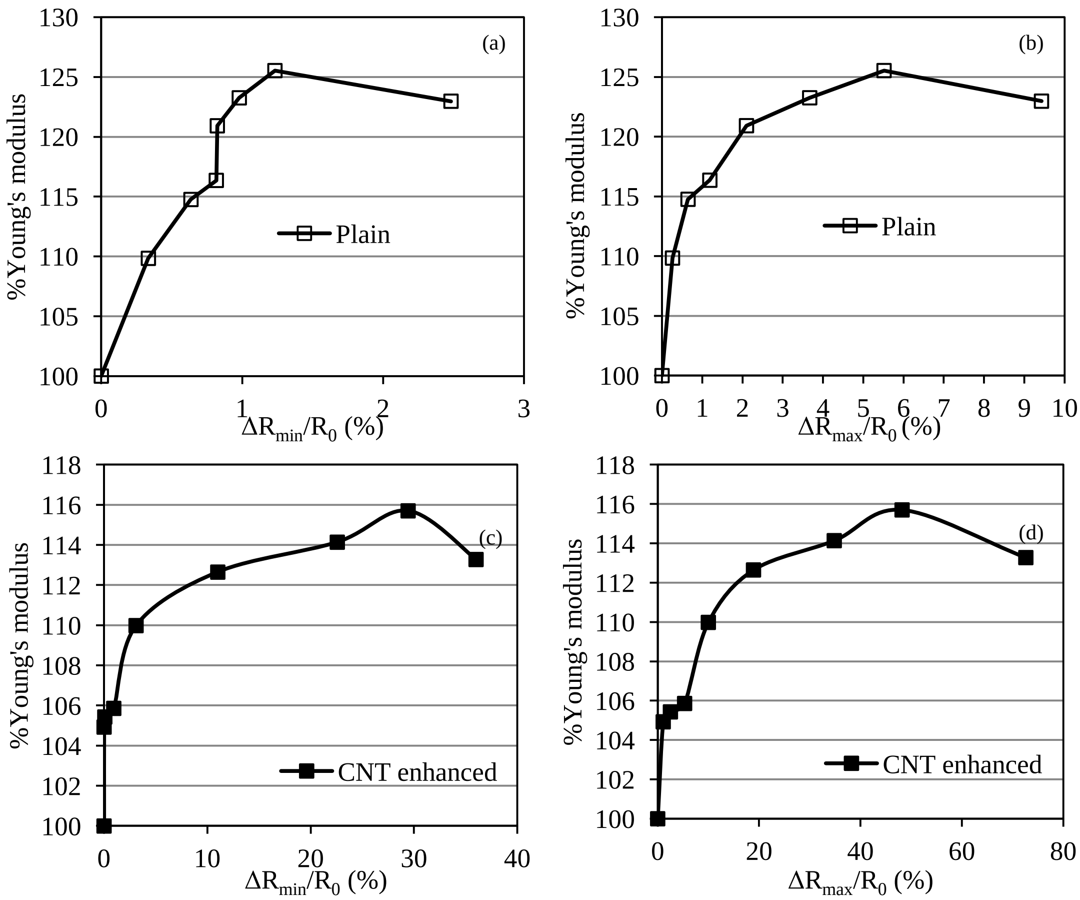

Figure 4.2.10 *$\Delta R_{min}/R_0$ and $\Delta R_{max}/R_0$ as a function of Young's modulus for the (a,b) plain and (c,d) modified specimens.*

For the CNT enhanced CFRPs although the increase of the resistance indices continues until the failure of the CFRPs. It is noteworthy that this phenomenon is not related to piezoresistive effects, as the measured residual strain does not change. It is also notable, that the cycle where the maximum residual strain is noted coincides with the minimum $\Delta R_{min}/R_0$ in the case of plain CFRPs (Fig.4.2.7b) and the significant slope increase (Fig.4.2.8b) in the case of the CNT enhanced CFRPs. This phenomenon coincides with the maximum recorded axial residual strain for both CFRP configurations (Fig.4.2.6c), which may be correlated to the "saturation" of the self alignment process. As is expected, the end of the self alignment process will allow for the activation of the typical failure mechanisms such as stochastic fibre failure /flaw accumulation and /or flaw size increase that typically lead to the brittle failure of the unidirectional composite. However, these degradation mechanisms cannot be readily traced from the change in macroscopic material metrics such as relative stiffness change (Fig.4.2.6b) or residual strain in brittle systems before the final loading cycles of the composites (see Fig.4.2.6b, where there is a traceable stiffness loss for the last loading cycles). It can therefore be concluded that the electrical resistance technique is capable of early detection of the damage accumulation mechanisms that finally lead to the failure of unidirectional composites.

Last but not least, the CNT modified CFRP specimens are more sensitive in terms of resistance changes both in absolute values and in correlation to relative stiffness. Although the effect of the incorporation of the CNTs on the absolute electrical longitudinal resistance values in the pristine state (R_0) was less than the experimental scatter to allow for conclusive observations (0.63±0.11 Ohm for the unmodified coupons and 0.62±0.21 Ohm for the CNT modified coupons), an extremely high increase in the electrical resistance change was observed. A 300% change compared to the initial value was recorded for the CNT-modified coupons, while only a 15% change for the conventional CFRPs. Thus, the CNT incorporation allows for the monotonic correlation between the resistance indices and the loading history (Fig.6a) and an increase in the sensitivity of the measurements by approximately an order of magnitude (2.5 % for the plain CFRPs as compared to approximately 36% for the CNT enhanced CFRPs for the $\Delta R_{min}/R_0$ (Fig.4.2.10a and 4.2.10c respectively) and 9.4% for the plain CFRPs as compared to approximately 78 % for the CNT enhanced CFRPs for the $\Delta R_{max}/R_0$ (Fig.4.2.10b and 4.2.10d respectively).

4.2.4.6 Memory effect of both CNT enhanced and plain CFRPs

In Fig.10, the 6th cycle of Fig.4.2.7a is shown in magnification. In this, three phases of electrical resistance increase are identified. In the first stage, there is an initial rapid increase which becomes slower with load application. In the second stage there is a deflection point, where the rate of resistance change increases again. It is noteworthy that this point is closely correlated with the maximum resistance of the previous cycle or else it corresponds to the maximum load that the coupon has experienced in the previous cycle. In other words, the coupon retains a memory of its previous loading history. The resistance is increasing exponentially at the third stage. As can be observed in Fig.4.2.7a and Fig.4.2.8a, this behavior is consistent for all loading cycles of both protocols plain and CNT-enhanced. The rate of electrical resistance change is indicative of the loading history of the composite material and the onset of more cumulative damage, similarly to what is well established in the case of Acoustic Emission as the Kaiser effect [282]. This memory effect results in the presence of an inflection point at the resistance-time curve as resistance value exceeds the previous maximum load level. Similar behavior has been reported for Carbon Nanotube Modified Glass/Vinylester Composites [192], for Carbon Nanotube Modified Glass/epoxy Composites [191] and also for Ceramic Matrix Composites (CMCs) [233, 235].

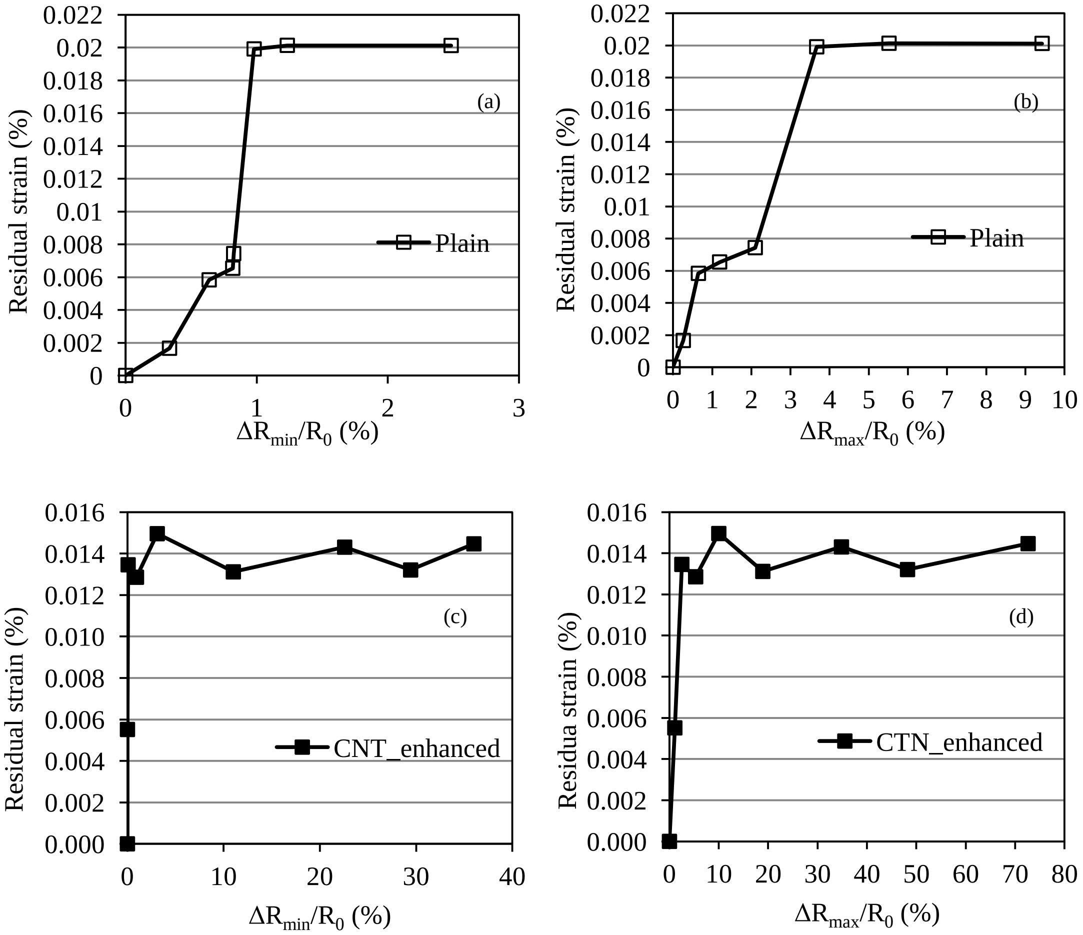

Figure 4.2.11 *$\Delta R_{min}/R_0$ and $\Delta R_{max}/R_0$ as a function of remaining strain at zero load for the (a,b)4plain and (c,d) modified specimens.*

The possibility of exploiting this observation with a view to identifying the previous stresses that the material has experienced lies in the ability to clearly define the inflection point during the second phase. The inflection point corresponds to a local extremum of the first derivative, or where the second derivative changes sign.

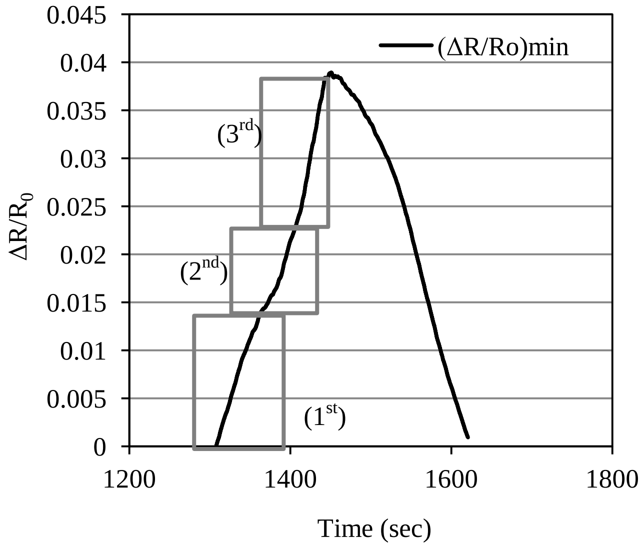

Figure 4.2.12 *6^{th} load-unload cycle of graph Fig.4.2.4b; different steps of electrical resistance increase.*

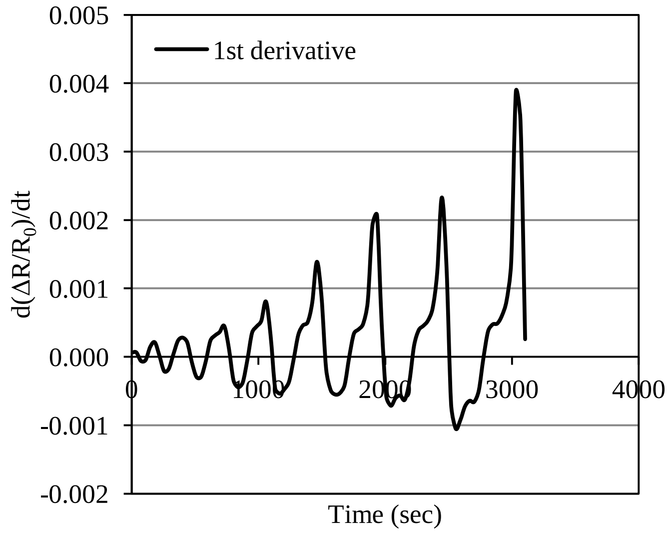

Figure 4.2.13 *Representative 1^{st} derivative of electrical resistance changes of CNT enhanced CFRP.*

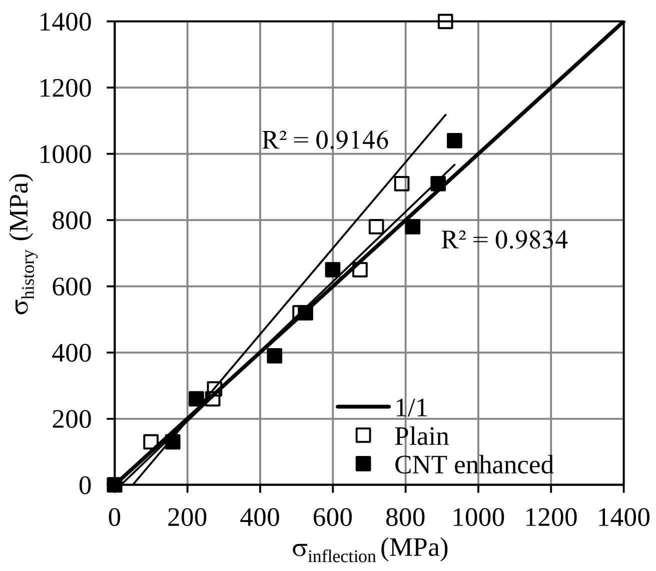

Figure 4.2.14 *Correlation between the predicted stress data and the real stresses; loading memory effect.*

Fig.4.2.13 depicts the first derivative of resistance-time curve of the CNT modified CFRP (Fig.4.2.8a). The experimental curve was interpolated employing cubic splines before differentiation in order to minimize the noise from the experimental data. Fig.4.2.14 depicts the correlation between the measured stress at the time of the recording of the inflection point, $\sigma_{inflection}$, as a function of the applied stress at the previous loading cycle, $\sigma_{history}$. The black line corresponds to the one to one relation or $\sigma_{inflection}=\sigma_{history}$, and is included for reference purposes, together with the linear regression curve of the experimental data. As should be noted, in the case of the plain CFRPs, there is a divergence from the one to one curve at the final loading stages which results to the worse R^2 value compared to the CNT enhanced CFRPs. It can be assumed that the induced damage in the case of the plain CFRPs compromises the memory effect, resulting to a considerable underestimation of the previous load at higher loading cycles. In contrast, for the CNT enhanced CFRPs, the correlation is achieved because of the increased sensitivity provided by the introduction of the conductive nanophase and is indicative of the potential of the electrical resistance technique to assess the loading history of the CNT enhanced structure. Lastly, Fig.4.2.14 depicts the correlation between the predicted by the system and the real applied load. The incorporation of the CNT allows for the retainment of the memory effect until the last loading cycles of the CFRPs.

4.2.5 Results and discussion-GFRP specimens

Four glass /epoxy GFRP embedded CNT fibre specimens were tested under monotonic tensile loading. Simultaneously to the mechanical testing electrical resistance changes of the fibres were measured. Fig.4.2.15a depicts the tensile stress and relative electrical resistance values as a function of the recorded mechanical strain. As can be seen, the relative resistance values are oscillating in a similar way following the mechanical stress pattern during loading. The recorded electrical resistance values at this case correspond to the deformation of the CNT fibre itself which shows a good correlation with the mechanical deterioration of the material. The loading – unloading protocol of the GFRP specimens with the embedded CNT fibres was similar to that performed in the CFRP testing. As aforementioned, the stress step of the test was kept to 100MPa. In Fig.4.2.15b, the mechanical stress and $\Delta R/R_0$ are depicted as a function of the axial strain for each specific loading-unloading cycle. Fig.4.2.15b shows the loading sequence of the GFRP material with the respective characteristic effect on the electrical properties of the CNT fibre as a function of time. As can be seen, the application of load is directly followed by changes in the electrical resistance measurements which might be connected to fibre internal micro-structural reformations. From Figs.4.2.16a-g the maximum relative electrical resistance values ($\Delta R_{max}/R_0$) for the particular loading steps of the GFRP specimens are illustrated. The initial resistance of the CNT fibre measured equal to 655 Ohm (R_0). It is evident that in all loading steps the electrical resistance measurements followed readily the loading trace. Until the 3rd loading step (Fig.4.2.16c) no significant remaining resistance was observed. However, after the 4th loading cycle, a quite more prominent change in electrical resistance values was noticed. This is a direct mirroring of the structural deterioration of the CNT fibre itself. It is noteworthy to mention, that the CNT fibre failure found to be similar to the global final failure of the structure or else the GFRP material. This argument verifies the initial target on the current task. The CNT fibre can work as damage sensor providing information about the internal state of the material.

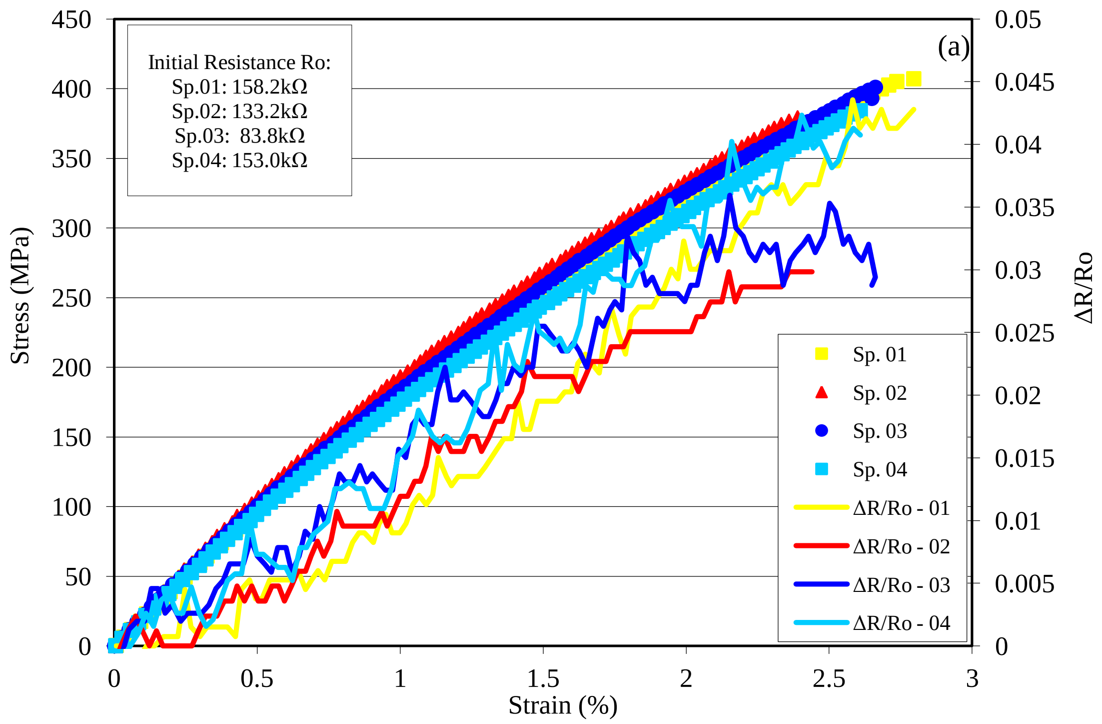

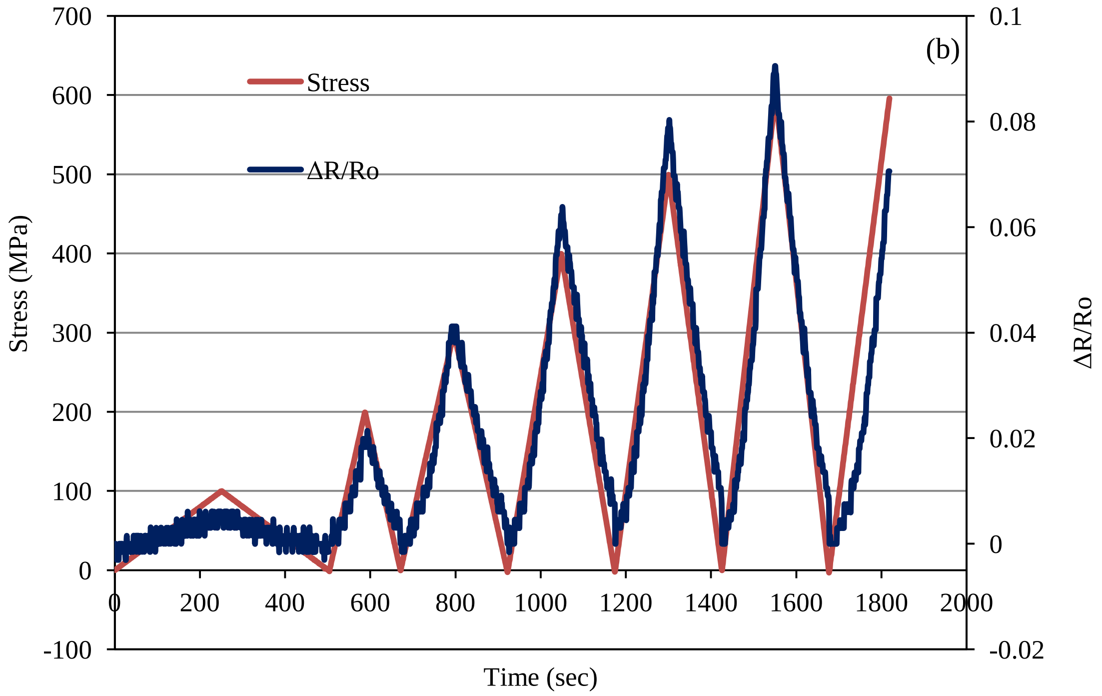

Figure 4.2.15 *(a) Monotonic tensile testing to failure (b) Mechanical stress and relative resistance change vs. time.*

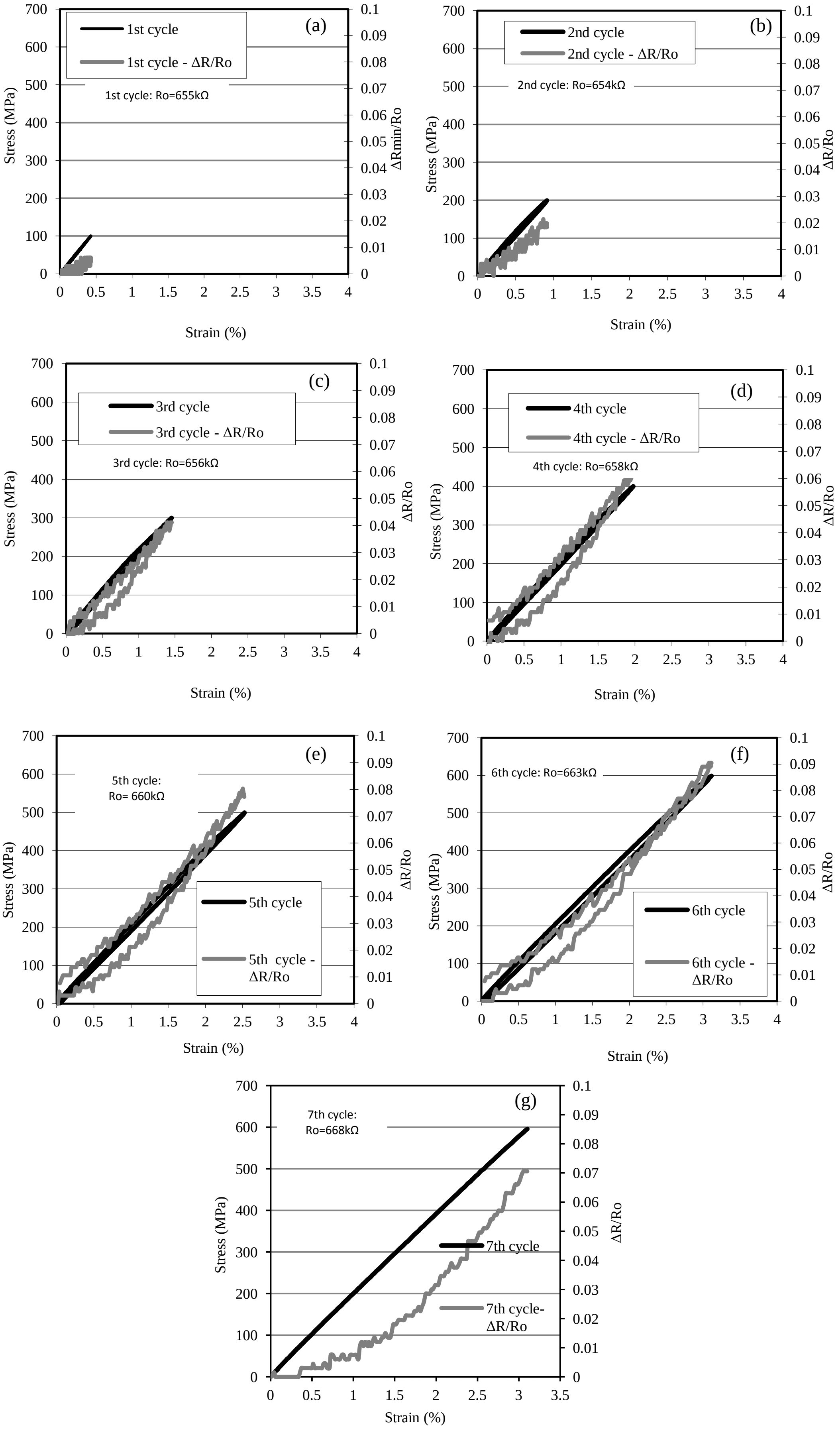
(a)
1st cycle
1st cycle - ΔR/Ro
1st cycle: Ro=655kΩ
Stress (MPa)
ΔRmin/Ro
Strain (%)
(b)
2nd cycle
2nd cycle - ΔR/Ro
2nd cycle: Ro=654kΩ
Stress (MPa)
ΔR/Ro
Strain (%)
(c)
3rd cycle
3rd cycle - ΔR/Ro
3rd cycle: Ro=656kΩ
Stress (MPa)
ΔR/Ro
Strain (%)
(d)
4th cycle
4th cycle - ΔR/Ro
4th cycle: Ro=658kΩ
Stress (MPa)
ΔR/Ro
Strain (%)
(e)
5th cycle:
Ro= 660kΩ
5th cycle
5th cycle - ΔR/Ro
Stress (MPa)
ΔR/Ro
Strain (%)
(f)
6th cycle: Ro=663kΩ
6th cycle
6th cycle - ΔR/Ro
Stress (MPa)
ΔR/Ro
Strain (%)
(g)
7th cycle:
Ro=668kΩ
7th cycle
7th cycle- ΔR/Ro
Stress (MPa)
ΔR/Ro
Strain (%)

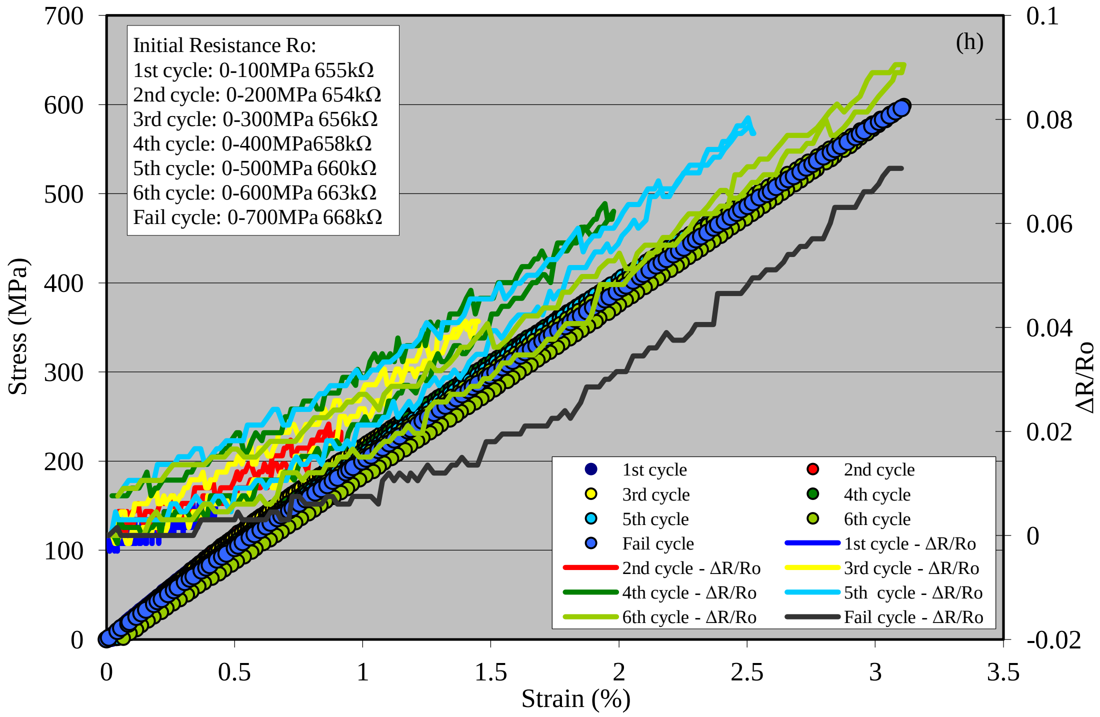

Figure 4.2.16 *GFRP embedded CNT fibres; stress and $\Delta R/R_0$ vs. axial strain: (a) 0-100-0 MPa, (b) 0-200-0 MPa, (c) 0-300-0 MPa, (d) 0-400-0 MPa, (e) 0-500-0 MPa, (f) 0-600-0 MPa, (g) 0-700 MPa, (h) total loading-unloading cycles.*

The most accurate way to correlate the electrical resistance values with the mechanical degradation of the composite is to plot the relative stiffness loss during loading steps against the relative resistance changes. As in the case of CFRP coupons, the modulus of elasticity was calculated for the specimens according to ASTM D 3039/D 3039M – 95a. Figs.4.2.17 and 4.1.18 present the stiffness loss (relative Young's modulus) and the relative electrical resistance maximum ($\Delta R_{max}/R_0$) and minimum ($\Delta R_{min}/R_0$) values, respectively, as acquired for the particular loading steps. As is shown, stiffness loss is increasing with load application. At the same time, a notable increase of the minimum electrical resistance values (Fig.4.2.18-unloaded stage) is recorded after the 3rd loading cycle. Afterwards both $\Delta R_{max}/R_0$ and $\Delta R_{min}/R_0$ increase monotonically. As was mentioned in the previous section, $\Delta R_{min}/R_0$ values correspond to zero load. Thus, this increase is attributed to the structural degradation of the CNT fibre itself. The remaining electrical resistance is recorded in parallel to the stiffness loss of the composite. This demonstrates that the residual resistance of the CNT fibre can be correlated with the structural degradation of the overall composite or in other words that the CNT fibre can work a strain or damage sensor.

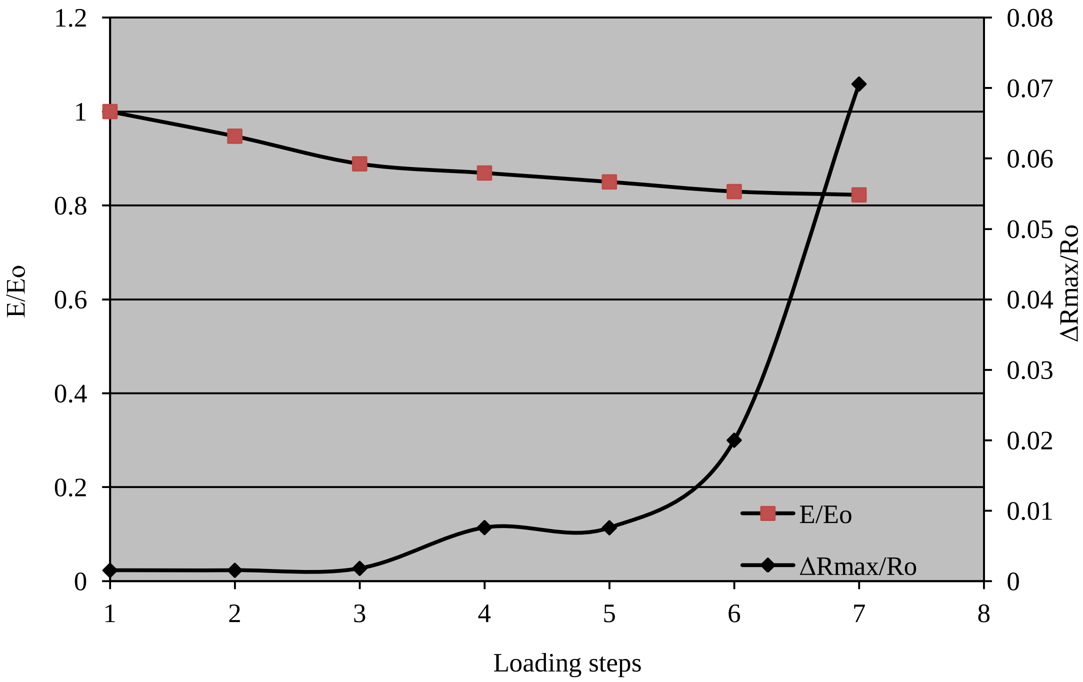

Figure 4.2.17 *Relative modulus of elasticity and Maximum relative electrical resistance change vs. loading steps.*

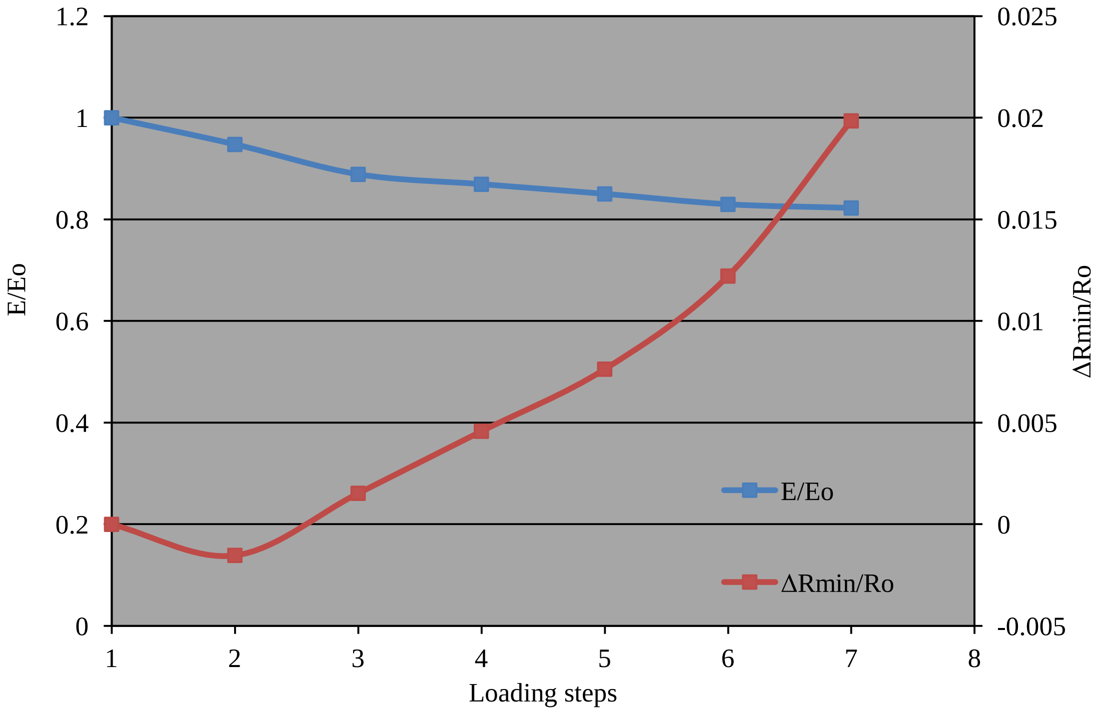

Figure 4.2.18 *Relative modulus of elasticity and Minimum relative electrical resistance change vs. loading steps.*

As resulted, CNT fibres can work as strain sensors embedded in glass /epoxy composite laminates. However, in order to verify that their incorporation will not affect the principle mechanical properties of the composite structure, reference GFRP specimens were manufactured and tested in monotonic tensile loading. Fig.4.2.19 depicts a correlation between the ultimate tensile strength of four reference and four hybrid GFRP specimens. As can be seen there is a slight deterioration of the hybrid when compared to the plain GFRPs. Nevertheless, this deviation is very close to the experimental scatter. This verifies from the mechanical point of view that there is a relatively small decrease of the principle material mechanical performance.

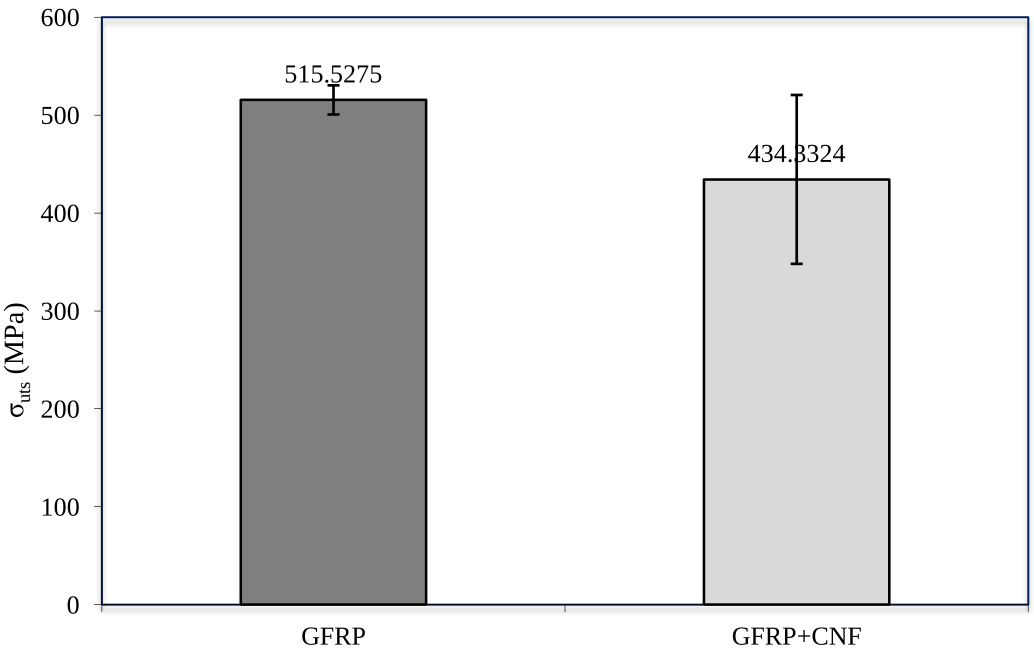

Figure 4.2.19 *Comparison between the ultimate tensile strength of reference and hybrid GFRP specimens.*

Section conclusions

The objective of this section was to explore the efficiency of electrical resistance technique for the monitoring of service damage accumulation in hybrid composites. Two different materials were investigated; (i) CFRPs with plain and CNT enhanced matrix, where the material itself was employed as a sensor for strain and damage and (ii) GFRPs, where an embedded CNT fibre functioned as an embedded sensor. In all cases, the two-wire electrical resistance method was adopted. Electrical resistance measurements were performed using a digital multimeter simultaneously to the mechanical testing.

With respect to CFPRs, the two-wire method proved to be reliable. Contact resistances were minimized by simply placing the recording electrodes between the grips of the testing machine. In both CFRP cases, the loading trace followed directly by distinct electrical resistance changes at the respective maxima and minima of each load cycle. Concerning the plain matrix specimens, the electrical resistance measurements were found to be dependent on Poisson's ratio effects; the decrease in the $\Delta R_{min}/R_0$ until the 5^{th} loading step is attributed to the creation of random conductive contacts between the reinforcement fibres. On the contrary, the incorporation of the nano-fillers reduced considerably the Poisson's effect and allowed for electrical resistance measurements to be employed in strain without artifacts introduced by secondary mechanisms. In this case, $\Delta R_{min}/R_0$ (resistance at zero load) exhibited a monotonic increase from the onset of the experiment up to the failure of the specimen. This increase was more pronounced after the maximum residual strain at zero load was recorded.

The incorporation of the nano-phase increased significantly the sensitivity of the electrical resistance measurements. For example, in the plain CFRPs case, a 3% increase of $\Delta R_{min}/R_0$ was recorded as compared to approximately 40% of the nano-modified composites. In other words, the nano-modification potentially increases the resolving ability of the methodology allowing the detection for minimal strain or damage induced changes.

It is noteworthy that although the residual strain at the end of the loading cycles does not change after the initial loading cycles, the resistance indices still increase with considerably higher rate. This irreversible increase that follows is indicative of damage accumulation and evolves independently of the recorded residual strain indicating that the technique allows the monitoring of damage mechanisms that are not readily mirrored in macroscopic material metrics before the final loading cycles.

In both CFRP material configurations, the relative electrical resistance change presented distinct stages in the course of every single loading cycle. The presence of an inflection point in the relative electrical resistance change second stage was found to correspond to the maximum recorded load of the previous load cycle. This implies that the material itself possesses a memory of its loading history prediction which relates to the rate of change of its electrical resistance value. The memory effect becomes less evident with increasing loading cycles, suggesting a similar behavior to the felicity effect in Acoustic Emission monitoring [103]. The incorporation of the CNT allows for the retainment of the memory effect until the last loading cycles of the CFRPs.

Concerning GFRP coupons with embedded CNT fibres, the electrical resistance technique was effective in monitoring both electrical resistance changes and overall structural degradation. In monotonic tensile loading testing, electrical resistance values related monotonically albeit with a non-linearly increasing rate to the mechanical deformation of the materials. In all monitored coupons and for the loading-unloading protocol, distinct changes at the respective maxima and minima of resistance corresponded exactly to the respective load changes.

The residual relative resistance change did not change significantly with load application until the 3rd loading step (45-50% of the σ_{uts}). However further increase of mechanical load led to more prominent increase of the residual $\Delta R/R_0$ which is attributed to the structural deterioration of the CNT fibre itself. The remaining electrical resistance after each particular load cycle may be attributed to the residual strain or damage accumulation of the CNT fibre.

Taking into account the material deterioration values as observed from the stiffness of the GFRP material, it is obvious that electrical resistance changes acquire higher values as the GFRP specimen is mechanically deformed. This electrical resistance increase corresponds to intrinsic changes or variations of the mechanical properties of the CNT fibre or else its mechanical degradation. The monotonic relation between stiffness loss of the GFRP material and the electrical resistance of the CNT fibres, is indicative of the ability of the CNT fibre to act as damage or strain sensor embedded in the GFRP structure.

Along with their sensing capabilities, CNT fibres possess a considerable low diameter (80 μm) meaning that their incorporation in the bulk material does not significantly affect its principle structural properties or else degrade its primary mechanical performance. Tensile testing of reference GFRP specimens showed that there is a decrease in strength followed by an increase in the experimental scatter of the hybrid GFRP materials strength compared to the reference ones, implying that similar values of strength may be reached with optimization of the embedding protocol. Thus it may be postulated that, CNT fibres may be embedded for the monitoring of service induced damage in GFRP composite laminates with minimal aggravation of the primary structure.

Summarizing the above, the electrical resistance technique was successfully employed as a tool to evaluate the structural integrity of hybrid composite materials. In the case of unidirectional CFRPs, health monitoring of composite materials in terms of monitoring initiation and propagation of internal damage due to mechanical load was considerably improved via the incorporation of the CNTs in the composite matrix. Considering GFRPs, CNT fibres may be artificially inserted at proper locations in a structure in order to locally monitor structural deterioration during service.

4.3 Real time debonding monitoring of composite repaired composite substrate materials via combined electrical, acoustic and thermographic methods

4.3.1 Introduction

In-service monitoring of the ‘structural health’ of a repaired component is the safest route towards (i) assessing its structural integrity, (ii) enhancing the reliability of the aircraft industry towards bonding technologies and ultimately (iii) reducing overall operational costs for safe airborne structures [258]. After the thorough examination of the on-line electrical and thermographic techniques (sections 4.1 & 4.2), they are concurrently performed in a comparative study along with AE, for the purposes of the current section. An Electrical Potential Change Monitoring technique-EPCM is investigated for the monitoring of initiation and propagation of damage in composite repaired materials. CFRP panels with an artificially induced circular notch were repaired using an adhesively bonded composite patch. The bonding repair efficiency was assessed in real time using EPCM, LT and AE under tension-tension cyclic loading. AE and IrT were utilized in order to benchmark the results provided by EPCM. AE is employed for the localization of critical and subcritical damage or else the damage between the repair and the parent material as well as the damage observed from the presence of an artificially induced circular notch. Irt is employed as a full field method to visualize and quantify debonding and stress concentrations around the artificially induced notch. Post mortem optical stereoscopic examination of the failed coupons was employed to verify the results provided by the aforementioned methods.

4.3.2 Materials

The examined coupons of the current task were identical to type I specimens of Section 4.1. In particular, the CFRP coupons consisted of composite plates (substrate) with a circular notch drilled in the middle to simulate service induced damage. The area of the notch was subsequently repaired using a tapered patch which was hand laid-up on the notched plate and subsequently cured in place. The circular notch was chosen as representative of damage in real conditions, as it is usual repair practice to drill a notch at the vicinity of the crack in order to retard its propagation [283, 284]. In Fig.4.3.1 the investigated coupon configuration is depicted.

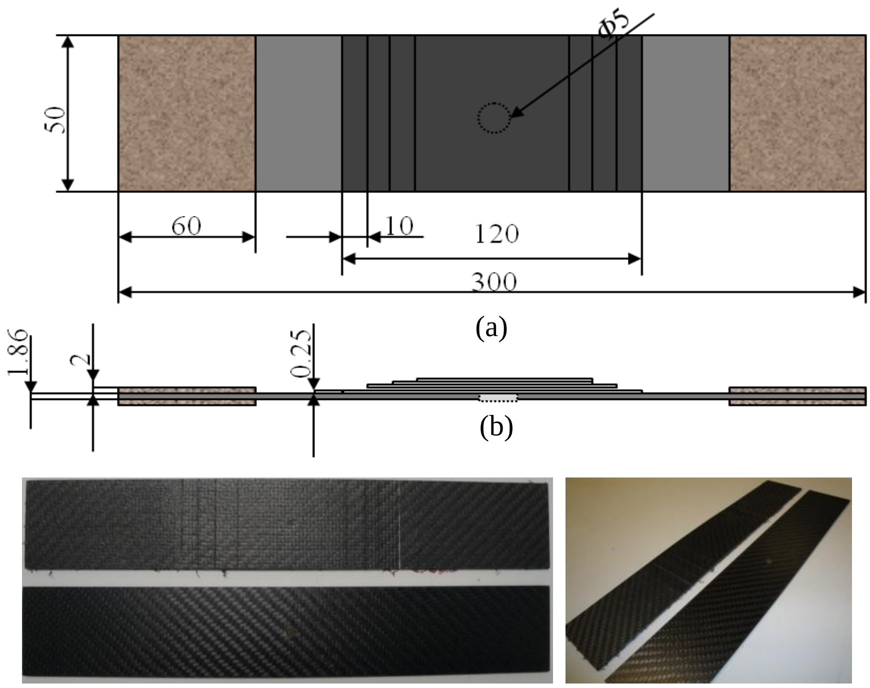

(c) (d)

Figure 4.3.1 *(a, b) Schematic configuration of the employed specimen, (c, d) snapshots of both front (patched) and back side of the specimens.*

4.3.3 Testing procedure

For the EPCM measurements, electrically conductive contacts at specific locations were applied on the surface of the coupons using conductive silver paint (Fig.4.3.2). Commercially available silver paint and silver loaded tape (RS–Components) (Fig.4.3.2a) were subsequently used in order to connect the cables of the multimeter (Agilent Technologies) connected to a PC for data acquisition and the DC power supply (XANDREX HPH 18-10DC). 150 mA direct current was injected in the specimen during mechanical loading and the electrical potential variation was concurrently recorded on both sides of the notch (V_A and V_B) (Fig.4.3.2b).

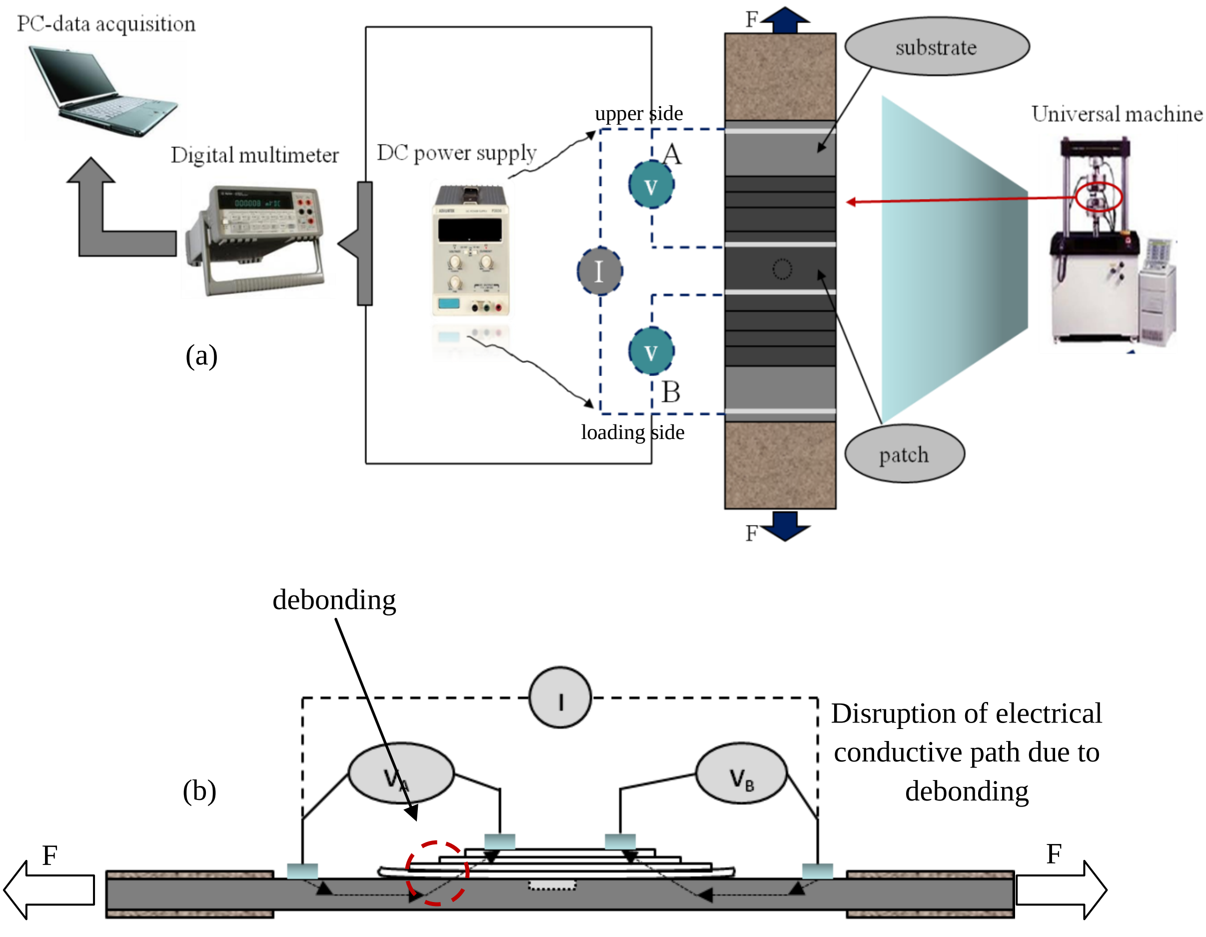

Figure 4.3.2 *(a) EPCM experimental setup, (b) EPCM measurement approach.*

As is shown in Fig.4.3.2b, the electrically conductive path between the substrate and the repair is through the patch /substrate interface. Apart from the conductive primary reinforcement i.e. the carbon fibres, the electrical continuity between the repair and the substrate was enhanced in the transverse direction by the electrical conductive network formed by the CNTs in the matrix of the patch. As the conductive path includes the interface of the patch and the substrate, any changes in the form of debonding are expected to affect it directly. More analytically, as the debonding front propagates, the electrical potential values are expected to change monotonically. More analytically, the evolution of the debonding during mechanical testing should result in the increase of the resistance or else the potential drop between the measuring points.

For the Acoustic Emission monitoring the, two broadband piezoelectric transducers (Pico, Physical Acoustics Corp., PAC) were attached on the specimen as shown in Figs.4.3.3a and 4.3.3b at specific distance (80mm). Ultrasonic gel was employed for the acoustic coupling. The pre-amplifier gain was set to 40 dB. After performing a pilot test, the threshold was also set to 40 dB, in order to avoid electronic/environmental noise. The signals were recorded employing a two-channel PCI-2 monitoring board of PAC with sampling rate of 5 MHz.

As is depicted in Fig.4.3.3b the propagation of the patch debonding front of the patch causes the generation of AE hits. The simultaneous recording by the two broadband AE sensors allowed for the location of the events due to debonding, along the length of the specimen. Thus, cumulative AE signals on either side of the patch along the loading axis may represent the length of the debonding front or else, the critical damage of the repaired material.

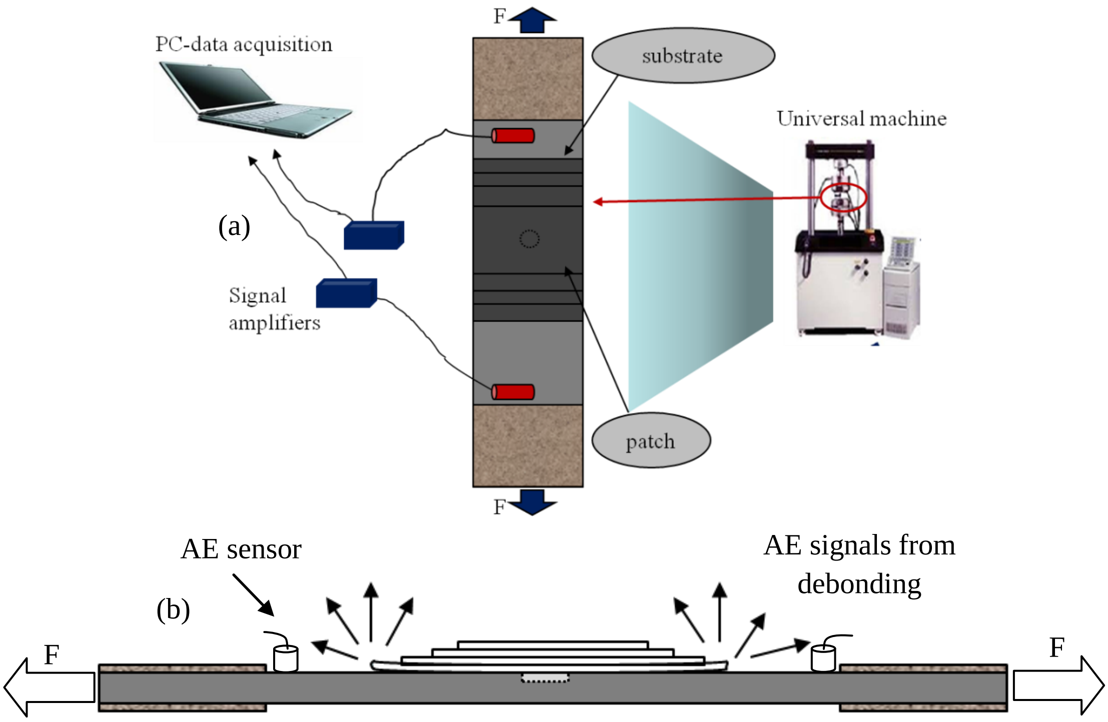

Figure 4.3.3 *(a) Schematic representation of AE technique, (b) AE signal measurement principle.*

For the thermographic inspection, the Jade 510-CEDIP-MW infrared camera, as has already been presented, was used (Fig.4.3.4). The camera was employed in lock-in mode at a frame frequency of 50 Hz. For the purposes of this work, the camera was positioned at approximately 1 m distance from the specimen in order to include the whole patched area in the Field Of View (FOV) of the camera (Figs.4.3.4a and 4.3.4b). At this distance the corresponding field of view was 208x156 mm^2 with a lateral and perpendicular resolution of 0.65 mm /pixel. Figs.4.3.4c and 4.3.4d are snapshots of experimental setup of the second pair; IrT versus AE. In the aforementioned configuration the cyclic loading is the source of thermal excitation of the material. As has been shown in a previous publication [73], debonding is manifested in the amplitude domain as a distinct discontinuity in the greyscale area, delineated by a hot zone which indicates the stress concentration at the debonding front.

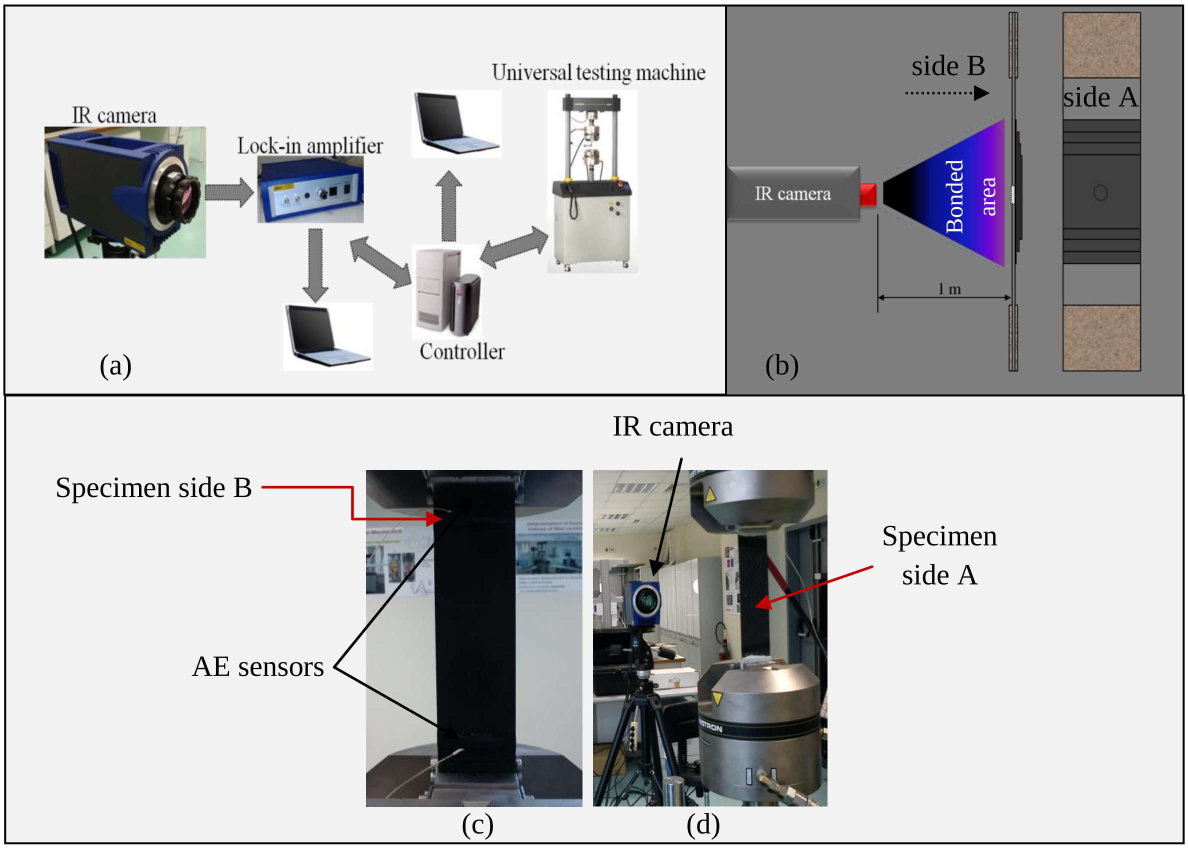

Figure 4.3.4 *(a) Schematic of the thermographic experimental setup (b) recorded field of view from the thermal camera (c, d) snapshots of both specimen sides.*

The aforementioned inspection techniques were employed in pairs, as the current injection would interfere with the thermographic inspection. This is due to the fact that the Joule heating effect due to the current injection is masking the heat generated either thermoelastically or due to irreversible damage. In a parallel study, the Joule effect has been successfully employed in conjunction with phase or lock-in thermography to assess delaminations in impacted composite panels [177]. More analytically, the mechanical testing protocol included real time monitoring of the fatigue loading by EPCM along with AE (1nd pair) and IrT together with AE (2nd pair).

Prior to the application of the monitoring techniques, preliminary mechanical testing was performed in order to define the stress level at which stable debonding took place with the application of cyclic loading. To this end, the coupons were subjected in fatigue at incremental load levels for 20kcycles at each level, until stable debonding was observed. The debonding process was monitored thermographically on line and assessed optically at the end of each load level increment, as was performed in [73]. Stable debonding was consistently observed for 80% of the static strength of the pristine laminate, as quoted by the manufacturer. A total of four coupons were tested in this load level (80%), two coupons with EPCM combined with AE monitoring and two coupons with thermography combined with AE monitoring.

Throughout the test campaign stress ratio of 0.1 and 5Hz frequency were adopted for the fatigue loading. All coupons failed consistently, starting with the progressive patch debonding of the patch from the side of the load application of the testing frame, the propagation towards the middle of the coupon and the brittle transverse failure once the notch was revealed.

4.3.4 Results

4.3.4.1 EPCM & AE

Fig.4.3.5 depicts the electrical potential changes (Fig.4.3.5a) and the acoustic activity (Fig.4.3.5b) recorded during the fatigue mechanical testing of one of the two tested coupons as a function of the loading cycles. The bottom side indicates the side at which the load was introduced by the loading frame. Both EPCM channels are depicted. The polarity was chosen so that increase in potential values corresponds to increase in the resistance of the monitored closed circuit, which would be the expected result from the propagation of the debonding front. With the selected formality, relative potential increase corresponds to increase in "potential drop" due to electrical resistance increase. AE activity snapshots are overlaid on the EPCM graphs indicating the location of the recorded events at specific instances during the experiment corresponding at the indicated EPCM measurements. The cumulative AE hits for the total duration of the experiment are shown in Fig.4.3.5b.

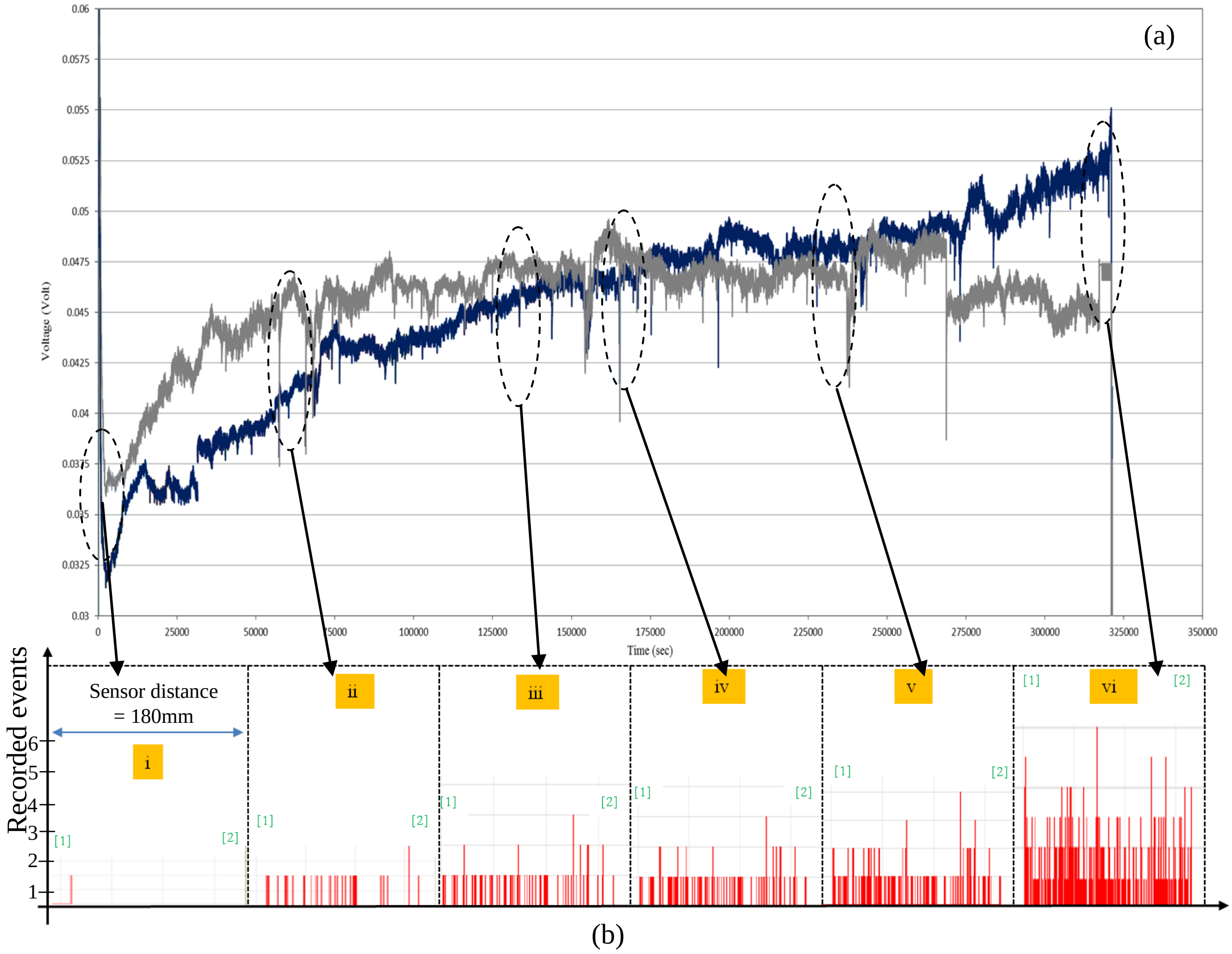

Figure 4.3.5 *Electrical potential changes along with the acoustic emission signals during the fatigue mechanical testing.*

For both the top and the bottom side, the recorded noise is of a typical amplitude of 5 mV and very high frequency. As has been shown in a previous study [256], this variation may be real and not merely system noise and can be attributed to typical strain variation within the fatigue cycle as is already observed for composite coupons. Additionally, there is a superimposed electrical potential oscillation of approximately 15 mV amplitude, for 25 kcycles period, manifested as “drops” and “peaks” in the potential along the fatigue cycles. It may be postulated that these changes are attributed to local disruptions of the electrical conductive path between the repair and the substrate mirroring the debonding evolution of the patch from the substrate which exhibits a “stick-slip” behaviour as it progresses. Finally, there is a large scale change with monotonic parts which is independent of the aforementioned oscillations. The discontinuity recorded at approximately 270 kcyles is not readily explained but may be attributed to sudden change in a part of the electrical circuit independent of the interrogated repair, such as the contact resistance of the copper wires.

The recorded large scale electrical potential change (EPC) as described in the previous paragraph, is distinctly different from the top to the bottom side. For both sides the EPC exhibits a steep decrease in the initial few loading cycles. As should be noted, the initial potential value for both sides corresponds to the unloaded coupon. In this respect the initial changes may be attributed to effects related to the local changes in contact resistance due to the initial cyclic loading. This monotonic potential decrease (which corresponds to resistance decrease) cannot be readily interpreted. However, similar effects have been recorded for the resistance change during step [124] or fatigue [247] loading. The initial decrease in the absolute potential values cannot be associated to damage but relates to other mechanisms, which are activated during the first stages of the fatigue loading and may include the increase of the 0º fibre alignment, the fibre piezo-resistive effect, the relaxation of the fibre pre-stressing and the decrease of the contact resistance [247].

Following the aforementioned decrease, the EPC is differentiated from the top to the bottom channel. The top channel (grey line) exhibits a small increase in potential of approximately 10 mV from its minimum value and thereafter the potential values oscillate around a mean (0.045-0.047 V) value, suggesting the existence of the “stick-slip” mechanism, which however has reached a steady state. However, the EPC for the bottom channel exhibits a monotonic increase until the specimen failure. This increase is more than 30 mV from the minimum recorded value. The sudden potential drop at the end of the fatigue life obviously indicates loss of continuity due to specimen failure, which occurred with the critical failure of the bottom part of the patch followed by brittle transverse failure at the vicinity of the notch. Obviously, EPCM was successful in identifying the most probable failure site of the patch coupon, as after the initial stage, progressive critical failure was clearly manifested as monotonic potential increase of the bottom part of the coupon. The relative potential increase values as a function of fatigue life fraction for the bottom part of the coupon is shown in Fig.4.3.6.

As far as AE is concerned, the acoustic events as recorded at the same time with the electrical potential values are shown in Fig.4.3.5b. Snapshots of the cumulative acoustic events are presented as a function of the sensor positions. Events correspond to acoustic activity recorded within the time difference that sound travels within the length of the coupon. The differential arrival time allows for the calculation of the location of the sound source. The acoustic events which reflect the presence and location of damage start to appear from the edges of the repair (critical damage) moving along the centre of the specimen indicating the debonding of the repair. As should be noted the bottom part of the coupon corresponds to the right side and the top part to the left side of the event location snapshots. The activity corresponding to the bottom channel appears consistently to be higher and this is indicative of the part where failure is most likely to take place. In the final stage of the test and prior the final failure of the specimen, the recorded acoustic events are concentrated in the centre of the specimen. At the same region the coupon eventually failed due to the presence of the circular notch (sub-critical damage).

Fig.4.3.6 depicts the cumulative events as a function of fatigue life fraction together with the relative potential change recorded by EPCM. As can be easily observed, the two techniques follow closely each other. Three distinct fatigue life stages may be clearly defined with EPCM, i.e. the onset of damage marked as stage 1, the increase in damage rate marked as stage 2 and finally the rapid deterioration that inevitably leads to failure (stage 3). AE is not as efficient in identifying the third stage of the fatigue life. As should be noted, this is not a typical fatigue life diagram as in a typical fatigue case, stage 1 should exhibit a higher damage rate than stage 2. Finally, Fig.4.3.7 depicts the cumulative events vs. the relative potential change. This may be regarded as typical benchmarking or calibration graph for EPCM against AE. As can clearly be the benchmarking scheme of both NDE methods is efficient in highlighting the distinct fatigue stages with approximately linear interdependence for each fatigue life stage.

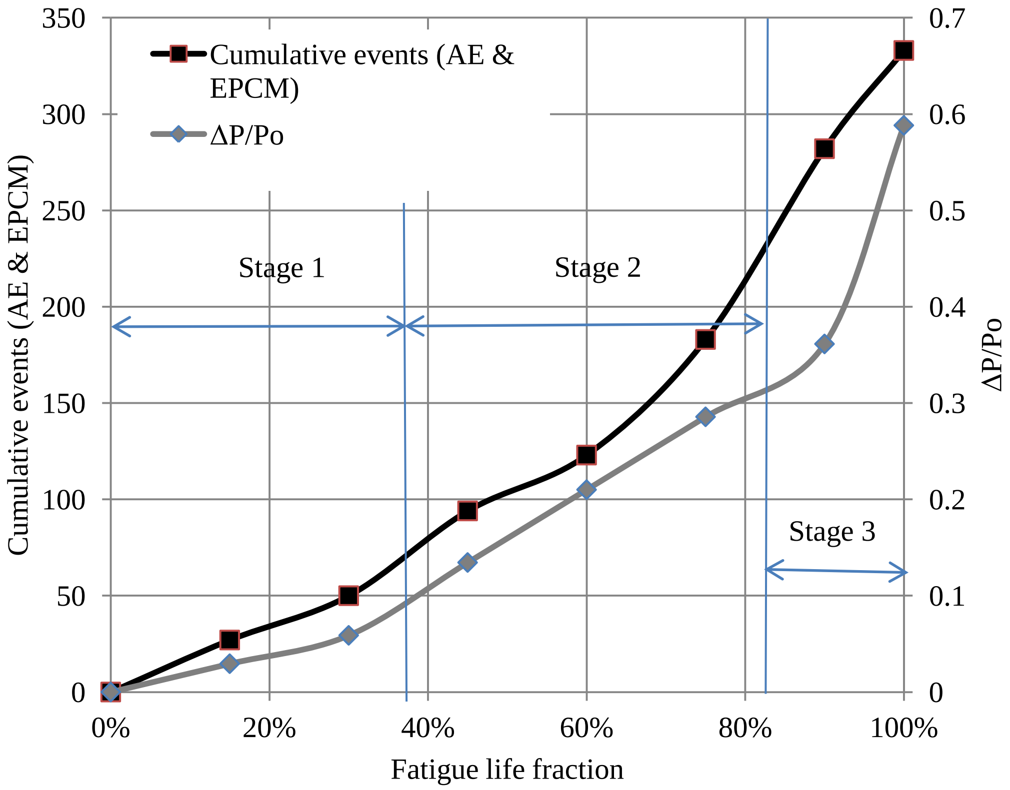

Figure 4.3.6 *Cumulative AE events and relative potential change as a function of fatigue life fraction. Distinct fatigue life stages may be discerned with both methodologies*

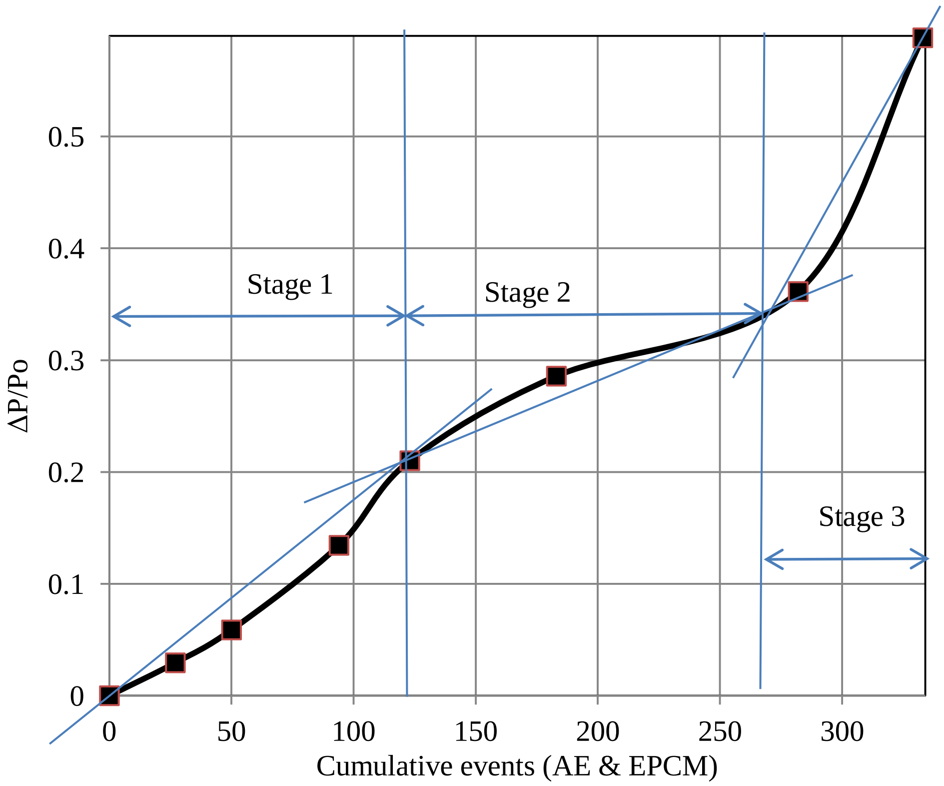

Figure 4.3.7 *Cumulative AE events vs. relative potential change*

4.3.4.2 IrT & AE

In the second testing configuration, IrT was employed together with AE simultaneously to the mechanical testing. Amplitude images at specific load cycles are shown in Fig.4.3.7 As was observed, debonding initiated at the 80% of the σ_{uts}. Hence, amplitude images at that load level are presented (Fig.4.3.8).

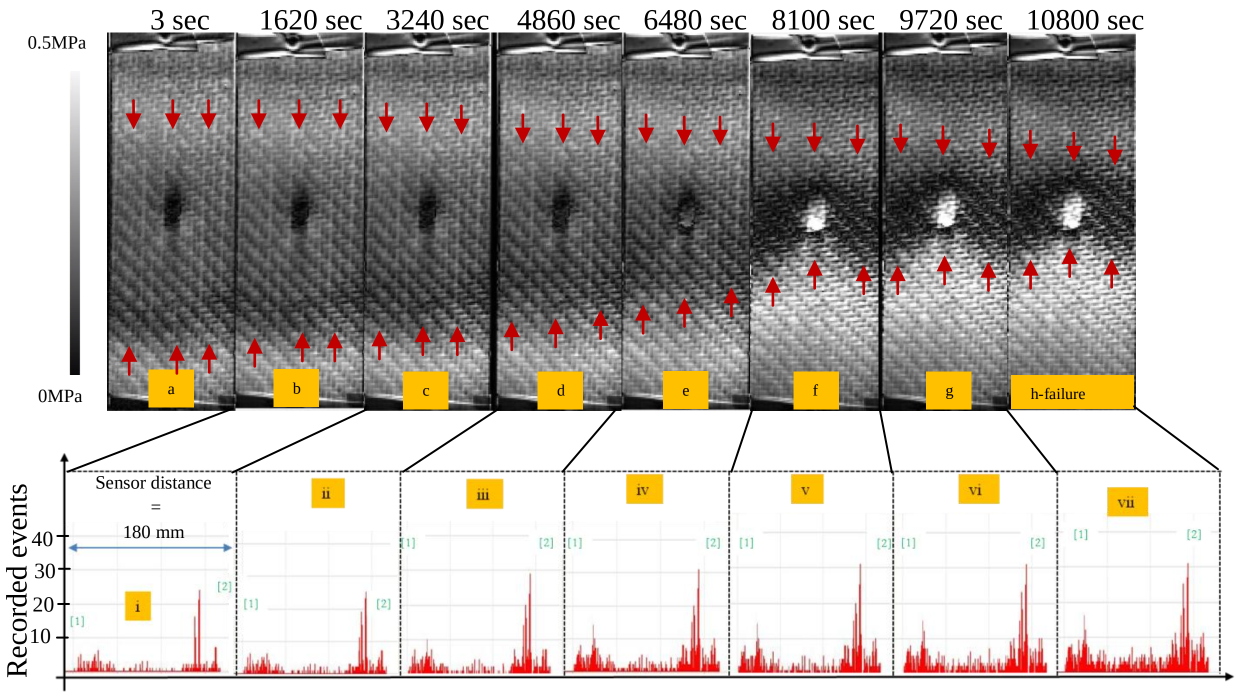

Figure 4.3.8 *Thermal images and acoustic events during fatigue mechanical loading at 80% of the σ_{uts} of the substrate.*

As is depicted in Figs.4.3.8a-h, stress concentration areas are present at the edges of the repair (critical damage) or at the loci where high stresses are expected to appear and are manifested in the amplitude domain as regions of increased intensity [73]. With fatigue loading, the high amplitude region is constricted from the bottom side towards the center of the specimen, implying that as debonding progresses, the debonded bottom area is practically relieved from stresses which are concentrated towards the middle of the coupon. As can be seen from the amplitude image series, the progress of critical damage of the coupon continued until the complete debonding of the bottom side of the repair from the substrate, which consistently failed in a transverse brittle manner at the notch edge. As is expected, the exposed “artificial” damage; or the circular notch created caused a stress concentration leading to subcritical failure. The arrows on amplitude images show the direction of the patch debonding from the substrate. In Fig.4.3.9, the debonded area normalized to the initial bonding area is depicted as a function of fatigue life fraction, together with the cumulative AE events.

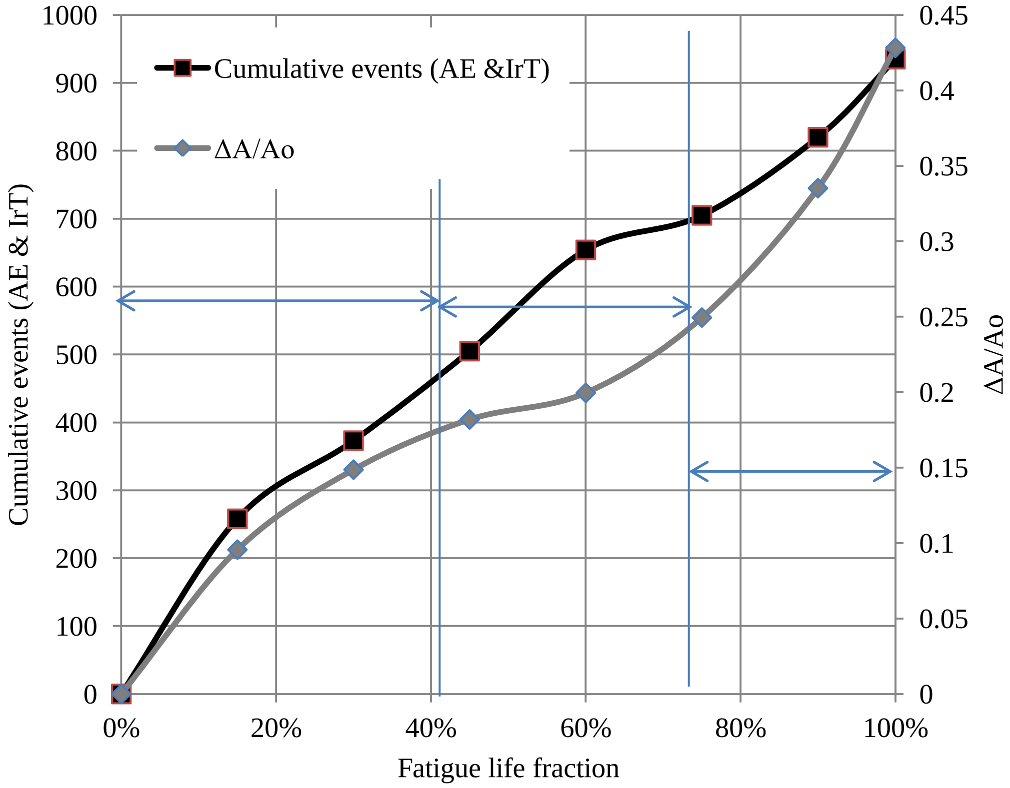

Figure 4.3.9 *Cumulative AE events and relative debonded area as a function of fatigue life fraction. Distinct fatigue life stages may be discerned with both methodologies*

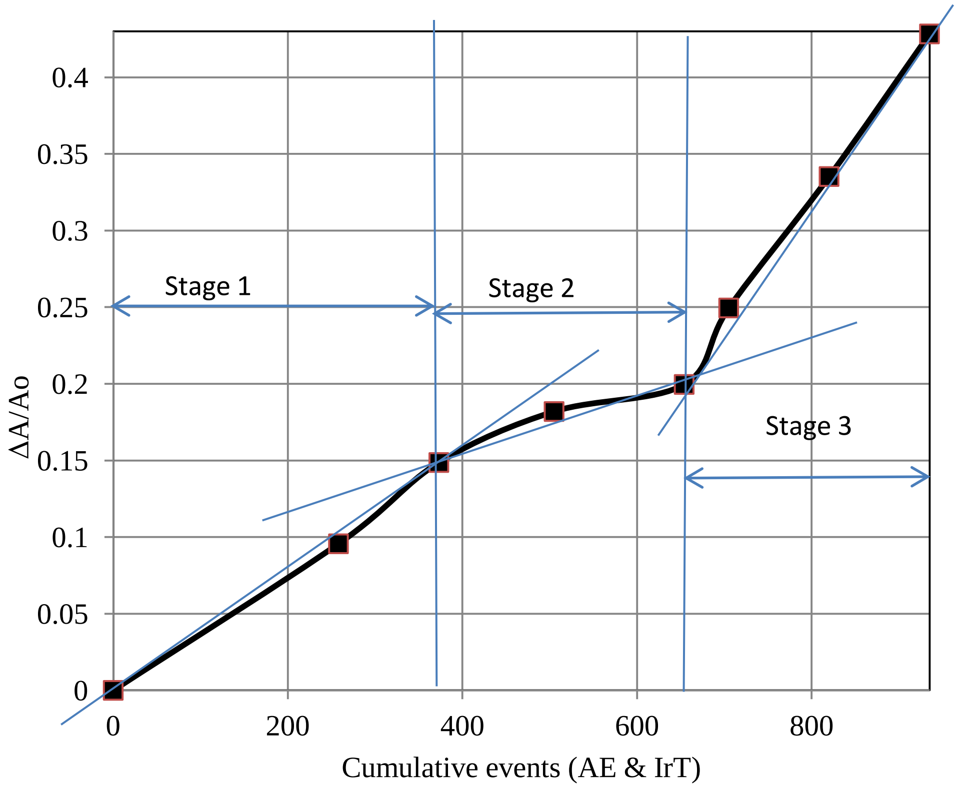

Figure 4.3.10 *Cumulative AE events vs. relative area change*

Along with the thermal assessment, acoustic events were recorded at the same timing as shown in Figs.4.3.8i-vii, were snapshots of the event location are presented for distinct cycles. As the acoustic events clearly pinpoint in Figs.4.3.5i-vi, the debonding process initiated from the edges of the patch and expanded towards the centre of the specimen where the circular notch is present. The acoustic events indicate the generation of a crack /damage due to mechanical loading. Similarly to the previous experimental configuration (EPCM & AE), there is considerably more activity at the side corresponds to the bottom part of the repaired coupon, which corresponds to the right hand side of the location snapshots. Again, the distribution of the acoustic activity is indicative of the failure site and was confirmed by the catastrophic failure of the specimen; after the complete debonding of the bottom side of the patch from the substrate the acoustic events appear to develop and basically concentrate around the loci of the artificial notch (in the middle of the specimen) until the catastrophic final failure of the coupon (sub-critical failure). In this configuration as well, AE is able to identify the location of damage as well as to verify what was efficiently observed from the thermal assessment.

Fig.4.3.9 depicts both the relative debonded area and the recorded cumulative AE events vs. the fatigue life fraction. As in the previous configuration, three distinct fatigue life stages are discernible with IrT, whereas this distinction is not obvious in AE. However there is a characteristic difference: the three fatigue stages as observed via the thermographic monitoring are typical of a fatigue life diagram, i.e. the initial fast damage progression stage (stage 1) is followed by a decreased rate (stage 2) and finally accelerates until failure (stage 3), indicating that the thermographic assessment provides a more reliable representation of damage which may also be readily quantified. This effect is more clearly depicted in Fig.4.3.10, where the cross correlation of the two methodologies are presented; in this representation all three stages may be clearly defined, with the acoustic activity being directly proportional to IrT data for each consecutive stage.

4.3.4.3 Cross validation of the applied NDE techniques

Figs.4.3.6 and 4.3.9 clearly show that EPCM and IrT are capable of identifying three distinct fatigue stages. These stages are better highlighted, when EPCM and IrT are interrelated with AE acoustic emission activity. In this way, the fatigue life stages are clearly defined. Interestingly enough though, the fatigue life stages are almost identical in the fatigue life fraction representation for the two studied configurations; i.e. stage 1 ranges ends at approximately 35-45% and stage 2 at 75-80%. In other words, provided that the correlation between the AE activities in the two scenarios is satisfactory, an indirect cross validation of IrT and EPCM may be performed; Fig.4.3.11a depicts the AE activity vs. lifetime fraction and Fig.4.3.11b depicts the correlation of the cumulative events as recorded for the two distinct configurations; the cross correlation of the acoustic activity for the two NDE scenarios presents an envelope which is directly relevant to the uncertainty provided by the indirect bench marking of IrT vs. EPCM because concurrent monitoring was not feasible with both techniques. Fig.4.3.12 depicts the benchmarking of IrT against EPCM; within the uncertainty of the approach, the indirect benchmarking of the two methodologies can be performed successfully in order to define the fatigue life stages as a function of the fatigue life fraction, providing a universal benchmarking for the two “incompatible” NDE methodologies (Fig.4.3.12).

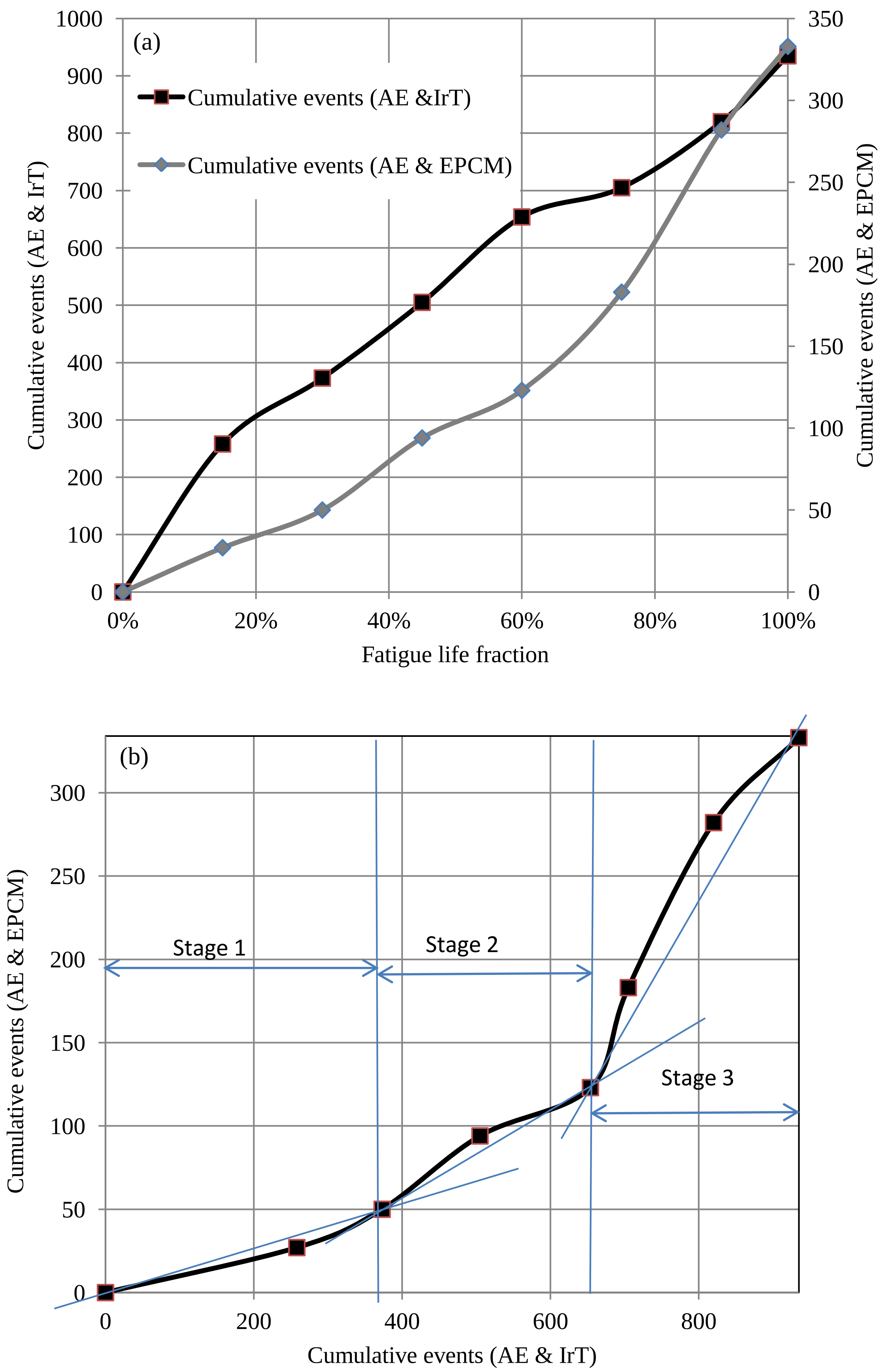

Figure 4.3.11 *(a) AE activity vs. lifetime fraction and (b) correlation of the cumulative events as recorded for the two distinct configurations*

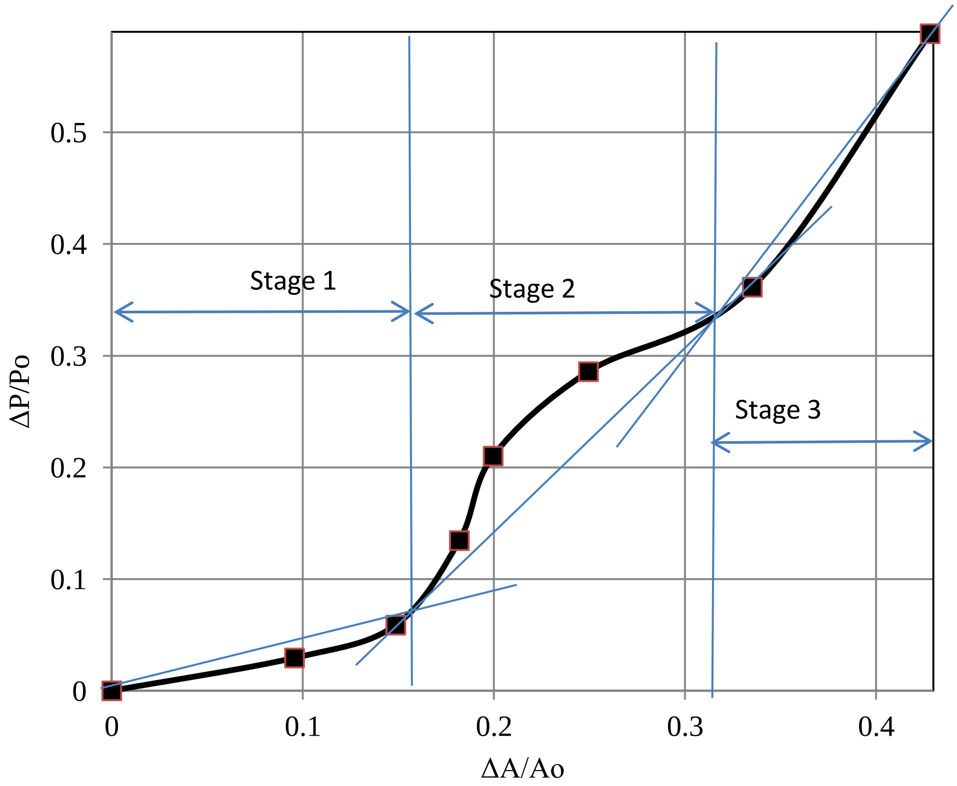

Figure 4.3.12 *Relative potential change vs. relative area change.*

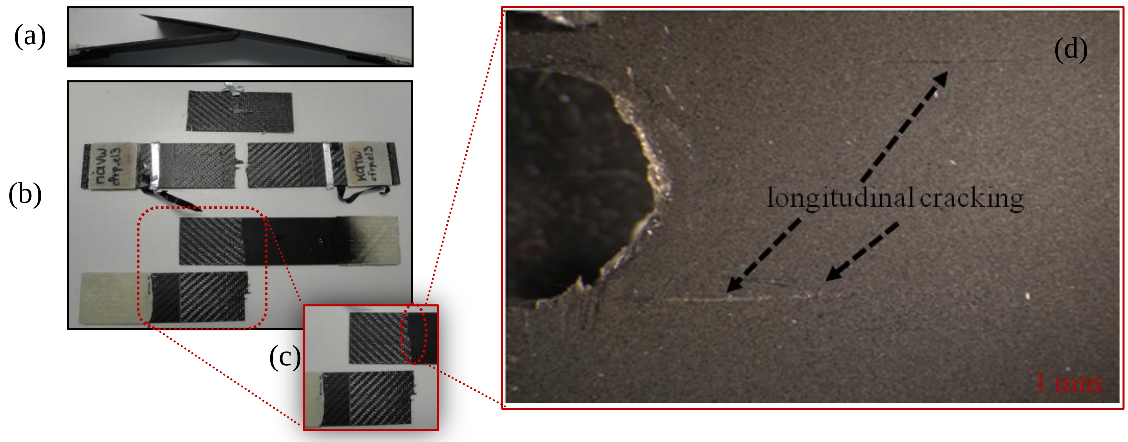

Figure 4.3.13 *(a, b, c) Post failure images, (d) image taken via a stereoscope.*

Fig.4.3.13 depicts post failure images (Figs.4.3.13a, b and c) as well as stereoscopic (Fig.4.3.13d) of a representative tested coupon. Longitudinal cracking (horizontal lines) on the surface of the upper side of the broken specimen are visible in Fig.4.3.13d. The post mortem images indicate the consistent type of failure as well as the characteristic behaviour of the composite where longitudinal cracks blunt the stress concentration at the edge of the notch.

Section conclusions

Within the scope of this section, a combined NDE system was developed through EPCM, AE and IrT for the monitoring of the repair integrity in composite repaired laminates with a central notch. The aim was to cross validate and benchmark all involved methodologies. Critical and sub-critical damage were efficiently identified and recorded during fatigue mechanical loading. Two scenarios were employed whereby the aforementioned techniques were employed in pairs, i.e. AE & EPCM and AE & IrT. The NDE methods were employed in real time simultaneously to the testing procedure. In all tested cases, the coupons failed in a consistent way, whereby critical failure initiated from one side of the specimen, was propagated towards the middle of the specimen and exposed the notch, inducing thus transverse failure.

All techniques sufficiently identified the debonding process. Both EPCM and IrT indicated well-defined stages along the fatigue life of the interrogated coupons. EPCM was successful in clearly identifying the topology of the progressive debonding as denoted by the monotonic potential increase which was only observed at the side where critical failure initiated and propagated. Secondary effects that are observed in the fluctuation of the electrical potential may be attributed to real time strain variations due to fatigue and a characteristic stick-slip behavior which is not directly related to damage propagation. The concurrent AE monitoring partially revealed the directionality of the critical failure. The correlation of the two techniques was very satisfactory and was feasible in enhancing the observed fatigue life stages.

The IrT technique was successful in identifying stress concentration areas at the edges of the repair which led to debonding from the substrate (critical failure). Stress concentrations were observed at either side of the circular notch. As fatigue loading continued, debonding was manifested by the restriction of high intensity areas in the amplitude domain towards the center of the specimen. The relative debonded area was calculated from the IrT thermographs. Again, three fatigue life stages were visible, which were found to correspond better to typical fatigue behavior, whereby the first stage possesses a higher gradient than the second and in the third, the damage rate is accelerated until failure. Both AE and EPCM did not identify the aforementioned sequence, and damage rate was mostly incasing during the fatigue life. In general, the interrelation of the IrT and AE performed concurrently in real time during the loading of the coupon, revealing a clear representation of the fatigue life stages.

Finally, a benchmarking of the employed methodologies was performed. It was shown that the correlation may be very good within the well-defined fatigue life stages for each method when plotted against lifetime fraction. The consistency of the failure process and the life time fraction representation allowed for an indirect correlation of the IrT and the EPCM methods which resulted as expected to the three distinct life stages representation.

4.4 Combined structural degradation monitoring of representative coupons /small scale components (composite repaired aluminum substrates) via electrical, acoustic and thermographic methods

4.4.1 Introduction

The present section is devoted to the combined structural health monitoring system for damage assessment in representative small scale components. On one hand, this approach allows for the cross validation of the employed methods with a view to applying NDE scenarios according to the specific requirements and restrictions. On the other hand, the interrogation of small scale representative components will provide the base for a future certification process that will be based upon a generic approach to patch design, validation and acquisition of material allowables. This approach includes testing of specimens which represent the repaired region.

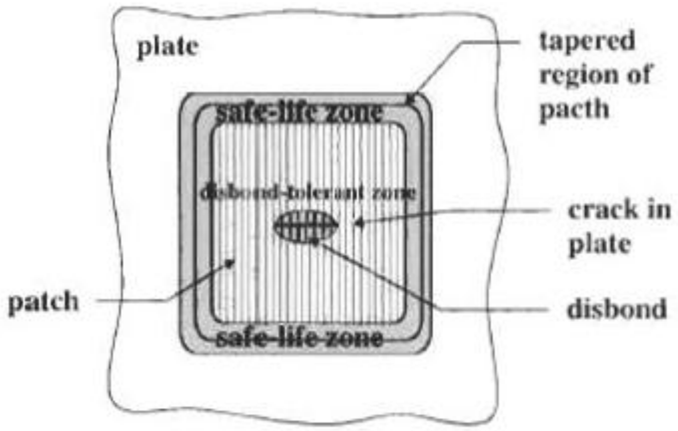

Figure 4.4.1 *Damage-tolerant and safe-life zones in a bonded repair [206, 285].*

In order to elucidate the adopted approach a schematic is shown in Fig.4.4.1. A bonded repair is applied to a cracked plate for which two distinctly different regions exist in terms of structural integrity requirements (Fig.4.4.1). The central damage-tolerant region is the zone where a significant disbond between the patch and parent material can be tolerated. This is because small disbonds reduce slightly the repair effectiveness. In addition, disbond growth when subjecting to repeated loading is slow and stable. The edges of the patch are in tapered configuration, thinning down to one layer of fibre composite at its ends. In this zone marked as safe life zone, disbonds cannot be tolerated because as the disbond grows it moves into a region of increasing patch thickness and consequently greater driving force for disbond growth. The result may be rapid debond growth and consequently patch separation. In order to represent these two regions, two types of coupons were tested:

1. The double overlap-joint fatigue specimen (DOFS), which represents the damage-tolerance region where the patch covers the crack
2. The skin doubler specimen (SDS), which represents the safe-life region at the termination of the patch.

Both specimens have CFRP outer adherends on both sides of an aluminum inner adherend in order to represent bonded repairs to aircraft skin, where there is substantial out-of-plane constraint from the substructure such as stringers, stiffeners or honeycomb core. The geometrical configuration of these specimens is presented below:

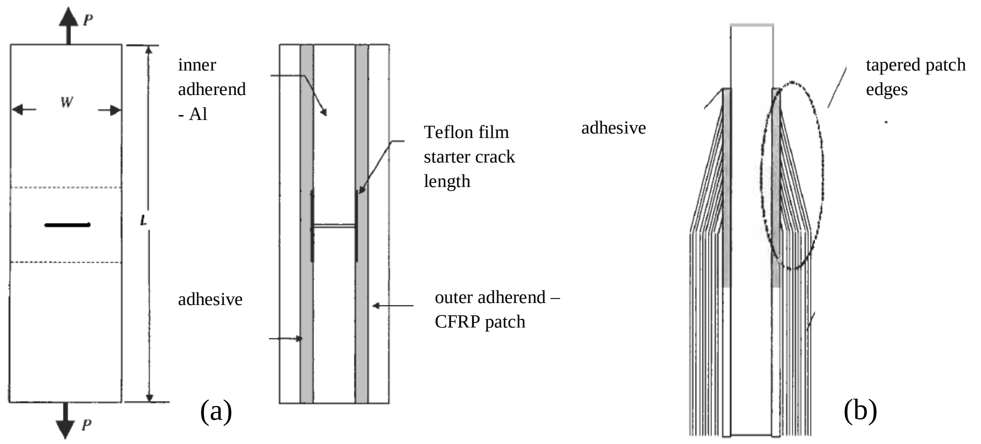

Figure 4.4.2 *(a) The double-overlap-joint fatigue specimen (DOFS), representing cracked region, (b) Schematic of the skin doubler specimen (SDS), representing patch termination [23].*

The present task focuses on the comparative evaluation of thermographic, electrical and acoustic emission techniques for the structural integrity monitoring of representative aerospace small scale components. In particular, the structural performance of the components was tested online using Lock-in Thermography (LT), Electrical Resistance Change Monitoring (ERCM) and Acoustic Emission (AE) under dynamic and tensile mechanical loading. For the SDS configuration, monotonic quasi static tension loading was employed. Concurrently with the mechanical testing thermographic monitoring of the deterioration of the bonded interface was enabled in live mode. On the other hand, DOF specimens were tested both in static and dynamic mechanical loading. In this case, the combined implementation of all proposed SHM strategies was feasible.

4.4.2 Experimental

4.4.2.1 Material preparation

Schematics of the Double Overlap Fatigue Specimens (DOFS) and Skin Doubler Specimen (SDS) configurations are depicted below (Fig.4.4.3).

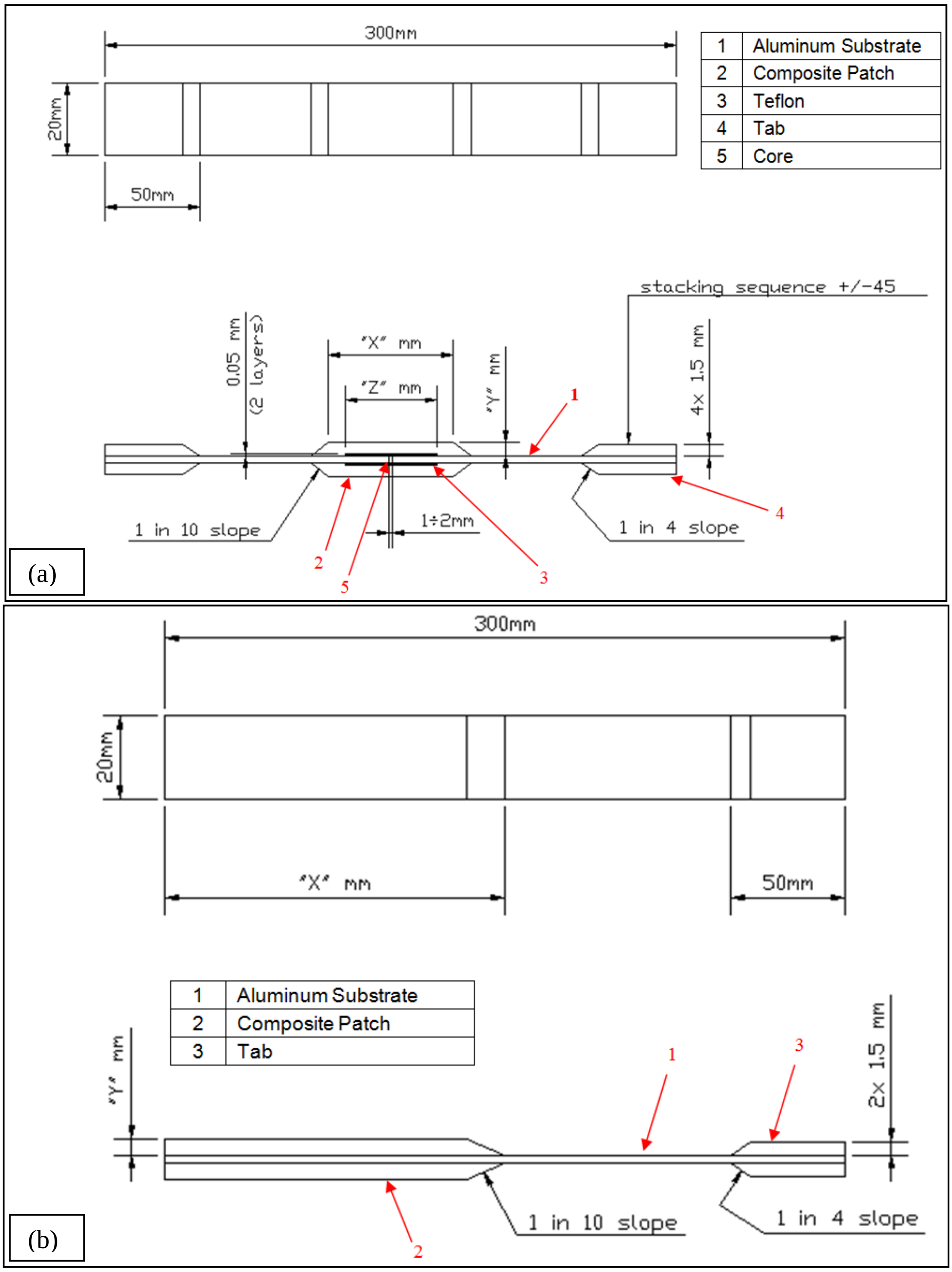

Figure 4.4.3 *(a) DOFS and (b) SDS configurations.*

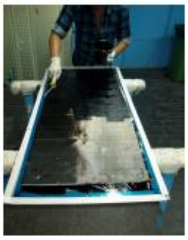

Epocast 52 A/B impregnation of 43280s carbon fabric on a preheated metallic table

Plies cutting to appropriate dimensions

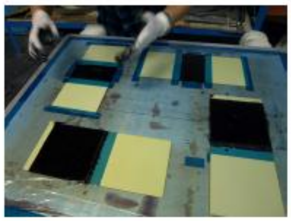

Bonding on the aluminum substrate

Curing in vacuum conditions for 2h at 93 ^{0}C using a heat blanket

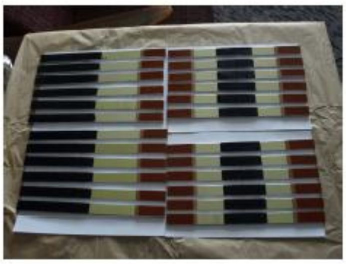

SD (left) and DOF (right)

Figure 4.4.4 *Snapshots during manufacturing of both DOFS and SDS [specimens manufactured by PZL-Swidnik /AgustaWestland[3]].*

In the case of DOF specimens, two Al parts were bonded together with a double sided CFRP patch. Teflon films were inserted close to the bonding region in the Al /patch interface (Fig.4.4.3a). Teflon films work as debond initiators because bonding at those areas is inhibited. For both DOF and SD specimens, a CNT modified epoxy matrix (EPOCAST 52)) was used (1% w/w CNTs). Anodized Al 2024 T3 was used for the inner adherend-substrate in all cases. The complete manufacturing procedure of the employed coupons is described below. The lay-up and curing procedures were as follows:

- Al surfaces preparation:

- Aluminum plate 2024-T3 CLAD , 3.18mm thickness
- Anodized OAC (according procedure IP-259)
- Primed with BR127
- Cleaning with acetone

- Adhesive:

- EPOCAST 52 A/B (weight mixed ratio A:B = 100 : 41) modified with 1% w/w CNTs
- Weight content CNT in EPOCAST 1%

- Impregnation of carbon fabric HEXCEL 43280S:

[3]The contained data belong to PZL-Swidnik S.A. and any further reprinting and usage cannot be made without PZL-Swidnik S.A. written permission.

 EPOCAST

 Performed in 60°C in order to achieve low viscosity

 Weight mixing ratio EPOCAST /dry carbon fabric 8:10

(the methodology provides a volume fiber content of 50%)

 Impregnation carbon fabric with EPOCAST within 2 plastic sheets

 Cutting and laying-up of the plies at the chosen orientation

- Curing:

 Curing cycle : 2 hours 93°C

 Vacuum pressure: ~700 mbar [4]

[4] The contained data belong to PZL-Swidnik S.A. and any further reprinting and usage cannot be made without PZL-Swidnik S.A. written permission.

4.4.2.2 Damage assessment

For the application of EPCM, electrically conductive contacts were applied on the surface of the edges of the coupons using a commercially available conductive silver paint (Fig.4.4.5). At the same areas, flexible electrodes were attached with silver loaded tape (Fig.4.4.5) in order to provide electrical connection with the cables of a multimeter (Agilent Technologies). Simultaneously to the mechanical testing, electrical resistance measurements were recorded using a digital multimeter connected to a PC for data acquisition. Fig.4.4.5 depicts the implementation of the electrical resistance measurement experimental setup as applied on DOF specimens.

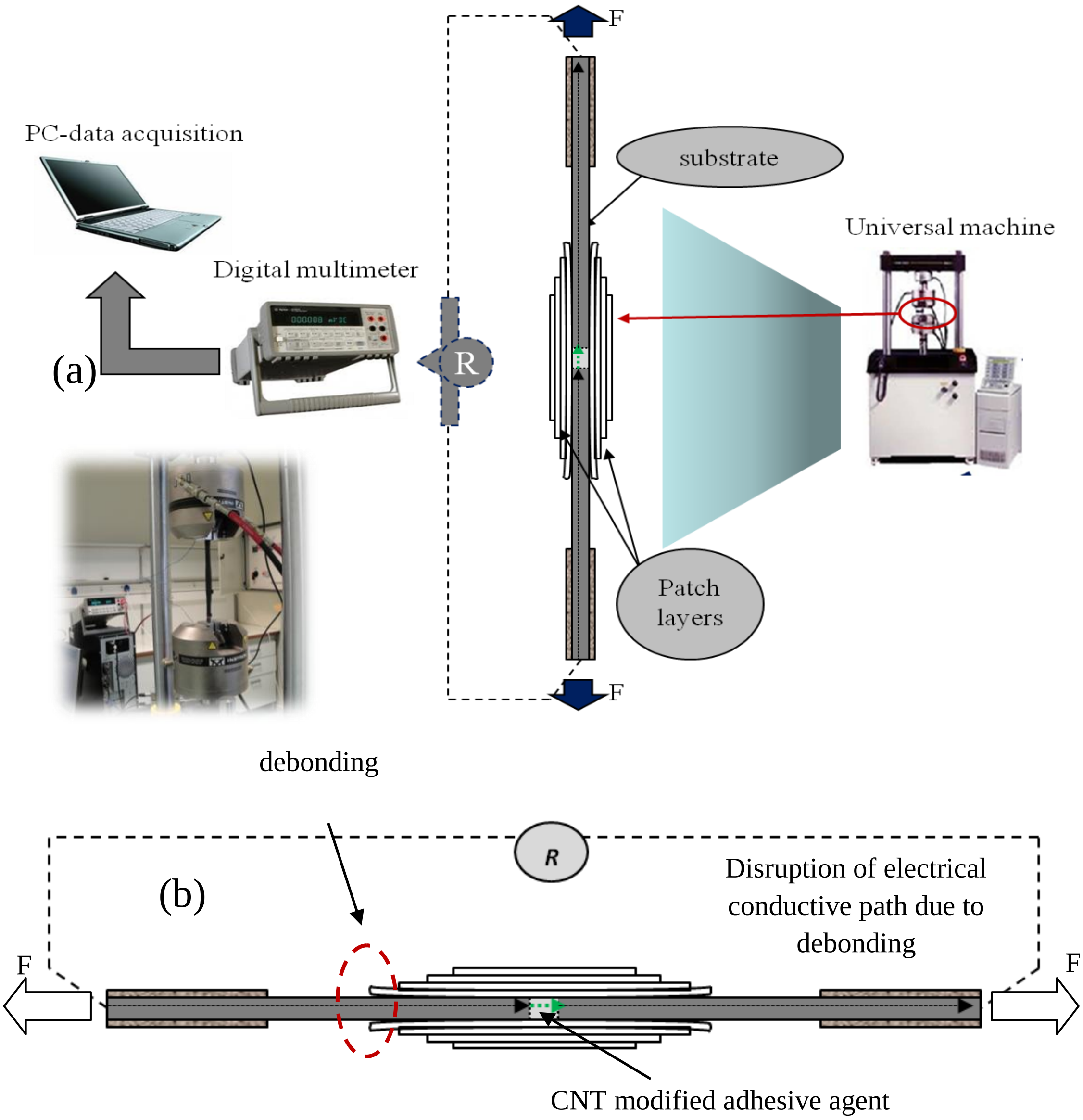

Figure 4.4.5 *(a) EPCM experimental setup, (b) EPCM measurement approach.*

In Figs.4.4.5a and 4.4.5b the measurement protocol is demonstrated. The closed electrical circuit is formed by the patch /parent material interface and the electrically conductive adhesive at the bonding /adjustment area of the two Al parts. As was expected, the evolution of the damage during mechanical testing directly related to variations in the monitored electrical resistance values. For the AE monitoring, two broadband piezoelectric transducers were used (Pico, Physical Acoustics Corp., PAC). The sensors were appropriately attached on the specimen surface as shown in Figs.4.4.6a and 4.4.6b at specific distance (~180mm). An ultrasonic gel was used to achieve acoustic coupling. A 40dB detection threshold was adopted to eliminate the presence of any external noise or needless experimental data. The gain of the employed signal amplifiers was set at 40 dB. The signals were recorded employing a two-channel PCI-2 monitoring board (PAC) with a sampling rate of 5 MHz. As is depicted in Fig.4.4.6b the deterioration of the bonded interface causes generation of AE signals. The acquired AE signals correspond to internal damage of the tested material.

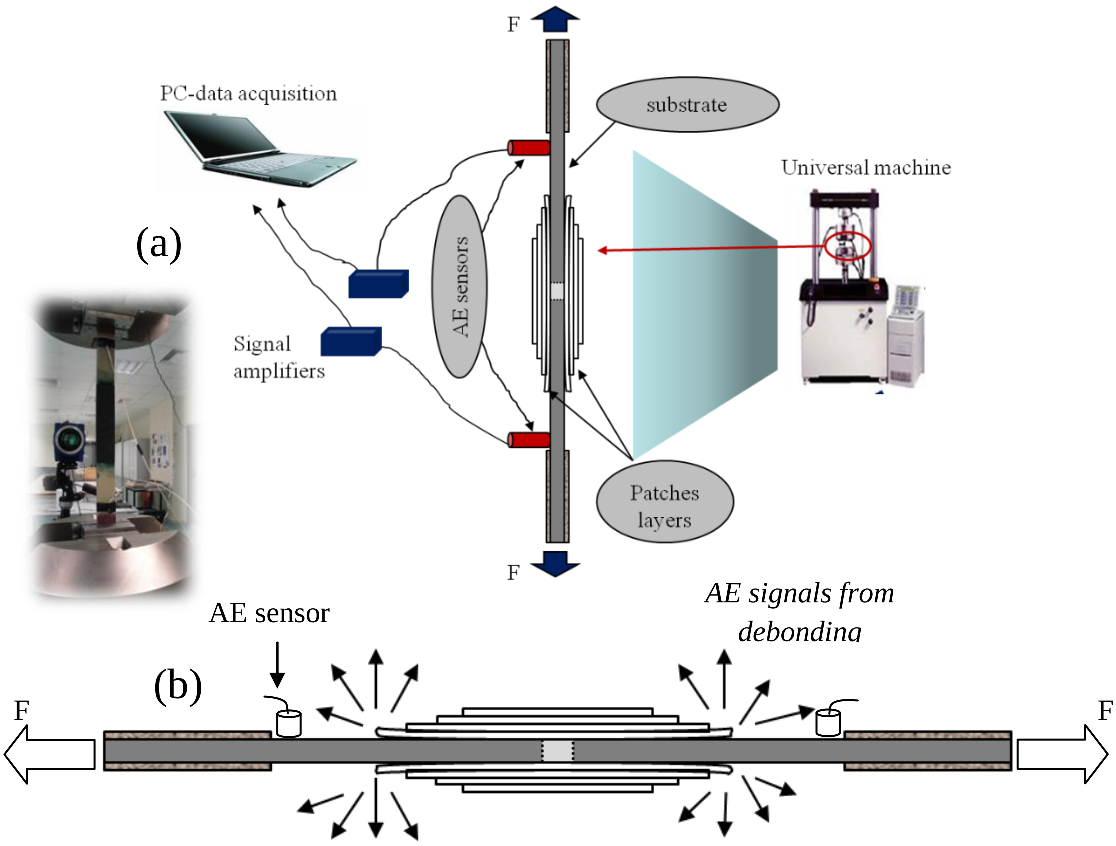

Figure 4.4.6 *(a) Schematic representation of AE technique, (b) AE signal measurement principle.*

For the thermographic inspection, the Jade 510-CEDIP-MW infrared camera was employed (Fig.4.4.7). For the tensile testing case, the camera was employed in live mode. Thus, thermal images were recorded during test procedure. Regarding fatigue testing, lock-in mode at a frame frequency of 50 Hz was employed. The infrared camera was positioned at approximately 1 m distance from the specimen in order to include the whole patched area in the Field Of View (FOV) of the camera (Figs.4a and 4b). At this distance the corresponding FOV was 208x156 mm^2 with a lateral and perpendicular resolution of 0.65 mm/pixel. Fig.4.4.7 illustrates the thermographic experimental setup.

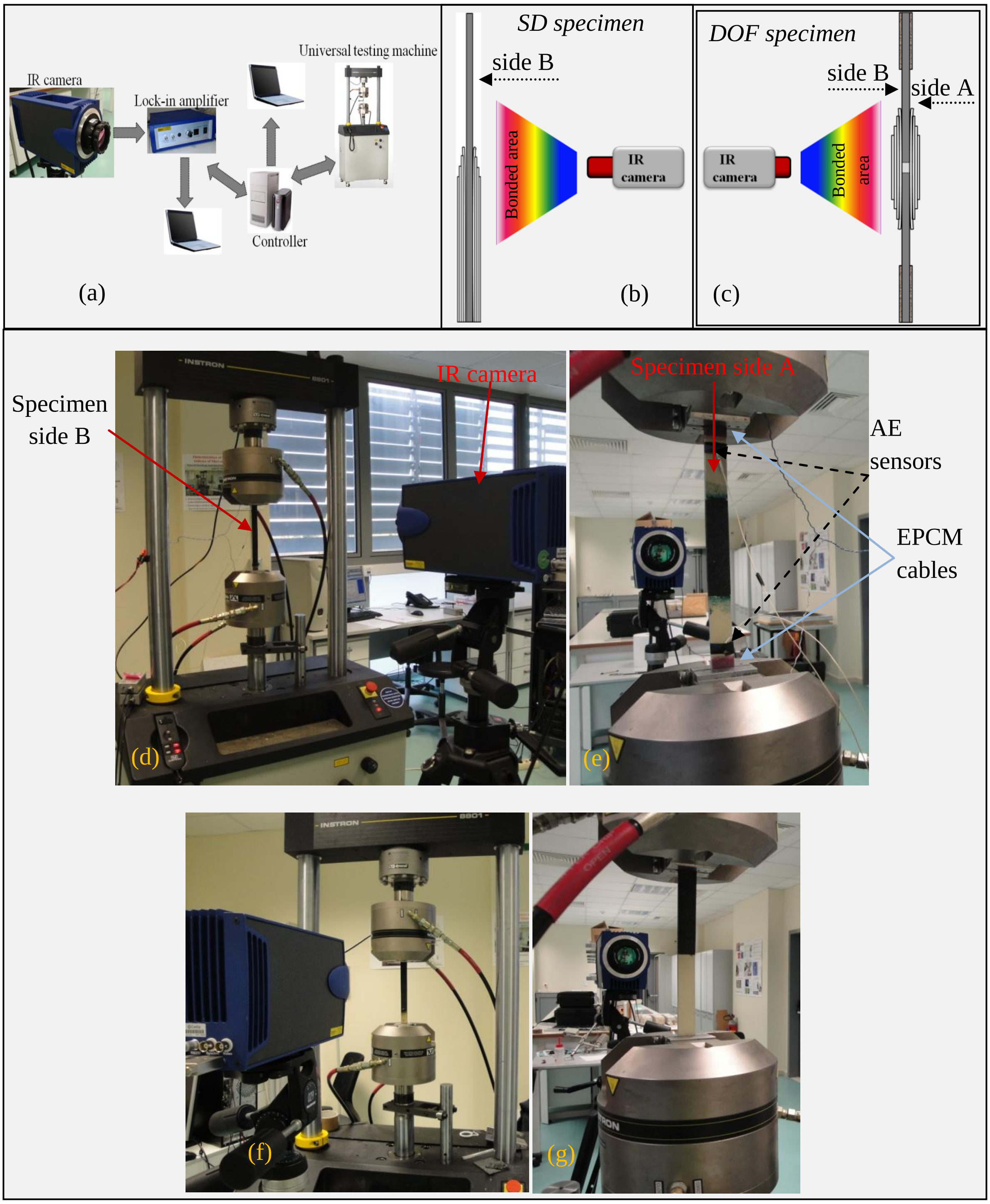

Figure 4.4.7 *(a) Schematic of the thermographic experimental setup, (b, c) recorded field of view from the thermocamera, (d, e) snapshots of both DOFS sides, (f, g) snapshots of both SDS sides.*

4.4.3 Results and discussion

4.4.3.1 Static testing

As previously noted, skin doubler specimens were tested under only static mechanical loading with IrT in live mode to monitor the deterioration of the patch /substrate interface. Thermal images at specific time intervals are depicted in Fig.4.4.8 show the irradiated temperature change along the coupon surface. Table 4.4.1 lists the tensile properties of the all tested materials.

Table 4.4.1 *Mechanical properties of SDS and DOFS.*

Representative coupon	Max tensile load [N]	Ave max tensile load [N]
	28109	
SDS	28109	28002
	27789	
	17458	
DOFS	18868	
	18034	18120

Fig.4.4.8 presents the temperature profile during the static mechanical testing of a representative SDS. A straight line was drawn along the coupon surface through the software of the camera (Altair). The maximum recorded values on a pixel by pixel basis along the straight line, are plotted against time-frames during loading (Fig.4.4.8). The Special /signal units manifested on the yy' axis is an uncalibrated display mode of the (Altair-Li) camera software which is proportional to the temperature difference, also called as Digital Level (DL). As is depicted in Fig.4.4.8, temperature is changing with the debonding of the patches from the aluminum substrate. On the onset of the experiment (Fig.4.4.8i) a relatively uniform color (blue color) is presented on the image corresponding to the bonded region. A small pink region which corresponds to increased temperature was recorded from the bottom area of the Al substrate, at the initial phase of the experiment. This recorded high temperature of the Al substrate (pink color) is attributed to the heat diffusion from the loading frame of the testing machine. As tensile loading continued the temperature profile changed along the patched area with the debonding of the outer adherends (Figs.4.4.8ii to 4.4.8vii). On the last thermal image (Fig.4.4.8viii), an area with increased temperature (pink color) is radiated from the Al surface. A small pink area on top of the same image (Fig.4.4.8viii) was considered as the last bonded

area of one of the outer adherends. After that observation, the test was stopped. In all cases the recorded temperature difference (ΔT) on the surface of the tested material (graph of Fig.4.4.8) shows that ΔT decreases gradually with the deformation of the outer composite adherends until their final complete detachment where a rapid increase is recorded.

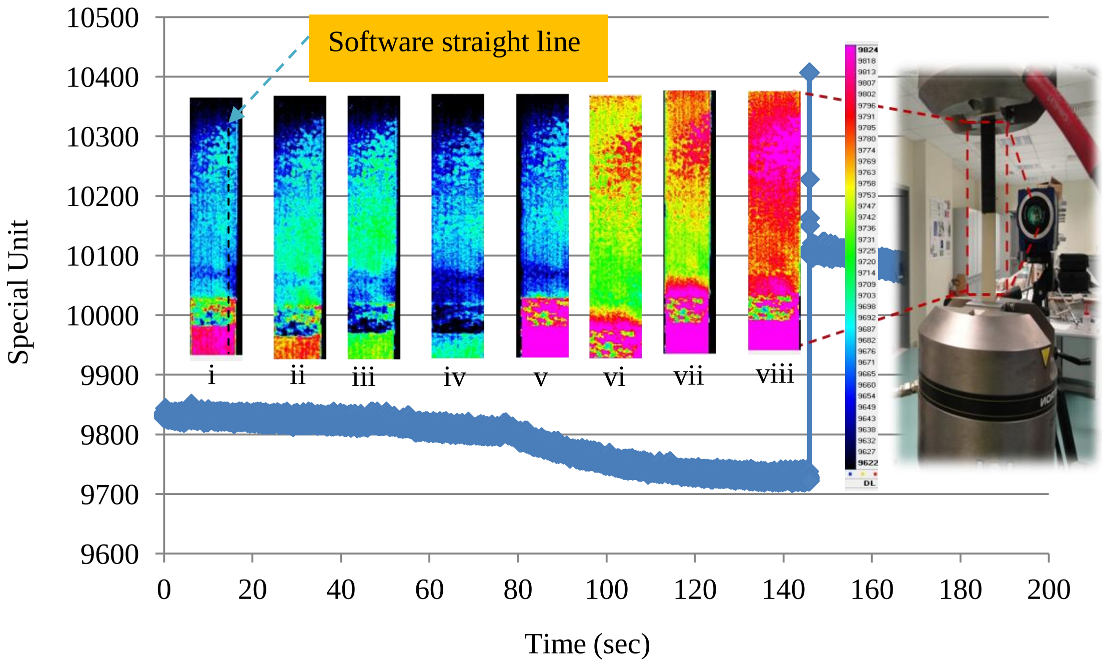

Figure 4.4.8 *Temperature profile recorded in real time during static testing of SDS.*

It is noteworthy that in these coupons, the monitored deterioration is a result of two adherends detachment. There is not sufficient information to distinguish which side of the two sided patch fails first. Thus, the thermographic methodology provided an overall damage metric of the material. Optical photographs during testing, show the deterioration of the patch bonded interface (Fig.4.4.9 (1-4)).

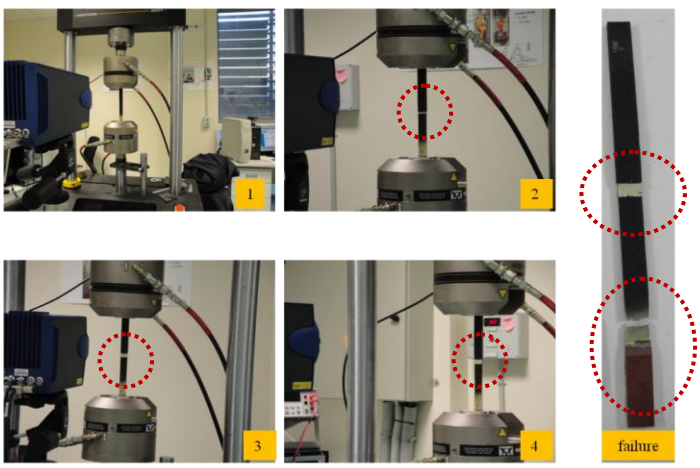

Figure 4.4.9 *Gradual failure of the SD coupon under static testing.*

Fig.4.4.10 depicts the temperature variation along the surface of a representative DOF specimen during static testing. As is shown, the deterioration of the patch /substrate interface can be monitored via the temperature differences radiated from the material surface. On the onset of the experiment (Fig.4.4.9i) a central red - slightly pink area is presented on the image. This is the un-bonded region (PTFE inserts) and also the very same area where debonding process initiates. With the deterioration of the interface, this pink region (Figs.4.4.10ii-4.4.10v) gradually diminished. After an initial detachment (Fig.4.4.10ii), the observed thermal imprint changed characteristically (Fig.4.4.10iii to 4.4.10iv) until final failure (Fig.4.4.10vi). When the patches on both sides completely failed, a pink color masked the image reflecting the compete separation of the patches from the inner aluminum parts. It is worth repeating that considering the double side patching of SDS and DOFS, it is difficult to discern with thermography which particular patch fails. However, in all cases the overall coupon degradation can be monitored via temperature variations irradiated from the coupon surface during mechanical loading.

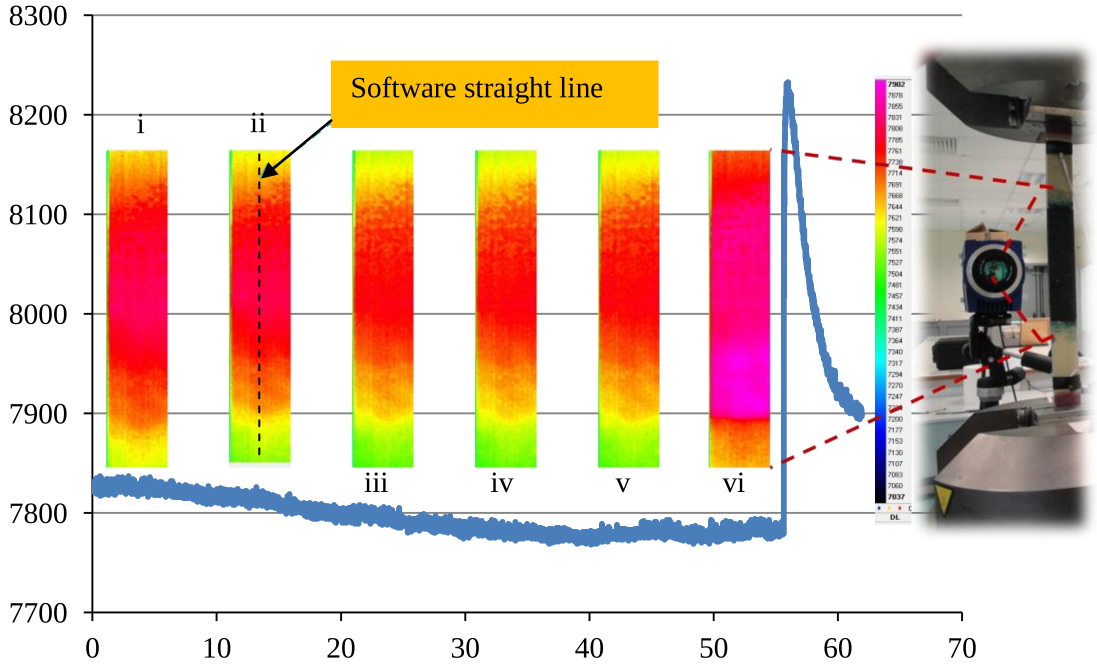

Figure 4.4.10 *Temperature profile recorded in real time during static testing of DOFS.*

In Fig.4.4.11a, the normalized to the initial value electrical resistance ($\Delta R/R_0$) and mechanical load recordings are plotted against time. $\Delta R/R_0$ increases with load application, following directly the loading profile. Initially, $\Delta R/R_0$ increases until approximately 18 seconds. At that point a drop in load value occurred. This drop straightforwardly mirrored in electrical resistance value with a similar to load profile, slight slope. After that point, $\Delta R/R_0$ increased again until one more change in load value which consequently altered the electrical resistance values. Afterwards, an incremental behavior was recorded until final failure of the coupon which occurred at approximately 56 seconds. The final breakage of the coupon inflicted an extremely rapid increment in electrical resistance values. This expected observation was obtained due to the disruption of the electrical conductive path of the coupon. Fig.4.4.11b depicts the acquired acoustic emission signals as a function of the length between the two piezoelectric sensors. Initially, the acoustic signals were released from a source emitting from the centre of the specimen. During tensile loading, AE activity was distributed along the whole patched length. This distribution is an indication of patch failure which started from the centre of the specimen and gradually reached the two patch edges.

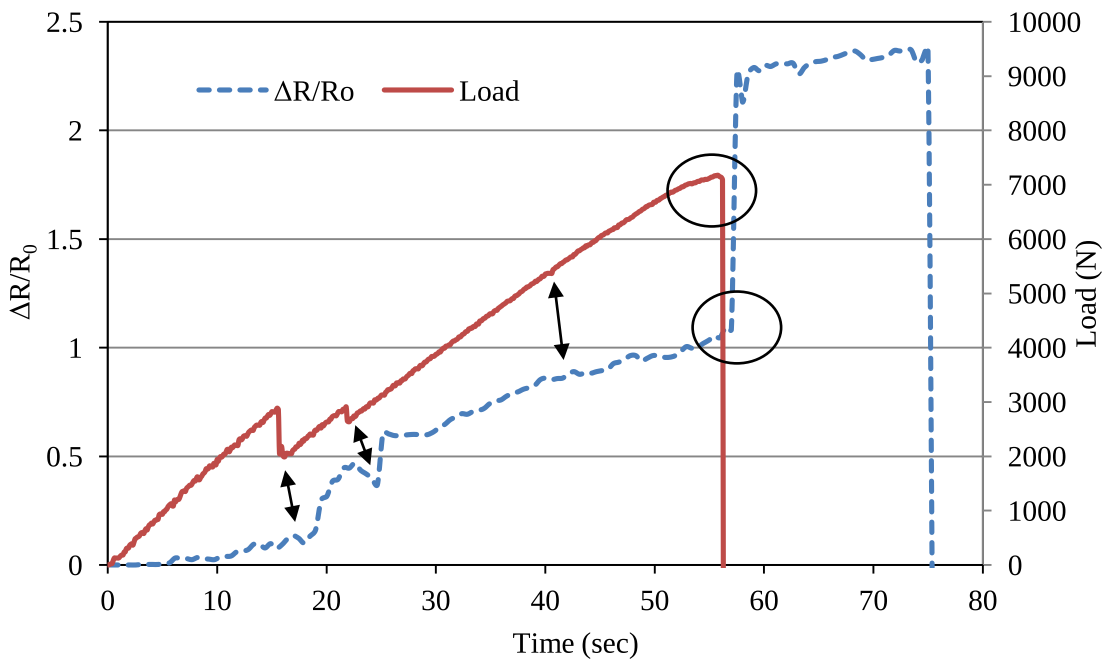

(a)

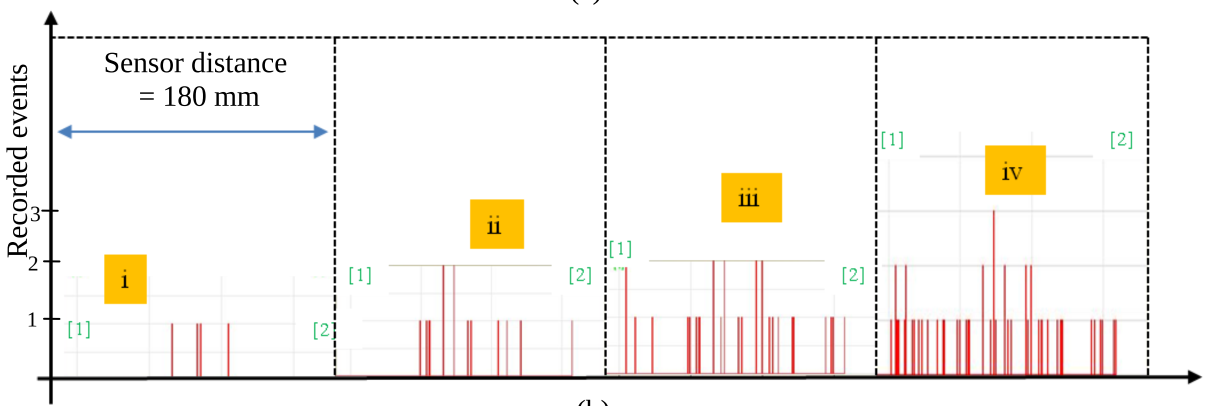

(b)

Figure 4.4.11 *(a) $\Delta R/R_0$ recorded in real time during static testing of DOFS as a function of load, (b) acoustic emission incidents released during test.*

Fig.4.4.12 shows optical photographs during tensile testing of the specimen. In end of the test the specimen had been separated into two parts. Outer adherends detached completely from one of two inner aluminum parts.

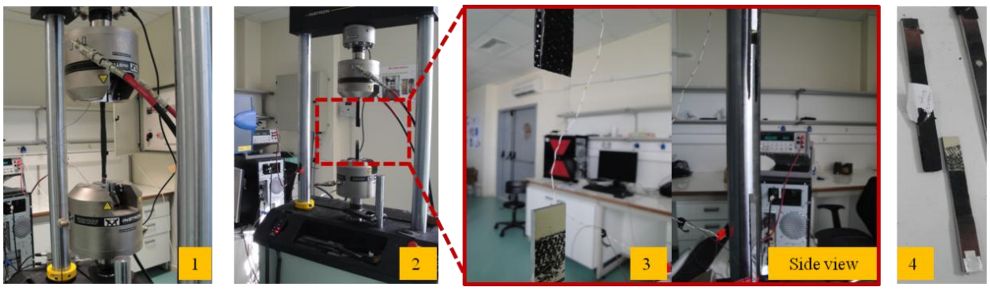

Figure 4.4.12 *(1) Image during test, (2-4) post failure images.*

4.4.3.2 Dynamic testing

Only double overlap fatigue specimens were dynamically tested. Tension-tension fatigue testing with incremental loading levels was performed. More specifically, the coupons were subjected to 35%, 40% and 50% of the maximum tensile load of the material. The maximum load was experimentally estimated to be equal to 18 ± 0.5 kN according to ASTM D3039 /D3039M - 08 (Standard Test Method for Tensile Properties of Polymer Matrix Composite Materials). A total of seven DOF specimens were tested in 10 Hz tension-tension fatigue and stress ratio approximately R=0.06. Table 4.4.2 lists the experimental parameters.

Table 4.4.2 *Experimental parameters of the dynamic mechanical testing.*

Load level	Average load [N]	Amplitude [N]	Stress ratio R	Max. No cycles	Maximum load frequency [Hz]
1	3400	±3000	0.059	$1*10^6$	**10**
2	3900	±3500	0.054	$1*10^6$	
3	4600	±4100	0.057	$1*10^6$	

All tests were performed until coupon fracture. Nevertheless, testing was decided to stop in the case a coupon help up to the $1{\cdot}10^6$ loading cycles. As resulted from the experimental series, only one coupon reached $1{\cdot}10^6$ cycles. Table 4.4.3 and Fig.4.4.13 depict the fracture loading cycles for the three different load levels.

Table 4.4.3 *Maximum fatigue cycles.*

Representative coupon	Max loading cycles
Level 1	$1{\cdot}10^6$
Level 2	850
	20972
	29436
Level 3	20772
	9812
	3970

Table 4.4.3 and Fig.4.4.13, indicated that the tested coupons failed consistently at similar loading cycles.

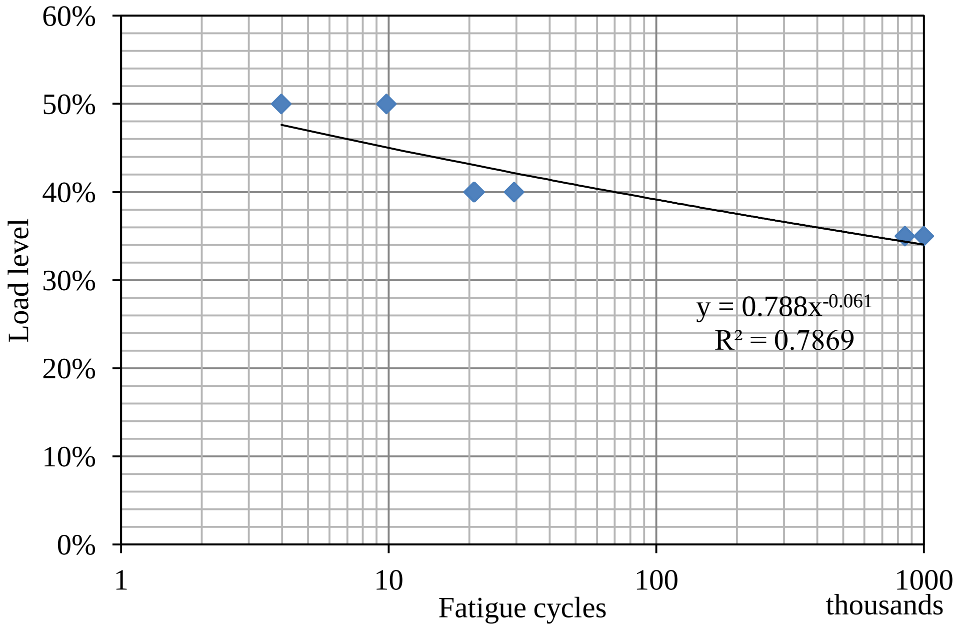

Figure 4.4.13 *Fatigue cycles as a function of load levels.*

Fig.4.4.14a demonstrates the loading profile of a representative DOF specimen when subjected to tension-tension fatigue. The load level was 40% of the maximum tensile load of the DOF specimen. The electrical resistance changes normalized to the initial value ($\Delta R/R_0$) are depicted vs. the maximum induced fatigue load as a function of time. The development of internal damage is mirrored in the recorded resistance fluctuations. Every increase of normalized resistance measurements potentially indicates damage propagation. The complex behavior of $\Delta R/R_0$ might be explained by the double patched material. Changes in the electrical conductive path take place with the initiation and propagation of the following failure modes i) patch debonding and ii) deformation of the adhesive which connects the two aluminum parts. At the same time, acoustic emission incidents show the location of the induced damage. As is indicated by the acoustic events during mechanical testing, damage initiates from the centre of the specimens (Figs.4.4.14b i-vi). As was also observed in static testing, initial acoustic emission signals emanated from the centre of the specimen (Fig.4.4.14b(i)). As fatigue loading continued, acoustic signals accumulated in the centre of the specimen as well as in the area between the centre and the bottom edge (transducer No.2) of the specimen.

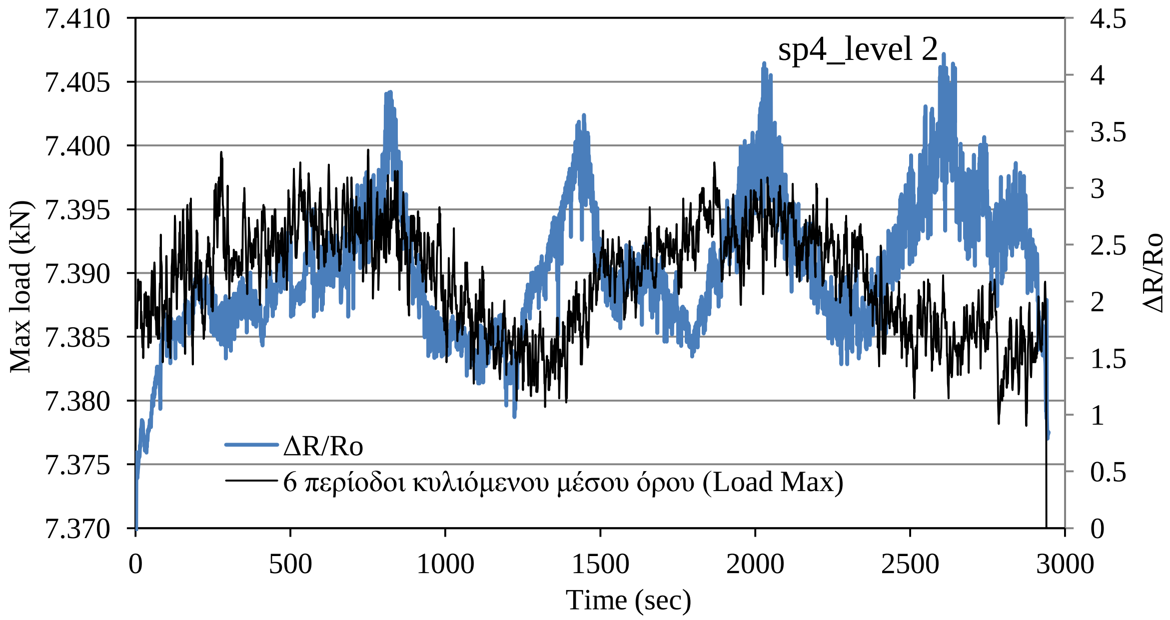

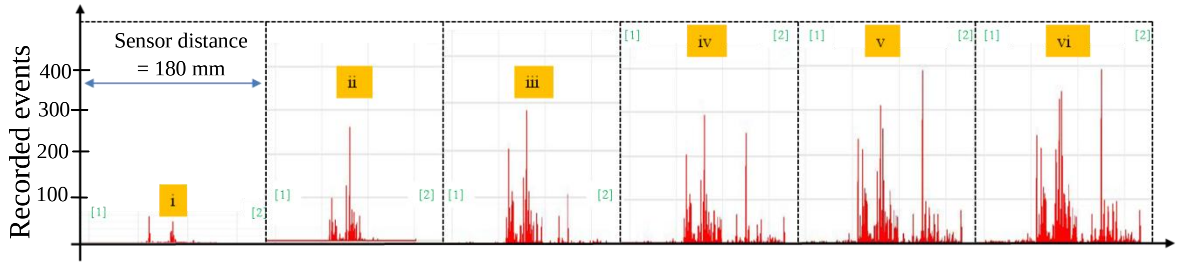

Figure 4.4.14 *(a) Loading profile vs. $\Delta R/R_0$ values as a function of time (b) acoustic emission incidents released during test.*

Taking into account the aforementioned considerations, it is difficult to discriminate the distinct failure mode. However, when damage occurs, it is clearly shown as changes in the electrical resistance values.

Figs.4.4.15 depict amplitude thermographic images at specific fatigue loading cycles of the tested specimen (sp4). On the onset of the experiment (106 sec), a high amplitude area is present on the image. Obviously, detachment of the patches starts from the centre of the specimen where PTFE tapes are located. As fatigue loading continued, the high amplitude area expanded along the longitudinal axis (loading axis) of the specimen denoting the debonding of the two outer adherends. This effect is more pronounced on the bottom side of the specimen or the side where load is imposed by the loading frame. This was also observed in the case of the acoustic monitoring, with the accumulation of AE incidents in the area between the centre and bottom (transducer No.2) edge of the specimen (Fig.4.4.14b(iii-vi)). After approximately 3000 seconds of fatigue testing, the high amplitude area gradually diminished. The generation of stress concentrations led to the debonding of the two composite patches. As a result, the coupon failed at its centre or else at its 'weak' point where the adhesive connects the two separated metal parts.

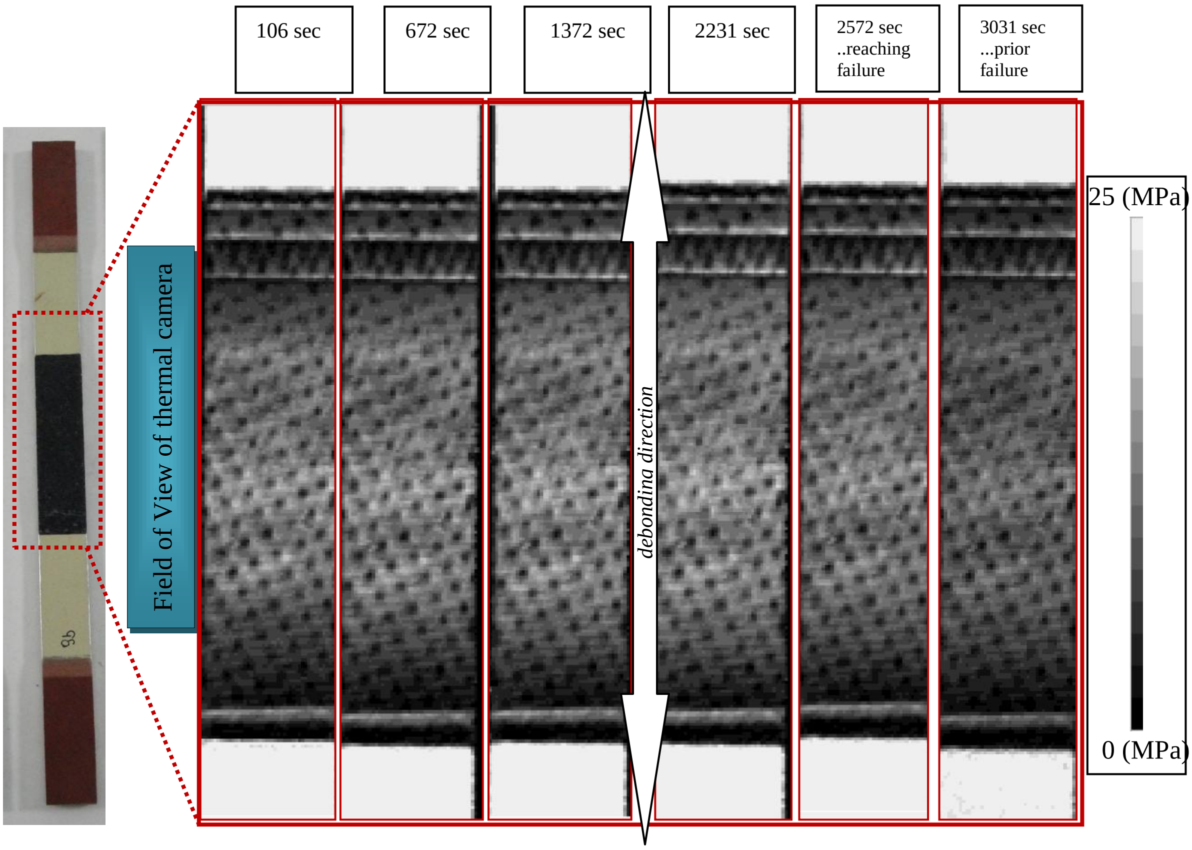

Figure 4.4.15 *Amplitude images during specific time intervals showing the structural deterioration of the specimen.*

Section conclusions

The aim of the section was to examine two different configurations of representative coupons with a view to addressing the damage tolerance of bonded composite repairs. To that respect, a combined NDE system was developed through EPCM, AE and IrT for the monitoring of debonding process. Double overlap fatigue and skin doubler specimens were mechanically tested. The latter were tested solely in static mechanical loading. Thermography was used at the static testing in live mode, monitoring the degradation of the two composite adherends. A gradual drop of temperature difference values was observed during tensile loading. The deterioration of the interface was imprinted on the acquired thermal images. The discrimination of the particular failure mode was inhibited by the double repair patch protocol. However, the overall structural degradation was assessed in real time via thermography. DOF specimen configuration allowed for the implementation of EPCM, AE and IrT methods simultaneously to the testing procedure, in real time. DOFS were tested in both static and dynamic mechanical loading conditions. As far as quasi-static tensile testing is concerned, noticeable thermal changes were recorded with the debonding of the two composite adherends. When both composite patches were completely detached from the aluminum parts, a uniform color - thermal image was observed, reflecting the complete patch /substrate interface failure. At the same time the electrical signature of the coupon followed directly damage progression at all phases. Acoustic emission signals accumulated in the centre of the specimen, highlighting the potential failure site. With the evolution of load, AE activity was distributed along the full length of the patch indicating the propagation of damage. At the time prior failure, AE signals accumulated again at the centre of the specimen where fracture finally occurred.

Concerning fatigue mechanical testing of DOFS, IrT identified and monitored in real time the stress concentration areas which led to debonding of the patches from the inner adherend (critical failure). During mechanical loading, debonding was manifested in the form of high amplitude sites expanding from the centre to the edges of the specimen contrarily to what was observed in the specimens of 4.1 & 4.3 sections of the thesis. As was noticed, stress concentrations (bright areas) were more pronounced at the loading axis of the specimen (lower side). Identical behavior was recorded from the AE signals which initially emanated from the centre of the specimen and gradually progressed along the loading side (right side – No.2 transducer). After the complete detachment of the patch, the coupon failed catastrophically at its centre i.e. at the connection point of the two aluminum parts. As far as the ERCM is concerned, the load induced a periodical change of electrical resistance values. Every increase of electrical resistance measurements has been considered as damage evolution due to the deformation of the electrical conductive path. It is highly probable that, in this case, the two composite adherends do not debond in a uniform way but separately, as the electrical resistance change was not monotonic, but periodically got higher and lower values.

4.5 System level integration: On-line structural degradation monitoring of structural components using lock-in thermographic imaging

4.5.1 Introduction

After the successful small scale investigation, the aim of the present section concerns the validation of the integrated system in a real aeronautical structure. This scaling up process from coupon to demonstrator level will assist the maturation and the industrialization of repair integrity monitoring technologies, setting the specifications and the guidelines for further development. Within the framework of the IAPETUS ACP8-GA-2009-234333 (FP7-Aeronautics) project, a wing structure was manufactured by PZL-AgustaWestland. The wing is the Vertical stabilizer of PZL SW-4 helicopter manufactured by PZL. A typical encountered type of damage was pre-introduced on the skin of such component. The wing structure was consequently repaired with the bonded repair methodology. The repaired structure was tested under bending fatigue loading condition and the propagation of damage was identified and monitored by the integrated thermographic monitoring system. To that respect, the developed technology presented in the previous sections (section 4.1, 4.3 and 4.4) was validated and integrated with the smart repair technologies in large scale applications. Testing was performed on-site at the PZL premises in Swidnik, Poland, with concurrent ERM, Lamb–wave and Thermographic monitoring. As should be noted, the role of the University of Ioannina in the specific IAPETUS task was the thermographic assessment of the structural deterioration of the wing to which this section is restricted. The acquired thermographs are juxtaposed with C-scans performed after substantial critical failure of the patch.

4.5.2 Aluminum wing structure

The PZL SW-4 Puszczyk (pl. Tawny Owl) is a Polish light single-engine multipurpose helicopter manufactured by PZL-Świdnik /AgustaWestland in Poland. The origins of PZL-Swidnik's SW-4 five seat light utility helicopter date back to the early 1980s.

Figure 4.5.1 *SW 4 helicopter.*

Fig.4.5.1 depicts the vertical stabilizer fixed on the helicopter (SW-4). The skin of the stabilizer is constituted of the 2024 T3 aluminum alloy sheet. The thickness of the external surface (skin) varies from 0.4mm to 1.5mm. The internal part of the stabilizer consists of a honeycomb core HexWeb CR III-3,8 5/32-10 (5052). The honeycomb thickness ranges from 32mm to 34.2mm across the longitudinal axis of the stabilizer. On Fig.4.5.2, a schematic representation of the cross section of the stabilizer is shown.

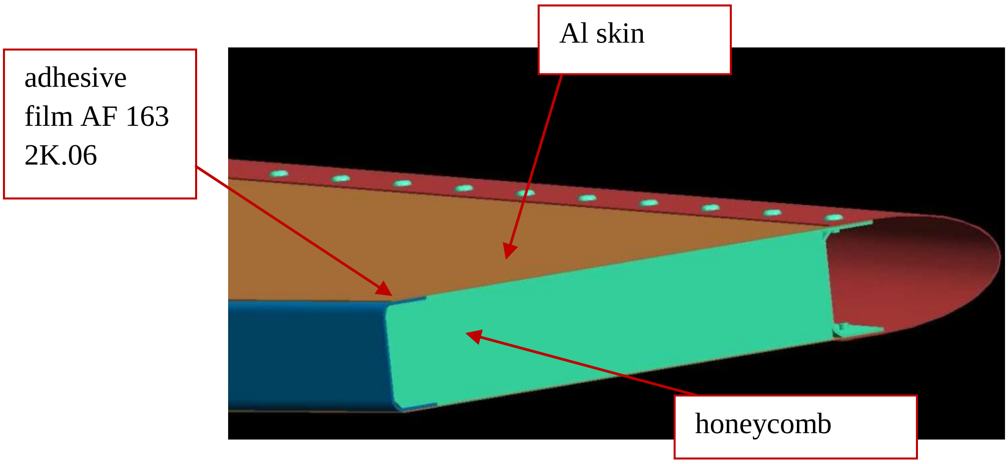

Figure 4.5.2 *Schematic of the cross section of the stabilizer*[5].

[5] The contained data belong to PZL-Swidnik S.A. and any further reprinting and usage cannot be made without PZL-Swidnik S.A. written permission.

As can be seen in Fig.4.5.1, the stabilizer is fastened on the tail of the helicopter using four bolted joints. Previous analyses and dynamic testing on the stabilizer indicated that typically damage initiated in the form of a crack which propagated in the vicinity of one of the four bolted joints (Fig.4.5.3a). As the specific area was considered as critical (Fig.4.5.3a), this location and type of damage were chosen as representative of failure initiation and propagation, and therefore as a highly probable location for the application of bonded repair. In the tested case, an intact stabilizer was artificially damaged in the specific site and repaired with a bonded composite patch. The location and configuration of the patch is shown in Fig.4.5.3b. The artificially induced crack is visible on Fig.4.5.4. As can be observed, the crack was created close to the bolted joint. Figs.4.5.5a and 4.5.5b depict the repaired stabilizer prepared for testing, as well as a schematic representation indicating its dimensions.

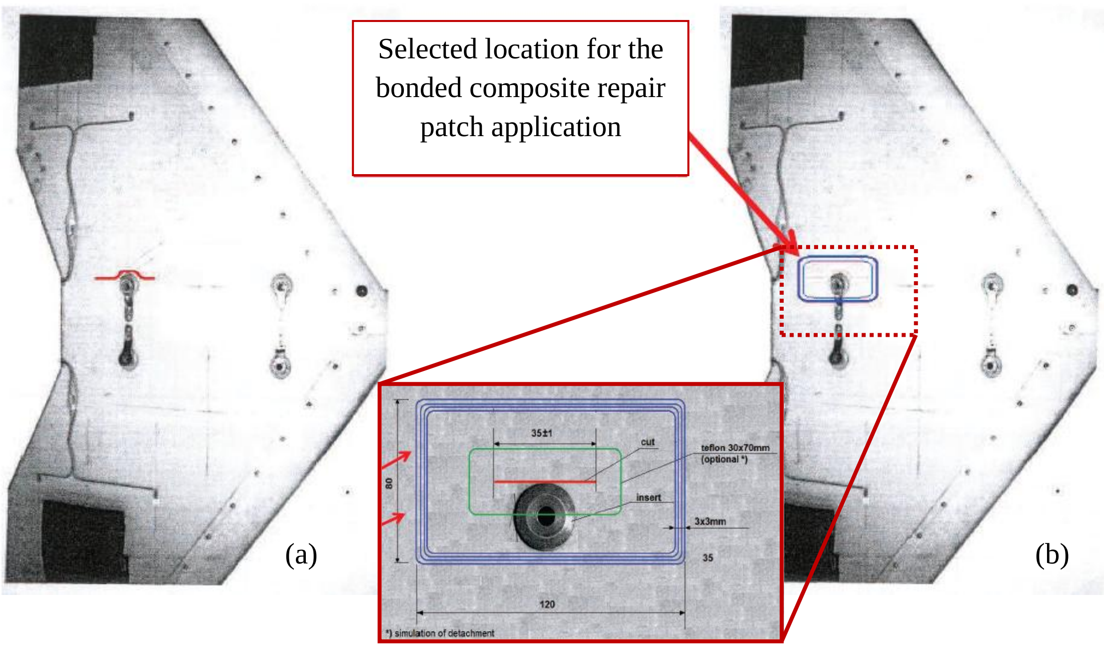

Figure 4.5.3 *(a) Crack initiation and propagation; critical area, (b) selected area to apply the bonded patch repair* [6].

[6] The contained data belong to PZL-Swidnik S.A. and any further reprinting and usage cannot be made without PZL-Swidnik S.A. written permission

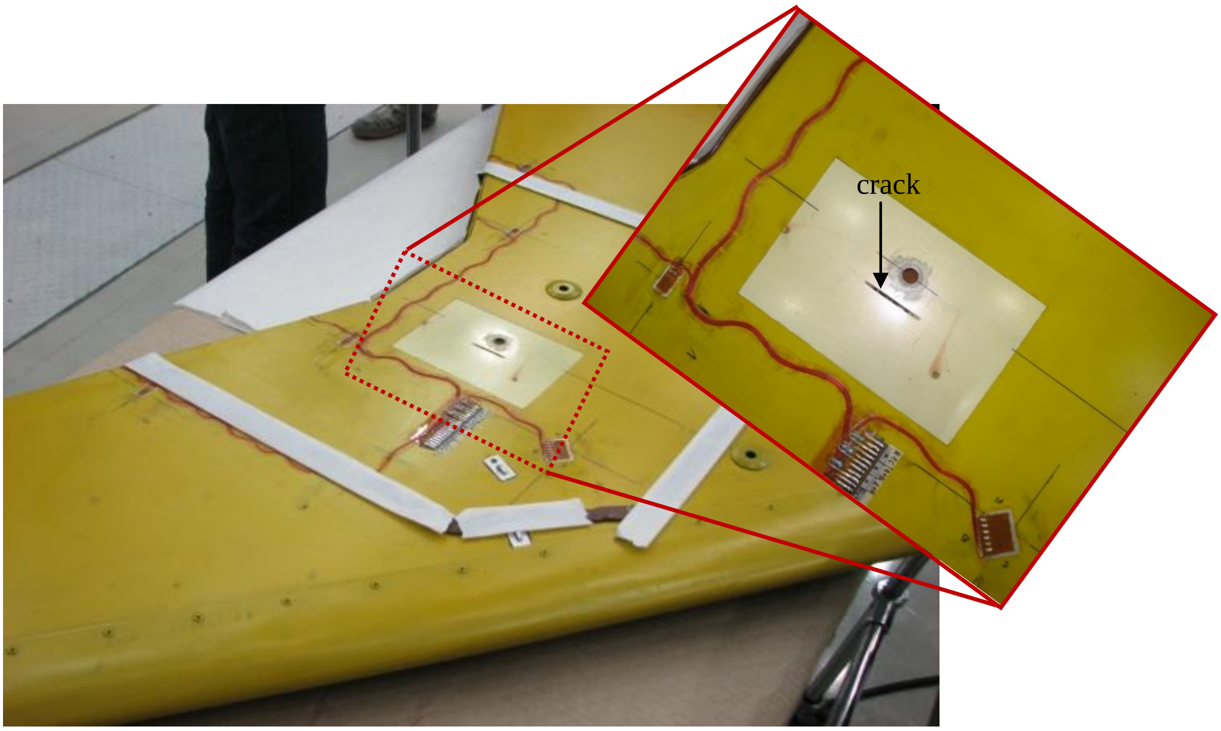

Figure 4.5.4 *Stabilizer before patch repair application; location of artificial crack*[7].

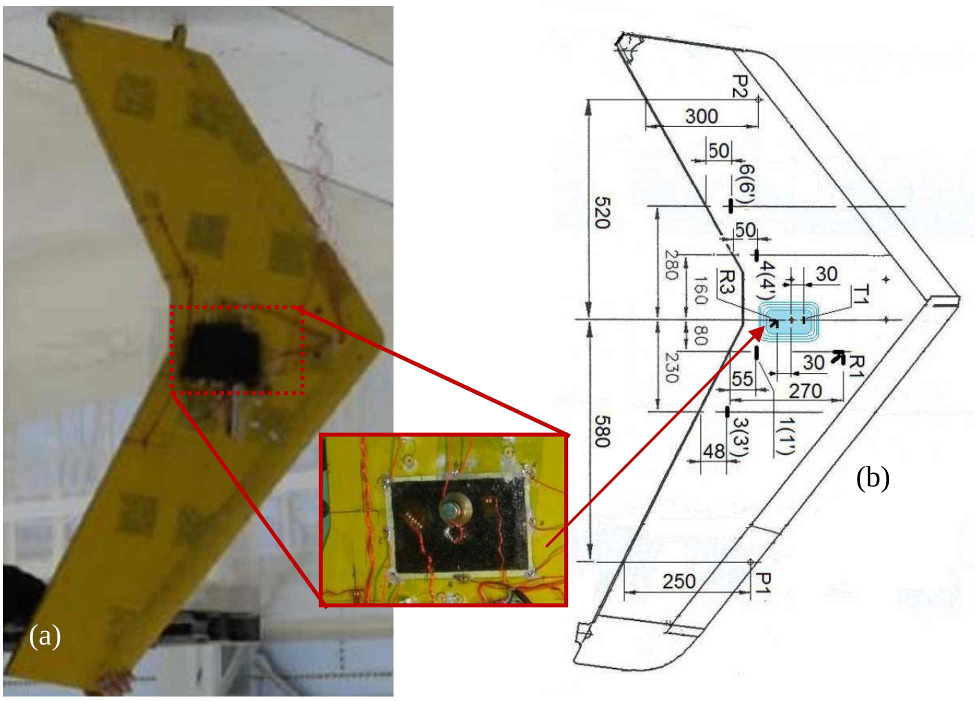

Figure 4.5.5 *(a) Stabilizer before testing, (b) schematic representation of the stabilizer*[8].

[7,7]The contained data belong to PZL-Swidnik S.A. and any further reprinting and usage cannot be made without PZL-Swidnik S.A. written permission.

On Fig.4.5.5a, one can distinguish the applied bonded composite patch. Since the patch was applied in the vicinity of the bolted joint, it covered the circular notch drilled for placing the rivet (Fig.4.5.4). To this end, after the curing of the patch, an additional hole was drilled on the patch in order to allow for rivet fastening. For the patch, the Hexcel 43280s series carbon fabric was adopted. As a matrix, the modified with 1% w/w CNTs Epocast 52 A/B was employed. The patch material configuration was the one employed in section 3.1 (*Case 3*). A four-layer bonded patch was applied using the hand lay-up method. The patch was vacuum bagged and cured under -700mbar vacuum pressure using a thermal blanket with multiple zone PID thermal control, as is usually the practice in the aircraft industry [286-288].

4.5.3 Mechanical testing

Based on the complex shape of the aluminum demonstrator, an in-house manufactured (PZL), purposely built hydraulic loading frame was used. The testing protocol was bending fatigue testing with two bending moments. A schematic of the testing setup is shown below (Fig.4.5.6):

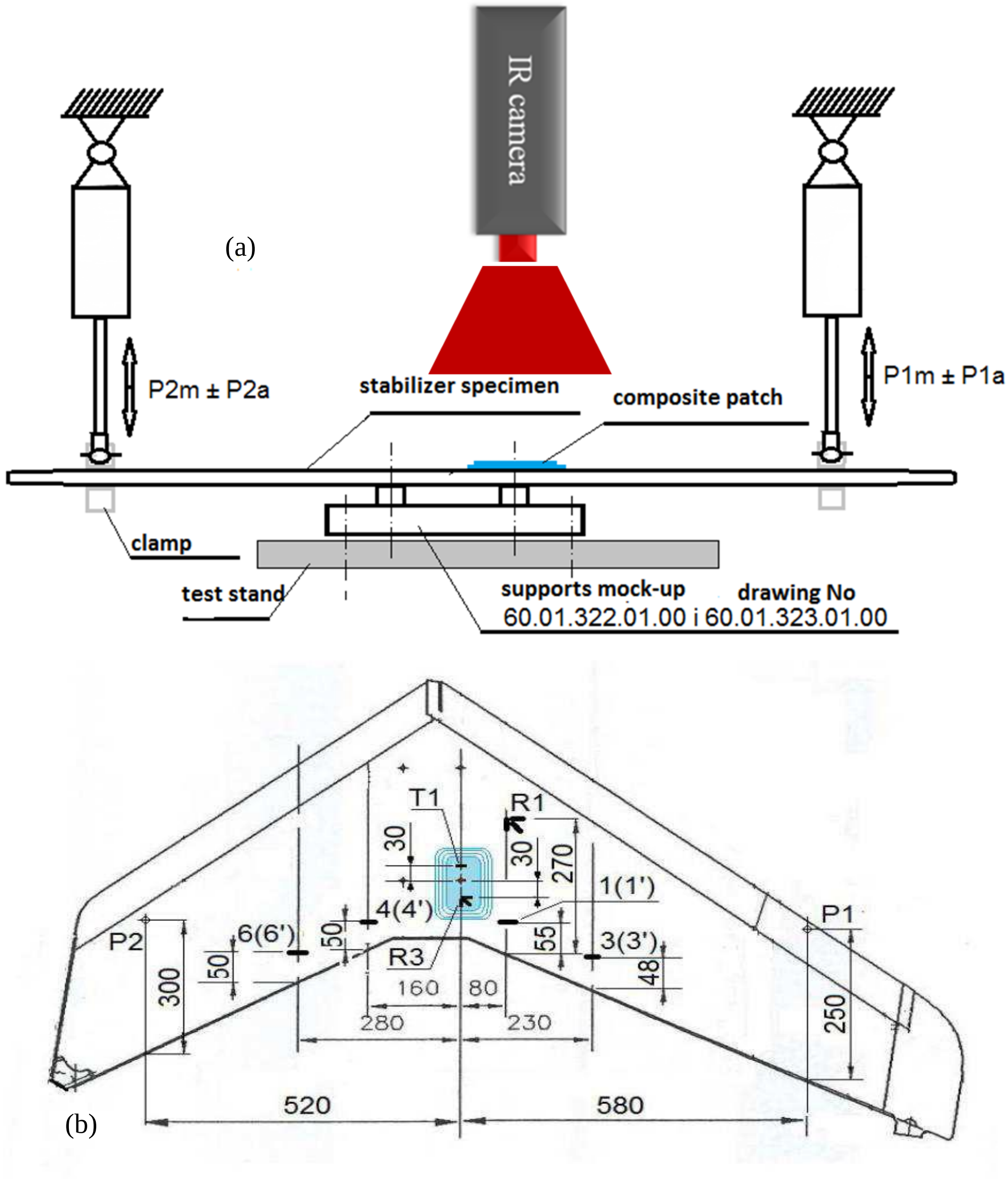

Figure 4.5.6 *Schematic representation of the testing setup; (a) side and (b) top view*[9].

As is shown in the above pictures, the induced bending moments were of different amplitudes in order to equilibrate the distance difference between the centre and the clamped points of

[9] The contained data belong to PZL-Swidnik S.A. and any further reprinting and usage cannot be made without PZL-Swidnik S.A. written permission.

the stabilizer. Table 4.5.1 lists the performed loading sequence which consisted of 13 successive incremental loading levels. The first loading level lasted for 280 kcycles. Thereafter, the loading level was increased after every 25 kcycles.

Table 4.5.1 *Applied mechanical loading parameters.*

STEP	Loading Cycles (kcycles)	P1 Mgm (Nm)	P1 Mga (Nm)	P2 Mgm (Nm)	P2 Mga (Nm)	F (Hz)
1	5	60.00	150.00	60.00	120.00	20
1	15	60.00	150.00	60.00	120.00	20
1	25	60.00	150.00	60.00	120.00	20
1	50	60.00	150.00	60.00	120.00	20
1	100	60.00	150.00	60.00	120.00	20
1	200	60.00	150.00	60.00	120.00	20
2	280	60.00	165.00	60.00	130.00	20
3	305	60.00	180.00	60.00	145.00	20
4	330	60.00	200.00	60.00	160.00	20
5	355	60.00	220.00	60.00	175.00	20
6	380	60.00	240.00	60.00	190.00	20
7	405	60.00	265.00	60.00	210.00	20
8	430	60.00	290.00	60.00	230.00	20
9	455	60.00	320.00	60.00	255.00	20
10	480	60.00	350.00	60.00	280.00	20
11	505	60.00	390.00	60.00	310.00	20
12	555	60.00	420.00	60.00	340.00	20
13	561	60.00	420.00	60.00	340.00	20

As for the thermographic assessment, the thermal camera was appropriately positioned vertically facing the top (repaired) surface of the stabilizer (Figs.4.5.7a and 4.5.7b). As this is usually the practice on thermographic imaging, the patched area was painted with black mat paint to render the emissivity of the inspected surface close to the black body (ε = 1). The distance between the camera and the stabilizer was approximately 0.8 m. Lock-in of the camera acquisition was performed utilizing the electrical waveform employed for the P1 loading moment (Fig.4.5.6 and 4.5.7). The frame rate of the infrared camera was set to 25Hz. Figs.4.5.7a and 4.5.7b depicts snapshots of the experimental setup during testing.

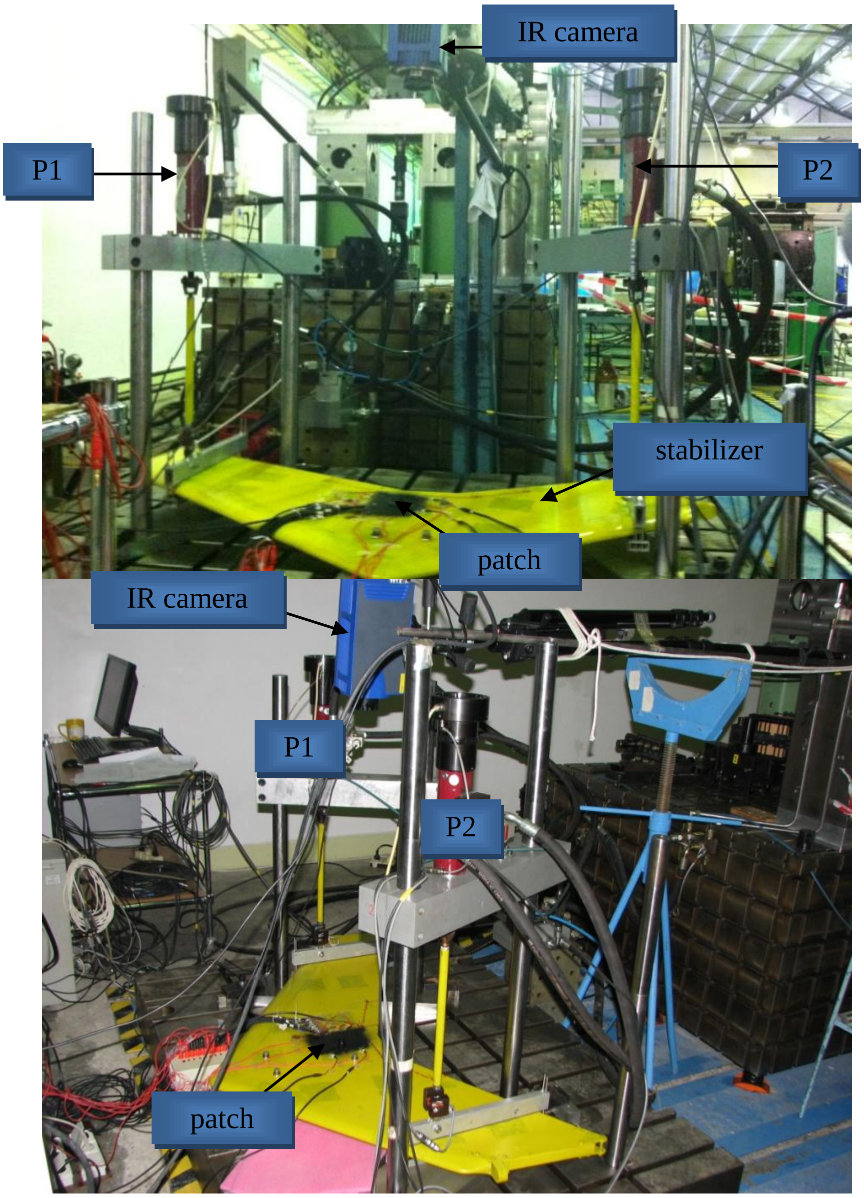

Figure 4.5.7 *Testing setup*[10].

[10] The contained data belong to PZL-Swidnik S.A. and any further reprinting and usage cannot be made without PZL-Swidnik S.A. written permission.

4.5.4 Results and discussion

During the testing of the vertical stabilizer, lock-in images were recorded. A close-up of the recorded area and a representative lock-in image are shown below (Fig.4.5.8):

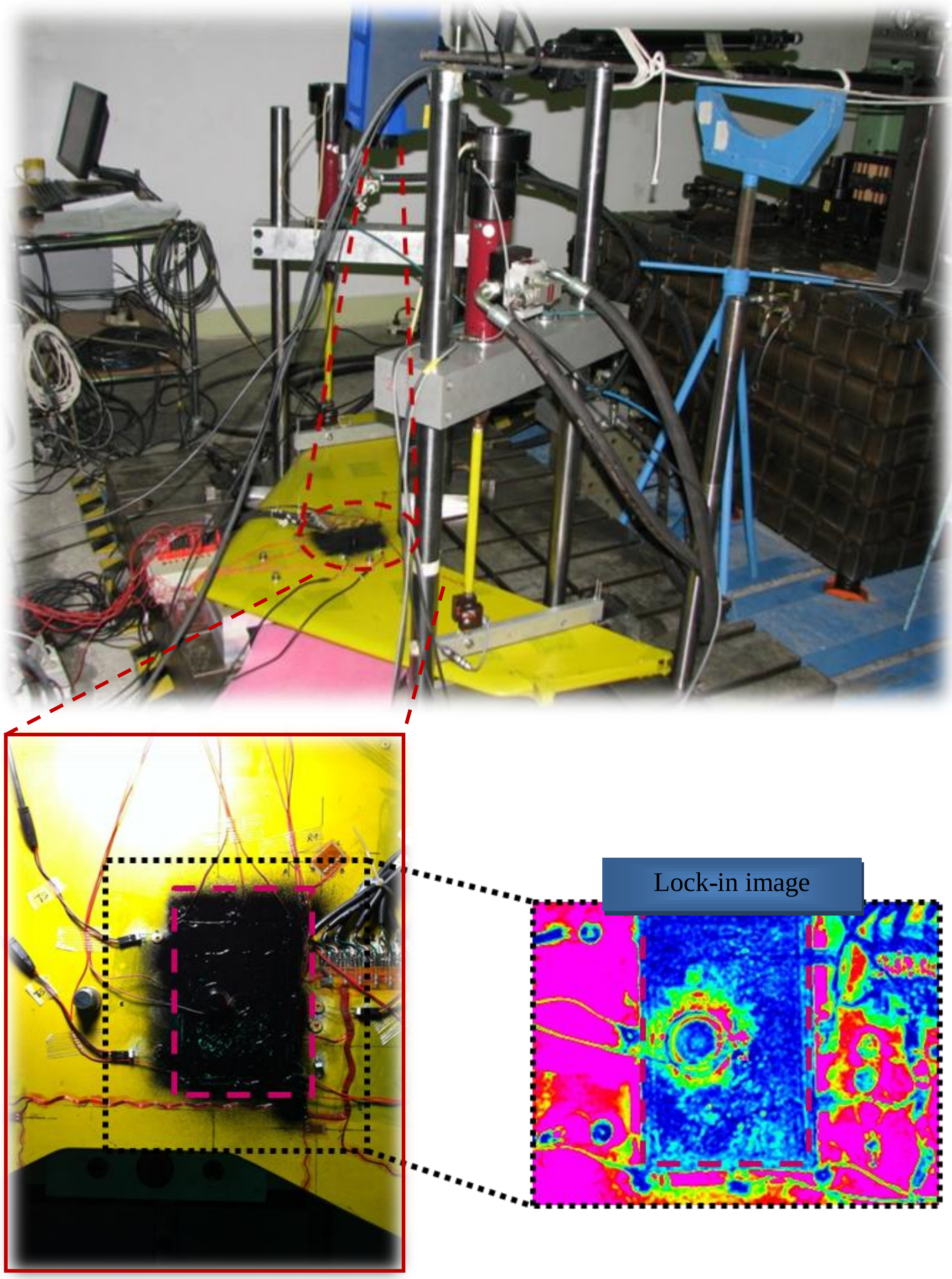

Figure 4.5.8 *Vertical stabilizer testing; monitored area and representative lock-in image*[11].

[11] The contained data belong to PZL-Swidnik S.A. and any further reprinting and usage cannot be made without PZL-Swidnik S.A. written permission.

Dynamic testing of the aluminum structure was performed until substantial critical failure of the patch (i.e. its detachment from the parent structure), as was indicated by the on-line thermographic inspection. The real time evaluation of the phase and amplitude images indicated that after approximately 600 kcycles, the CFRP patch was almost fully detached from the aluminum substrate. Only one small area exhibited some bonding with the substrate. As was decided, the test was stopped before the complete separation of the patch from the parent surface took place. In this way, a cross-validation with ultrasonics (C-scan) would be feasible to benchmark the efficiency of thermography.

Hereunder, phase and amplitude images at specific loading cycles are presented illustrating the whole deterioration evolution of the patch /substrate interface.

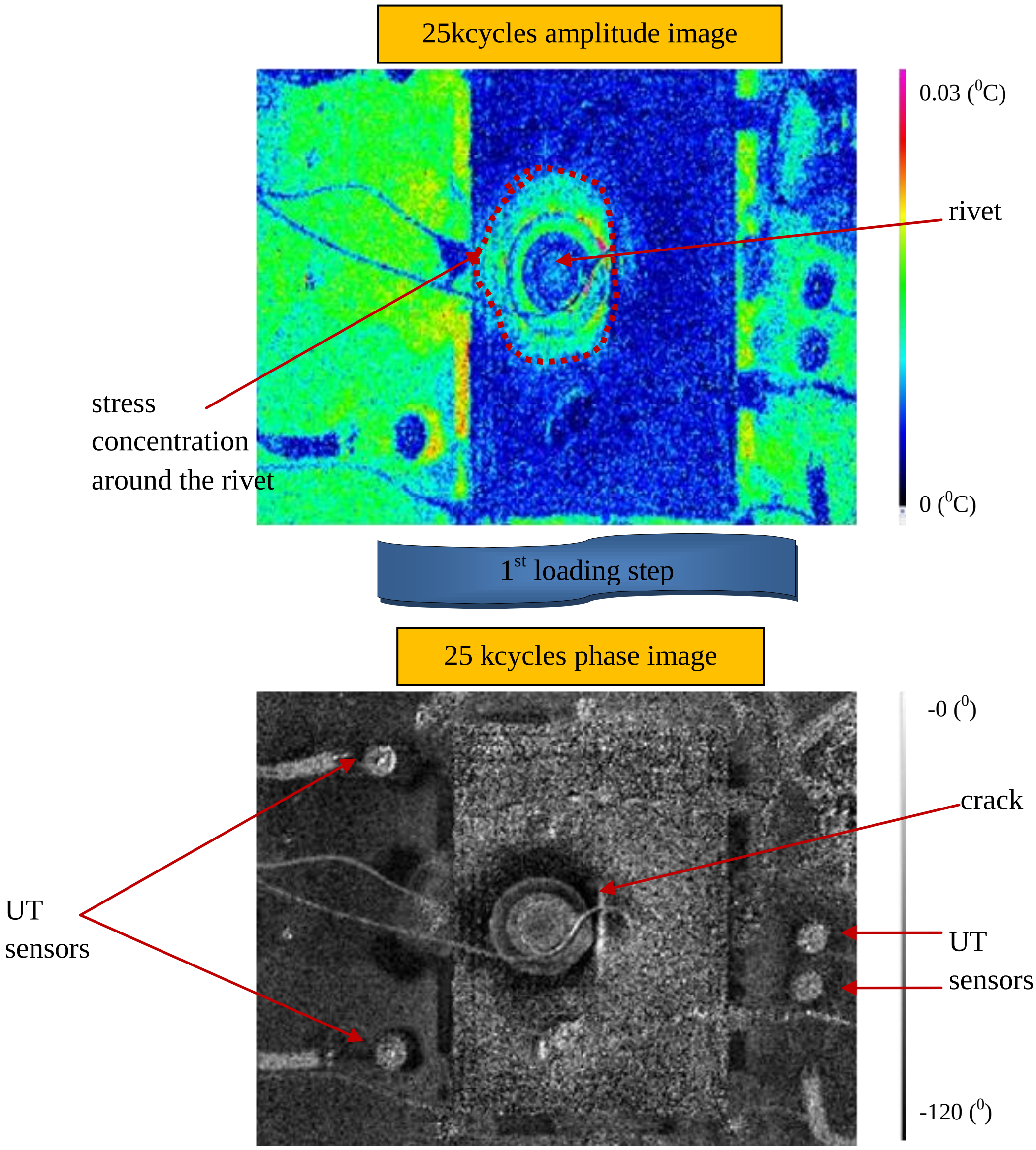

Figure 4.5.9 *Representative lock-in images; initial loading step.*

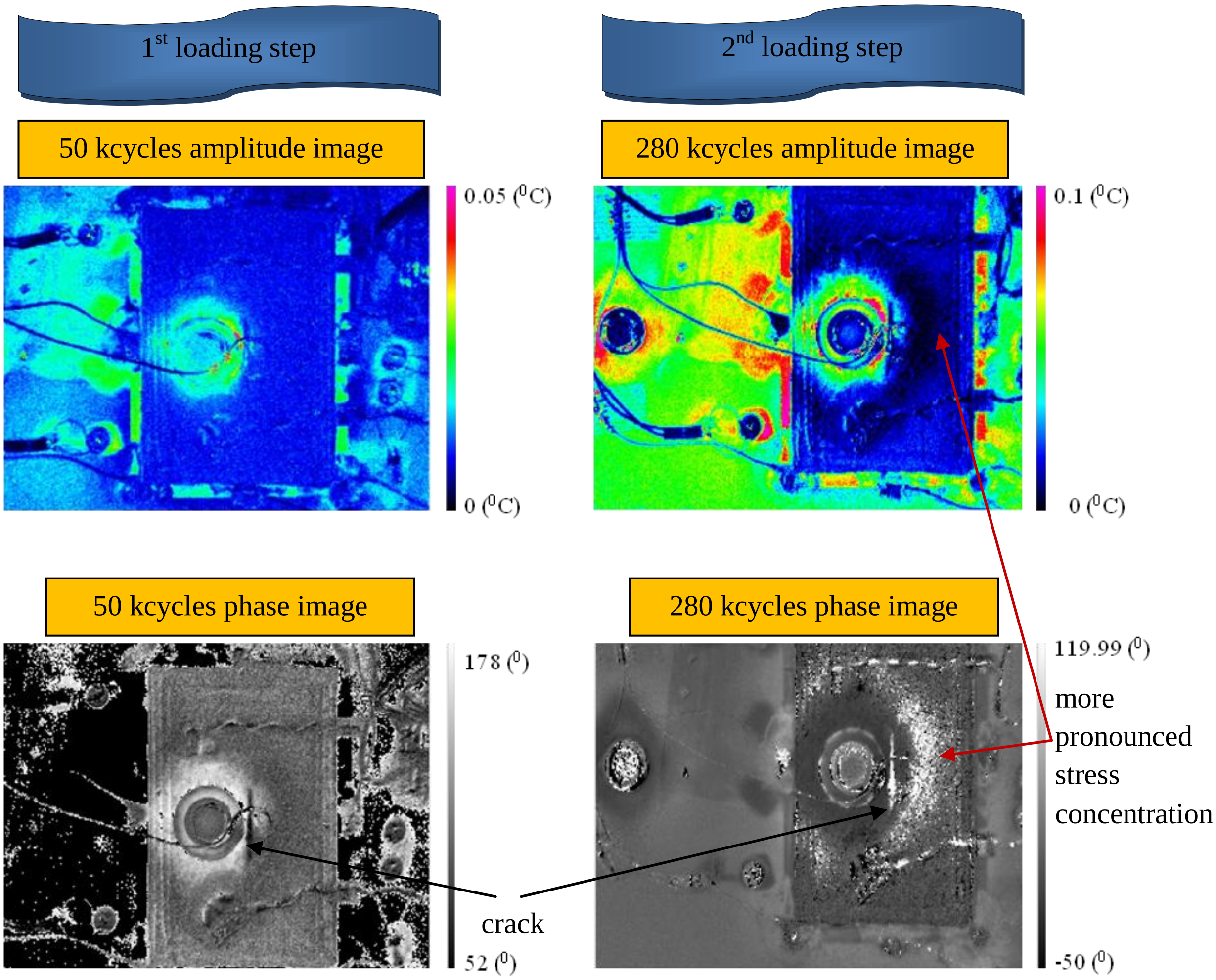

Figure 4.5.10 *Lock-in images at specific loading cycles.*

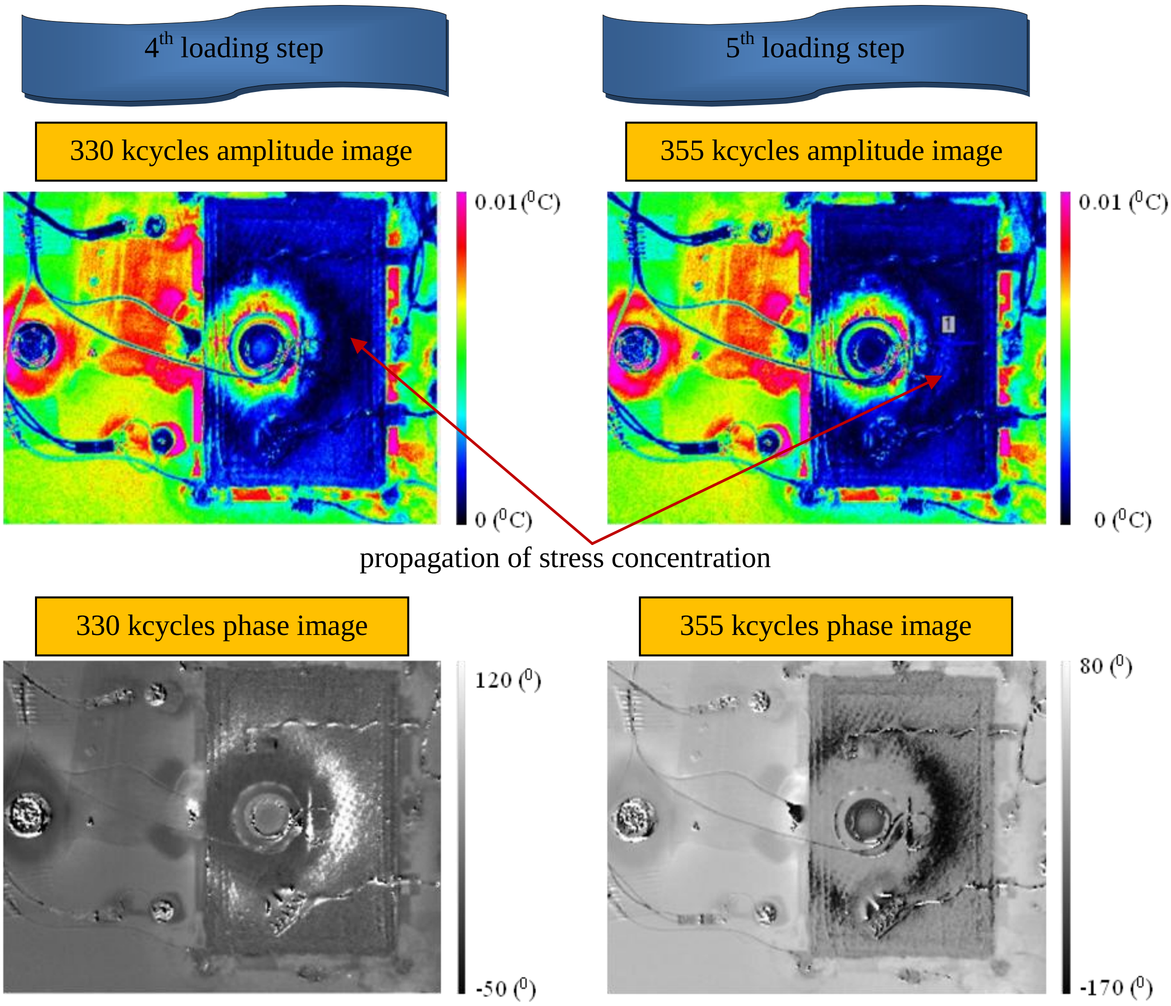

Figure 4.5.11 *Lock-in images at specific loading cycles.*

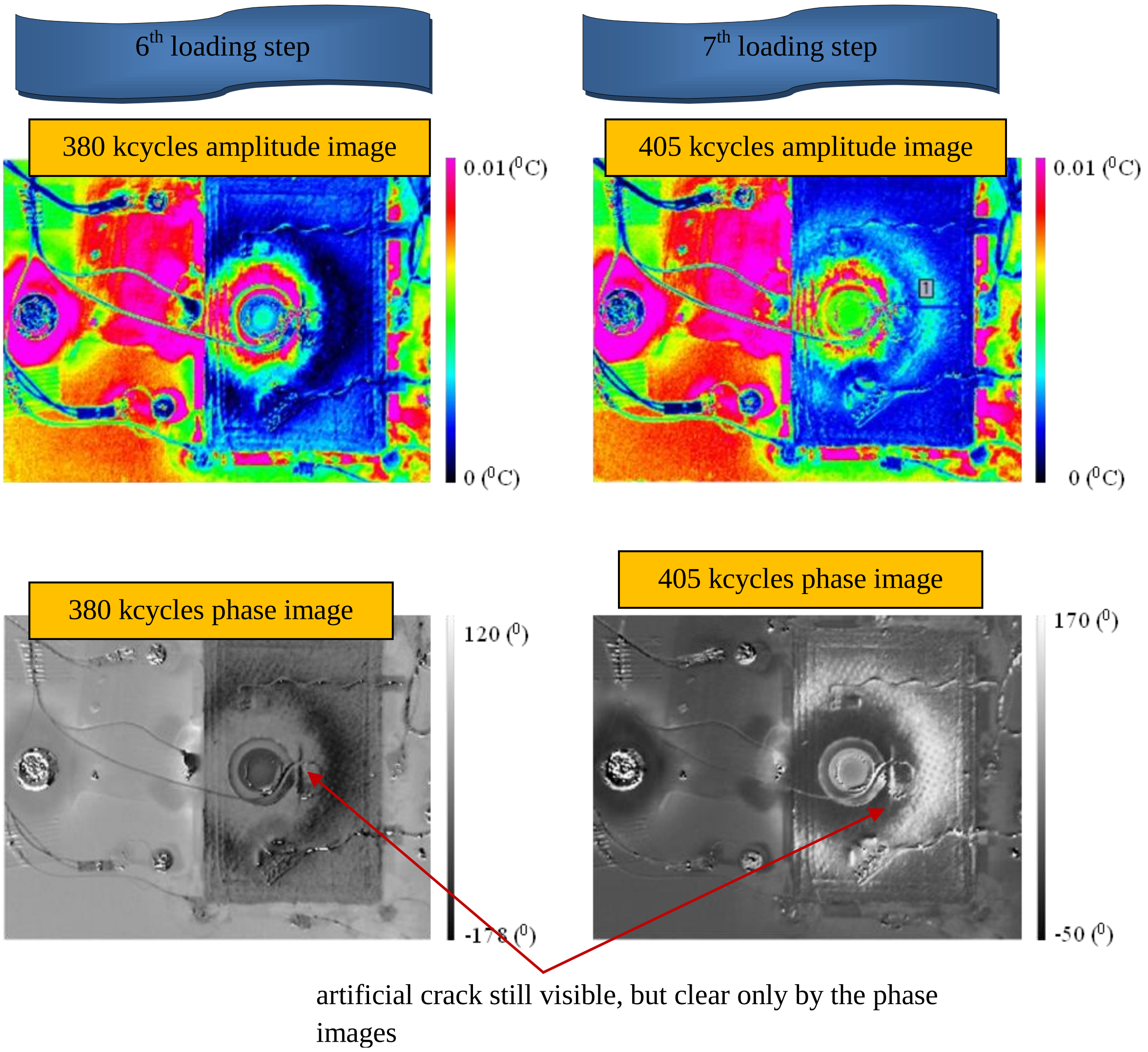

Figure 4.5.12 *Lock-in images at specific loading cycles.*

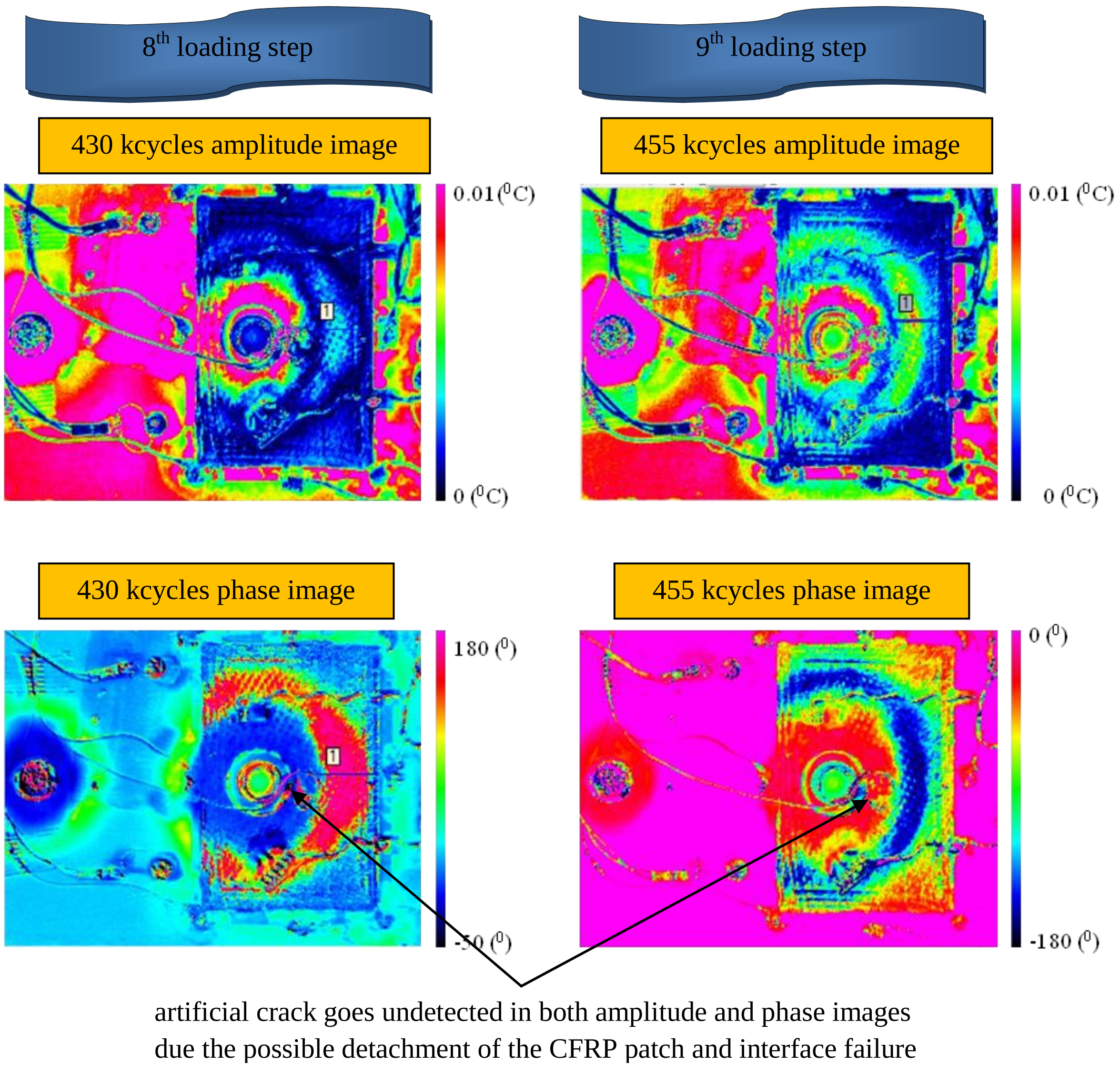

Figure 4.5.13 *Lock-in images at specific loading cycles.*

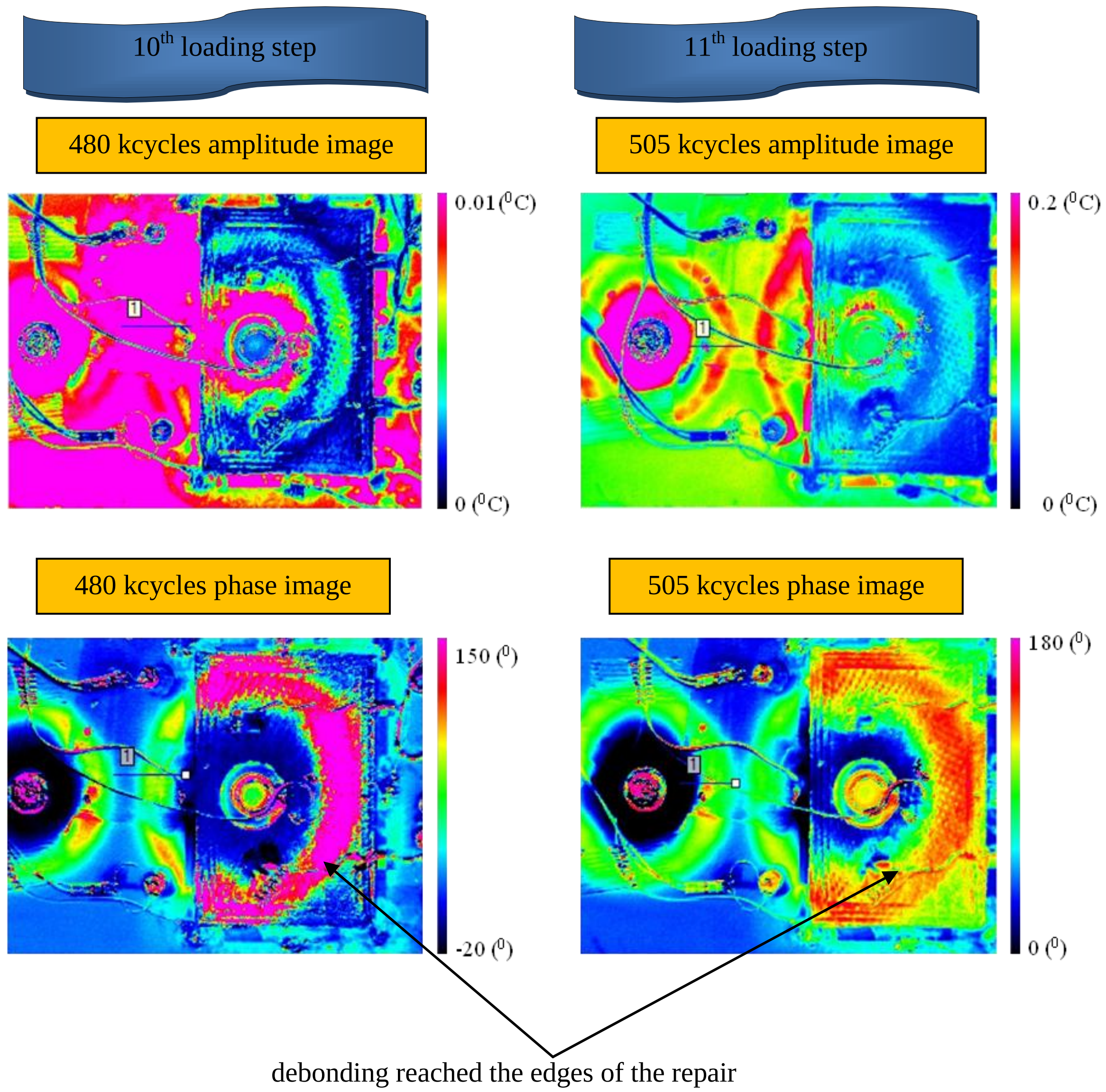

Figure 4.5.14 *Lock-in images at specific loading cycles.*

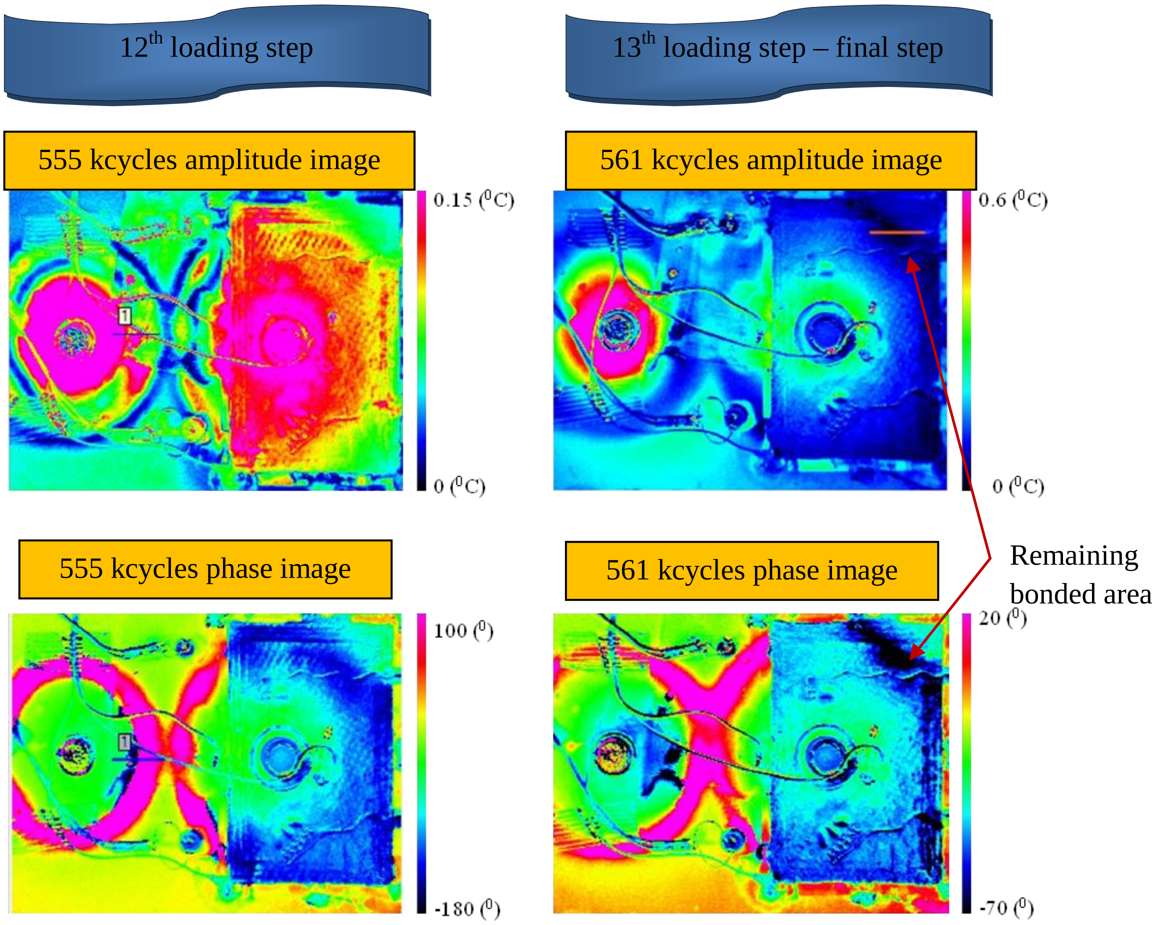

Figure 4.5.15 *Lock-in images at specific loading cycles.*

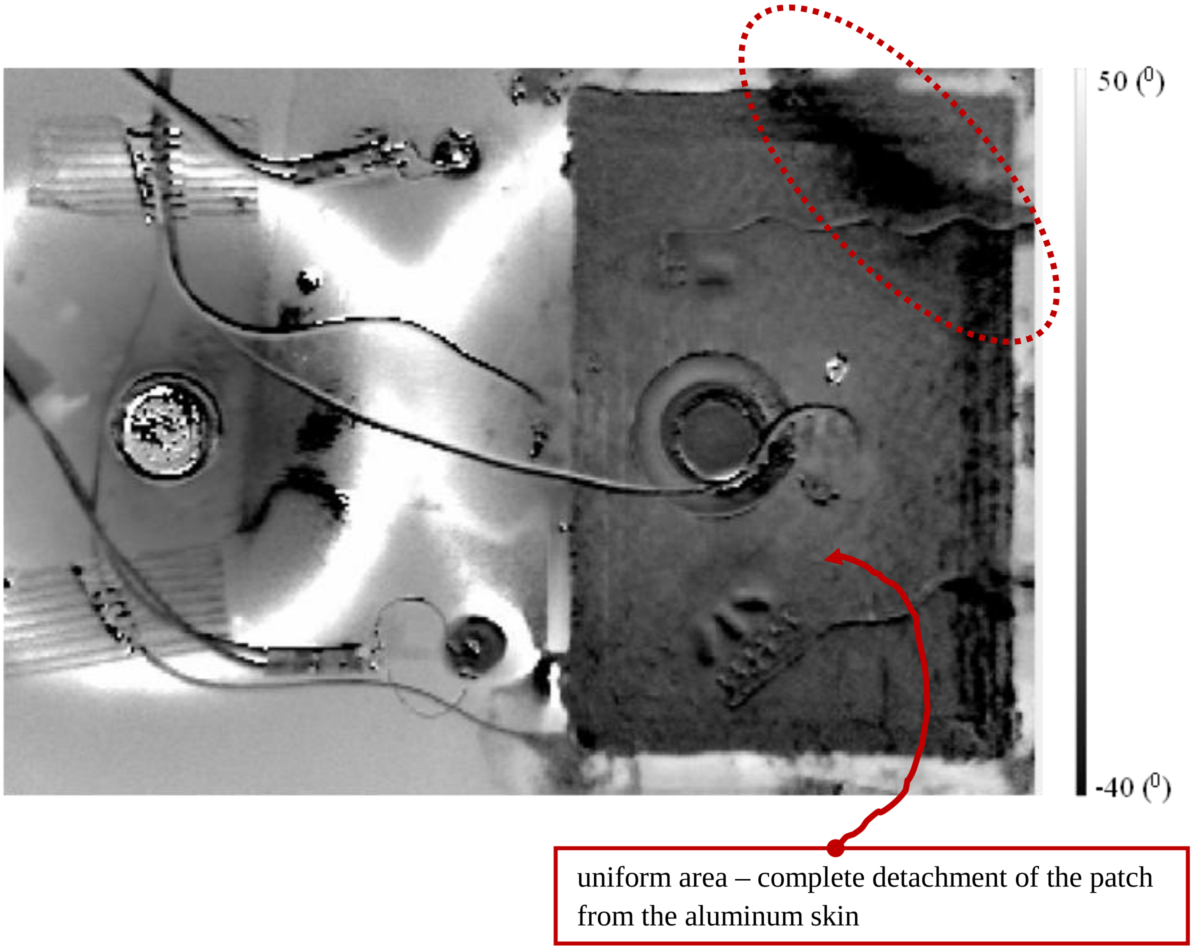

Figure 4.5.16 *Final image at 561 loading cycle and 13th loading level.*

Figs.4.5.9 to 4.5.16 depict juxtaposed amplitude and phase images recorded at representative loading cycles in order to present the complete deterioration evolution of the bonded patch repair. As aforementioned (see chapter 1), amplitude images present the temperature-difference acquired on a pixel by-pixel-basis; phase delay images are time - dependent showing the thermal wave decay in time.

Starting with the 1st lock-in amplitude image in Fig.4.5.8, the applied bonded patch is clearly identified. As may be observed next to the bonded patch, the piezoelectric sensors and electrodes employed for ERM and Lamp wave monitoring may be discerned. The bolted joint thermal imprint is also clearly visible. Moreover, a relatively small stress concentration area around the rivet was acquired. The rest of the patched area does not exhibit amplitude or phase gradients, suggesting a uniform temperature and stress distribution all over the bonded zone. At this stage, the artificially induced crack is not discernible, suggesting that the patch eliminates locally induced stress concentrations. At 25 kcycles, the phase and amplitude gradients become significant and in both lock-in (magnitude and phase) images (Fig.4.5.9) the crack was visible. In the phase image, the full length of the crack can be seen. This is not the case for the amplitude image, probably because the surface topology inhibits the observation of internal defects. There are no significant changes until the 50 kcycles step (Fig.4.5.10). At approximately 280 kcycles concurrently with the load level increased, stress concentrations around the bolted joint became more pronounced. The relative phase and amplitude gradients increased, suggesting a substantial increase of the stress concentration in the region surrounding the rivet. At 330 kcycles (Fig.4.5.11) a dark region was detected in the amplitude image. The same region was clearly presented with bright color by the phase one. With the increase in load level and fatigue progression this behavior became more prominent with the enlargement of the dark region shown in the amplitude imprint as well as its gradual shifting towards the horizontal axis of the image. At 430 kcycles (Fig.4.5.13) the dark region on the amplitude image reached the right edge of the patch. This is verified by the phase image (430 kcycles), which shows an extended dark area (shown as pink in the color phase image) which propagates to the tapered right edge of the patch.

This gradual radial propagation of stress concentration areas with the same profile was noted, as fatigue loading continued. At 455 kcycles (Fig.4.5.13), the area with increased stress concentration caused by the bolted joint, reached the left (as indicated on the image) edge of the patch. The same behavior consistently continued up to the final loading step of the fatigue testing (Fig.4.5.15 and 4.5.16) at 561 kcycles. At the acquired last lock-in images, only a small dark region is presented on the right upper corner of the patch. This was considered as the last bonded area of the patch. For this reason, it was decided to stop the test process and verify this observation with c-scanning of the patched area. The verification with ultrasonic imaging would assure the effectiveness of the thermographic method on monitoring damage initiation and propagation during service.

A closer examination of the whole lock-in image sequence denotes that besides stress concentration around the patched rivet, circularly-shaped stresses were recorded around the patch-free rivet. It is noteworthy, that as the last recorded lock-in images indicate, the mechanical stresses have diminished from the patched rivet. This observation suggests the following (and probably complementary effects): i) complete stress relaxation on the patched area and ii) complete failure of the patch /substrate interface. The latter inhibits the visibility of stress concentrations around bolted joint which are clearly identified around the un-patched rivet area. Figs. 4.5.17a and 4.5.17b depict a comparative evaluation between a lock-in image at 480kcycles and the one acquired at the final stage. The stress concentrations around the bolted joints of Fig.4.5.17a form patterns possessing a radial symmetry. These circular patterns indicate stress concentrations both in the unrepaired and the repaired rivet sites. Mechanically-induced stresses around the patched joint can be distinguished, due to the fact the patch remains bonded with the substrate. However, this is not the case in the final recorded image. After the almost complete separation of the patch, the suggested stress concentration areas were not detected on the patched zone. To further elucidate the above statements, circles showing the presence (or absence) of stress concentration areas around the bolted joints were drawn (Fig.4.5.17a and 4.5.17b). The centers of the drawn circles correspond to the position of the rivets.

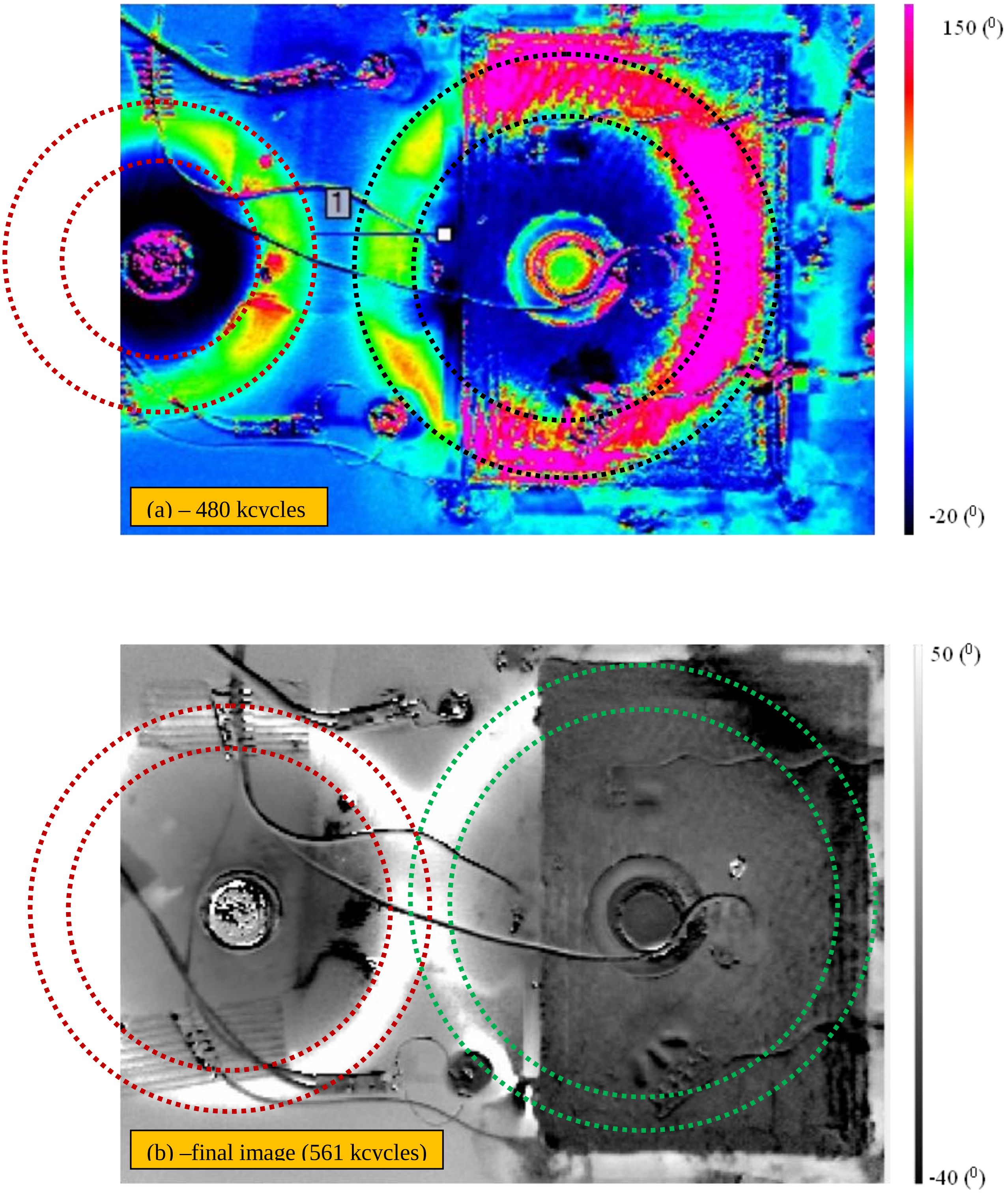

Figure 4.5.17 *Comparison of lock-in phase images.*

Moreover, the juxtaposition of images in Fig.4.5.17 denotes that the diameters of the figurative stress concentration circles around the rivets have increased. This suggests that apart from the degradation of the patch /substrate interface, a second deterioration mechanism may be present; as the interrogated vertical stabilizer is a sandwich structure, it is highly probable that the local stress concentration also invoke the failure of the interface between the honeycomb and the aluminum skin. Ultrasonic imaging verified this hypothesis.

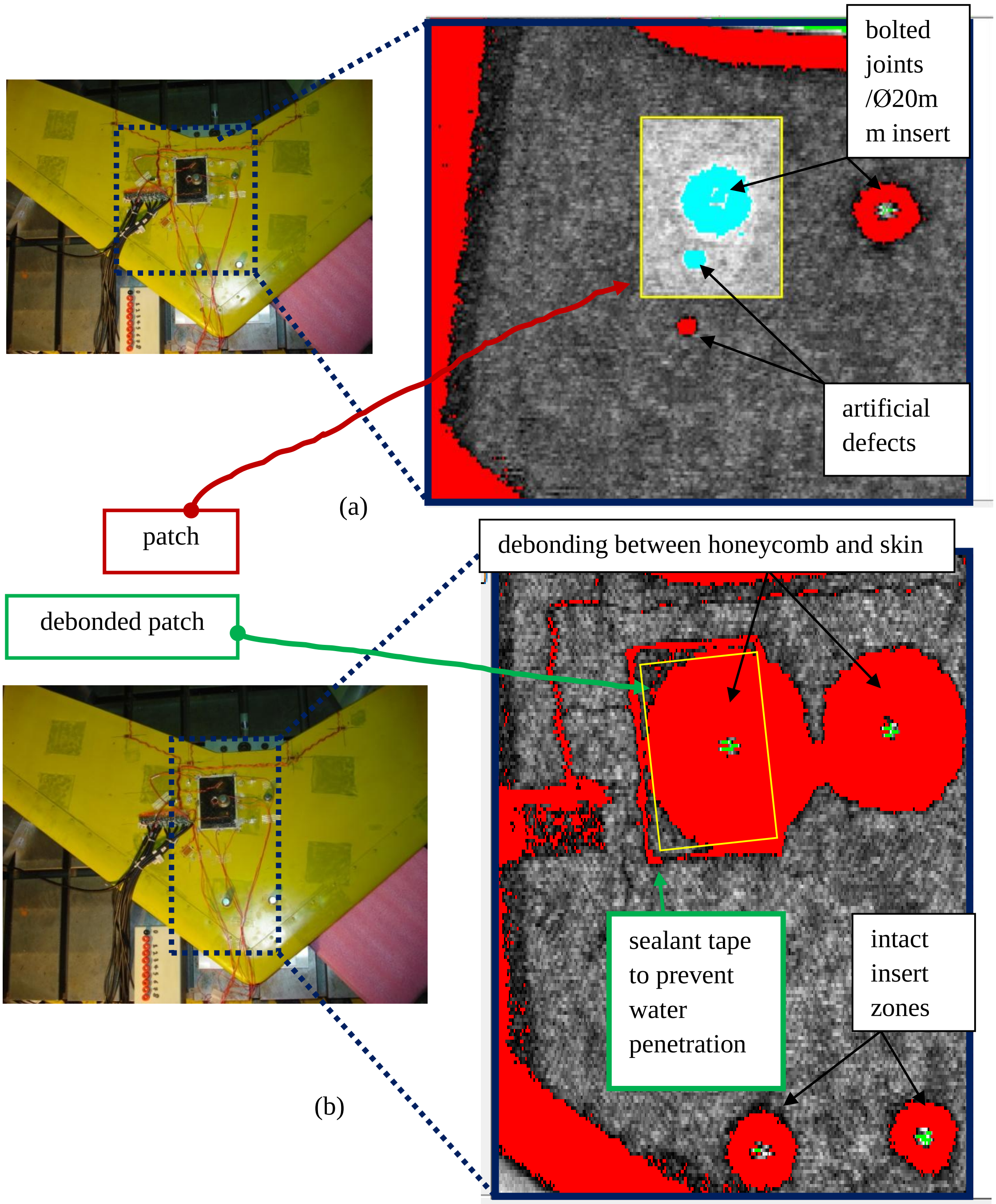

Figure 4.5.18 *Ultrasonic images of the stabilizer (a) prior and (b) post testing*[12].

[12] The contained data belong to PZL-Swidnik S.A. and any further reprinting and usage cannot be made without PZL-Swidnik S.A. written permission.

As is clear from Fig.4.5.18a where the C-scan of the repaired stabilizer prior to testing is shown, the rectangle-shaped CFRP patch can be seen upon the Ø20mm insert. The patched and unpatched cylindrical insert, where the rivets are fixed are well discerned and, in addition, two artificially induced flaws (simulating manufacturing defects) were also visible. On the contrary, in the post-testing c-scan imaging, the patch goes totally undetected. Only the edges of the patch can be seen, at the very same peripheral areas where the sealant tape was placed (to prevent from water penetration after immersion in the c-scan tank). Together with the edges of the patch, the debonded honeycomb /skin interface is well verified with ultrasonics. Fatigue mechanical testing led to detachment of the internal core of the stabilizer from the aluminum skin, at the very same areas where the cylindrical inserts of the bolted joints are located. Fig.4.5.19 shows an overlapping of an optical, the final phase and the post-testing c-scan image. The areas around the inserts /rivets which exhibited stress concentrations can be identified and correlated both via the ultrasonic and thermal imaging. It is also worth mentioning that the area in the vicinity of the other two bolted joints remained intact after the test procedure (discernible in the c-scan image).

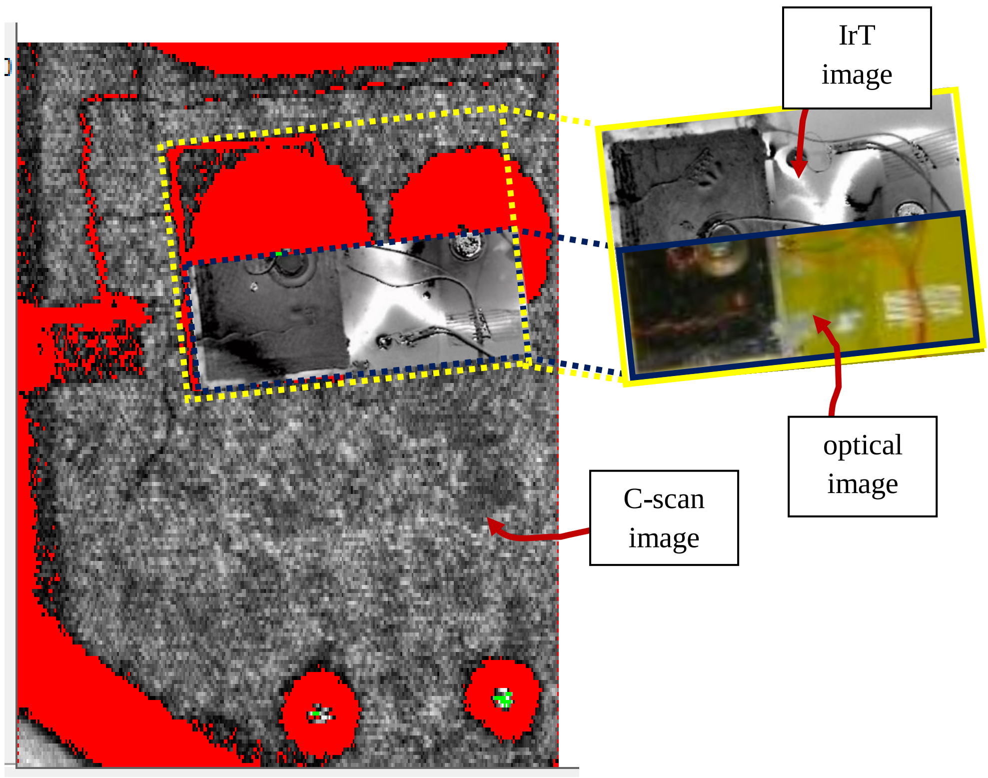

Figure 4.5.19 *Overlapping of ultrasonic, optical and thermographic images*[13].

Post-failure photographs are depicted below. Figs.4.5.20a to 4.5.20d show the disruption of the black paint which was primarily applied on the patched zone. It is worth noting that the

[13] The contained data belong to PZL-Swidnik S.A. and any further reprinting and usage cannot be made without PZL-Swidnik S.A. written permission.

black paint film remains intact at the top right corner of the patch (Figs. 4.5.20a and 4.5.20b) suggesting through thickness continuity between the patch and the substrate, an observation that confirms optically what has been assessed thermographically.

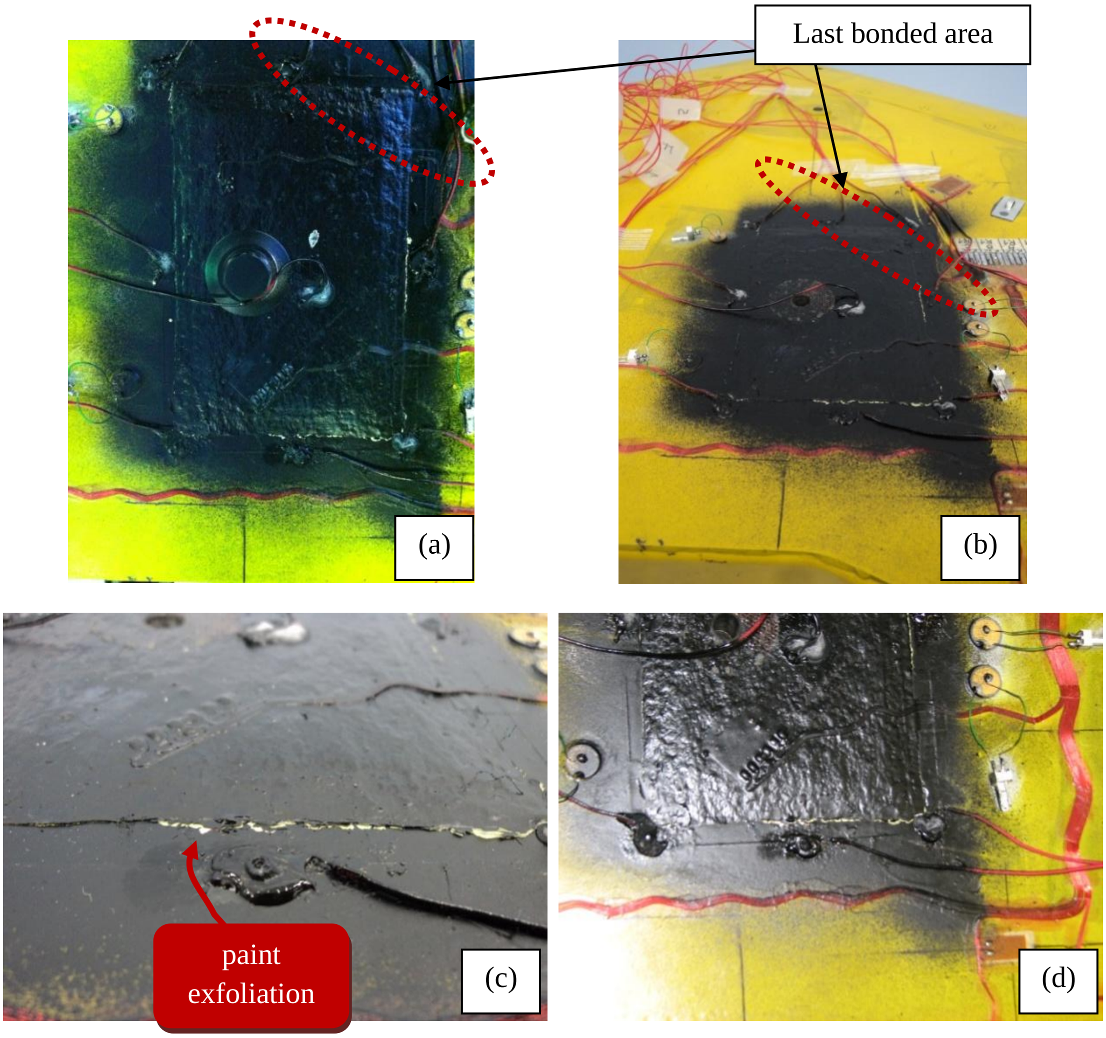

Figure 4.5.20 *Post failure images; disruption of the black paint film at the patch periphery*[14].

[14] The contained data belong to PZL-Swidnik S.A. and any further reprinting and usage cannot be made without PZL-Swidnik S.A. written permission.

Section conclusions

The scope of the current task was the single platform integration of the thermographic system to monitor damage initiation and propagation in large scale structures. To this end, the vertical stabilizer of the SW-4 helicopter (PZL-Swidnik /AgustaWestland, Poland) was tested in a purposely made dual action load frame and monitored on-line. The vertical stabilizer is fastened on the helicopter tail with four bolted joints. After analytical and experimental testing, a crack was noticed in the vicinity of one of the four bolted joints. The aim of this section was to assess the efficiency and counter validate adopted NDE methodologies on-line. An artificial crack simulating what was observed from experimental campaigns and predicted from finite element was introduced in a real scale component and repaired with the bonded repair patch methodology. Subsequently, the repaired wing was tested under bending fatigue mechanical loading in order to examine the applied patch performance in simulated service load conditions. Simultaneously to the mechanical testing, thermography was employed in lock-in mode, synchronized with the testing machine in order to monitor the bonding efficiency of the applied repair. The mechanical testing frame imposed 20Hz-frequency bending fatigue. The infrared camera was placed in the required distance in order to provide the necessary field of view above the repaired surface of the stabilizer. Amplitude and phase images were acquired during mechanical testing depicting the evolution of the structural deterioration of the bonded repair. From the onset of the experiment, increased stress concentrations were recorded around both patched and un-patched bolted joints. A radial progress of the circular area with stress concentration was observed in both amplitude and phase images which became more pronounced as fatigue testing continued. This area gradually reached all edges of the applied patch indicating the complete patch debonding. At the final recorded lock-in images, the figurative stress concentration ring had totally vanished from the patch zone, verifying the above suggestion. Comparing the stress concentration rings formed around the patched and un-patched rivets, showed that stresses, which were identically distributed during testing, are no longer visible on the patched zone. This was attributed to the patch /skin interface failure. Along with the patch /substrate interface deterioration, thermography detected a secondary deformation mechanism of the stabilizer; the honeycomb /skin interface failure. C-scanning inspection, prior to and after testing, verified this hypothesis. The post-failure ultrasonic image could not identify the patch, albeit is showed an extensive debonding between the skin and the underlying honeycomb core of the sandwich structure. The composite image where thermographic, ultrasonic and optical photographs are juxtaposed is also indicative of the honeycomb core/skin interlaminar failure. Finally, post-failure optical images show the disruption of the black mat paint film in all patch edges, but the one where a small remaining bonded area was observed via the evaluation of the phase and amplitude thermographic images.

All these demonstrate the capability of IrT as a method for the monitoring of the structural integrity and repair efficiency in aircraft structures. IrT can be employed to provide qualitative and quantitative information even in full scale aircraft structural components in relation to the efficiency of the applied repair methodology with a view to its qualification, certification and endorsement by the aircraft industry.

CHAPTER 5

Final conclusions and suggestions for future work

5.1 Final conclusions

This study involved the development and use of innovative Non-Destructive Evaluation (NDE) techniques for damage assessment in composite materials and structures. Various non-destructive methodologies were employed for damage inspection and monitoring. The demonstration of the investigated NDE techniques in both off-line and on-line conditions posed a challenge in the work. The study accomplished two aims: i) to address damage in hybrid composites and bonded composite repaired materials using a variety of non-destructive techniques (off-line), ii) to monitor the initiation and propagation of damage in hybrid composite and bonded composite repaired materials and structures in real time (on-line).

In the off-line concept, various modes of infrared thermography, electrical potential mapping technique, a novel current injection thermographic method and finally ultrasonics were applied on different material and damage scenarios. The on-line implementation of the non-destructive techniques under loading conditions, presupposed the system level integration. In that sense, electrical, thermographic and acoustic emission techniques were employed for structural health monitoring is small scale structures. The highlight of the study was the performance of the developed technology for real time structural integrity assessment in a real aircraft wing structure (helicopter vertical stabilizer).

The 3rd chapter of the thesis expanded on the use and implementation of novel non-destructive techniques for the off-line identification of damage, in hybrid composites as well as in bonded composite repaired laminates. Both simulated and induced low velocity impact damage were interrogated using Thermography, Electrical potential mapping and C-scan as a benchmarking technique. The thermographic assessment of the simulated damage with various optical excitation modes led to the conclusion that lock-in thermography (LT) proved to be the most effective over pulsed (PT) and pulsed phase (PPT) modes. More analytically, PT was inadequate in identifying low thickness defects. In sequence, PPT was more efficient in identifying internal damage as it is less sensitive to surface morphology than PT. Finally, LT was capable in identifying introduced defects of all morphologies with adequate resolution. Moving from PT to PPT and then to LT, the detection capabilities of the thermographic method were increased. In addition, it was feasible to interrogate deeper in the materials with less energy. In all cases, the implementation of LT involved the synchronization of the camera with the source of heating (lamps). It was also shown that material and orientation of the reinforcement, as well as the matrix material, affect the thermal properties of the material which were noticeable when “passing” from cross-ply laminates to unidirectional and then to patch repaired substrates. In particular, in the case of patched aluminum substrates, the differential thermal properties of the substrate, Teflon and composite patch did not impede the interrogation capabilities of the thermographic methods, but enhanced the simulated defect detection ability.

An innovative mode of thermographic technique was developed in the same chapter. It dealt with the thermal excitation of materials using electrical current injection. The inherent properties of the material were exploited for the thermal excitation via the Joule effect. The major challenges for the application of the method were (i) the minimization of the contact resistance at the current injection sites (ii) the uniform thermal stimulation of the composite structures so as to clearly pinpoint the internal characteristics which were imposed by LVI and (iii) the optimisation of the current injection protocol so as to avoid overheating and efficiently record the transient thermal gradient on the surface of the laminate. The incorporation of a CNT conductive nanophase led in the clear thermal imprint of the current flow disturbance induced by the impact damage. This effect was manifested by two cold elliptical spots on either side of the impact location along the current flow axis, which was less obvious in the case of the unmodified laminates. This effect was attributed to the enhanced though thickness conductivity of the CNT enhanced laminate. The energy input required for the identification of LVI damage was three to four orders of magnitude less than the typical energy input required with optically excited PPT. In all thermographic cases, it was observed that heat pulses of both high amplitude and duration inhibited the detection ability as this resulted in a high uniform temperature on the whole surface of the material; the material reached a steady state and no information was available.

With respect to the electrical potential mapping technique, preliminary work proved reliable in identifying local potential differentiations. The electrical network of the CFRP laminates was interrogated through electrical property measurements. Internal damage changes the electrical properties by deforming the electrical grid of an intact laminate. In the case of LVI damaged specimens, the surface-EPM snapshots indicated a color variation in the centre whereas the bulk-EPM imaging exhibited a similar response with a slight deviation from the centre. Comparing EPM images of specimens damaged with 3J and 5J impact energy, it was noted that a more uniform damaged area is observed in the 5J impact case. This may be attributed to higher applied impact energy. In both EPM images, the differentiation on the images reflected the presence of induced damage i.e. delamination around the impaction point. In the case of the 5mm drilled hole, the potential difference in the centre of the image represented the presence of the drilled hole in the centre of the specimen. In this case bulk EPM images were less affected by the artificial damage. The implementation of the EPM technique proved promising in identifying damage in composite laminates particularly in the case of blind delamination damage providing a strong motivation for further investigation of the technique.

The 4th chapter dealt with the development and use of NDE techniques in on-line conditions. Electrical resistance change monitoring, lock-in thermography and acoustic emission techniques were applied in various specimen and structure configurations for the monitoring of service induced damage. LT was employed for the monitoring and characterization of service induced damage in bonded composite repaired materials. In this concept both composite and aluminum strips were examined as substrates. Both substrate cases were artificially damaged and subsequently repaired with the bonded repair methodology. The patch repaired specimens were submitted to dynamic mechanical loading. Lock-in images acquired during load and bonding repair efficiency monitoring was feasible. Critical and subcritical damage was monitored in real time.

In the composite substrate case, the relative amplitude variations at the vicinity of the crack were found to correspond to local stress variations. The relative amplitudes as recorded by the thermal camera were equivalent to the Stress Intensity Factor (SIF) at the loci of the discontinuity. At 80% σ_{uts} of the substrate, fatigue level, debonding initiated and steadily propagated. A non monotonic behaviour of the SIF during load was observed. It was attributed to the critical debonding failure of the patch in combination with the damage tolerant behaviour of the coupon, where extensive longitudinal splitting led to the relief of the stress concentration. In the aluminum /CFRP patch strips case, debonding evolution was acquired for 30% fatigue of σ_{uts} of the substrate. Well bonded areas appeared darker than debonded areas enabling the monitoring of the critical failure process. In the on-line scenario, the LT mode proved very efficient in characterizing bonded repairs in laboratory environment, before their qualification and validation as common practice in the aircraft industry.

In the same chapter, ERCM was developed and implemented for structural integrity monitoring of CFRP and GFRP laminates. In the CFRP case, CNTs were dispersed in the epoxy matrix. The CNT effect on the sensing properties of the materials was evaluated by comparing plain and CNT modified CFRPs. It was shown that the nano-incorporation allowed for more reliable electrical resistance measurements to be employed for strain/ damage monitoring. CNTs eliminated artifacts introduced by secondary mechanisms, such as a non-monotonic resistance vs. time behavior attributed to Poisson effects. In addition CNTs increased the sensitivity of the electrical resistance measurements from 3% to 40%. Concluding, the nano-modification potentially increased the resolving ability of the methodology allowing the detection for minimal strain or damage induced changes. Moreover, the presence of an inflection point in the relative electrical resistance change second stage was found to correspond to the maximum recorded load of the previous load cycle. This implied that the material itself possesses a memory of its loading history prediction which relates to the rate of change of its electrical resistance value. The memory effect became less evident with increasing loading cycles, suggesting a similar behavior to the felicity effect in Acoustic Emission monitoring.

A new perspective of CNTs in composite laminates was the incorporation of organized CNT structures in a GFRP structure, in the form of all CNT fibres. The measurement of the electrical resistance changes (at the edges of the fibres) during mechanical loading resulted to the deformation of the CNT fibres. In monotonic tensile loading testing, electrical resistance values related monotonically albeit with a non-linearly increasing rate to the mechanical deformation of the materials. Taking into account the material deterioration values as observed from the stiffness of the GFRP material, it was obvious that electrical resistance changes acquire higher values as the GFRP specimen was mechanically deformed. The monotonic relation between stiffness loss of the GFRP material and the electrical resistance of the CNT fibres, was indicative of the ability of the CNT fibre to act as damage or strain sensor embedded in the GFRP structure. In addition, the considerable low diameter (80 μm) of the CNT fibres did not affect significantly the principle structural properties of the GFRP structure. The electrical resistance technique was successfully employed as a tool to evaluate the structural integrity of hybrid composite materials.

Acoustic emission was employed as a complementary NDE technique. It was chosen as the 3rd real time assessment technique in a common NDE platform which constituted of EPCM, LT and AE. The three techniques were successfully applied to monitor the deterioration of bonded repairs. Both EPCM and IrT indicated well-defined stages along the fatigue life of the interrogated coupons. EPCM was successful in clearly identifying the topology of the progressive debonding as denoted by the monotonic potential increase which was only observed at the side where critical failure initiated and propagated. The concurrent AE monitoring partially revealed the directionality of the critical failure. The correlation of the two techniques was very satisfactory and was feasible in enhancing the observation of the fatigue life stages. In the case of LT, again, three fatigue life stages were visible, which were found to correspond better to typical fatigue behavior. Interrelation of LT and AE was performed concurrently in real time during the loading of the coupon, revealing a clear representation of the fatigue life stages. In addition, the consistency of the failure process and the life time fraction representation allowed for an “indirect” correlation of the IrT and the EPCM methods which resulted as expected to the three distinct life stages representation.

After a complete testing series, the combined NDE system used to monitor service damage in representative small scale components. Double overlap fatigue and skin doubler aluminum substrates were examined. The representative configurations were subjected to dynamic and quasi-static loading. In this approach, the combined NDE system was appropriately applied in order to study the joints representing the repaired region. Concerning, SDS only quasi-static testing was feasible. With thermography employed in live mode, the debonding of patches was monitored throughout tensile loading. In the DOF specimen configuration, the combined NDE system applied in proper way for the monitoring of the induced damage under both the quasi-static and tensile loading. In such coupon cases, the discrimination of the particular failure mode was inhibited by the double repair patch protocol. However, the overall structural degradation was assessed in real time via the combined thermographic, electrical and acoustic emission techniques.

The last part of the study involved the use of the developed NDE technology in large scale structures. The vertical stabilizer of the SW-4 helicopter (PZL-Swidnik /AgustaWestland) was tested under dynamic mechanical testing. The tested structure was artificially damaged with a frequently encountered form of damage i.e. a crack and subsequently repaired with a bonded repair patch. The bonded repair integrity was monitored via LT during bending fatigue. A radial progress of circular area with stress concentration was observed in both amplitude and phase images which became more pronounced as fatigue testing continued. This area gradually reached all edges of the applied patch revealing the complete patch debonding. Along with the patch /substrate interface deterioration, thermography detected a secondary deformation mechanism of the stabilizer; the honeycomb /skin interface failure. C-scanning inspection, prior to and after testing, verified this hypothesis.

5.2 Suggestions for future work

A complete investigation regarding structural integrity assessment of materials both in off-line and on-line conditions, in small scale and large levels took place, notwithstanding inevitably led to the rise of challenging research issues for further investigation.

Regarding the off-line identification of damage with optical thermography, an array of flash lamps instead of incandescent, would be preferable for optical excitation, as they would minimize all the effects induced by the inertia of the incandescent lamps. Flash lamps are capable of providing a more accurate square signal excitation. Concerning LT, a correlation between phase and amplitude images in many excitation frequencies is suggested for further examination. Also, a complete examination in a complete frequency series is an interesting approach to determine the blind frequency. A frequency modulated lock-in thermography which may provide a solution to the blind frequency "band" is also an interesting concept for further work. Various excitation modes such as ultrasonics and eddy currents can be further examined, particularly within the context of in-service maintenance. Eddy current thermography is a challenging method for damage inspection in CFRPs particularly when employed for hybrid CFRPs and GFRPs (with CNTs, CNFs, graphene or iron particles).

Within the scope of this study, the current injection thermographic concept proved highly efficient and produced impressive results. However a number of issues would require more investigation particularly for its qualification as an established NDE methodology. In terms of system level, the provision for efficient electrical coupling is very challenging, particularly as they may have a multifunctional role, e.g. matrix curing, deicing, self healing and activation and of course real time monitoring. Copper electrochemical plating and artificially embedded copper parts (copper mesh) may improve the current injection mechanism by eliminating any contact resistance. Again, various contents of different nanophases such as CNTs and iron particles in the epoxy matrix need further investigation, particularly in relation to the electrical anisotropy of the (usually orthotropic) primary reinforcement.

In the case of electrical potential mapping technique the improvement of electrical contacts is of primary concern. Both silver paint and electrochemical copper plating have been successfully examined in the framework of the study. The use of silver paint has proved very convenient compared to the copper plating. The latter, involves a difficult and time-consuming procedure however is capable of providing long-term electrical contacts. Artificially embedded electrical contacts during the manufacturing process, such as a metallic grid or copper mesh, may prove useful providing enhanced electrical connection with the conductive phase(s) of the material and hence minimize any contact resistance. Moreover, it is apparent that a manual measurement series is quite slow and thus an automated data acquisition system for fast measurement is essential. The automated system could be the primary proposition for further work however it is already a matter of work in progress. A finite element analysis would provide direction to the measurement and acquisition protocol. Needless to mention that, the solution of the inverse problem is a necessary step, particularly for damaged electrically anisotropic media for the application of the method to define system properties. The solution of the inverse problem would provide the form and location of damage based on the potential mapping, acquired either analytically /numerically or experimentally. A comparative study of CNT modified and plain matrix CFRPs could also be an interesting task.

In the on-line repair integrity monitoring with thermography concept, a mathematical description of the patch repair debonding based on shear-lag methods is currently investigated in order to provide a theoretical benchmarking of the thermographic data. This is also under investigation for the estimation of the stress concentration around patched circular notches.

In the case of ERCM, different loadings of dispersed CNTs in the matrix could be further investigated in the case of CFRP materials. In addition, graphene modified CFRPs and iron modified CFRPs pose a great challenge in the field of this electrical technique. Of course the electrical contact is once again an impediment in this task and a matter of further investigation. With regard to embedded CNT fibres, further work is needed in order to better correlate the electrical resistance measurements at the edges of the fibres with the structural degradation of the material. Moreover, an optimization of the CNT fibre embedding protocol is essential in order to minimize its adverse effect on the mechanical properties of the final laminated coupons.

With regard to EPCM of bonded composite repaired materials, a faster data acquisition system (currently being built) would give the opportunity to provide rapid resistance measurements during fatigue mechanical loading. This would allow for more resistance monitoring within the period of a loading cycle, and allow for the investigation of extremely challenging secondary effects. Again, on a system level approach, the concurrent implementation of the studied techniques is certainly a challenge in order to minimize the interference particularly between the EPCM and the thermographic system.

CHAPTER 6

Publications and Curriculum Vitae

6.1 Scientific papers in peer-reviewed conferences proceedings

1. **S. A. Grammatikos**, E. Z. Kordatos, N.-M. Barkoula, T. E. Matikas, A. S. Paipetis. Innovative non-destructive evaluations and damage characterization of composite aerostructures. ECCM14, Budapest, 2010. (oral)
2. **S. A. Grammatikos**, E. Z. Kordatos, N-M. Barkoula, T. E. Matikas, A. S. Paipetis. In-service damage monitoring of bonded composite repairs. Duracosys2010, Patras, 2010. (oral)
3. **S. A Grammatikos**, E.Z. Kordatos, N-M. Barkoula, T.E. Matikas, A. Paipetis. Innovative non-destructive evaluations and damage characterization of composites. First Greek and First Greek – Ukrainian Conference on Fracture Mechanics of Materials and Structures, Xanthi, Greece 20 – 23 October 2010. (oral)
4. **S. A. Grammatikos**, E. Z. Kordatos, N. M. Barkoula, T. E. Matikas, and A. S. Paipetis. Repair integrity monitoring of composite aerostructures using thermographic imaging. San Diego, CA, USA, 2010, SPIE, 76491D-76412. (oral-presented by A. S. Paipetis)
5. **S. A. Grammatikos**, G Gkikas, A. S. Paipetis. Monitoring strain and damage in multi phase composite materials using electrical resistance methods. vol. 79822011. San Diego, CA, USA, 2011, SPIE. (oral)
6. A. S. Paipetis, **S. A. Grammatikos**, E. Z. Kordatos, N.-M. Barkoula, T. E. Matikas. In service damage assessment of bonded composite repairs with full field thermographic techniques. vol. 79832011. San Diego, CA, USA, 2011, SPIE. (oral)
7. **S. A. Grammatikos**, D. G. Aggelis, A. S. Paipetis. Continuous monitoring of setting and hardening of epoxy resin. NDTMS, 2011, Istanbul. (oral)
8. **S. A. Grammatikos** and A. S. Paipetis. Monitoring strain and damage in multi phase composite materials using electrical resistance methods. Mini-Symposium: Micromechanics and modeling of Multifunctional Materials, 14-15 July 2011, Thessaloniki, Greece. (oral)
9. **S. A. Grammatikos**, E. Z. Kordatos, N-M. Barkoula, T. E. Matikas and A. S. Paipetis. In service damage assessment of bonded composite repairs with full field thermographic techniques. Mini-Symposium: Micromechanics and modeling of Multifunctional Materials, 14-15 July 2011, Thessaloniki, Greece. (oral)
10. **S. A. Grammatikos** and A. S. Paipetis. Electrical resistance and electrical potential studies for the detection and monitoring of damage in hybrid composites. ETNDT5, 2011, Ioannina. (oral)

11. **S. A. Grammatikos**, M.-E. Kouli, G. Gkikas, A. S. Paipetis. Structural health monitoring of aerospace materials used in industry using electrical potential mapping methods. San Diego, CA, USA, 2012, SPIE. (poster)
12. **S. A. Grammatikos**, E. Z. Kordatos, T. E. Matikas, A. S. Paipetis. Low-velocity impact damage identification using a novel current injection thermographic technique. San Diego, CA, USA, 2012, SPIE. (oral)
13. **S. A. Grammatikos**, E. Z. Kordatos, D. G. Aggelis, T. E. Matikas, A. S. Paipetis. Critical and subcritical damage monitoring of bonded composite repairs using innovative non-destructive techniques. San Diego, CA, USA, 2012, SPIE. (Invited oral-presented by A.S. Paipetis)
14. G. Gkikas, **S. A. Grammatikos**, D. G. Aggelis and A. S. Paipetis. Simultaneous acoustic and dielectric real time curing monitoring of epoxy systems. San Diego, CA, USA, 2012, SPIE. (poster)
15. G. Gkikas, C. Saganas, **S. A. Grammatikos**, G. M. Maistros, N.-M. Barkoula, A. S. Paipetis. Dispersion monitoring of carbon nanotube modified epoxy systems. San Diego, CA, USA, 2012, SPIE. (poster)
16. **S. A. Grammatikos**, E. Z. Kordatos, D. G. Aggelis, T. E. Matikas and A. S. Paipetis. Critical and subcritical damage monitoring of bonded composite repairs using innovative non-destructive techniques. Athens, TRA 2012. (Invited student as a finalist in the top 30 European students – poster)
17. **S. A. Grammatikos**, E. Z. Kordatos, T. E. Matikas and A. S. Paipetis. Bonded repair integrity monitoring of aerospace materials using combined non-destructive methods. Brussels, Belgium, 2012, Duracosys2012.
18. **S. A. Grammatikos**, E. Z. Kordatos, T. E. Matikas and A. S. Paipetis. A combination of novel thermographic and electrical techniques for low-velocity impact damage identification in multifunctional composites. San Diego, CA, USA, 2013, SPIE. (Invited oral)

6.2 Scientific papers in peer-reviewed journals

1. **S. A. Grammatikos**, E. Z. Kordatos, N. M. Barkoula, T. E. Matikas, and A. S. Paipetis. Innovative non-destructive evaluation and damage characterization of composite aerostructures using thermography. *Plastics, Rubber and Composites*. 2011;40 (6-7):342-8.
2. **S. A. Grammatikos** and A. S. Paipetis. On the electrical properties of multi scale reinforced composites for damage accumulation monitoring. *Composites Part B: Engineering*. 2012;43 (6):2687-96.

Also four papers already submitted in peer-reviewed scientific journals:

3. **S. A. Grammatikos**, E. Z. Kordatos, T. E. Matikas and A. S. Paipetis. Lock-in thermography of bonded composite repair: critical vs. subcritical damage assessment and quantification. *International Journal of Adhesion and Adhesives* (submitted)
4. **S. A. Grammatikos**, E. Z. Kordatos, T. E. Matikas, A. S. Paipetis. Real time debonding monitoring of composite repaired materials via electrical, acoustic and thermographic methods. *Journal of Materials Engineering and Performance*. (submitted)
5. **S. A. Grammatikos**, E. Z. Kordatos, T. E. Matikas, A. S. Paipetis. Current injection phase thermography for low-velocity impact damage identification. *Materials and Design*. (submitted)
6. O. Boura, E. Diamanti, **S. A. Grammatikos**, D. Gournis, D. Aggelis, N.-M. Barkoula and A. S. Paipetis. Carbon nanotube growth on high modulus carbon fibers and interfacial characterization. *Surface and Interface Analysis*. (submitted)

6.3 Curriculum Vitae

Name		**Sotiris Grammatikos** *Dipl. of Materials Science & Engineering, M.Sc*
Address		**33/1Γ, Ergatikes Katoikies E', 50200 Ptolemaida, Greece**
Mobile		**6936 18 18 57**
E-mail		**sgrammat@cc.uoi.gr /sotos22@windowslive.com**
Nationality		GREEK
Date of birth		06/09/1985

WORK EXPERIENCE		
Dates		**01/03/2008 - 31/05/2008 (3 months)**
Name and address of employer		Hellenic Aerospace Industry, P.O. Box 23 GR 320 09, Schimatari - Greece
Type of business or sector		Research & Product Design
Occupation or position held		Scientific Researcher (training practice & conduction of undergraduate thesis)
Main activities and responsibilities		Research, manufacturing and study of Advanced Composite Materials and Non-Destructive Evaluations [In the framework of the EU project NOESIS – Contract No.: AST4-CT-2005-516150]

Dates		**01/07/2003 - 30/06/2008 (5 years)**
Name and type of organisation providing education and training		University of Ioannina, Greece *Dept. of Materials Science & Engineering, Mechanics*
Title of qualification awarded		B.Sc in the Department of Materials Science & Engineering

Dates		**01/08/2008-01/11/2010 (2 years)**
Name and type of organisation		University of Ioannina, Greece *Dept. of Materials Science & Engineering, Mechanics*

providing education and training		M.Sc "Chemistry & Technology of Materials"
Principal subjects/occupational Skills covered		Spectroscopy & material characterization techniques, Science & technology of polymers & ceramics, Catalysts & catalytic activities-polymers, Crystalic structure and special properties of materials, Micro and Nano MaterialsTechnology Thesis in: Mechanics of Composite & Smart Materials laboratory Thesis subject: On line repair integrity monitoring of aerostructures and estimation of their remaining operational life using innovative non-destructive techniques

Dates		**01/01/2009-07/02/2013 (4 years)**
Name and type of organisation providing education and training		University of Ioannina, Greece *Dept. of Materials Science & Engineering, Mechanics*
Principal subjects/occupational Skills covered		PhD Researcher Thesis in: Mechanics of Composite & Smart Materials laboratory Thesis subject: Structural integrity assessment of aerostructures using innovative Non-Destructive Evaluation Techniques

PERSONAL SKILLS AND COMPETENCES		
MOTHER TONGUE		**GREEK**
OTHER LANGUAGES		
		ENGLISH
Reading skills		Excellent
Writing skills		Excellent
Verbal skills		Excellent
		GERMAN
Reading skills		Basics
Writing skills		Basics
Verbal skills		Basics

SOCIAL SKILLS AND COMPETENCES		• Acquired skills in communication and co-operation, work organization and consistency • Ability to understand new technologies quickly

TECHNICAL SKILLS AND COMPETENCES		Excellent knowledge of Microsoft Windows, MS-Office, Internet applications Good knowledge of MS-DOS, FORTRAN, C++, Autocad, Matlab, Origin

SCIENTIFIC INTERESTS .		Composites, Mechanical Testing, Fracture Mechanics, Aerospace, Mechanics of Materials, NDE, Materials Science, Structural Health Monitoring, Smart Materials
SCIENTIFIC ACTIVITIES .		• Participation with oral presentation in 6 International, 2 European and 2 more conferences • 2 publications in international journals and 4 more submitted • 13 scientific papers published in proceedings (2 invited papers) • Assistant in supervising 4 undergraduate thesis and 2 masters • Lecture-conduction of undergraduate student laboratory courses, (a) Composite materials: characterization and properties, (b) Structural integrity and quality assessment • PhD thesis funded by a European project (IAPETUS-Innovative repair of aerospace structures with curing optimization and life cycle monitoring abilities, Grant Agreement Number: ACP8-GA-2009-234333)

References

[1] Hull D, Clyne TW. An introduction to composite materials: Cambridge University Press; 1996.

[2] Aghazadeh Mohandesi J, Majidi B. Fatigue damage accumulation in carbon/epoxy laminated composites. Materials & Design. 2009;30(6):1950-6.

[3] Wang S, Kowalik DP, Chung DDL. Effects of the temperature, humidity, and stress on the interlaminar interface of carbon fiber polymer-matrix composites, studied by contact electrical resistivity measurement. Journal of Adhesion. 2002;78(2):189-200.

[4] Παπασεραφείμ Α. Ενίσχυση των κατασκευών με χρήση συνθέτων υλικών από ινοπλισμένα πολυμερή. 13ο Φοιτητικό Συνέδριο Σκυροδέματος. Πάτρα2007.

[5] Μιτολίδης Γ, Σαλονικιός Θ, Κάππος Α. Μηχανικά Χαρακτηριστικά Ανθρακοϋφασμάτων (CFRP) και Χαλυβδοϋφασμάτων (SRP) και Διερεύνηση της Εφαρμογής τους στην ενίσχυση Δοκών Οπλισμένου Σκυροδέματος. 15ο Συνέδριο Σκυροδέματος. Αλεξανδρούπολη: Εκδόσεις ΤΕΕ; 2006.

[6] www.Eurofighter.com.

[7] www.boeing.com.

[8] Reifsnider KL. Chapter 2 - Damage and Damage Mechanics. In: Reifsnider KL, editor. Composite Materials Series: Elsevier; 1991. p. 11-77.

[9] Chen WQ, Wang YF, Cai JB, Ye GR. Three-dimensional analysis of cross-ply laminated cylindrical panels with weak interfaces. International Journal of Solids and Structures. 2004;41(9–10):2429-46.

[10] Kam TY, Sher HF, Chao TN, Chang RR. Predictions of deflection and first-ply failure load of thin laminated composite plates via the finite element approach. International Journal of Solids and Structures. 1996;33(3):375-98.

[11] Eckold GC. Design and Manufacture of Composite Structures: McGraw-Hill; 1994.

[12] Bader MG. Microstructural design of fiber composites. By Tsu- Wei Chou, Cambridge University Press, Cambridge 1992, X, 569 pp, hardback, $150, ISBN 0-523-35482. Advanced Materials. 1992;4(10):693-4.

[13] Case SW, Reifsnider KL. 4.16 - Fatigue of Composite Materials. In: Editors-in-Chief: IM, Ritchie RO, Karihaloo B, editors. Comprehensive Structural Integrity. Oxford: Pergamon; 2003. p. 405-41.

[14] Mouzakis DE, Zoga H, Galiotis C. Accelerated environmental ageing study of polyester/glass fiber reinforced composites (GFRPCs). Composites Part B: Engineering. 2008;39(3):467-75.

[15] Parvatareddy H, Wang JZ, Dillard DA, Ward TC, Rogalski ME. Environmental aging of high-performance polymeric composites: Effects on durability. Composites Science and Technology. 1995;53(4):399-409.

[16] Paipetis A, Katerelos DTG. Post-Impact Fatigue Behavior of Composite Laminates: Current and Novel Technologies for Enhanced Damage Tolernace: Nova Science Pub Inc; 2011.

[17] Baker A, Rajic N, Davis C. Towards a practical structural health monitoring technology for patched cracks in aircraft structure. Composites Part A: Applied Science and Manufacturing. 2009;40(9):1340-52.

[18] Baker AA. Repair of cracked or defective metallic aircraft components with advanced fibre composites—an overview of Australian work. Composite Structures. 1984;2(2):153-81.

[19] Gkikas G, Sioulas D, Lekatou A, Barkoula NM, Paipetis AS. Enhanced bonded aircraft repair using nano-modified adhesives. Materials and Design. 2012;41:394-402.

[20] Korakis N. Composite patch repair of glare structures [MsC]. Cranfield: Cranfield University; 2005.

[21] Baker AA, Roberts JD, Rose LRF. Use of joint parameters in estimating the K reduction due to crack patching. Proc of an Int Workshop on Defence Applications for Advanced Repair Technology for Metal and Composite Structure, Naval Research Labs. Washington1981.

[22] Baker A. Bonded composite repair of fatigue-cracked primary aircraft structure. Composite Structures. 1999;47(1–4):431-43.

[23] Baker AA, Rose LRF, Jones R. Advances in the Bonded Composite Repair of Metallic Aircraft Structure: Elsevier Science; 2003.

[24] Baker A. Bonded Repair of Aircraft Structures: Springer; 1988.

[25] Tay TE, Chau FS, Er CJ. Bonded boron-epoxy composite repair and reinforcement of cracked aluminium structures. Composite Structures. 1996;34(3):339-47.

[26] Ouinas D, Bouiadjra BB, Serier B. The effects of disbonds on the stress intensity factor of aluminium panels repaired using composite materials. Composite Structures. 2007;78(2):278-84.

[27] Bachir Bouiadjra B, Oudad W, Albedah A, Benyahia F, Belhouari M. Effects of the adhesive disband on the performances of bonded composite repairs in aircraft structures. Materials & Design. 2012;37(0):89-95.

[28] Bachir Bouiadjra B, Belhouari M, Serier B. Computation of the stress intensity factors for repaired cracks with bonded composite patch in mode I and mixed mode. Composite Structures. 2002;56(4):401-6.

[29] Park C, Gott JR, III, Melott AL, Karachentsev ID. The topology of large-scale structure. VI - Slices of the universe. Astrophysical Journal, Part 1. 1992; vol. 387:1-8.

[30] Seo D-C, Lee J-J. Fatigue crack growth behavior of cracked aluminum plate repaired with composite patch. Composite Structures. 2002;57(1–4):323-30.

[31] Megueni A, Lousdad A. Comparison of symmetrical double sided and stepped patches for repairing cracked metallic structures. Composite Structures. 2008;85(1):91-4.

[32] Duong CN. A unified approach to geometrically nonlinear analysis of tapered bonded joints and doublers. International Journal of Solids and Structures. 2006;43(11–12):3498-526.

[33] Duong CN, Wang CH. Chapter 4 - Mathematical Theory of Supported One-Sided Crack Patching or Two-Sided Crack Patching. Composite Repair. Oxford: Elsevier Science Ltd; 2007. p. 95-145.

[34] Duong CN, Wang CH. Chapter 2 - Theory of Bonded Doublers and Bonded Joints. Composite Repair. Oxford: Elsevier Science Ltd; 2007. p. 16-68.

[35] Duong CN, Wang CH. Chapter 9 - A Preliminary Design Approach for Crack Patching. Composite Repair. Oxford: Elsevier Science Ltd; 2007. p. 300-35.

[36] Maldague XPV, Moore PO. Nondestructive Testing Handbook: Infrared and Thermal Testing: American Society for Nondestructive Testing, American Society for Metals; 2001.

[37] Kessler SS, Spearing SM, Atalla MJ, Cesnik CES, Soutis C. Damage detection in composite materials using frequency response methods. Composites Part B: Engineering. 2002;33(1):87-95.

[38] Moss SD, Galea SC, Powlesland IG, Konak MJ, Baker AA. In-situ health monitoring of a bonded composite patch using the strain ratio technique. 2001:363-74.

[39] Zou Y, Tong L, Steven GP. Vibration-based model-dependent damage (delamination) identification and health monitoring for composite structures — A REVIEW. Journal of Sound and Vibration. 2000;230(2):357-78.

[40] Wu Z, Qing XP, Ghosh K, Karbhar V, Chang F-K. Health monitoring of bonded composite repair in bridge rehabilitation. Smart Materials and Structures. 2008;17(4):045014.

[41] Okasha NM, Frangopol DM, Decò A. Integration of structural health monitoring in life-cycle performance assessment of ship structures under uncertainty. Marine Structures. 2010;23(3):303-21.

[42] Stull CJ, Earls CJ, Koutsourelakis P-S. Model-based structural health monitoring of naval ship hulls. Computer Methods in Applied Mechanics and Engineering. 2011;200(9–12):1137-49.

[43] Silva IC, Rebello JMA, Bruno AC, Jacques PJ, Nysten B, Dille J. Structural and magnetic characterization of a carburized cast austenitic steel. Scripta Materialia. 2008;59(9):1010-3.

[44] da Silva IC, da Silva RS, Rebello JMA, Bruno AC, Silveira TF. Characterization of carburization of HP steels by non destructive magnetic testing. NDT & E International. 2006;39(7):569-77.

[45] Staszewski WJ, Mahzan S, Traynor R. Health monitoring of aerospace composite structures – Active and passive approach. Composites Science and Technology. 2009;69(11–12):1678-85.

[46] Buschke P, Schappacher W. Trends in the automotive industry steer new NDT applications. Insight: Non-Destructive Testing and Condition Monitoring. 2006;48(9):532-6.

[47] García-Álvarez J, García-Hernández MJ, Novoa-Díaz DF, Turó Peroy A, Chávez Domínguez JA, Salazar Soler J. Resizing buffer rods for ultrasound testing of food products with acoustic noise considerations. Ultrasonics. 2013;53(1):294-301.

[48] García-Álvarez J, Salazar J, Rosell CM. Ultrasonic study of wheat flour properties. Ultrasonics. 2011;51(2):223-8.

[49] Hughes N, Baker M. The use of radiography in forensic medicine. Radiography. 1997;3(4):311-20.

[50] Maitino AJ, Levin DC, Rao VM, Parker L, Sunshine JH. Do emergency medicine physicians perform ultrasound and conventional radiography in the emergency department? Recent trends from 1993 to 2001. Journal of the American College of Radiology. 2005;2(3):274-8.

[51] Zanetta P, Solomos GP, Zürn M, Lucia AC. Holographic detection of defects in composites. Optics & Laser Technology. 1993;25(2):97-102.

[52] Borza DN. Specialized techniques in holographic non-destructive testing of composites. Composites Part B: Engineering. 1998;29(4):497-504.

[53] Hung YY. Shearography and applications in experimental mechanics. 1997:2-28.

[54] Hung YY, Chen YS, Ng SP, Liu L, Huang YH, Luk BL, et al. Review and comparison of shearography and active thermography for nondestructive evaluation. Materials Science and Engineering: R: Reports. 2009;64(5–6):73-112.

[55] Cartz L. Nondestructive Testing: Radiography, Ultrasonics, Liquid Penetrant, Magnetic Particle, Eddy Current: Asm International; 1995.

[56] Rebello JMA. Materials characterization by electromagnetic nde focusing on the petrochemical industry. National Seminar & Exhibition on Non-Destructive Evaluation India 2011.

[57] Hasegawa K, Oikawa T, Kasai N. Development of an Eddy Current Inspection Technique with Surface Magnetization to Evaluate the Carburization Thickness of Ethylene Pyrolysis Furnace Tubes. Journal of Nondestructive Evaluation. 2012:1-8.

[58] Roach DP, Scala CM. Chapter 23 - Non-Destructive Evaluation and Quality Control for Bonded Composite Repair of Metallic Aircraft Structures. In: Baker AA, Rose LRF, R. JonesA2 - A.A. Baker LRFR, Jones R, editors. Advances in the Bonded Composite Repair of Metallic Aircraft Structure. Oxford: Elsevier Science Ltd; 2002. p. 659-726.

[59] Shepard SM. Introduction to active thermography for non-destructive evaluation. Anti-Corrosion Methods and Materials. 1997;44(4):236-9.

[60] Maldague X. Applications of Infrared Thermography in NonDestructive Evaluation. In: Testing TiON, editor.: Pramod Rastogi e-Journal of Nondestructive Testing & Ultrasonics; 2000. p. 591-609.

[61] Maldague X. Theory and practice of infrared technology for nondestructive testing: Wiley; 2001.

[62] Meola C, Carlomagno GM. Recent advances in the use of infrared thermography. Measurement Science and Technology. 2004;15(9):R27-R58.

[63] Mackenzie AK. Effects Of Surface Coatings On Infra-Red Measurements Of Thermoelastic Responses. 1989:59-71.

[64] Quinn S, Dulieu-Barton JM. Identification of the sources of non-adiabatic behaviour for practical thermoelastic stress analysis. The Journal of Strain Analysis for Engineering Design. 2002;37(1):59-71.

[65] Avdelidis NP, Moropoulou A, Marioli Riga ZP. The technology of composite patches and their structural reliability inspection using infrared imaging. Progress in Aerospace Sciences. 2003;39(4):317-28.

[66] Maldague X, Galmiche F, Ziadi A. Advances in pulsed phase thermography. Infrared Physics and Technology. 2002;43(3-5):175-81.

[67] Avdelidis NP, Ibarra-Castanedo C, Maldague X, Marioli-Riga ZP, Almond DP. A thermographic comparison study for the assessment of composite patches. Infrared Physics and Technology. 2004;45(4):291-9.

[68] Almond DP, Peng W. Thermal imaging of composites. Journal of Microscopy. 2001;201(2):163-70.

[69] Vavilov VP, Marinetti S. Pulsed phase thermography and fourier-analysis thermal tomography. Russian Journal of Nondestructive Testing. 1999;35(2):134-45.

[70] Ciliberto A, Cavaccini G, Salvetti O, Chimenti M, Azzarelli L, Bison PG, et al. Porosity detection in composite aeronautical structures. Infrared Physics & Technology. 2002;43(3–5):139-43.

[71] Busse G. Nondestructive evaluation of polymer materials. NDT and E International. 1994;27(5):253-62.

[72] Grammatikos S, Kordatos E, Barkoula NM, Matikas T, Paipetis A. Repair integrity monitoring of composite aerostructures using thermographic imaging. Proceedings of SPIE - The International Society for Optical Engineering 2010:76491D-D.

[73] Grammatikos SA, Kordatos EZ, Barkoula NM, Matikas TE, Paipetis AS. Innovative non-destructive evaluation and damage characterisation of composite aerostructures using thermography. Plastics, Rubber and Composites. 2011;40(6-7):342-8.

[74] Avdelidis NP, Almond DP, Dobbinson A, Hawtin BC, Ibarra-Castanedo C, Maldague X. Aircraft composites assessment by means of transient thermal NDT. Progress in Aerospace Sciences. 2004;40(3):143-62.

[75] Ludwig N, Teruzzi P. Heat losses and 3D diffusion phenomena for defect sizing procedures in video pulse thermography. Infrared Physics & Technology. 2002;43(3–5):297-301.

[76] Balageas DL. Thermal Imaging Methods. Encyclopedia of Structural Health Monitoring: John Wiley & Sons, Ltd; 2009.

[77] Avdelidis NP, Almond DP, Marioli-Riga ZP. Pulsed thermography: philosophy, qualitative & quantitative analysis on aircraft materials & applications. In: Proceedings of Vth International Workshop held, Advances in Signal Processing for Non Destructive Evaluation of Materials. Conference August 2-4, Conference 2005.

[78] Zacharija SG, Lahiri J. Data analysis techniques in thermographic NDT of composite: A critical comparison. National Seminar of ISNT. Chennai2002.

[79] Kopal I, Koštial P, Hutyra J, Mokryšová M, Rusnáková S. Pulsed phase thermographic defects detection by scanning thermovision camera. 4th Youth Symposium on Experimental Solid Mechanics. Castrocaro Terme2005.

[80] Kaplan H. Practical applications of infrared thermal sensing and imaging equipment: SPIE Optical Engineering Press; 1999.

[81] Wu D, Busse G. Lock-in thermography for nondestructive evaluation of materials. Revue Generale de Thermique. 1998;37(8):693-703.

[82] Myriounis DP, Kordatos EZ, Hasan ST, Matikas TE. Crack-tip stress field and fatigue crack growth monitoring using infrared lock-in thermography in a359/sicp composites. Strain. 2011;47(SUPPL. 1):e619-e27.

[83] Kordatos EZ, Aggelis DG, Matikas TE. Monitoring mechanical damage in structural materials using complimentary NDE techniques based on thermography and acoustic emission. Composites Part B: Engineering. 2012;43(6):2676-86.

[84] Bremond P. New developments in thermoelastic stress analysis by infrared thermography. 2007.

[85] Krstulovic-Opara L, Klarin B, Neves P, Domazet Z. Thermal imaging and Thermoelastic Stress Analysis of impact damage of composite materials. Engineering Failure Analysis. 2011;18(2):713-9.

[86] Thomson W. On the dynamical theory of heat. Trans Roy Soc Edin. 1853;20:261-83.

[87] Benammar A, Drai R, Guessoum A. Detection of delamination defects in CFRP materials using ultrasonic signal processing. Ultrasonics. 2008;48(8):731-8.

[88] Berketis K, Tzetzis D, Hogg PJ. Impact damage detection and degradation monitoring of wet GFRP composites using noncontact ultrasonics. Polymer Composites. 2009;30(8):1043-9.

[89] Bastianini F, Di Tommaso A, Pascale G. Ultrasonic non-destructive assessment of bonding defects in composite structural strengthenings. Composite Structures. 2001;53(4):463-7.

[90] Adams RD, Cawley P. A review of defect types and nondestructive testing techniques for composites and bonded joints. NDT International. 1988;21(4):208-22.

[91] Růžek R, Lohonka R, Jironč J. Ultrasonic C-Scan and shearography NDI techniques evaluation of impact defects identification. NDT & E International. 2006;39(2):132-42.

[92] Malhotra VM, Carino NJ. Handbook on nondestructive testing of concrete: CRC; 2004.

[93] Grosse CU, Ohtsu M. Acoustic emission testing: Springer; 2008.

[94] Kurz JH, Finck F, Grosse CU, Reinhardt HW. Stress drop and stress redistribution in concrete quantified over time by the b-value analysis. Structural Health Monitoring. 2006;5(1):69-81.

[95] Aggelis DG, Shiotani T, Terazawa M. Assessment of construction joint effect in full-scale concrete beams by acoustic emission activity. Journal of Engineering Mechanics. 2010;136(7):906-12.

[96] Aggelis DG, Barkoula NM, Matikas TE, Paipetis AS. Acoustic emission monitoring of degradation of cross ply laminates. The Journal of the Acoustical Society of America. 2010;127(6):EL246-EL51.

[97] Ohno K, Ohtsu M. Crack classification in concrete based on acoustic emission. Construction and Building Materials. 2010;24(12):2339-46.

[98] Overgaard LCT, Lund E, Camanho PP. A methodology for the structural analysis of composite wind turbine blades under geometric and material induced instabilities. Computers and Structures. 2010;88(19-20):1092-109.

[99] Aggelis DG, Matikas TE, Shiotani T. Advanced acoustic techniques for health monitoring of concrete structures. In: Kim SH, Ann KY, editors. Advanced acoustic techniques for health monitoring of concrete structures. Seoul: Middleton Publishing Inc.Advanced acoustic techniques for health monitoring of concrete structures; 2010. p. 331–78.

[100] Soulioti D, Barkoula NM, Paipetis A, Matikas TE, Shiotani T, Aggelis DG. Acoustic emission behavior of steel fibre reinforced concrete under bending. Construction and Building Materials. 2009;23(12):3532-6.

[101] Philippidis TP, Nikolaidis VN, Anastassopoulos AA. Damage characterization of carbon/carbon laminates using neural network techniques on AE signals. NDT and E International. 1998;31(5):329-40.

[102] Kaiser J. Results and conclusions from measurements of sound in metallic materials under tensile stress 1950.

[103] Group AE. Journal of Acoustic Emission: Acoustic Emission Group; 1997.

[104] Grammatikos SA, Kordatos EZ, Aggelis DG, Matikas TE, Paipetis AS. Critical and subcritical damage monitoring of bonded composite repairs using innovative non-destructive techniques. Proceedings of SPIE - The International Society for Optical Engineering 2012:834611-.

[105] Genest M, Martinez M, Mrad N, Renaud G, Fahr A. Pulsed thermography for non-destructive evaluation and damage growth monitoring of bonded repairs. Composite Structures. 2009;88(1):112-20.

[106] Manjunath Rao Pawar Dasarath Rao. Review of nondestructive evaluation techniques for frp composite structural components [Master of Science in Civil Engineering]. West Virginia: College of Engineering and Mineral Resources at West Virginia University; 2007.

[107] Galea SC. Monitoring damage in bonded composite repairs of cracked metallic components using surface strain measurements. 11th International Conference on Composite Materials. Gold Coast, Australia1997.

[108] Baker AA, Chester RJ, Davis MJ, Roberts JD, Retchford JA. Reinforcement of the F-111 wing pivot fitting with a boron/epoxy doubler system—materials engineering aspects. Composites. 1993;24(6):511-21.

[109] Rees D, Chiu WK, Jones R. A numerical study of crack monitoring in patched structures using a piezoelectric sensor. Modelling and Simulation in Materials Science and Engineering. 1992;1(3):202-5.

[110] Wilson AR, Sbiaa Z, Hopcroft M, Laskowski BC. MEMS adhesive bond degradation sensor. 2001:252-9.

[111] Chiu WK, Galea SC, Koss LL, Rajic N. Damage detection in bonded repairs using piezoceramics. Smart Materials and Structures. 2000;9(4):466-75.

[112] Koh YL, Rajic N, Chiu WK, Galea S. Smart structure for composite repair. Composite Structures. 1999;47(1-4):745-52.

[113] Chehura E, Skordos AA, Ye C-C, James SW, Partridge IK, Tatam RP. Strain development in curing epoxy resin and glass fibre/epoxy composites monitored by fibre Bragg grating sensors in birefringent optical fibre. Smart Materials and Structures. 2005;14(2):354.

[114] Black CA, Udd E, Schulz WL, Kreger ST, Kunzler M, Taylor T, et al. Using multi-axis fiber grating strain sensors to measure transverse strain and transverse strain gradients in composite materials with complex weave structures. 2002:162-7.

[115] Palaniappan J, Ogin SL, Thorne AM, Reed GT, Crocombe AD, Capell TF, et al. Disbond growth detection in composite–composite single-lap joints using chirped FBG sensors. Composites Science and Technology. 2008;68(12):2410-7.

[116] Mizutani T, Okabe Y, Takeda N. Crack identification in CFRP laminates using small-diameter FBG sensors. 2002. p. 330-40.

[117] Okabe Y, Tsuji R, Takeda N. Application of chirped fiber Bragg grating sensors for identification of crack locations in composites. Composites Part A: Applied Science and Manufacturing. 2004;35(1):59-65.

[118] Tsutsui H, Kawamata A, Kimoto J, Sanda T, Takeda N. Impact damage detection of curved stiffened composite panels by using wavy embedded small-diameter optical fibers. 2002:454-61.

[119] Jabir SAA. Thick film electronic ceramic sensors for civil structures health monitoring [PhD]. Edinburgh: Edinburgh Napier University; 2011.

[120] Galea SC. Chapter 20 - Smart Patch Systems. In: Baker AA, Rose LRF, R. JonesA2 - A.A. Baker LRFR, Jones R, editors. Advances in the Bonded Composite Repair of Metallic Aircraft Structure. Oxford: Elsevier Science Ltd; 2002. p. 571-613.

[121] Kemp M. Self-sensing composites for smart damage detection using electrical properties. 1994:136-9.

[122] Abry JC, Bochard S, Chateauminois A, Salvia M, Giraud G. In situ detection of damage in CFRP laminates by electrical resistance measurements. Composites Science and Technology. 1999;59(6):925-35.

[123] Grammatikos S. Electrical resistance and electrical potential studies for the detection and monitoring of damage in hybrid composites. Emerging Technologies in Non-Destructive Testing V: CRC Press; 2012. p. 401-6.

[124] Grammatikos SA, Paipetis AS. On the electrical properties of multi scale reinforced composites for damage accumulation monitoring. Composites Part B: Engineering. 2012;43(6):2687-96.

[125] Grammatikos SA, Kouli ME, Gkikas G, Paipetis AS. Structural health monitoring of aerospace materials used in industry using electrical potential mapping methods. Proceedings of SPIE - The International Society for Optical Engineering 2012:83461K-K.

[126] Kostopoulos V, Vavouliotis A, Karapappas P, Tsotra P, Paipetis A. Damage monitoring of carbon fiber reinforced laminates using resistance measurements. Improving sensitivity using carbon nanotube doped epoxy matrix system. Journal of Intelligent Material Systems and Structures. 2009;20(9):1025-34.

[127] Christopoulos A, Hristoforou E, Tsamasphyros G. Strain sensing capabilities of iron/epoxy composites. Smart Materials and Structures. 2012;21(8).

[128] Oyharçabal M, Olinga T, Foulc MP, Vigneras V. Polyaniline/clay as nanostructured conductive filler for electrically conductive epoxy composites. Influence of filler morphology, chemical nature of reagents, and curing conditions on composite conductivity. Synthetic Metals. 2012;162(7-8):555-62.

[129] Nanni F, Ruscito G, Puglia D, Terenzi A, Kenny JM, Gusmano G. Effect of carbon black nanoparticle intrinsic properties on the self-monitoring performance of glass fibre reinforced composite rods. Composites Science and Technology. 2011;71(1):1-8.

[130] Baughman RH, Zakhidov AA, De Heer WA. Carbon nanotubes - The route toward applications. Science. 2002;297(5582):787-92.

[131] Paipetis A, Kostopoulos V. Carbon Nanotube Enhanced Aerospace Composite Materials: A New Generation of Multifunctional Hybrid Structural Composites: Springer; 2012.

[132] Todoroki A, Yoshida J. Apparent negative piezoresistivity of single-ply CFRP due to poor electrical contact of four-probe method. 2005. p. 610-5.

[133] Wang S, Chung DDL. Apparent negative electrical resistance in carbon fiber composites. Composites Part B: Engineering. 1999;30(6):579-90.

[134] Louis M, Joshi SP, Brockmann W. An experimental investigation of through-thickness electrical resistivity of CFRP laminates. Composites Science and Technology. 2001;61(6):911-9.

[135] Owston CN. Electrical properties of single carbon fibres. Journal of Physics D: Applied Physics. 1970;3(11):1615-26.

[136] Schulte K, Baron C. Load and failure analyses of CFRP laminates by means of electrical resistivity measurements. Composites Science and Technology. 1989;36(1):63-76.

[137] Irving PE, Thiagarajan C. Fatigue damage characterization in carbon fibre composite materials using an electrical potential technique. Smart Materials and Structures. 1998;7(4):456-66.

[138] Seo D-C, Lee J-J. Damage detection of CFRP laminates using electrical resistance measurement and neural network. Composite Structures. 1999;47(1-4):525-30.

[139] Schueler R, Joshi SP, Schulte K. Damage detection in CFRP by electrical conductivity mapping. Composites Science and Technology. 2001;61(6):921-30.

[140] Wen J, Xia Z, Choy F. Damage detection of carbon fiber reinforced polymer composites via electrical resistance measurement. Composites Part B: Engineering. 2011;42(1):77-86.

[141] Park J-M, Kim D-S, Kim S-J, Kim P-G, Yoon D-J, DeVries KL. Inherent sensing and interfacial evaluation of carbon nanofiber and nanotube/epoxy composites using electrical resistance measurement and micromechanical technique. Composites Part B: Engineering. 2007;38(7–8):847-61.

[142] Wang X, Chung DDL. Self-monitoring of fatigue damage and dynamic strain in carbon fiber polymer-matrix composite. Composites Part B: Engineering. 1998;29(1):63-73.

[143] Luo X, Chung DDL. Carbon-fiber/polymer-matrix composites as capacitors. Composites Science and Technology. 2001;61(6):885-8.

[144] Wang S, Chung DDL. Temperature/light sensing using carbon fiber polymer-matrix composite. Composites Part B: Engineering. 1999;30(6):591-601.

[145] Fiedler B, Gojny FH, Wichmann MHG, Bauhofer W, Schulte K. Can carbon nanotubes be used to sense damage in composites? Annales de Chimie: Science des Materiaux. 2004;29(6):81-94.

[146] Chung DDL, Wang S. Self-sensing of Damage and Strain in Carbon Fiber Polymer-Matrix Structural Composites by Electrical Resistance Measurement. Polymers and Polymer Composites. 2003;11(7):515-25.

[147] Wang W, Chung DDL. Fiber Breakage in Polymer-Matrix Composite during Static and Dynamic Loading, Studied by Electrical Resistance Measurement. Journal of Materials Research in Nondestructive Evaluation. 1999;14(11):4224-9.

[148] Todoroki A, Kobayashi H, Matuura K. Application of electric potential method to smart composite structures for detecting delamination. JSME International Journal, Series A: Mechanics and Material Engineering. 1995;38(4):524-30.

[149] Angelidis N, et al. Experimental and finite element study of the electrical potential technique for damage detection in CFRP laminates. Smart Materials and Structures. 2005;14(1):147.

[150] Kupke M, Schulte K, Schüler R. Non-destructive testing of FRP by d.c. and a.c. electrical methods. Composites Science and Technology. 2001;61(6):837-47.

[151] Daily W, Ramirez A. Electrical Resistance Tomography Hanford Washington Lawrence Livermore National Laboratory, Contract W-7405-Eng-48; 2000. p. 34.

[152] Mondal SK, Sastry RG, Pachauri AK, Gautam PK. High resolution 2D electrical resistivity tomography to characterize active Naitwar Bazar landslide, Garhwal Himalaya, India. Current Science. 2008;94(7):871-5.

[153] Williams RA, Wang M. Dynamic Imaging of Process Plant Reactors and Separators using Electrical Process Tomography. Oil and Gas Science and Technology. 2000;55(2):185-6.

[154] Oldenborger GA, Routh PS, Knoll MD. Model reliability for 3D electrical resistivity tomography: Application of the volume of investigation index to a time-lapse monitoring experiment. Geophysics. 2007;72(4):F167-F75.

[155] Pidlisecky A, Knight R, Haber E. Cone-based electrical resistivity tomography. Geophysics. 2006;71(4):G157-G67.

[156] Ueda M, Todoroki A. Delamination monitoring of CFRP laminate using the two-stage electric potential change method with equivalent electric conductivity. Engineering Fracture Mechanics. 2008;75(9):2737-50.

[157] Hou L, Hayes SA. A resistance-based damage location sensor for carbon-fibre composites. Smart Materials and Structures. 2002;11(6):966.

[158] Wang D, Wang S, Chung DDL, Chung JH. Sensitivity of the two-dimensional electric potential/resistance method for damage monitoring in carbon fiber polymer-matrix composite. Journal of Materials Science. 2006;41(15):4839-46.

[159] Baltopoulos A, Vavouliotis A, Kostopoulos V, Polydorides N, Pambaguian L. Electrical tomography as a tool for non-destructive assessment of composite structures. Emerging Technologies in Non-Destructive Testing V: CRC Press; 2012. p. 389-94.

[160] Todoroki A. Electric resistance change method for cure/strain/damage monitoring of CFRP laminates. Key Engineering Materials 2004. p. 1812-20.

[161] Athanasopoulos N, Kostopoulos V. Resistive heating of multidirectional and unidirectional dry carbon fibre preforms. Composites Science and Technology. 2012;72(11):1273-82.

[162] Athanasopoulos N, Kostopoulos V. Prediction and experimental validation of the electrical conductivity of dry carbon fiber unidirectional layers. Composites Part B: Engineering. 2011;42(6):1578-87.

[163] Hung C-c, Dillehay ME, Stahl M. Heater made from graphite composite material for potential deicing application. Journal of Aircraft. 1987;24(10):725-30.

[164] Hou M, Yang M, Beehag A, Mai Y-W, Ye L. Resistance welding of carbon fibre reinforced thermoplastic composite using alternative heating element. Composite Structures. 1999;47(1–4):667-72.

[165] Florea RS, Bammann DJ, Yeldell A, Solanki KN, Hammi Y. Welding parameters influence on fatigue life and microstructure in resistance spot welding of 6061-T6 aluminum alloy. Materials and Design. 2013;45:456-65.

[166] Göttmann A, Bailly D, Bergweiler G, Bambach M, Stollenwerk J, Hirt G, et al. A novel approach for temperature control in ISF supported by laser and resistance heating. International Journal of Advanced Manufacturing Technology. 2012:1-11.

[167] Wan N, Sun LT, Ding SN, Xu T, Hu XH, Sun J, et al. Synthesis of graphene-CNT hybrids via joule heating: Structural characterization and electrical transport. Carbon. 2013;53:260-8.

[168] Zhao H, Wu Z, Wang S, Zheng J, Che G. Concrete pavement deicing with carbon fiber heating wires. Cold Regions Science and Technology. 2011;65(3):413-20.

[169] Zhang K, Han B, Yu X. Nickel particle based electrical resistance heating cementitious composites. Cold Regions Science and Technology. 2011;69(1):64-9.

[170] Farzaneh M, Ryerson CC. Anti-icing and deicing techniques. Cold Regions Science and Technology. 2011;65(1):1-4.

[171] García Á, Schlangen E, van de Ven M, Liu Q. Electrical conductivity of asphalt mortar containing conductive fibers and fillers. Construction and Building Materials. 2009;23(10):3175-81.

[172] Thostenson ET, Chou TW. Carbon Nanotube Networks: Sensing of Distributed Strain and Damage for Life Prediction and Self Healing. Advanced Materials. 2006;18(21):2837-41.

[173] Chen X, Dam MA, Ono K, Mal A, Shen H, Nutt SR, et al. A thermally re-mendable cross-linked polymeric material. Science. 2002;295(5560):1698-702.

[174] Park JS, Kim HS, Thomas Hahn H. Healing behavior of a matrix crack on a carbon fiber/mendomer composite. Composites Science and Technology. 2009;69(7-8):1082-7.

[175] Park JS, Takahashi K, Guo Z, Wang Y, Bolanos E, Hamann-Schaffner C, et al. Towards development of a self-healing composite using a mendable polymer and resistive heating. Journal of Composite Materials. 2008;42(26):2869-81.

[176] Fosbury A, Wang S, Pin YF, Chung DDL. The interlaminar interface of a carbon fiber polymer-matrix composite as a resistance heating element. Composites Part A: Applied Science and Manufacturing. 2003;34(10):933-40.

[177] Grammatikos SA, Kordatos EZ, Matikas TE, Paipetis AS. Low-velocity impact damage identification using a novel current injection thermographic technique. Proceedings of SPIE - The International Society for Optical Engineering. 2012;8346.

[178] Suzuki Y, Todoroki A, Matsuzaki R, Mizutani Y. Impact-damage visualization in CFRP by resistive heating: Development of a new detection method for indentations caused by impact loads. Composites Part A: Applied Science and Manufacturing. 2012;43(1):53-64.

[179] Sandler J, Shaffer MSP, Prasse T, Bauhofer W, Schulte K, Windle AH. Development of a dispersion process for carbon nanotubes in an epoxy matrix and the resulting electrical properties. Polymer. 1999;40(21):5967-71.

[180] Kostopoulos V, Karapappas P, Loutas T, Vavouliotis A, Paipetis A, Tsotra P. Interlaminar fracture toughness of carbon fibre-reinforced polymer laminates with nano- and micro-fillers. Strain. 2011;47(SUPPL. 1):e269-e82.

[181] Kostopoulos V, Baltopoulos A, Karapappas P, Vavouliotis A, Paipetis A. Impact and after-impact properties of carbon fibre reinforced composites enhanced with multi-wall carbon nanotubes. Composites Science and Technology. 2010;70(4):553-63.

[182] Czech Z, Kowalczyk A, Pełech R, Wróbel RJ, Shao L, Bai Y, et al. Using of carbon nanotubes and nano carbon black for electrical conductivity adjustment of pressure-sensitive adhesives. International Journal of Adhesion and Adhesives. 2012;36(0):20-4.

[183] Thostenson ET, Ren Z, Chou TW. Advances in the science and technology of carbon nanotubes and their composites: A review. Composites Science and Technology. 2001;61(13):1899-912.

[184] Chou TW, Thostenson ET, Gao L. Advances in the science and technology of carbon nanotube composites. Proceedings of ICCM International Conferences on Composite Materials 2009.

[185] Coleman JN, Curran S, Dalton AB, Davey AP, McCarthy B, Blau W, et al. Percolation-dominated conductivity in a conjugated-polymer-carbon-nanotube composite. Physical Review B. 1998;58(12):R7492-R5.

[186] Coleman JN, Curran S, Dalton AB, Davey AP, McCarthy B, Blau W, et al. Percolation-dominated conductivity in a conjugated-polymer-carbon-nanotube composite. Physical Review B - Condensed Matter and Materials Physics. 1998;58(12):R7492-R5.

[187] Rochefort A, Avouris P, Lesage F, Salahub DR. Electrical and mechanical properties of distorted carbon nanotubes. Physical Review B - Condensed Matter and Materials Physics. 1999;60(19):13824-30.

[188] Kostopoulos V, Tsotra P, Vavouliotis A, Karappapas P, Nikolaou N, Paipetis A, et al. Damage Detection During Monotonic And Cyclic Tensile Loading Of CNT Doped CFRPs Via Resistance Measurements. 12th European Conference in Composite Materials. Biarritz, France2006.

[189] Gkikas G, Barkoula NM, Paipetis AS. Effect of dispersion conditions on the thermo-mechanical and toughness properties of multi walled carbon nanotubes-reinforced epoxy. Composites Part B: Engineering. 2012;43(6):2697-705.

[190] Kostopoulos V, Baltopoulos A, Karapappas P, Paipetis A. Nano-enhanced impact properties of carbon fibre reinforced composites. 13th European Conference on Composite Materials. Stockholm, Sweden 2008.

[191] Thostenson ET, Chou TW. Real-time in situ sensing of damage evolution in advanced fiber composites using carbon nanotube networks. Nanotechnology. 2008;19(21).

[192] Sotiriadis G, Tsotra P, Paipetis A, Kostopoulos V. Stiffness degradation monitoring of carbon nanotube doped Glass / Vinylester composites via resistance measurements. Journal of Nanostructured Polymers and Nanocomposites. 2007;3(3):90-5.

[193] Nofar M, Hoa SV, Pugh MD. Failure detection and monitoring in polymer matrix composites subjected to static and dynamic loads using carbon nanotube networks. Composites Science and Technology. 2009;69(10):1599-606.

[194] Liu JW, Dong F. Electrical resistance tomography based on the single drive electrode method.. Proceedings of International Conference on Machine Learning and Cybernetics, 2004. p. 632-7.

[195] Vigolo B, Penicaud A, Coulon C, Sauder C, Pailler R, Journet C, et al. Macroscopic fibers and ribbons of oriented carbon nanotubes. Science. 2000;290(5495):1331-4.

[196] Vigolo B, Poulin P, Lucas M, Launois P, Bernier P. Improved structure and properties of single-wall carbon nanotube spun fibers. Applied Physics Letters. 2002;81(7):1210-2.

[197] Muto N, Arai Y, Shin SG, Matsubara H, Yanagida H, Sugita M, et al. Hybrid composites with self-diagnosing function for preventing fatal fracture. Composites Science and Technology. 2001;61(6):875-83.

[198] Ampatzoglou A, Vavouliotis A, Baltopoulos A, Kostopoulos V. Non destructive evaluation of artificially induced damage in composite structures using electrical resistance/potential mapping. 2012. p. 381-7.

[199] Vavouliotis A, Loutas T, Sotiriadis G, Kostopoulos V. On line monitoring of damage during fatigue loading of composite patch repair of composite structures. Emerging Technologies in Non-Destructive Testing V: CRC Press; 2012. p. 395-9.

[200] Meola C, Carlomagno GM, Squillace A, Vitiello A. Non-destructive evaluation of aerospace materials with lock-in thermography. Engineering Failure Analysis. 2006;13(3):380-8.

[201] Tehrani M, Boroujeni AY, Hartman TB, Haugh TP, Case SW, Al-Haik MS. Mechanical characterization and impact damage assessment of a woven carbon fiber reinforced carbon nanotube-epoxy composite. Composites Science and Technology. 2013;75:42-8.

[202] Jasiüniené E, Raišutis R, Šliteris R, Voleišis A, Vladišauskas A, Mitchard D, et al. NDT of wind turbine blades using adapted ultrasonic and radiographic techniques. Insight: Non-Destructive Testing and Condition Monitoring. 2009;51(9):477-83.

[203] Karpur P, Benson DM, Matikas TE, Kundu T, Nicolaou PD. Approach to determine the experimental transmitter-receiver geometry for the reception of leaky Lamb waves. Materials Evaluation. 1995;53(12):1348-52.

[204] Kundu T, Maslov K, Karpur P, Matikas TE, Nicolaou PD. A Lamb wave scanning approach for the mapping of defects in [0/90] titanium matrix composites. Ultrasonics. 1996;34(1):43-9.

[205] Sophian A, Tian GY, Taylor D, Rudlin J. Electromagnetic and eddy current NDT: A review. Insight: Non-Destructive Testing and Condition Monitoring. 2001;43(5):302-6.

[206] Baker AA. Repair of cracked or defective metallic aircraft components with advanced fibre composites-an overview of Australian work. Composite Structures. 1984;2(2):153-81.

[207] Castanedo CI. Quantitative subsurface defect evaluation by pulsed phase thermography: depth retrieval with the phase [PhD]. QUÉBEC: UNIVERSITÉ LAVAL; 2005.

[208] Avdelidis NP, Almond DP. Through skin sensing assessment of aircraft structures using pulsed thermography. NDT and E International. 2004;37(5):353-9.

[209] Chatterjee K, Tuli S, Pickering SG, Almond DP. A comparison of the pulsed, lock-in and frequency modulated thermography nondestructive evaluation techniques. NDT & E International. 2011;44(7):655-67.

[210] Pan M, He Y, Tian G, Chen D, Luo F. Defect characterisation using pulsed eddy current thermography under transmission mode and NDT applications. NDT and E International. 2012;52:28-36.

[211] Tian GY, He Y, Cheng L, Jackson P. Pulsed eddy current thermography for corrosion characterisation. International Journal of Applied Electromagnetics and Mechanics. 2012;39(1-4):269-76.

[212] Malhotra VM, Carino NJ. Handbook on Nondestructive Testing of Concrete Second Edition: Taylor & Francis; 2003.

[213] Cooley JW, Tukey JW. An Algorithm for the Machine Calculation of Complex Fourier Series. Mathematics of Computation. 1965;19(90):297-301.

[214] Pickering S, Almond D. Matched excitation energy comparison of the pulse and lock-in thermography NDE techniques. NDT and E International. 2008;41(7):501-9.

[215] Wallbrink C, Wade SA, Jones R. The effect of size on the quantitative estimation of defect depth in steel structures using lock-in thermography. Journal of Applied Physics. 2007;101(10).

[216] Bai W, Wong BS. Evaluation of defects in composite plates under convective environments using lock-in thermography. Measurement Science and Technology. 2001;12(2):142-50.

[217] Chatterjee K, Tuli S, Pickering SG, Almond DP. A comparison of the pulsed, lock-in and frequency modulated thermography nondestructive evaluation techniques. NDT & E International. 2011;44(7):655-67.

[218] Mulaveesala R, Tuli S. Implementation of frequency-modulated thermal wave imaging for non-destructive sub-surface defect detection. Insight: Non-Destructive Testing and Condition Monitoring. 2005;47(4):206-8.

[219] Kaplan H. Practical Applications of Infrared Thermal Sensing and Imaging Equipment, Third Edition: Society of Photo Optical; 2007.

[220] Kažys R, Svilainis L. Ultrasonic detection and characterization of delaminations in thin composite plates using signal processing techniques. Ultrasonics. 1997;35(5):367-83.

[221] Biggiero G, Canella G, Mossini A. Ultrasonic scanning and spectrum analysis for inspection of bond efficiency of metal-to-metal structural adhesive joints. NDT International. 1983;16(2):67-73.

[222] www.ge-mcs.com/.

[223] Stoessel R. Air-coupled ultrasound inspection as a new non-destructive testing tool for quality assurance [PhD]. Stuttgart: University of Stuttgart; 2004.

[224] Ravikiran NK, Venkataramanaiah A, Bhat MR, Murthy CRL. Detection and Evaluation of Impact damage in CFRP Laminates Using Ultrasound C-Scan and IR Thermography
National Seminar on Non-Destructive Evaluation Hyderabad Indian Society for Non-Destructive Testing Hyderabad Chapter 2006.

[225] McMaster RC, Testing SfN-d. Nondestructive testing handbook: edited for the Society for Nondestructive Testing: Ronald Press Co.; 1959.

[226] Richardson MOW, Wisheart MJ. Review of low-velocity impact properties of composite materials. Composites Part A: Applied Science and Manufacturing. 1996;27(12):1123-31.

[227] Karhunen K, Seppänen A, Lehikoinen A, Monteiro PJM, Kaipio JP. Electrical Resistance Tomography imaging of concrete. Cement and Concrete Research. 2010;40(1):137-45.

[228] Baloch TM, Yu KC. Monitoring of industrial process using intelligent tomography system. 2007. p. 1115-9.

[229] Schulte K, Baron C. Composite Sci Technol. 1989;36(1):63.

[230] Chung DDL. Self-monitoring structural materials. Materials Science and Engineering R: Reports. 1998;22(2):57-78.

[231] Todoroki A, Omagari K, Shimamura Y, Kobayashi H. Matrix crack detection of CFRP using electrical resistance change with integrated surface probes. Composites Science and Technology. 2006;66(11-12):1539-45.

[232] Ueda M, Todoroki A. Asymmetrical dual charge EPCM for delamination monitoring of CFRP laminate. Key Engineering Materials 2006. p. 1309-15.

[233] Smith CE, Morscher GN, Xia ZH. Monitoring damage accumulation in ceramic matrix composites using electrical resistivity. Scripta Materialia. 2008;59(4):463-6.

[234] Gao L, Thostenson ET, Zhang Z, Byun JH, Chou TW. Damage monitoring in fiber-reinforced composites under fatigue loading using carbon nanotube networks. Philosophical Magazine. 2010;90(31-32):4085-99.

[235] Smith C, Gyekenyesi A. Detecting cracks in ceramic matrix composites by electrical resistance. 2011.

[236] A High-Performance EIT System. IEEE Sensors J. 2005;5(2):289.

[237] Design of ERT system. J Zhejiang Univ SCI. 2005;6a(12):1446.

[238] He CL, Zhu SR, Zhang XY. Study on electrical resistance tomography simulation of carbon fiber smart layers on two-dimensional curved surface. 2011. p. 2185-90.

[239] Zhang X, Li Z, Zhu S. A novel electrical resistance tomography system of carbon fiber smart layer for structural health monitoring. 2009. p. 132-5.

[240] Todoroki A, Tanaka Y, Shimamura Y. Delamination monitoring of graphite/epoxy laminated composite plate of electric resistance change method. Composites Science and Technology. 2002;62(9):1151-60.

[241] Angelidis N, Khemiri N, Irving PE. Experimental and finite element study of the electrical potential technique for damage detection in CFRP laminates. Smart Materials and Structures. 2005;14(1):147.

[242] Todoroki A. Long life durability of electrodes of electrical resistance change method for damage monitoring of CFRP composite structures. Department of Mechanical Sciences and Engineering, Tokyo Institute of Technology, 2008.

[243] Angelidis N, Irving PE. Detection of impact damage in CFRP laminates by means of electrical potential techniques. Composites Science and Technology. 2007;67(3-4):594-604.

[244] Meola C, Carlomagno GM. Impact damage in GFRP: New insights with infrared thermography. Composites Part A: Applied Science and Manufacturing. 2010;41(12):1839-47.

[245] Paipetis A, Katerelos DTG. Post-impact fatigue behavior of composite laminates : current and novel technologies for enhanced damage tolerance. New York: Novinka/Nova Science Publishers Inc.; 2010.

[246] Meola C, Carlomagno GM, Squillace A, Vitiello A. Non-destructive evaluation of aerospace materials with lock-in thermography. Engineering Failure Analysis. 2006;13(3 SPEC. ISS.):380-8.

[247] Vavouliotis A, Paipetis A, Kostopoulos V. On the fatigue life prediction of CFRP laminates using the Electrical Resistance Change method. Composites Science and Technology. 2011;71(5):630-42.

[248] Böger L, Wichmann MHG, Meyer LO, Schulte K. Load and health monitoring in glass fibre reinforced composites with an electrically conductive nanocomposite epoxy matrix. Composites Science and Technology. 2008;68(7-8):1886-94.

[249] Gao L, Thostenson ET, Zhang Z, Chou TW. Sensing of damage mechanisms in fiber-reinforced composites under cyclic loading using carbon nanotubes. Advanced Functional Materials. 2009;19(1):123-30.

[250] Kar P, Khatua BB. Effect of coefficient of thermal expansion on positive temperature coefficient of resistivity behavior of HDPE-Cu composites. Journal of Applied Polymer Science. 2010;118(2):950-9.

[251] Kulkarni R, Ochoa O. Transverse and longitudinal CTE measurements of carbon fibers and their impact on interfacial residual stresses in composites. Journal of Composite Materials. 2006;40(8):733-54.

[252] Rogers K, Kingston-Lee D, Phillips L, Yates B, Chandra M, Parker S. The thermal expansion of carbon-fibre reinforced plastics. Journal of Materials Science. 1981;16(10):2803-18.

[253] Takahashi K, Hahn HT. Investigation of temperature dependency of electrical resistance changes for structural management of graphite/polymer composite. Journal of Composite Materials. 2011;45(25):2603-11.

[254] Gkikas G, Barkoula NM, Paipetis AS. Effect of dispersion conditions on the thermo-mechanical and toughness properties of multi walled carbon nanotubes-reinforced epoxy. Composites Part B: Engineering. 2012;43(6):2697-705.

[255] Poeller M, Chung DDL. Effect of heating on the structure of an adhesive joint, as indicated by electrical resistance measurement. Journal of Adhesion. 2003;79(6):549-57.

[256] Vavouliotis A, Karapappas P, Loutas T, Voyatzi T, Paipetis A, Kostopoulos V. Multistage fatigue life monitoring on carbon fibre reinforced polymers enhanced with multiwall carbon nanotubes. Plastics, Rubber and Composites. 2009;38(2-4):124-30.

[257] Baker AA, Jones R, Callinan RJ. Damage tolerance of graphite/epoxy composites. Composite Structures. 1985;4(1):15-44.

[258] Aghazadeh Mohandesi J, Majidi B. Fatigue damage accumulation in carbon/epoxy laminated composites. Materials and Design. 2009;30(6):1950-6.

[259] Kordatos EZ, Myriounis DP, Hasan ST, Matikas TE. Monitoring the fracture behavior of SiCp/Al alloy composites using infrared lock-in thermography. 2009.

[260] Maldague XPV. Introduction to NDT by active infrared thermography. Materials Evaluation. 2002;60(9):1060-73.

[261] Toubal L, Karama M, Lorrain B. Damage evolution and infrared thermography in woven composite laminates under fatigue loading. International Journal of Fatigue. 2006;28(12):1867-72.

[262] Melvin AD, Lucia AC, Solomos GP. The thermal response to deformation to fracture of a carbon/epoxy composite laminate. Composites Science and Technology. 1993;46(4):345-51.

[263] Pitarresi G, Galietti U. A quantitative analysis of the thermoelastic effect in CFRP composite materials. Strain. 2010;46(5):446-59.

[264] Belakhdar K, Tounsi A, Benyoucef S, Bedia EAA, El Hassar SM. On the reduction of the interfacial stresses in a repaired beam with an adhesively bonded FRP plate. Composite Interfaces. 2010;17(1):1-14.

[265] Aglan H, Rowell T, Ahmed T, Thomas R. Durability assessment of composite repairs bonded to aircraft structures. Journal of Adhesion Science and Technology. 1999;13(1):127-48.

[266] Berbinau P, Filiou C, Soutis C. Stress and failure analysis of composite laminates with an inclusion under multiaxial compression-tension loading. Applied Composite Materials. 2001;8(5):307-26.

[267] Rose AABRJF. Advances in the bonded composite repair of metallic aircraft structure. Elsevier; 2002. p. 530.

[268] Hall SR. The Effective Management and Use of Structural Health Data. 2nd International Workshop on Structural Health Monitoring. Technomic, Lancaster PA1999. p. 265-75.

[269] Robertson J. Realistic application of CNTs. Materials Today. 2004;7(9):46-52.

[270] Shindo Y, Kuronuma Y, Takeda T, Narita F, Fu SY. Electrical resistance change and crack behavior in carbon nanotube/polymer composites under tensile loading. Composites Part B: Engineering. 2012;43(1):39-43.

[271] Popov VN. Carbon nanotubes: Properties and application. Materials Science and Engineering R: Reports. 2004;43(3).

[272] Vavouliotis A, Tsotra P, Kostopoulos V, Karapappas P, Miaris A, Nikolaou N. MWCNT-modified fiber reinforced composites with nano-sensing capabilities: A way towards the development of the new functional materials for space applications. 2006. p. 5523-30.

[273] Monti M, Natali M, Petrucci R, Kenny JM, Torre L. Carbon nanofibers for strain and impact damage sensing in glass fiber reinforced composites based on an unsaturated polyester resin. Polymer Composites. 2011;32(5):766-75.

[274] Angelidis N, Wei CY, Irving PE. The electrical resistance response of continuous carbon fibre composite laminates to mechanical strain. Composites Part A: Applied Science and Manufacturing. 2004;35(10):1135-47.

[275] Wang X, Wang S, Chung DDL. Sensing damage in carbon fiber and its polymer-matrix and carbon-matrix composites by electrical resistance measurement. Journal of Materials Science. 1999;34(11):2703-13.

[276] DeTeresa SJ. Piezoresistivity and failure of carbon filaments in axial compression. Carbon. 1991;29(3):397-409.

[277] Todoroki A, Omagari K, Shimamura Y, Kobayashi H. Matrix crack detection of CFRP using electrical resistance change with integrated surface probes. Composites Science and Technology. 2006;66(11–12):1539-45.

[278] Li C, Thostenson ET, Chou TW. Sensors and actuators based on carbon nanotubes and their composites: A review. Composites Science and Technology. 2008;68(6):1227-49.

[279] Okuhara Y, Matsubara H. Memorizing maximum strain in carbon-fiber-reinforced plastic composites by measuring electrical resistance under pre-tensile stress. Composites Science and Technology. 2005;65(14):2148-55.

[280] Grammatikos SA, Gkikas G, Paipetis A. Monitoring strain and damage in multi-phase composite materials using electrical resistance methods. In: Ecke W, Peters KJ, Matikas TE, editors. 1 ed. San Diego, California, USA: SPIE; 2011. p. 79820K-6.

[281] Lu KL, Lago RM, Chen YK, Green MLH, Harris PJF, Tsang SC. Mechanical damage of carbon nanotubes by ultrasound. Carbon. 1996;34(6):814-6.

[282] Kaiser J. Results and conclusions from measurements of sound in metallic materials under tensile stress [PhD]. Munich1950.

[283] Landy MA, Armen Jr H, Eidinoff HL. ENHANCED STOP-DRILL REPAIR PROCEDURE FOR CRACKED STRUCTURES. 1986. p. 190-220.

[284] Ghfiri R, Amrouche A, Imad A, Mesmacque G. Fatigue life estimation after crack repair in 6005 A-T6 aluminum alloy using the cold expansion hole technique. Fatigue and Fracture of Engineering Materials and Structures. 2000;23(11):911-6.

[285] Baker AA. Fibre composite repair of cracked metallic aircraft components - practical and basic aspects. Composites. 1987;18(4):293-308.

[286] www.heatcom.com.

[287] www.afrl.af.mil.

[288] www.zimaclaboratories.com.